Design and Performance Optimization of the LHC Collimation System

by

Guillaume Robert-Demolaize

Engineering Degree, spec. Accelerator Physics,
Ecole Nationale Superieure de Physique de Grenoble, 2003

A dissertation submitted in partial satisfaction of the
requirements for the degree of
Doctor of Physics

in

Physics of Large Instruments

in the

GRADUATE DIVISION
of the
UNIVERSITE JOSEPH FOURIER, GRENOBLE

Committee in charge:
Prof. Bernard Vignon, Chair
Dr. Ralph Assmann
Prof. Jean-Marie De Conto
Dr. Angeles Faus-Golfe
Dr. Yannis Papaphilippou

November 2006

The dissertation of Guillaume Robert-Demolaize is approved:

Chair Date

Date

Date

Date

Date

Université Joseph Fourier, Grenoble

November 2006

Design and Performance Optimization of the LHC Collimation System

Abstract

Design and Performance Optimization of the LHC Collimation System

by

Guillaume Robert-Demolaize
Doctor of Physics in Physics of Large Instruments

Université Joseph Fourier, Grenoble

Prof. Bernard Vignon, Chair

The Large Hadron Collider (LHC) is presently under construction at CERN. The LHC is a circular accelerator that stores proton beams and accelerates them to a 7 TeV beam energy. The required bending fields are achieved with super-conducting magnets. The stored proton beams are collided in experimental detectors and produce a design luminosity of 10^{34} $\mathrm{cm}^{-2}\mathrm{s}^{-1}$. Every storage ring encounters unavoidable proton losses. The protons that diffuse into the so-called beam halo can touch accelerator components. In order to avoid quenches of the superconducting magnets, the halo protons must be removed before reaching the magnets. This is achieved with a multi-stage cleaning system, built out of two-sided collimators that are located at adequate positions in the machine. Due to the high stored beam intensity (required for high luminosity), the efficiency of the LHC beam cleaning must be much better than in any other exisiting machine: not more than 0.00002 % of protons hitting the collimators may escape and impact on any meter of super-conducting magnet at 7 TeV.

Detailed simulations of realistic operational conditions were performed to address the performance of the cleaning system. Beam loss maps show the distribution of proton losses around the machine down to the 10 cm level. The simulations were used for optimizing the system design and improving its overall efficiency by more than a factor of 10. The final performance of the so-called "phase 1" collimation system is discussed for the ideal LHC machine and for a case with a realistically perturbed orbit. For the phase 1 system, it is predicted that the allowable LHC intensity is limited to 43 % (ideal case) or 27 % (nominal orbit) of the nominal design value. The limitations and the assumptions used to derive theses limits are explained, including a list of characteristic loss locations around the ring.

A prototype LHC collimator was tested in the SPS with LHC-like proton beam conditions (injection energy). The control and beam-based alignment of the collimator gap was demonstrated down to the 50 μm level. Interesting results on the beam dynamics for halo particles were obtained, including slowly decaying beam losses after movement of collimator jaws. The robustness of the CFC (fiber-reinforced graphite) collimator jaws was experimentally confirmed and results were compared with predictions from numerical models.

Acknowledgments

I would like to take a moment to thank all the people that contributed to the completion of my PhD work: my supervisors, Ralph Assmann and Jean-Marie De Conto, for guiding me through all along the past 3 years; my reporters, Angeles Faus Golfe and Yannis Papaphilippou, for taking the time to read this whole report while already having a busy schedule; and Bernard Vignon whom I thank for agreeing to be part of my PhD committee.

Thanks also go to many of the people from the AB/ABP group at CERN, who welcomed me and helped me out with the understanding of all the physics aspects covered by the large topic of beam collimation: Jean-Pierre Riunaud, Oliver Bruning, Jean-Bernard Jeanneret, Stephane Fartoukh, Massimo Giovannozzi, Werner Herr, Elias Metral, Frank Schmidt, Frank Zimmermann, Helmut Burkhardt, Thys Risselada, Juliette Thomashausen, Muriel Macchi and Beatrice Hadorn. Thank you so much all of you. I also got some help from people from the collimation working group on collimator design and machine protection: Oliver Aberle, Verena Kain, Brennan Goddard and Rudiger Schmidt. Thanks a lot for dedicating some of your time for my understanding.

To my colleagues of the beam simulations for collimation: Stefano Redaelli, Chiara Bracco, Thomas Weiler and Javier Resta Lopez- thank you guys, I really appreciated working with you.

Thank you to the FLUKA team, responsible of the energy deposition studies: Alessandro Bertarelli, Matteo Magistris, Mario Santana Leitner, Andy Presland and Lucia Sarchiapone. Thanks for taking care of the magnets that my simulations were showering a bit too much. For the studies on collimation related background, many thanks go to Vadim Talanov and his group. They were of good help in reminding me that protecting is ok, but protecting too much could harm as well. I would also like to acknowledge the people working on the LHC beam loss monitoring system: Bernd Dehning, Eva Barbara Holzer, Laurette Ponce - it has been a great collaboration both inside and outside of the control room. And Laurette, promise, statistics are coming!!

Many thanks too to some people of the LHC Integration group: Samy Chemli, Catherine Magnier, Yvon Muttoni and Christian Rathjen. These people did an amazing job in finding some space in the tunnel for our collimators in regions where it was impossible to fit even a small slice of Swiss cheese!!

A special thank you to Nuria Catalan Lasheras for sharing with me her deep knowledge of the collimation theory. Congratulations again and best wishes for the future!!

During this PhD, I had the opportunity to work in collaboration with people of the Brookhaven National Laboratory. So many thanks to Angelika Drees, Steve Peggs, Wolfram Fischer, Fulvia Pilat, Steve Tepikian and Rama Calaga.

And I will always be grateful to my family for their continuous love and support during this entire period. This achievement is yours as well.

Lastly, huge thanks to all of my friends in Grenoble (and soon to be Toronto, pas vrai JB), St Genis, Geneva, Luton, Karlsruhe, Enschede and Gainesville. You cannot imagine how important you have been over the last 3 years...

A Albert et Yves.

Contents

List of Figures

List of Tables

Introduction (french)

Le Conseil Européen pour la Recherche Nucléaire (CERN) est en charge de la construction du Large Hadron Collider (LHC), un anneau de collision pour faisceaux de protons à hautes énergies (jusqu'à 7 TeV). Le LHC va permettre d'étudier des domaines de la physique des particules encore jamais atteints, grâce principalement aux 4 points d'expérience répartis autour de l'anneau souterrain et aux détecteurs qui y sont associés. Les nouvelles limites établies par ces expériences sont liées (1) à l'énergie des faisceaux de protons et (2) au nombre d'évènements mesurés par les détecteurs.

1. Comme indiqué sur la Figure 0.1, les faisceaux du LHC peuvent être accélérés jusqu'à une énergie 7 fois plus grande que pour toute autre machine actuelle. Ceci est rendu possible par l'utilisation d'aimants supraconducteurs (SC), qui donnent une trajectoire circulaire aux faisceaux de protons, maintiennent ces protons groupés autour de cette trajectoire et les concentrent aux points de collisions. Les dipôles du LHC ont une architecture à double chambre avec un champ nominal de 8.33 T, ce qui implique un fonctionnement à des températures cryogéniques de 1.8 K et 4.5 K. Chaque aimant SC est alors particulièrement sensible à la moindre source de chaleur, comme des pertes locales de protons par exemple. Il existe un niveau d'échauffement au delà duquel les câbles de courant perdent leur propriétés SC et redeviennent résistants : ce changement d'état est appelé *quench*. Pour des pertes de faisceau dites lentes (c.a.d. sur plusieurs tours), le niveau de quench pour un aimant du LHC se situe autour de 10 $\mathrm{mJ/cm^3}$.
2. Le nombre d'évènements mesurés par l'un des détecteurs du LHC est directement lié à la luminosité L de la machine, ayant pour valeur nominale 10^{34} $\mathrm{cm^{-2}s^{-1}}$ pour les faisceaux de protons. Une telle luminosité est obtenue lors de collisions de paquets de protons de petite taille et de haute intensité. Dans le cas du LHC, cela se traduit par une énergie totale d'environ 360 MJ stockés dans chaque faisceau (3×10^{14} protons à 7 TeV), soit près de 200 fois plus que ce que peuvent produire des machines telles que le TEVATRON (USA) ou encore HERA (Allemagne), et 10 ordres de grandeurs plus grand que le niveau de quench des aimants SC de la machine. A titre de comparaison, chaque faisceau représente l'équivalent de 90 kg de TNT en terme d'énergie transportée.

Le design du LHC confère une stabilité maximale à chacun des deux faisceaux de protons, qui peuvent ainsi être conservés dans l'anneau principal pendant plusieures heures, avec un temps de vie pour l'intensité nominale avoisinant les 30 heures. Cependant, même dans ces conditions, si des protons venaient à être perdus dans l'un des aimants SC de la

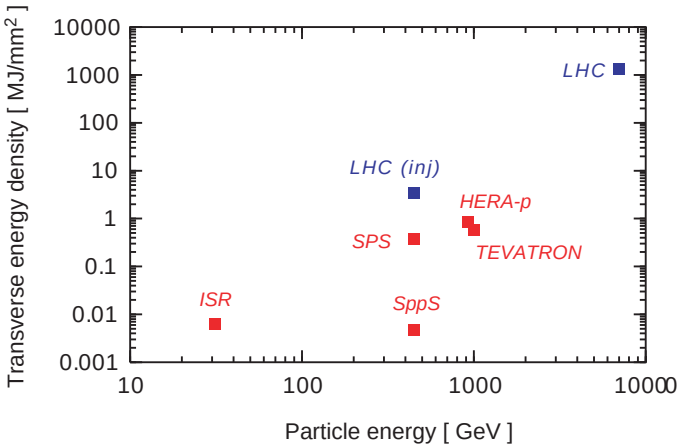

FIG. 0.1: Transverse energy density at the collimators versus beam energy for different proton storage rings. Courtesy of R. Assmann et al. from [6].

machine, le dépôt d'énergie occasionné serait toujours suffisant pour provoquer un quench et par conséquent l'arrêt des opérations, du moins jusqu'à ce que l'aimant en question ait retrouvé ses propriétés SC. L'expérience a de plus démontré, lors de l'utilisation de machines similaires au LHC, que des phénomènes de pertes instantanées pouvaient se produire. Pour le LHC, un scénario réaliste voudrait que, dans le pire des cas, 1 % du faisceau puisse être perdu en 10 secondes, soit un ratio de 4×10^{11} protons/s.

Dans le cas du LHC, aucune perte de faisceau dans les aimants SC n'est permise, du fait de la différence entre l'énergie stockée et le niveau de quench. Un système de collimation (ou "nettoyage") de faisceau est donc obligatoire afin de réduire le niveau des pertes protoniques qui auront nécessairement lieu au cours des opérations de la machine. La collimation de faisceau dans le cadre du LHC doit entre autres :

- empêcher tout quench d'aimant SC pendant l'utilisation de la machine ; l'efficacité du système doit pour cela être maximale (au moins 99.9 % dans tous les cas),
- protéger tous les éléments de l'anneau contre les pertes de faisceau, qu'elles soient propres au fonctionnement de la machine ou accidentelles (casse d'un équipement ou erreur humaine),
- permettre un certain niveau de contrôle sur le bruit de fond dans les détecteurs,
- limiter le niveau de radiation reçu par les divers équipements électroniques et magnétiques de la machine.

Cette thèse de doctorat traite de l'état d'avancement et l'efficacité du système de collimation du LHC tel qu'il sera installé pour permettre le début des opérations machine en 2007. Pour y arriver, un modèle détaillé de la séquence de l'anneau principal avec collimateurs a été mis en place, modèle qui inclut également une définition complète de l'ouverture de la machine. L'efficacité du système de collimation est établie à partir d'un outil de simulations numériques spécifiquement créé et installé sur des serveurs de calculs appropriés. Ce programme permet de suive les trajectoires d'un grand nombre de particules (environ 5 millions) sur une centaine de tours selon divers modes de fonctionnement de la machine. Les résultats obtenus ont alors permis d'optimiser les paramètres mécaniques du système

de collimation : nombre d'éléments, position, orientation transverse et choix du matériau.

Ce processus de simulation et le niveau d'efficacité du système ainsi simulé sont présentés en détail dans ce rapport. Les Chapitres 1 et 2 introduisent les concepts de base sur le mouvement des protons dans le LHC, les différents types d'ouverture pour une machine de ce type ainsi que les divers mécanismes physiques qui peuvent expliquer les pertes de protons dans l'anneau. Le Chapitre 3 est une revue du système de collimation du LHC et du modèle numérique utilisé pour simuler son action sur des faisceaux de protons. Les cartes de pertes obtenues à partir des outils numériques développés pour cette thèse sont présentées dans le Chapitre 4 ; un scénario plausible de perturbation de la machine est également étudié dans ce chapitre afin d'évaluer la sensitivité du système face à des conditions réalistes d'opération. La limite en intensité de faisceau fixée par le système de collimation tel qu'il sera installé peut ainsi être établie à la fois pour le cas idéal et pour un cas réel. Enfin, le Chapitre 5 fait un compte-rendu des résultats expérimentaux obtenus lors des tests sur le contrôle des collimateurs en conditions réelles (c.a.d. avec un faisceau type LHC).

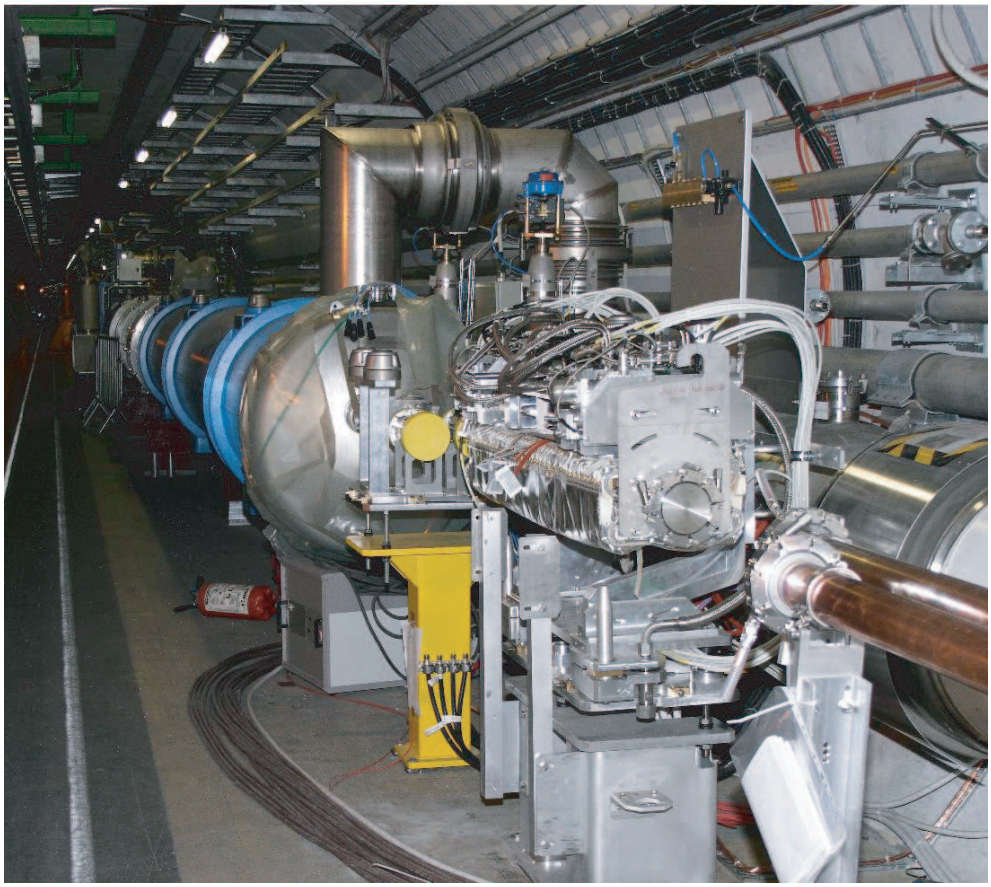

FIG. 0.2: Collimator installed in front of a series of LHC dipole magnet (blue elements).

Introduction

The European Organization for Nuclear Research (CERN) is presently constructing the Large Hadron Collider (LHC) [1], a circular proton-proton collider with 7 TeV beam energy. The LHC will extend the knowledge of particle physics into a new regime. Four major particle physics experiments are located in the underground ring of the LHC accelerator [2, 3, 4, 5]. The discovery reach for particle physics is given (1) by the beam energy (or particle momentum) of the protons and (2) by the event rate in the particle physics experiments.

1. As seen in Figure 0.1, the LHC extends the frontier in beam energy by a factor 7 with the use of highly advanced super-conducting (SC) magnets. These magnets bend the charged proton beams into a circle, provide the required focusing fields for the stored beams and focus the beams into the collision points. The LHC bending magnets are two-bore magnets with a nominal field of 8.33 T. Magnets are operated at cryogenic temperatures of 1.8 K and 4.5 K. At these temperatures, the SC magnets become very sensitive to any heat sources like e.g. beam losses. If any magnet heating exceeds a particular threshold called *quench limit*, the SC cables change state and become resistive ("quench"). Typical quench limits in the LHC are around 10 mJ/cm^3 for slow losses.

2. The event rate in the LHC experimental insertions is described by the accelerator given luminosity L with a nominal design value of 10^{34} cm^{-2}s^{-1}. This high luminosity is achieved with high-intensity proton beams that are collided at special places of small transverse beam area. The LHC will feature proton beams with a total stored energy of up to 360 MJ per beam (3×10^{14} protons at 7 TeV). This extends present achievements at TEVATRON (USA) and at HERA (Germany) by about a factor 200, as shown in Figure 0.1. It is noted that the stored beam energy is 10 orders of magnitude higher than the quench limit of SC magnets and corresponds to the equivalent of 90 kg of TNT explosives.

The LHC beams are designed to have maximum stability and to be stored for many hours. The nominal beam intensity lifetime should be around 30 h. Already in this nominal case, beam losses would induce enough heating in the SC magnets to cause quenches and interruption of the beam operation (until magnets have been recovered to their full SC state). In addition, it is experienced in all accelerators that additional transient losses (spikes of short duration) occur. A "realistic" peak beam loss rate of 1 % in 10 s has been specified for the LHC (4×10^{11} protons/s).

Beam losses in the LHC cannot occur directly at the SC magnets, due to the high stored energy and the low quench limits. A sophisticated collimation (or "beam cleaning") system [7, 8] is therefore required in order to intercept the unavoidable beam losses in the LHC. Collimation must fulfill several important functions for the LHC:

- Cleaning of the LHC beam losses with sufficient efficiency (> 99.9 % in all conditions) to avoid quenches of SC magnets for regular operation.
- Protection of the LHC equipment against regular and irregular beam losses (including survival of collimators themselves). Irregular losses may come from equipment failure or wrong operation.
- Limited control of beam induced background in the particle physics experiments.
- Handling of beam-induced radiation effects on electronics and other accelerator equipment.

This doctoral thesis describes the LHC collimation system as it is now being constructed for completion of the LHC in 2007. In course of the work, a complete LHC accelerator model was set up with collimators and a full aperture model. In order to assess the expected performance of the collimation system, advanced simulation tools were developped and installed on special computer clusters. Large ensemble particle tracking (5×10^6 protons over hundreds of turns) was used to predict the efficiency of the system for many different scenarios. The results were used iteratively to optimize the final number, locations, orientations and materials of collimators.

This simulation procedure and the ideal performance of the final collimation system are presented in detail in this thesis. Chapters 1 and 2 review the basics of protons motion in the LHC, the different types of machine aperture and the loss mechanisms experienced by the circulating beam. Chapter 3 presents the LHC Collimation System and the way it is simulated in the tracking software for collimation studies. Distribution of LHC losses around the ring are analyzed in detail in Chapter 4; studies for an imperfection scenario are presented in order to describe the sensitivity of cleaning efficiency against realistic perturbations. In that same chapter, the intensity reach of the LHC is predicted for the system presently under construction. Finally, experimental results from beam tests of prototype LHC collimators are discussed in Chapter 5.

Chapter 1

Theory of the LHC accelerator and its collimation system

When it comes to the study of beam dynamics in an accelerator, the first step is to assume a linear approximation of the magnetic fields used for keeping the particles in their designed trajectories. Real machines like the LHC are generally not highly linear, but the design is still based on this approximation because of its simplicity and the fact that most of the functions used to define the motion of beam in the machine are derived from it.

In the following, the basics of particles motion in a circular accelerator using the linear approximation are presented, following the derivation of [9, 10, 11]. They are then developed taking into account non-linearities which lead to the idea of a machine dynamic aperture. The design goals and characteristics of an efficient collimation system for a circular machine are also reviewed.

1.1 Basic Principles of Linear Beam Dynamics

1.1.1 Equations of motion

Derivation of the equations of motion in a circular accelerator can be found in Appendix A. Using the longitudinal coordinate s along the curved design orbit and a moving frame along this trajectory (see Figure A.2), one can find the coupled equations of transverse motion for charged particles (as it is the case for the LHC with circulating protons):

$$\boxed{\begin{array}{c} x'' + (K_0 + \frac{1}{\rho_x^2}) \cdot x = \frac{1}{\rho_x} \cdot \frac{\Delta p}{p_0} + \underline{K_0} \cdot y \\ \\ y'' - K_0 \cdot y = \underline{K_0} \cdot x \end{array}} \quad . \tag{1.1}$$

In the system (1.1), the time coordinate t is replaced by the s coordinate to define the particle trajectory, with $s = c \cdot t$ and c the speed of light. The notation z' (z'') corresponds to the first (second) derivative of the transverse coordinate z versus s.

The terms K_0 and $\underline{K_0}$ are the regular and skew normalized magnetic gradients of the quadrupole magnets of the machine. K_0 is called the *focusing gradient*, while $\underline{K_0}$

introduces *linear coupling* between the two planes. ρ_x is the bending of the design orbit in the horizontal plane and the term $\frac{1}{\rho_x^2}$ is the *weak sector magnet focusing*. Lastly, the term $\frac{\Delta p}{p_0}$ (with $\Delta p = p - p_0$) is the momentum deviation of particles which leads to an orbit shift in the horizontal plane; it is known as the *chromatic* term.

1.1.2 Solutions of the equations of motion

Using z for either transverse coordinate x or y and $K_z(s)$ the corresponding focusing function, and assuming that all particles have no energy spread (ie. $\frac{\Delta p}{p_0} = 0$), the system (1.1) can be generalized to:

$$z''(s) + K_z(s) \cdot z(s) = 0 \ . \tag{1.2}$$

Equation (1.2) is also called the Hill's equation. Its general solution can be written as:

$$z(s) = z_{betatron}(s) = \sqrt{A_z \beta_z(s)} \cdot \sin(\mu_z(s) + \mu_{z_0}), \tag{1.3}$$

with $\beta_z(s)$ the amplitude modulation of the oscillation in the transverse z plane. It is referred to as the *betatron function*, and $\mu_z(s)$ is the *phase advance* of this oscillation, defined as:

$$\mu_z(s) = \int_0^s \frac{ds}{\beta_z(s)} \ .$$

From (1.3), the invariants of motion are the amplitude A_z and the initial phase μ_{z_0}. By taking the derivative of the Hill's solution, one has the following equation for A_z:

$$\boxed{\beta_z(s) \cdot (z'(s))^2 + 2\alpha_z(s) \cdot z(s) \cdot z'(s) + \gamma_z(s) \cdot z^2(s) = A_z} \quad , \tag{1.4}$$

with $\alpha_z(s) = -\frac{1}{2}\beta_z'(s)$ and $\gamma_z(s) = \frac{1+\alpha_z^2(s)}{\beta_z(s)}$ called, together with $\beta_z(s)$, the *Twiss parameters*. From (1.4), the map of the particle trajectory at any given s in a one-dimensional phase space $z - z'$ has an elliptic shape of area πA_z (e.g. Figure A.3). This value remains constant for any s along the machine, even though the shape of the ellipse is s-dependent. The definition of the *beam emittance* ϵ is related to the area of the ellipse as:

$$\text{area of the ellipse} = \pi \cdot \epsilon \ .$$

Based on the multi-particle nature of the beam, one can define a statistical quantity, the root mean square emittance $\epsilon_{rms,z} = \sqrt{\overline{z^2 z'^2} - \overline{zz'}^2}$. The *betatronic beam size* $\sigma_z^\beta(s)$ and the *beam divergence* $\omega_z(s)$ shown in Figure A.4 are then derived as:

$$\begin{aligned} \sigma_z^\beta(s) &= z_{max}(s) = \sqrt{\epsilon_{rms,z}\beta_z(s)} \\ \omega_z(s) &= z'_{max}(s) = \sqrt{\epsilon_{rms,z}\gamma_z(s)} \end{aligned} \quad . \tag{1.5}$$

In the following, the betatronic beam size in the transverse plane z at a location s along the

machine will be referred to as $\sigma_z(s)$. With (1.5), the transverse coordinates (z, z') can be normalized locally into the coordinates (Z, Z') to describe the trajectory in phase-space of any given particle with a circle (instead of an ellipse). Following the derivations in Appendix A, one gets as a definition for the normalized coordinates.

$$\begin{aligned} Z(s) &= \frac{1}{\sigma_z(s)} \cdot z(s) \\ Z'(s) &= \frac{1}{\sigma_z(s)}(\alpha_z(s) \cdot z(s) + \beta_z(s) \cdot z'(s)) \end{aligned} \quad , \tag{1.6}$$

with $Z^2(s)+Z'^2(s) = N_z^2(s)$ where $N_z(s)$ is an integer value called the *normalized amplitude* of the considered particle at a given location s in the machine. The system (1.6) can also be described using matrices:

$$\begin{pmatrix} Z(s) \\ \\ Z'(s) \end{pmatrix} = \frac{1}{\sigma_z(s)} \begin{pmatrix} 1 & 0 \\ \\ \alpha_z(s) & \beta_z(s) \end{pmatrix} \begin{pmatrix} z(s) \\ \\ z'(s) \end{pmatrix} \quad . \tag{1.7}$$

Using normalized coordinates, one can obtain an expression of the equations of motion (1.1) between two points 1 and 2 of the machine through the matrices

$$\begin{pmatrix} Z_2(s) \\ \\ Z_2'(s) \end{pmatrix} = \begin{pmatrix} \cos(\Delta\mu_{1-2}) & \sin(\Delta\mu_{1-2}) \\ \\ -\sin(\Delta\mu_{1-2}) & \cos(\Delta\mu_{1-2}) \end{pmatrix} \begin{pmatrix} Z_1(s) \\ \\ Z_1'(s) \end{pmatrix} \quad , \tag{1.8}$$

with $\Delta\mu_{1-2}$ the difference in phase advance between the two locations. Considering the case in which points 1 and 2 are identical (i.e. the considered particle performs a complete turn in the machine), $\Delta\mu_{1-2}$ can be considered as the phase difference over one turn: $\Delta\mu_{1-2} = \Delta\mu_{turn}$.

An important quantity that can now be defined is the *tune* $Q_z = \frac{\Delta\mu_{turn}}{2\pi}$ of the machine, which corresponds to the number of periods of oscillations of the solution to Hill's equation (see (1.3)) performed by the considered particle over one turn. Q_z should be a non-integer value, and is even always chosen to be an irrational number for circular machines in order to avoid resonances (see Appendix B).

Considering now the real case of a distribution of particles with some energy spread, the complete solution of the equations of motion can be written as the sum of the betatronic solution to Hill's equation and the term coming from the energy spread:

$$z(s) = z_{betatron}(s) + D_z(s) \cdot \frac{\Delta p}{p_0}, \tag{1.9}$$

with $\frac{\Delta p}{p_0}$ the relative momentum deviation and $D_z(s)$ the dispersion function in the corresponding transverse plane. $D_z(s)$ fulfills the particular inhomogeneous Hill's equation:

$$D_z''(s) + K_z(s) \cdot D_z(s) = \frac{1}{\rho(s)} \ .$$

As for the $\beta_z(s)$ function, $D_z(s)$ depends only on the lattice and not on the beam parameters. In the following, the dispersion function $D_x(s)$ in the horizontal plane will be large because of horizontal bending dipoles, while the vertical dispersion $D_y(s)$ will only be fed by parasitic vertical dipole components. The *normalized dispersion* is defined as $\mathcal{D}_z(s) = \frac{D_z(s)}{\sigma_z^{\beta}(s)}$.

1.2 The LHC accelerator

The term LHC in this report always refer to the main ring lattice which installation is being finalized in the former LEP tunnel of CERN. With a circumference close to 27 km (see Table 1.1), this machine is the largest one of all accelerator physics experiments and will accelerate proton beams up to 7 TeV. The two proton beams injected in the LHC ring are issued from other CERN accelerator structures: once generated, the protons are sent via a linear accelerator (LINAC) into the PS synchrotron, then in the SPS circular booster which makes the bunch energy reach the injection value of 450 GeV. The main purpose of the LHC is the discovery of the Higgs boson, for which two dedicated experimental insertions are set up and include gigantic particle detectors [2, 4]. Various other particle physics experiments will also be performed thanks to the LHC like b-physics, collisions with lead ions as well as an attempt to measure the complete proton-proton cross section (the TOTEM experiment [12]).

Table 1.1: LHC storage ring parameters. Taken from [1].

		Injection	**Collision**
Geometry			
Ring circumference	[m]	26658.8832	
Ring separation in arcs	[mm]	194	
Main magnet			
Effective vacuum screen height (with tolerances)	[mm]	44.04	
Effective vacuum screen width (with tolerances)	[mm]	34.28	
Number of main bending magnets		1232	
Length of main bending magnets	[m]	14.3	
Field of main bending magnets	[T]	0.535	8.33
Bending radius	[m]	2803.95	

The nominal luminosity will be achieved with 2808 bunches stored in each of the two circulating beams, each bunch containing 1.15×10^{11} protons. The two beams have the same transverse beam emittances: $\epsilon_x = \epsilon_y = \frac{1}{\gamma_{rel}} \cdot 3.75$ μm, with γ_{rel} the relativistic factor. The transverse energy density in the LHC at 7 TeV reaches about 1 GJ/mm^2, which is three orders of magnitude larger than what is handled in any other present machine (see Figure 0.1). This energy circulates in a lattice which is mostly made of superconducting magnets, with about 10^{-8} of the beam power being sufficient to quench one of them.

Tables 1.2 and 1.3 list the nominal and ultimate parameters achieved in the LHC main ring once commissioning has been performed. The value quoted for the emittance at injection energy corresponds to the transverse distribution of particles as it is delivered by the SPS accelerator via the injection points in IR2 and IR8. One would have to take into account increases due to injection errors and optics mis-match. The transverse RMS beam sizes mentioned in Table 1.2 are calculated from the respective values given for the Twiss parameter β^* in Table 1.3, with $\beta^* = \beta_x = \beta_y$ at the location of the interaction point (IP) only.

Table 1.2: LHC beam parameters for peak luminosity. Taken from [1].

		Injection	**Collision**
Beam data			
Proton energy	[GeV]	450	7000
Relativistic gamma		479.6	7461
Number of particles per bunch		1.15×10^{11}	
Number bunches		2808	
Longitudinal emittance (4 σ)	[eVs]	1.0	2.5
Transverse normalized emittance	[μm rad]	3.5	3.75
Stored energy per beam	[MJ]	23.3	362
Peak luminosity related data			
RMS bunch length	[cm]	11.24	7.55
RMS energy spread $\delta E/E_0$	[10^{-4}]	3.06	1.129
RMS beam size at the IP1 and IP5	[μm]	375.2	16.7
RMS beam size at the IP2 and IP8	[μm]	279.6	70.9
Peak luminosity in IP1 and IP5	[cm^{-2} sec^{-1}]	-	1.0×10^{34}

Table 1.3: LHC machine parameter for peak luminosity. Taken from [1].

		Injection	**Collision**
Half crossing angle for IP1 and IP5	[μrad]	$\pm$ 160	$\pm$ 142.5
Half parallel separation at IP1 and IP5	[mm]	$\pm$ 2.5	0.0
Half crossing angle at IP2	[μrad]	$\pm$ 240	$\pm$ 150
Half parallel separation at IP2	[mm]	$\pm$ 2.0	$\pm$ 0.178
Half crossing angle at IP8	[μrad]	$\pm$ 300	$\pm$ 200
Half parallel separation at IP8	[mm]	$\pm$ 2.0	0.0
Plane of crossing in IP1 and IP2		vertical	
Plane of crossing in IP5 and IP8		horizontal	
β^* at IP1 and IP5	[m]	17	0.55
β^* at IP2	[m]	10	0.5 (Pb runs) 10 (p runs)
β^* at IP8	[m]	10	$1.0 \leftrightarrow 50$

In the 4 experimental insertions, the closed orbit of each beam is modified to make the beams collide at the designed interaction point (IP) with an angle, in order to avoid multiple crossing points locally. Collisions occur in the plane mentioned in Table 1.3. These modifed trajectories are called *crossing schemes* and are generated by dedicated pairs of dipole magnets. Crossing schemes for the two high luminosity experimental insertions are shown in Figures 1.1 and 1.2 for both injection and collision energy.

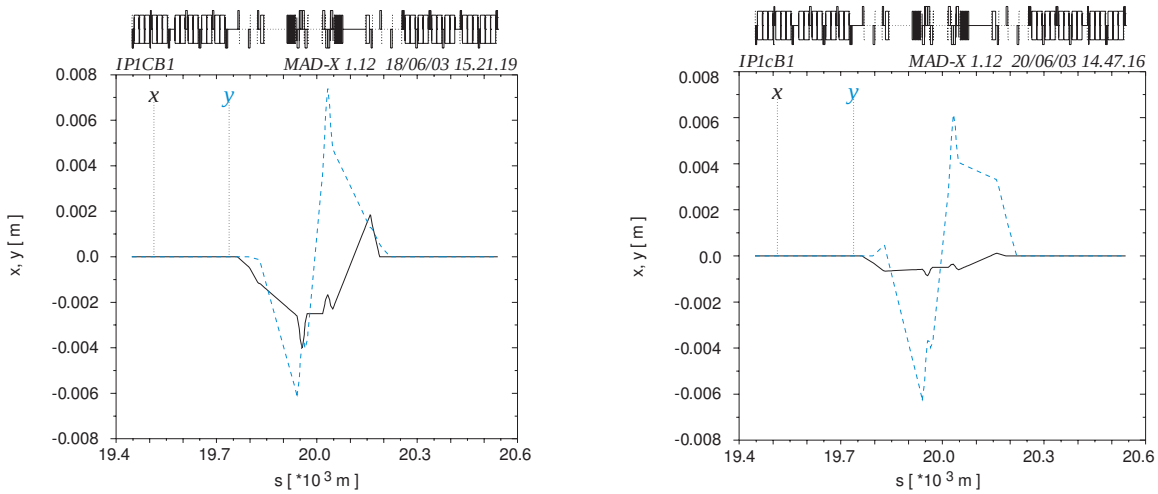

Figure 1.1: Horizontal (solid line) and vertical (dashed line) crossing schemes in IR1 at injection (left) and collision (right) energy. The longitudinal s position refers to IP3.

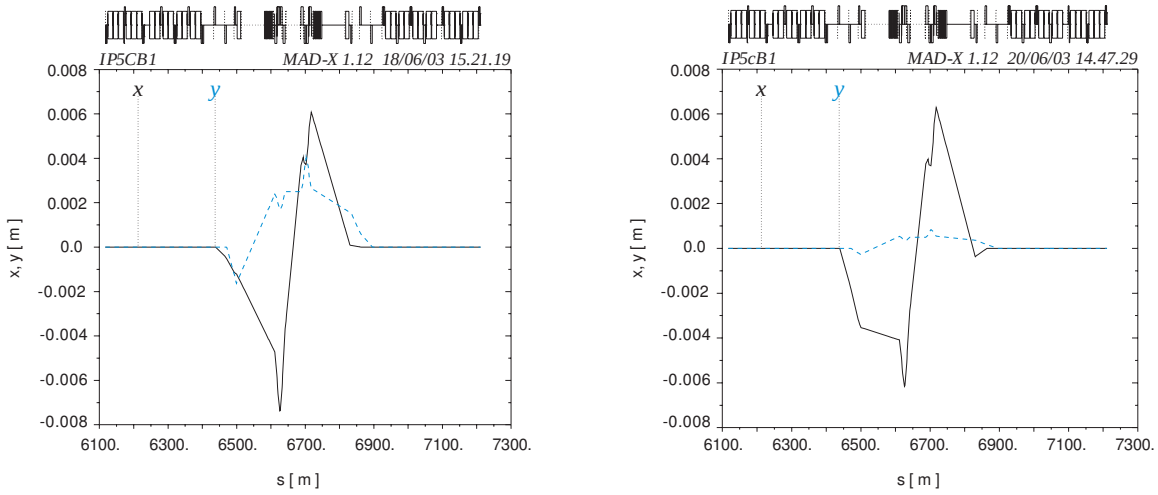

Figure 1.2: Horizontal (solid line) and vertical (dashed line) crossing schemes in IR5 at injection (left) and collision (right) energy. The longitudinal s position refers to IP1.

1.3 Definition of the machine aperture

1.3.1 Linear case: geometrical aperture

The aperture available by construction of the lattice is called the geometric aperture of the ring A_{geom}. It corresponds to the limitations in both transverse planes set by the mechanical openings of the machine equipments (e.g. magnets, instruments). It is generally given in units of the *real* beam size σ_z^{real} defined as:

$$\sigma_z^{real}(s) = \sqrt{\beta_z(s) \cdot \epsilon_{rms} + \left(D_z(s) \cdot \left(\frac{\Delta p}{p_0} \right)_{rms} \right)^2} \ , \tag{1.10}$$

and calculated from the estimated specific parameters of the machine (see previous section for LHC values). The geometric aperture is directly related to the maximum area that can be covered by the phase-space ellipse at any location in the machine. This area is called the *beam acceptance* $\mathcal{A}_z$ of the machine, given by:

$$\mathcal{A}_z(s) = \frac{\left(A_{geom}(s) \cdot \sigma_z^{real}(s) \right)^2}{\beta_z(s)} \ . \tag{1.11}$$

A particle is considered lost at the first s location in the machine where $z \geq A_{geom} \cdot \sigma_z^{real}$; such a location is referred to as an *aperture restriction*. Due to the variation of both the betatron and the dispersion functions with s, the shape of the *real-space beam ellipse*, which can be defined as an ellipse containing a distribution of particles with normalized amplitudes up to 1 σ_z^{real}, is not constant around the ring. Beam losses can therefore occur anywhere in a lattice, though most of the time the design of the machine allows pointing out some specific locations at which the beam can be predicted to be lost in a controlled way.

1.3.2 Non-linear case: dynamic aperture

In a real machine, the lattice presents non-linearities coming from different types of elements, which create some distortion in the linear model orbit. Non-linear elements include e.g. sextupole magnets, used to correct the chromaticity of the machine. Multipole field errors coming from magnets fabrication are another example. Due to these non-linearities, a given stable particle will achieve betatronic oscillations with a limited maximum amplitude called the *dynamic aperture* A_{dyn}, illustrated in Figure 1.3. Some particles drift away from the beam core due to machine operations (like machine tuning or error during orbit correction) and other processes. These particles may reach an amplitude larger than the dynamic aperture and are then said to be part of the *beam halo*, corresponding to the fraction of the beam which will either intercept the geometric aperture and get lost or get scraped by beam collimators (if there are any in the machine).

For linear machines, the dynamic aperture is infinite, while real machines present a limited value which is often larger than the geometric aperture. It is only in the case of a machine with strong non-linearities like the LHC that A_{dyn} can be smaller than A_{geom}. The value of A_{dyn} is obtained via tracking simulations and analytical models [14, 15].

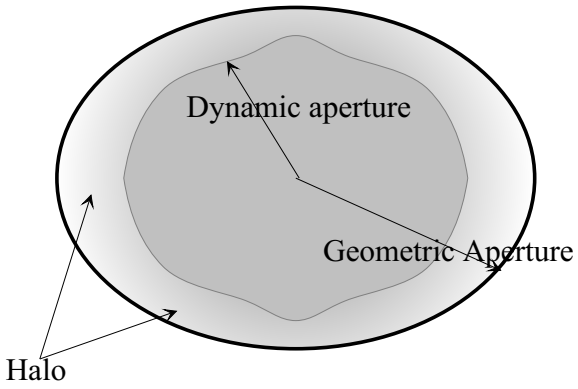

Figure 1.3: Geometric and dynamic aperture in a circular accelerator. Particles outside the dynamic aperture form the beam halo. For each of the two types of aperture, the value is given by the smaller one in the x-y plane. Courtesy of N. Catalan-Lasheras from [13].

These models are derived from experience and operation of comparable machine like SPS and HERA. Models are required to estimate the value of A_{dyn} since a finite value for the dynamic aperture can only be achieved after some minutes in realistic beam conditions (a LHC fill already taking 7 minutes to complete), as some chaotic particles can circulate in the machine for 10^5 turns and get lost before 10^6 turns. Even with an upgrade in computing resources, tracking codes still need about two days to perform the full dynamic aperture simulations for about ten seconds of real LHC time (about 10^5 turns).

For the tracking studies, the relevant number of turns can be taken from the length of the injection plateau, as most of the instabilities will occur during the filling of the machine. Results of studies of the model of the LHC lattice give a dynamic aperture of 12 σ_z. For a pair of primary collimators with half-openings $n_1 = 7\sigma_r$, the beam halo extends to $A_r \approx 10\sigma_r$ with a maximum value in each transverse plane $A_{x,y} \approx 8.4\sigma_{x,y}$, well inside the dynamic aperture [7]. Since the efficiency of the cleaning system is another major concern in the design of the collimators, the nominal setting for the opening of LHC collimators was set to 6 σ_r. Based on studies in the LHC case presented in [16], once a particle reaches the unstable region (i.e. with a normalized amplitude larger than the dynamic aperture) its diffusion speed away from the core of the beam is about 5.3 nm/turn. Such a value has no impact on the settings of the collimators as the drift should not be significant considering the cleaning times in the machine, roughly 100 turns.

1.3.3 Longitudinal aperture

Once particles are injected, they get accelerated by a radio-frequency (RF) field synchronized with the increase of the magnetic field each turn in order for the orbit to remain constant. Particles are then said to follow a *synchrotron motion*. The RF field used to perform the acceleration is usually sinusoidal, therefore the process is strongly related to a determined phase and energy gain [11].

There is a well defined synchronous particle which always passes through the accelerating cavity at the same phase ϕ_s and has the nominal energy E_s. It is therefore sufficient

to follow the rest of the particles with respect to the synchronous one. The longitudinal equations of motion using these two coordinates are writen:

$$\begin{aligned} \frac{d}{dt}(\frac{\Delta E}{h\omega_{turn}}) &= k(\sin(\phi) - \sin(\phi_s)) \\ \frac{d}{dt}(\phi - \phi_s) &= -k'(\frac{\Delta E}{h \cdot \omega_{turn}}) \end{aligned} \quad , \tag{1.12}$$

with k, k' two constants and $\Delta E = E - E_s$ the energy offset which is normalised to the RF frequency (being equal to an integer number h times the revolution frenquency ω_{turn}).

The synchronous phase ϕ_s is taken at the centre of the bunch: a particle located at this position will therefore receive the exact amount of energy to keep up with the increase of the magnetic field. For particles around the synchronous one, it depends on a criteria known as the *slip factor* χ_c which gives the variation of the revolution frequency versus the change in momentum for a given particle:

$$\frac{d\omega_{turn}}{\omega_{turn}} = \chi_c \cdot \frac{dp}{p} = (\frac{1}{\gamma_{rel}^2} - \alpha_c) \cdot \frac{dp}{p} \ ,$$

where γ_{rel} is the relativistic factor between the energy of the considered particle and its rest mass E_0: $\gamma_{rel} = \frac{E}{E_0}$. α_c is the *momentum compaction factor* and can be roughly estimated in terms of the horizontal tune as $\alpha_c \approx \frac{1}{Q_x^2}$. A given particle is said below (respectively above) transition when its γ_{rel} is smaller (resp. larger) than the transition energy $\gamma_{trans} = \frac{1}{\sqrt{\alpha_c}}$.

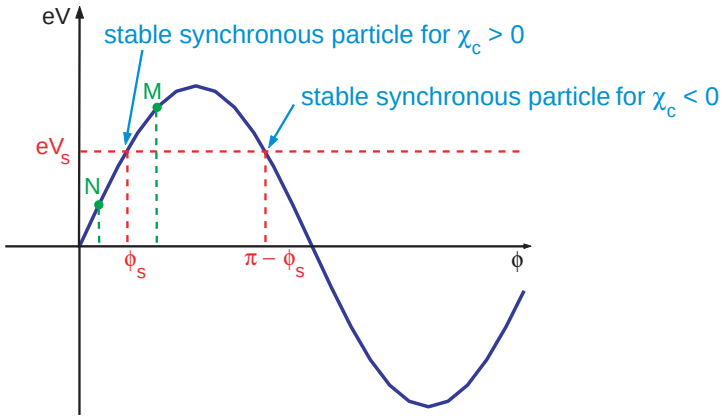

Figure 1.4: Example of phase stability for particles around the synchronous phase ϕ_s. The cases below and above transition energy are represented.

In Figure 1.4, considering the "below transition" case, the particle N is in advance compared to the synchronous particle. It will get a smaller acceleration, therefore a smaller revolution frequency ($\chi_c > 0$). The next time the bunch gets to the accelerating cavity, this particle will be late compared to the synchronous particle (equivalent M position) and get a larger acceleration, i.e. a larger ω_{turn}: this particle is stable around ϕ_s. For the "above

transition" case ($\chi_c < 0$, the LHC configuration), the synchronous phase would have to shift to $\pi - \phi_s$ for the considered particle to remain stable.

Figure 1.5 shows an example of particle trajectories in the longitudinal phase-space for a machine with acceleration. Particles with small energy offsets follow bounded trajectories called *synchrotron oscillations* around the synchronous particle at ϕ_s. When the beam is accelerated, since the system 1.12 is non-linear, there is a maximum amplitude called *separatrix* which sets a limit outside of which particles are not stable anymore and start loosing energy during each turn untill they get lost in the machine. The phase-space area inside of the separatrix is called the *RF bucket* and is the equivalent of the beam core in the transverse plane.

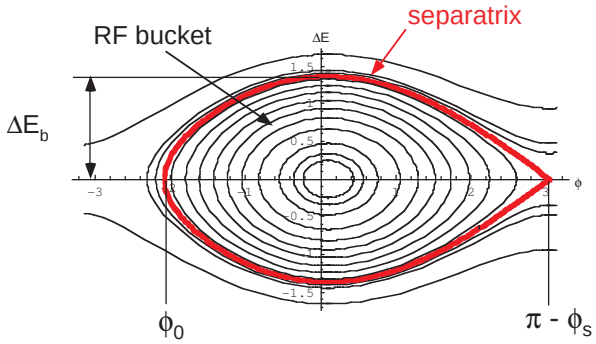

Figure 1.5: Example of particle trajectories in the longitudinal phase-space for a machine with acceleration. Trajectories are centered around the synchronous phase ϕ_s. The separatrix (red line) is the border between bounded and unbounded motion. Taken from [17].

ΔE_b and ϕ_0 from Figure 1.5 can be expressed as functions of ϕ_s:

$$\begin{aligned} \Delta E_b &= k'' \sqrt{1 - (\frac{\pi}{2} - \phi_s) \cdot \tan(\phi_s)} \\ \cos(\phi_0) + \phi_0 \cdot \sin(\phi_0) &= -\cos(\phi_s) + (\pi - \phi_s) \cdot \sin(\phi_0) \end{aligned} \tag{1.13}$$

The half-height ΔE_b of the RF bucket determines the *energy acceptance* of the machine, which can be assimilated to the longitudinal dynamic aperture. The geometric longitudinal aperture is also given in terms of energy spread, and can be defined as the minimum value of $\frac{A_z(s)}{D_z(s)}$ around the machine. Most of the time, for the longitudinal motion, the geometric aperture for off-momentum particles is smaller than the dynamic aperture; it is often taken as the main longitudinal aperture.

For particles inside the longitudinal dynamic aperture, the motion can be considered as linear. Losses can occur but are mostly caused by pertubative effects, like RF noise or energy loss of particles from collisions, beam-gas interaction or interaction with the collimators. On the other hand, particles outside of the dynamic aperture loose their linear behaviour and form the longitudinal halo. They eventually get lost in the beam pipe after some time, typically during the ramping of the magnets.

1.3.4 Available aperture in the LHC

The LHC aperture is calculated using a simplified linear model whose goal is to give the maximum transverse amplitude which can be reached by primary halo particles. This is performed all around the machine, taking into account all mechanical and optical tolerances listed in Table 1.4. The main assumption is that the limit reached by primary halo particles is the inner part of the aperture of cold elements, and is given by the design value $n_1 = 7\sigma_r$ in the LHC case. For studies on the LHC collimation system, the secondary halo has to be taken into account as well: the upper limit in that case corresponds to a horizontal and vertical acceptance of 8.5 σ_z^{β}, as seen in section 1.3.2 and reported in [18].

Table 1.4: Tolerances taken into account in the design of the LHC aperture. Courtesy of S. Redaelli from [18].

Tolerance	Design value
Manufacturing	$\leq$ 1.6 mm
Alignment	$\leq$ 1.6 mm
Separation/crossing schemes	$\leq$ 1.5 mm
Spurious dispersion	27 % of arc (normalized)
Momentum offset $\Delta p/p$	0.05 %
Closed orbit @ 450 GeV	4 mm
Closed orbit @ 7 TeV	3 mm (IP) / 4 mm (Arc)
Beta-beat $\Delta\beta/\beta$	21 %

The LHC optics currently used at CERN is the version 6.5 and allows calculating the mechanical opening of any given element of the lattice. This is illustrated in Figure 1.6 which shows the distribution of vertical aperture at injection energy (450 GeV). At this energy, the main aperture limitations come from the arcs and are distributed all along the machine, with a large fraction of the total number of dipole (MB) and quadrupole (MQ) magnets presenting an aperture below 8.5 σ_z. At collision energy (7 TeV), the values of the Twiss parameter β_z are 4 times smaller than at injection energy, and the beam emittance is reduced by a factor $\gamma_{rel}^{lowb}/\gamma_{rel}^{inj} \approx 16$: the arcs are therefore no longer the limiting aperture in the machine. The peak luminosity configuration in IP1 and IP5 requires a minimum β^* value of 0.55 metres, settings which are refered to as the *squeezed optics configuration* (see Table 1.3). Such a small beam size can only be achieved with dedicated magnet assemblies called *triplet magnets* [68] characterized by β values of about 4500 metres, making them the aperture bottleneck for collision optics. Table 1.5 lists the aperture limits for both beam lines in the two energy cases.

1.4 The LHC Collimation System

Beam losses in a circular machine can occur due to various mechanisms. Particles drift out of the stable dynamic aperture (as discussed in the previous section) and get

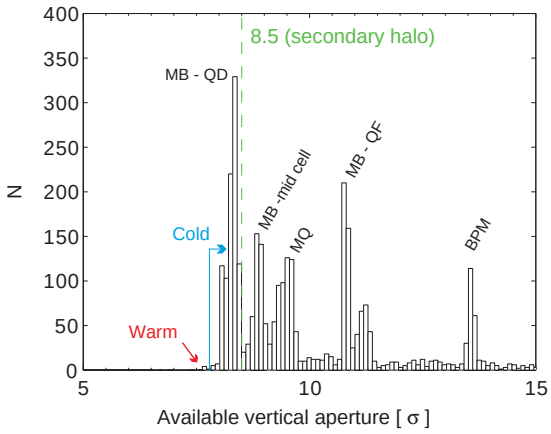

Figure 1.6: Distribution of vertical available mechanical aperture for the full LHC ring at injection (450 GeV). The peak below the design value of 8.5 σ corresponds to the arc dipole close to the horizontally defocusing quadrupoles MB-QD, where the vertical beam size is larger. Courtesy of S. Redaelli from [18].

Table 1.5: Minimal horizontal and vertical apertures at injection (450 GeV) and top energy (7 TeV, with $\beta^* = 0.55$ m) for warm and cold elements. Courtesy of S. Redaelli from [18].

Energy	450 GeV		7 TeV	
Magnet type	Warm	Cold	Warm	Cold
Beam 1				
Horizontal	6.78	7.88	28.1	8.90
Vertical	7.68	7.79	8.34	8.43
Beam 2				
Horizontal	6.68	7.70	27.6	8.13
Vertical	7.65	7.60	8.69	8.75

intercepted by the geometric aperture of the machine. A review of these loss mechanisms is done in the next chapter. There is a need for a collimation system to:

- avoid beam-induced quenches of the superconducting magnets during operation or after a beam dump (**quench protection** aspect),
- minimise the halo-induced background in the experimental detectors,
- provide radiation protection for machine equipments close to the beam,
- protect the elements of the machine against damage due to high intensity beams (**machine protection** aspect).

In the case of the LHC main ring, collimators are needed for both injection energy (450 GeV) and collision energy (7 TeV). For the latter, the main sources of halo population are the operational scenarios and the related instabilities (tuning procedure and orbit stabilisation give the highest loss rates), inducing accidental quenches. An efficient collimation system may also be required to improve the signal-to-noise ratio in the detectors.

Beam collimation in circular machines is generally performed using a mechanical system. Such a system is made of blocks of material placed between the beam and the geometric aperture of the machine (i.e. the size of the vacuum chamber) to intercept particles whose amplitude gets critically high. These blocks are commonly named *jaws*, as they "swallow" the particles that can become dangerous for the magnetic elements of the machine. The distance between the surface of the jaw and the centre of the beam is the *collimator half-opening* (as described in section 1.3.2). A collimator can be made of a single jaw (as in the RHIC collimation system for example) or a pair of jaws (LHC case). The material selected for the jaw has to be robust enough to perform all the tasks listed above without being damaged both in normal and abnormal operation conditions.

1.4.1 Requirements for the LHC collimators

Based on what is presented in section 1.2, one can clearly appreciate that handling the LHC beams safely in the superconducting elements of the lattice is not an easy task. This implies strong requirements on the design on the collimation system, presented in [6] and reported here:

- the collimator jaws must be robust enough to withstand beam impacts of up to 500 kW deposited energy; at the same time, the surface that faces the beam halo must remain flat on the 10-25 μm level,
- the system must have a good cleaning efficiency (see also section 1.7),
- the choice of the material for the collimator jaws is critical regarding impedance issues,
- due to the estimated radiation levels in the collimation insertions, the handling of collimators must be done remotely,
- commissioning and operating the collimators is also demanding in machine performance and control of instabilities: tolerances on phenomena like β-beating and perturbation of the design orbit are therefore modified accordingly.

Out of the list above, some of the points are closely related: a heavy material (high atomic number) may absorb particles easily but the induced radiation can damage equipments downstream, while a lighter material may minimise the number of proton-matter interactions suffered by the impacting particles but the dose gets considerably reduced. This makes the choice of an appropriate material for collimators more difficult. Section 3.1 reviews these requirements in more details.

1.4.2 Betatron and Momentum cleaning for protons

The concepts of transverse and longitudinal apertures were introduced in the previous section. From there it appears that a collimation system needs to perform two different types of cleaning:

- a *betatron cleaning* to remove halo particles with large transverse amplitudes A_z,

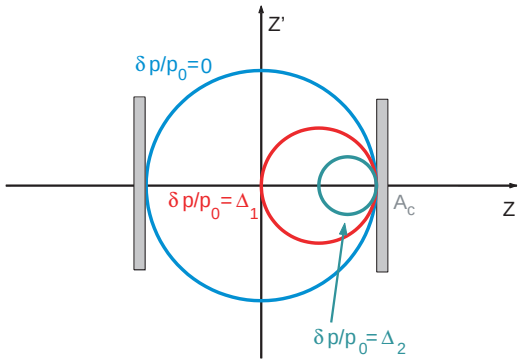

Figure 1.7: Representation in the normalized phase-space of a pair of collimator jaws (grey blocks) opened at distance A_c from the centre of the beam at a location in the machine where the dispersion is not zero (taken as positive in this figure). The different circles correspond to different particle distributions depending on their respective root mean square energy spread.

- a *momentum cleaning* to remove halo particles with large energy offsets $\frac{\Delta p}{p_0}$.

The basic principles of collimator jaws are illustrated in Figures 1.7 and 1.8. By putting a block of material into the beam halo, this block acts like a limitation of betatronic oscillations which makes the opening of the jaw turn into the aperture bottleneck of the machine. As seen in the previous sections, the trajectories are represented by circles in normalized transverse phase-space, with respective centers at the coordinates $Z_C = D_z(s) \cdot \frac{\Delta p}{p_0}$ and $Z'_C = D'_z(s) \cdot \frac{\Delta p}{p_0}$. A collimator jaw is placed at a normalized amplitude A_c in such a way that particles that will eventually hit this "wall" would be close to their maximum excursion and their Z' would be close to zero. Studies can therefore be limited to the case $Z'_C = 0$ as in Figure 1.7. In that case, the betatronic cut in amplitude for any circle depends on Z_C and can be written as:

$$A_{cut}(s) = A_c(s) - D(s) \cdot \frac{\Delta p}{p_0} \,. \tag{1.14}$$

From there, the two different types of cleaning can be treated either by two different systems (one for each type) or by a single system that would take care of strong betatronic and momentum offsets at the same time. Figure 1.8 shows an example of collimator jaws dedicated to one type of cleaning. Jaws "1" are part of a betatron cleaning collimator which limits the betatronic oscillations of circulating particles to a normalized amplitude A_β. Jaws "2" represents a momentum cleaning collimator located at $D(s) = \mathcal{D}$, which limits the longitudinal aperture to a value $A_{\Delta p_1/p_0}$ for the maximum betatronic aperture A_β. Particles outside of this restricted longitudinal aperture can still survive in the machine even for large values of $D(s)$ but only if they perform small betatronic oscillations. This is achieved by installing the momentum collimators at locations where the normalized dispersion $\mathcal{D}$ (see end of section 1.1.2) is close to the maximum value of the nominal dispersion $D(s)$ over the ring. This is the method used in the LHC case, with two-sided jaws in each collimator.

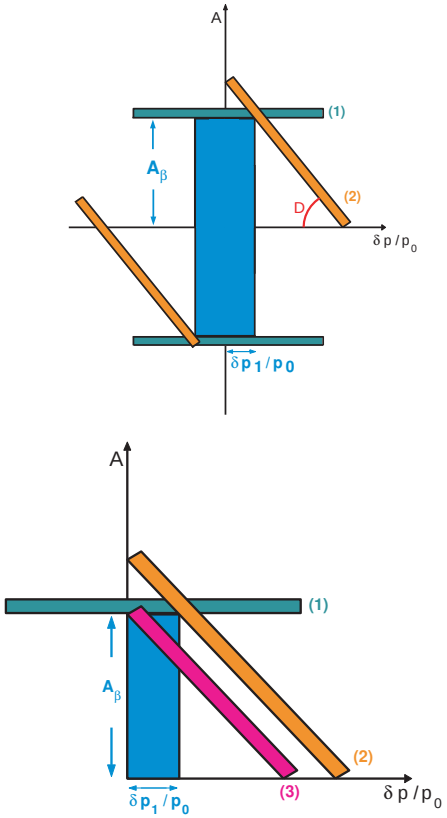

Figure 1.8: Top: Collimation for betatron cleaning collimator jaws (1) and momentum cleaning jaws (2). The stable motion is represented by the colored box. Jaws labeled "2" are located at $D(s) \neq 0$ and limit the energy offsets of particles to a value δp_1. - Bottom: Comparison of the effects of various collimator types: jaws number 1 and 2 are the same as in Figure 1.8, and jaw number 3 is a dual type collimator jaw, absorbing particles with both high betatronic amplitudes and large momentum spreads.

Another possibility for a collimation system in a circular machine is to combine the two previous features and have a single collimator for both betatron and momentum cleaning, as shown in Figure 1.8): one would then have to work with the value of $\mathcal{D}$ (i.e. the optics and location of the collimator) in order not to remove a large fraction of the stable beam and to optimize the cuts in betatronic amplitude and momentum deviation.

1.5 Scattering of high energy protons in a collimator jaw

This section contains a review of the four main scattering processes that take place when halo particles impact on a collimator jaw, following the work presented in [13, 20]. The modelization of these mechanisms for Monte Carlo tracking codes is also presented.

1.5.1 Multiple Coulomb Scattering (*MCS*)

A charged particle travelling through matter faces numerous small angle deflections, most of them due to Coulomb scattering from the nuclei and electrons. The trajectory of particles is described by a statistical process along the length of material, referred to as multiple Coulomb scattering (*MCS*). The theory of *MCS* has been studied extensively, like in Moliere's theory of multiple scattering [21].

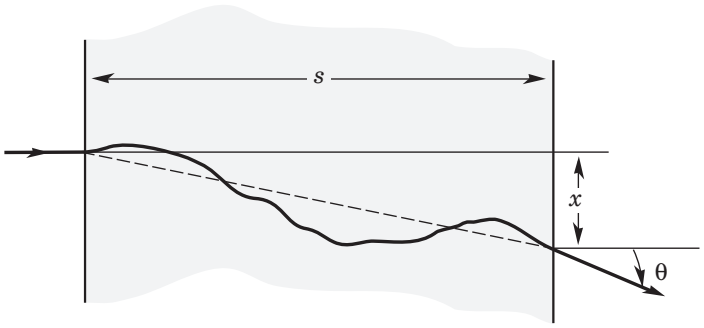

Figure 1.9: Schematic view of *MCS* in one plane. From [22].

The following is derived from the work presented in [20]. One needs to determine the distribution function $f(s, x, \theta)$ of a given particle after passing through a length s of matter. Along s, the considered particle receives an angular deflection θ and a transvere offset x. The function f is one solution of the following partial differential equation:

$$\left[\frac{\partial}{\partial s} + \theta \cdot \frac{\partial}{\partial x}\right] f = \frac{4}{w^2} \cdot \frac{\partial^2 f}{\partial \theta^2} \ , \tag{1.15}$$

$$\text{with } \frac{1}{w} = \frac{E_s}{\beta_{rel} \cdot cp} \cdot \frac{1}{\sqrt{\chi_0}} = \text{rms scattering angle per unit length,}$$

where β_{rel} is the relativistic ratio, p is the momentum of the incoming particle, E_s a constant with the dimension of an energy (= 21.2 MeV) and χ_0 the radiation length of the considered material. f represents in fact the *probability* of a certain offset x and angular deflection θ in one plane for a thickness s of material "seen" by the considered particle. The system (1.15) has been solved by Fermi [23] and the solution writes:

$$f(s, x, \theta) = \frac{2\sqrt{3}}{\pi s^2 w^2} \exp\left[-\frac{4}{w^2} \cdot \left(\frac{\theta^2}{s} - \frac{3x\theta}{s^2} + \frac{3x^2}{s^3}\right)\right] \ . \tag{1.16}$$

Here the variables are x and θ; Moliere's theory deals with small scattering angles and a fit for the angular distribution gives the rms angle after a length of matter s [22]:

$$\theta(s) = \frac{13.6 \text{ MeV}}{\beta_{rel} cp} \cdot \sqrt{\frac{s}{\chi_0}} \left[1 + 0.038 \cdot \ln\left(\frac{s}{\chi_0}\right)\right] \ , \tag{1.17}$$

using a Gaussian approximation for the central 98% of the distribution. It can already be noted that MCS has a smaller effect on high energy protons: it gets more difficult for the LHC collimators to scatter 7 TeV protons, as shown in Figure 1.10.

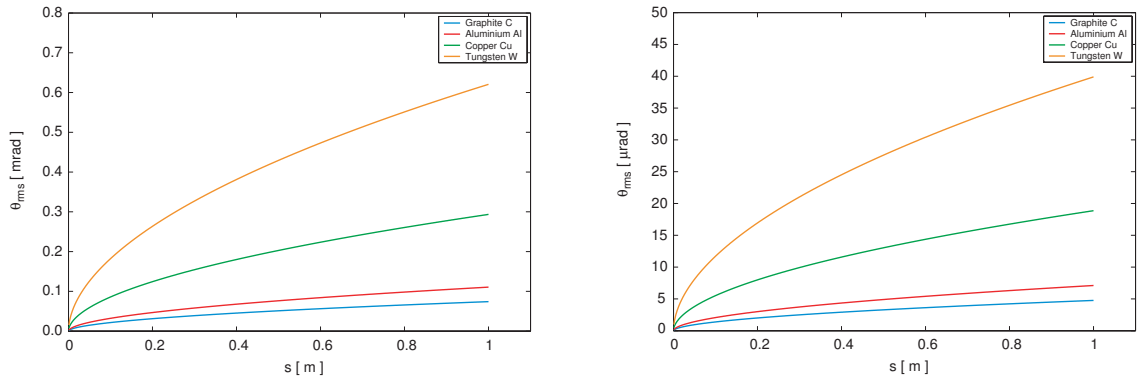

Figure 1.10: RMS scattering angle from Monte-Carlo scattering for various collimator jaw material in the injection (left) and collision (right) energy cases. Calculations were performed for Graphite, Aluminium, Copper and Tungsten.

For Monte Carlo simulations, one needs to calculate for any incoming particle the final coordinates at the end of a given length of material for the calculated (x, θ) and the initial coordinates (x_{init}, x'_{init}). In the present case, working with independent Gaussian random variables (ξ_1, ξ_2) with average zero and variance one allows doing a factorisation of the Fermi function (1.16) in two Gaussian functions. One can then obtain the two *Monte Carlo random variables* (x, x') [20, 22]:

$$\begin{aligned} x &= x_{init} + s \cdot x'_{init} + s \cdot \theta(s) \cdot \left(\frac{\xi_1}{\sqrt{12}} + \frac{\xi_2}{2} \right) \\ x' &= x'_{init} + \theta(s) \cdot \xi_2 \end{aligned} \quad . \tag{1.18}$$

From Figure 1.9 and equation (1.18) it can be seen that the scattering angle x' and the transverse displacement x are correlated, i.e. a random choice for x' must depend on the previous choice of x and vice versa. This is even more obvious for particles impacting on one edge of the material ($x_{init} = 0$) with a direction parallel to the length of the block ($x'_{init} = 0$).

In the Monte Carlo simulations, (1.18) is used over small slices of the total length of material. Special care has to be taken to determine the step length: this is presented in section 1.5.4.

1.5.2 Ionization

When passing through matter, relativistic charged particles loose a fraction of their energy by ionization and atomic excitation [22]. The amount of energy loss, equivalent to the *stopping power* of the material, is given by the Bethe-Bloch equation:

$$-\frac{dE}{dx} = Kz^2 \frac{Z}{A} \frac{1}{\beta_{rel}^2} \left[\frac{1}{2} \ln \left(\frac{2 \cdot m_e c^2 \cdot \beta_{rel}^2 \gamma_{rel}^2 \cdot T_{max}}{I^2} \right) - \beta_{rel}^2 - \frac{\delta}{2} \right] , \tag{1.19}$$

where γ_{rel} is the relativistic factor, Z and A are the atomic number and the atomic mass of the material, m_e the electron mass, z the charge of the considered particle and K a constant. I is known as the *mean excitation energy* and is taken as $(10 \pm 1$ eV)·Z for elements heavier than Oxygen [13].

The function T_{max} is the maximum energy that can be transfered to a free electron during a collision; its value depends on the mass of the impacting particle. If M is taken as this mass, the value of T_{max} is given by:

$$T_{max} = \frac{2 \cdot m_e c^2 \cdot \beta_{rel}^2 \gamma_{rel}^2}{1 + 2\gamma_{rel} \cdot m_e/M + (m_e/M)^2} \ . \tag{1.20}$$

Finally, the term in δ in equation (1.19) is a corrective term to take density effects into account [22]. Figure 1.11 is taken from [22] and shows the behaviour of the energy loss dE/dx stated in MeV.g^{-1}.cm^2 versus the particle energy. A correction factor has to be added for high energy protons though, as Figure 1.11 only takes into account the fast recombination electrons (i.e. the ones which travel short distances before a recombination with another nucleus of matter).

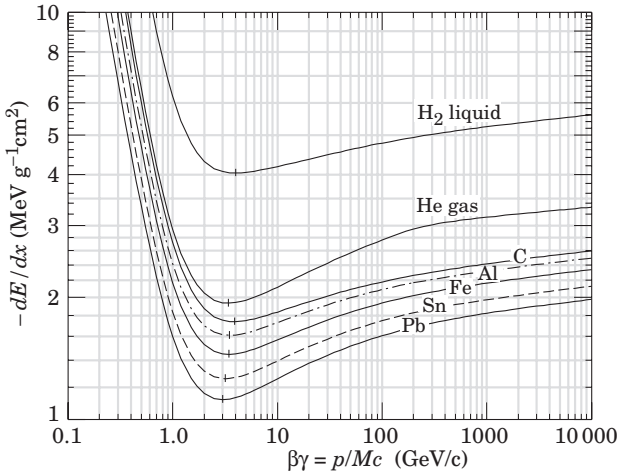

Figure 1.11: Mean energy loss rate in liquid (bubble chamber) hydrogen, gaseous helium, carbon, aluminium, iron, tin and lead. From [22].

Using each material density, the energy loss rate per unit length can be calculated assuming that the slopes of the curves shown in Figure 1.11 are small for energies larger than 100 GeV. Therefore, taking $E_{ref} = 450$ GeV would be sufficient to get the value of dE/dx in both the injection energy and the collision energy case. Taking into account the correction factor mentioned earlier, one gets the values listed in Table 1.6 in GeV/m.

1.5.3 Point-like interactions

The two mechanisms previously presented take place over a certain length of material; the other type of proton-matter interaction is localized and describes the scattering of an

Table 1.6: Radiation length and corresponding normalized energy loss rate (in Gev/m) for material that were studied for the LHC collimator jaws. The reference energy is 450 GeV. Adapted from [13].

Material	Radiation Length [cm]	dE/dx (GeV/m)
Beryllium (Be)	35.28	0.55
Graphite (C)	18.80	0.68
Aluminium (Al)	8.90	0.81
Copper (Cu)	1.43	2.69
Tungsten (W)	0.35	5.79
Lead (Pb)	0.56	3.40

incoming proton on one of the components of the atomic structure of the traversed material (proton, neutron or even an entire nucleus). These events are also known as *point-like interactions*. All processes are defined by their respective *cross-section* σ_{scat} corresponding to the probability of this process to take place per unit length of material. In case of a scattering that is not destructive for the incoming particle (known as elastic or quasi-elastic scatterings), the final coordinates are calculated from another quantity called *differential cross-section* $d^2\sigma/d\theta dp$ which is the probability to find the scattered particle at a given angle $d\theta$ and/or with a given momentum offset dp with respect to its initial momentum.

To determine analytically the cross-section and differential cross-section of each process, one can follow the method presented in [13] and use a *Lorentz-invariant* coordinate system for high energies in which:

- the scattering angle θ is replaced by the *momentum transfer* $t = (p\theta)^2$,
- the beam momentum p is replaced by *the square of the center of mass energy* $s_{c.o.m.} \approx 2m_p \cdot p$ (m_p being the proton mass).

Elastic proton-proton (pp) scattering

Variations of the elastic pp cross-section with respect to the momentum of the incomping proton can be found in various references, including [24] from where is taken Figure 1.12. The description of the process as done in this section is also valid for describing elastic proton-neutron scattering processes.

For the two beam energies at which the LHC will be operated (450 GeV and 7 TeV), Figure 1.12 show that the changes for σ_{el}^{pp} are small enough that its variations in this range can be taken as linear (in logarithmic scale though). Taking $p_{ref} = 450$ GeV, one gets $\sigma_{pp-inj}^{el} \approx 7.0$ mb; using the curve for the elastic cross-section value on Figure 1.12 to determine the slope of the linear function, one gets [13]:

$$\sigma_{pp}^{el} = \sigma_{pp-inj}^{el} \cdot \left(\frac{p}{p_{ref}}\right)^{4.79\times10^{-2}} , \tag{1.21}$$

leading to a value at 7 TeV of $\sigma_{pp-coll}^{el} \approx 7.98$ mb. As mentioned earlier, one also needs to know the differential cross-section to determine the change in momentum and the deflection

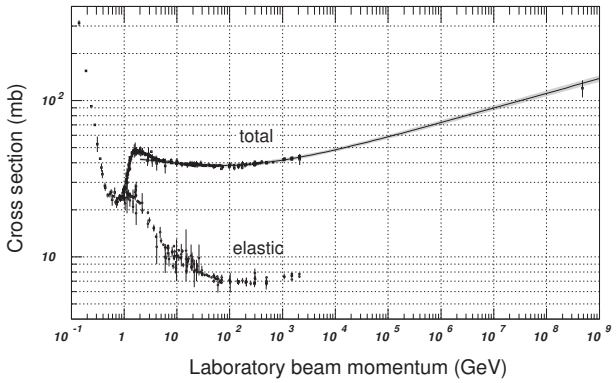

Figure 1.12: Total and elastic cross-sections for *pp* events as functions of the particle momentum in the laboratory frame. From [24].

angle of the scattered proton. From [20], one gets the following expression:

$$\frac{d\sigma}{dt} = K \cdot \exp\left(-b(s_{c.o.m.}, t) \cdot t\right) \ , \tag{1.22}$$

where $b(s_{c.o.m.}, t)$ is the slope factor of the differential cross-section. Its dependence with the parameter t is very limited for ranges of energy such that $|t| < 0.1$ GeV^2 [12]. In the LHC case, it is stated in [13] that only scattering angles smaller than 10 times the beam deviation ($\theta < 10\ \sigma'$) shall be considered, so that the scattered particle reaches amplitudes small enough to experience other point-like processes when passing through a given length of material (and not be "kicked out" at the very first interaction). This leads to:

- injection energy: $p_{inj} = 450$ GeV, $\sigma'_{inj} = 6.0\ \mu$rad $\Rightarrow 0 < t_{inj} < 7.3 \times 10^{-4}$ GeV^2,
- collision energy: $p_{coll} = 7000$ GeV, $\sigma'_{coll} = 1.5\ \mu$rad $\Rightarrow 0 < t_{coll} < 1.1 \times 10^{-2}$ GeV^2,

both below the value stated in [12]. One can then use the approximation $b(s_{c.o.m.}, t) \approx b(s_{c.o.m.})$.

In some accelerator experiments (ISR at CERN, TEVATRON at Fermilab, RHIC at BNL), the *pp* scattering process has been investigated in detail for energies up to $\sqrt{s} = 200$ GeV [25], and the results are reported in Figure 1.13. The slope factor b has a quasi-linear behaviour in logarithmic scale around the LHC collision energy ($\sqrt{s^{coll}_{c.o.m.}} \approx 114.59$ GeV), and can be represented by the simple function:

$$b_{pp}(s) = 8.5 + 1.086 \cdot \ln\left(\sqrt{s_{c.o.m.}}\right) \ . \tag{1.23}$$

Inelastic diffractive *pp* scattering

This process is also known as *single diffractive (SD) scattering* and is similar to a quasi-elastic interaction, since there is a non-zero probability that one of the initial protons

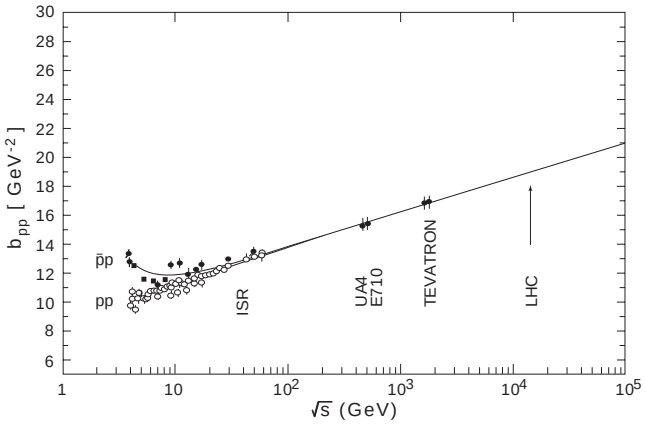

Figure 1.13: Slope parameter $b(s_{c.o.m.}, t)$ for pp and $p\bar{p}$ interactions versus $s_{c.o.m.}$. The cited names of experiments and machines give the value of the respective centre of mass energy of the colliding beams. From [12].

survives the interaction and keeps circulating in the machine for some turns. This mechanism features a coherent excitation of one of the protons into a state X with a high mass M_X during the momentum transfer collision $pp \rightarrow Xp$, with the corresponding differential cross-section [26]:

$$\frac{d^2\sigma}{dtdM_X^2} = \frac{A \cdot \exp\left(-b(M_X) \cdot t\right)}{M_X^2} \tag{1.24}$$

for small values of t (which is the case, see previously) and A a constant value taken as 0.68 mb. For an incoming proton to remain intact during SD means that the sources of excitation to X add up coherently; this is achieved "only if the target proton does not emit any pions" according to [26], which gives the upper limit for M_X^2 as:

$$M_X^2 = M_p^2 + 0.15 \cdot s_{c.o.m.} \ , \tag{1.25}$$

with M_p^2 being the squared proton rest mass and corresponding to the lower limit for M_X^2. Integrating equation (1.24) for $|t| \leq 0.1$ GeV^2 and the range of M_X^2 just defined gives (still quoting [26]):

$$\sigma_{pp}^{SD}(s_{c.o.m.}) = (A \pm 0.05) \cdot \left(1 + \frac{36 \pm 8}{s_{c.o.m.}}\right) \cdot \ln(0.6 + 0.15 \cdot s_{c.o.m.}) \tag{1.26}$$

For LHC values, $p_{inj} = 450$ GeV leads to $\sigma_{pp}^{\mathrm{SD,inj}} \approx 3.15$ mb while $p_{coll} = 7000$ GeV leads to $\sigma_{pp}^{\mathrm{SD,coll}} \approx 4.90$ mb. These values can be compared to the pp elastic cross-section that can be seen on Figure 1.12.

This process is rather important for LHC collimation as part of the betatron halo is converted into an off-momentum halo. Cross-section values are to be compared with the ones of other processes to check wether SD can become a dominant effect.

Proton-nucleon (pn) inelastic scattering

Here n stands for nucleon, i.e. for either proton or neutron. The cross-section is equal for pp and pn interactions with good precision; pn will stand for both processes in this section. It can be directly derived from the total pp cross-section shown on Figure 1.12:

$$\sigma_{pn}^{inel} \approx \sigma_{pn-ref}^{tot} \cdot \left(\frac{p}{p_{ref}} \right)^{5.79\times10^{-2}} - \sigma_{pn}^{el} \ , \tag{1.27}$$

where once again $p_{ref} = p_{inj} = 450$ GeV as in (1.21), which leads to $\sigma_{pn-inj}^{inel} \approx 33$ mb. At $p_{coll} = 7$ TeV, one gets $\sigma_{pn-coll}^{inel} \approx 38.9$ mb.

Proton-nucleus (pN) scattering

Incoming protons impacting on a given collimator jaw may also interact with the entire nucleus of the material structure instead of just one of its nucleons. The corresponding total and inelastic cross-section for various materials and gases can be found in [27]. These values are valid in the 80-240 GeV range, but only minor changes are expected for higher energies. Still in [27], the total cross-section is stated to scale with the atomic mass in $\sigma_{pN}(A) \sim \sigma_{pN}(A=1) \cdot A^{0.77}$.

A "parasitic" mechanism can interfere during regular pN scattering. As mentioned earlier, this process relies on all nucleons acting coherently to deflect the incoming protons; but it can also happen that the protons interact with individual nucleons only, mainly the ones on the outer layer of the nucleus structure. This incoherent scattering can be either elastic or single diffractive (see previous descriptions), with cross-sections values modulated by a coefficient $n_{eff}(A)$ corresponding to the effective number of deflecting nucleons as a function of the atomic mass [28]:

$$\begin{aligned} \sigma_{pn}^{el} &= n_{eff}(A) \cdot \sigma_{pp}^{el} \ , \\ \sigma_{pn}^{SD} &= n_{eff}(A) \cdot \sigma_{pp}^{SD} \ . \end{aligned} \tag{1.28}$$

A good approximation for $n_{eff}(A)$ is also given in [28] as:

$$n_{eff}(A) = 1.6 \cdot A^{1/3} \ . \tag{1.29}$$

A comparison of n_{eff} values as measured in [28] at 20 GeV and as computed with (1.29) is given in Table 1.7.

Overall, the total pN cross-section writes:

$$\sigma_{pN}^{tot} = \sigma_{pN}^{el} + \sigma_{pn}^{el} + \sigma_{pN}^{SD} + \sigma_{pN}^{inel} \ . \tag{1.30}$$

σ_{pn}^{el} is explicited in equation (1.28) and σ_{pN}^{SD} can be taken as equivalent to σ_{pp}^{SD} which is also given in equation (1.28); the two components left are the elastic and inelastic coherent scattering of the incoming proton with the entire nucleus.

Table 1.7: Comparison of n_{eff} values for possible collimator jaw materials. The 20 GeV values are the one experimentally measured in [28] while the values reported in the last column were obtained using (1.29). No experimental record is available for Tungsten (W) from the cited references.

Material	A	20 GeV	Model
Beryllium (Be)	9.01	3.50	3.33
Graphite (C)	12.01	3.40	3.66
Aluminium (Al)	26.98	4.60	4.80
Copper (Cu)	63.55	6.70	6.38
Tungsten (W)	183.85	n/a	9.10
Lead (Pb)	207.19	9.50	9.47

- Inelastic pN scattering:

The neutron-nucleus scattering has been studied extensively for energies in the 160-375 GeV range in [29]. According to the results obtained, one can assume $\sigma_{pN}^{inel} \approx \sigma_{nN}^{inel}$, the latter value being found in [27] for all collimator jaw materials previously listed in Table 1.7.

- Elastic pN scattering:

As for elastic pp scattering, one needs to determine both the cross-section and the differential cross-section. The cross section can be calculated using (1.30) by taking σ_{pN}^{tot} as given in [27] and substract all the other measured cross-sections. For the differential cross-section $d\sigma/dt$, one can expect the same expression as in (1.22) but the slope factor b_{pN} is scaled with a factor $K' \cdot A^{2/3}$, i.e. proportional to the square of the radius of the nucleus [20]. Experimental measurements were done for hadron beams on various target materials at different energies on the order of 100 GeV [30]; results are reported in Figure 1.14. By doing a linear fit, one gets the A-dependance of the elastic pN scattering slope factor:

$$b_{pN} = 14.1 \cdot A^{0.66} \ . \tag{1.31}$$

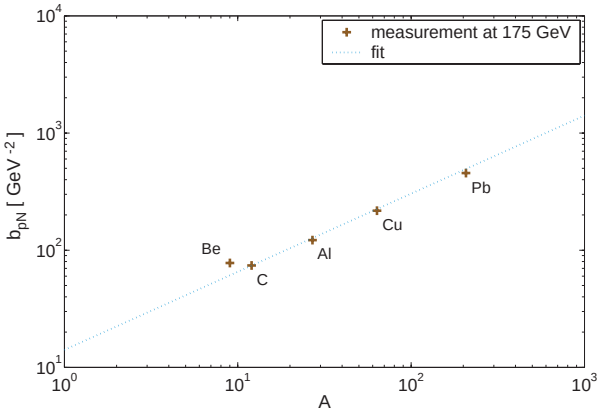

Figure 1.14: Slope parameter b for pN interaction versus the atomic mass A from experimental measurements at 175 GeV. Data taken from [30].

- Rutherford scattering:

This mechanism is directly derived from Rutherford's model of the nucleus [31] and implies that an incoming proton coming very close to a nucleus would be deflected away from it by a large electrostatic (Coulomb) force due to the positive charge of the nucleus, inducing large scattering angles. The Rutherford scattering formula reads:

$$\frac{d\sigma_{rth}}{dt} = 4\pi\alpha^2(\hbar c)^2 \cdot \frac{Z^2}{t^2} \cdot \exp\left(-0.856 \times 10^3 \cdot t \cdot R^2\right) \tag{1.32}$$

with $\alpha \approx 1/137$ the fine-structure constant, $(\hbar c)^2 = 0.389$ GeV^2.mb the conversion constant, Z the atomic number and R[m] $\approx 1.2 \times 10^{-15} \cdot A^{1/3}$ the radius of the considered nucleus with A its atomic mass [1].

Table 1.8: Cross section σ values for point-like pN processes for different collimation jaw materials included in the tracking code. Non measured values are written in italics. Slope factors b_{pN} and Rutherford scattering cross-sections are the ones used in the scattering routines (see section 3.3.2), some being calculated from [32].

Material	σ_{pN}^{tot} barn	σ_{pN}^{in} barn	b_{pN} GeV^{-2}	σ_{rth} mbarn
Beryllium (Be)	0.268	0.199	74.7	0.035
Graphite (C)	0.331	0.231	70.0	0.076
Aluminium (Al)	0.634	0.421	120.3	0.34
Copper (Cu)	1.232	0.782	217.8	1.53
Tungsten (W)	2.767	1.65	*440.3*	*7.68*
Lead (Pb)	2.960	1.77	455.3	9.07

Rutherford scattering is considered only for energies large enough for MCS not to be considered valid any longer [13]; from this reference, the lower limit is set as $t_{cut} = 0.998 \times 10^{-3}$ GeV^2, and one can obtain the values of the Rutherford scattering cross-section σ_{rth} by integrating equation (1.32) for $t \geq t_{cut}$. From [27, 32] one can also extract the point-like interaction cross-sections for the possible collimator jaw materials, reported in Table 1.8.

1.5.4 Mean free path of particles

The processes of finite cross-sections described in the previous section take place in average once the incoming particle (proton in the LHC case) has been travelling through a characteristic length of the material called the *mean free path*. It corresponds to the average distance that a particle can go through without suffering any collision with another particle or nucleus. From [32] and using a uniform density of scatterers, one gets:

$$\lambda = \frac{1}{\pi\left(\frac{d_1+d_2}{2}\right)^2 \cdot n_V} = \frac{A}{N_A \cdot \rho \cdot \sigma} \approx \frac{1}{\sigma} \ . \tag{1.33}$$

[1] This approximation comes from the estimate of the nuclear radius of hydrogen $r_H \approx 1.2 \times 10^{-15}$ metres.

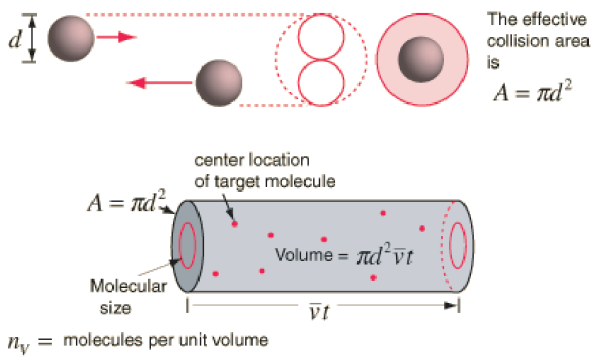

Figure 1.15: Illustration of the mean free path definition for impacting particles with identical diameters. In the case of proton matter interaction, the term in d^2 can be replaced by $(d_1 + d_2)^2/4$ with d_1 the proton diameter and d_2 the target (nucleon or nucleus) diameter. From [32].

To obtain equation (1.33), one has to use the geometrical definition for the cross-section of a given process which is the effective area of space where the impact is taking place; therefore $\sigma = \pi \cdot 0.25\,(d_1 + d_2)^2$, as seen on Figure 1.15. N_A stands for the Avogadro number and ρ is the material density.

For point-like interactions, equations (1.33) and (1.30) imply that the mean free path between each interaction is given by:

$$\begin{aligned} \frac{1}{\lambda_{tot}} = \sigma_{tot} = \sigma_{pN}^{tot} + \sigma_{Ruth} = \sigma_{pn}^{el} + \sigma_{pN}^{el} + \sigma_{pn}^{SD} + \sigma_{pN}^{inel} + \sigma_{Ruth} \\ \Leftrightarrow \lambda_{tot} = \left(\frac{1}{\lambda_{pn}^{el}} + \frac{1}{\lambda_{pN}^{el}} + \frac{1}{\lambda_{pn}^{SD}} + \frac{1}{\lambda_{pN}^{inel}} + \frac{1}{\lambda_{Ruth}} \right)^{-1} \end{aligned} \tag{1.34}$$

In Monte-Carlo simulations, the distance Δs between two point-like interactions is determined from the computed value of λ_{tot} [13]:

$$\Delta s = -\lambda_{tot} \cdot \ln(u)\ , \tag{1.35}$$

where u is a variable with uniform distribution between 0 and 1. After a length Δs of material, the point-like process applied to a given proton is randomly selected proportionally to each partial cross-section. Over Δs, *MCS* and ionization processes are taken into account as well. If after any point-like interaction the remaining length of material is smaller than the next randomly computed Δs step, then no other point-like process is considered till the end of the jaw. In the simulations performed for the LHC collimation system, impacting protons can leave the material before its end due to the fact that the impact takes place at small distances from the edge of the jaw block. This effect is called the *edge escape*.

1.6 Multi-stage collimation system

Figure 1.7 shows the effect of aperture restriction from a primary collimator jaw. What actually happens to an impacting proton is pictured in Figure 1.16. Due to *MCS*, a

proton impacting on a collimator oriented in one transverse plane only (i.e. purely horizontal or purely vertical) will get a change in both coordinates by z_{kick} and z'_{kick}.

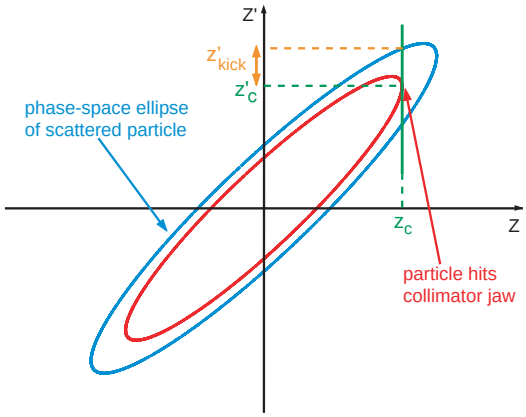

Figure 1.16: Scattering of particles in the z-z' phase space. This plot shows an example of the new phase-space trajectory (blue line) for a particle which gets a larger divergence z' after impact.

The transverse displacement z_{kick} is typically of the same range as the impact parameter i.e. on the order of 1 μm. The scattered protons are roughly populating a region of the phase-space (z-z') corresponding to an almost straight line located at the amplitude of the collimator jaw. Due to z'_{kick}, the particles can be scattered either back into the beam pipe or further outside of the beam core. The latter particles form what is called the *secondary halo*. To control this halo one needs additional jaws (or pair of jaws) from so-called secondary collimators, which are placed downstream of the primary jaws. This combination of the two types of collimators forms what is referred to as a *two stage collimation system*.

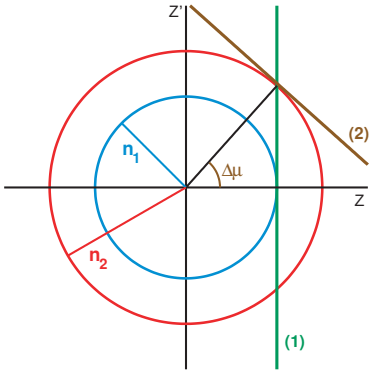

Figure 1.17: Example of a two-stage betatronic collimation system in normalized phase-space for one transverse plane. A particle is scattered close to its maximum transverse position by a primary collimator at Z = n_1 with jaw number 1. If it is not absorbed, it is scattered along the vertical line Z = n_1. If a secondary collimator is at the depth n_2, the shortest cut along this line is made with a secondary collimator (jaw number 2) at the phase advance $\Delta\mu$.

As seen in Figure 1.16, the scattered particle has its maximum betatronic excursion increased. Therefore it is possible to locate the secondary collimators in the shadow of the primary collimators and clean efficiently the secondary halo. This is typically achieved by setting the secondary jaws at the same opening as the primary ones plus some additional distance d_σ for safety reasons. This offset is required in order to avoid that any secondary collimator would become a primary one: in such a situation, the rest of the cleaning system is not efficient enough and the induced halo could create quenches and/or high uncontrolled background levels in experimental areas. A safe relative transverse retraction d_σ for the LHC is estimated to 1 σ in both transverse planes, taking into account dynamic changes in the orbit during machine operation and non-linearities within the beam. For the longitudinal distance between primary and secondary collimators, from Figure 1.17 and [7] it can be seen that primary and secondary collimators should ideally be separated by a phase advance $\Delta\mu$ such that

$$\cos(\Delta\mu) = \frac{n_1}{n_2} \ , \ n_2 = n_1 + d_\sigma \tag{1.36}$$

in order to have an optimum two-stage cleaning system. At least two secondary collimators are required per primary collimator installed: one at the distance $d_{\Delta\mu_1}$ and the other at $d_{\Delta\mu_2}$, since the new maximum amplitude of the scattered particle can be reached for two different values of phase-advance $\Delta\mu_1$ and $\Delta\mu_2$, as seen in Figure 1.18.

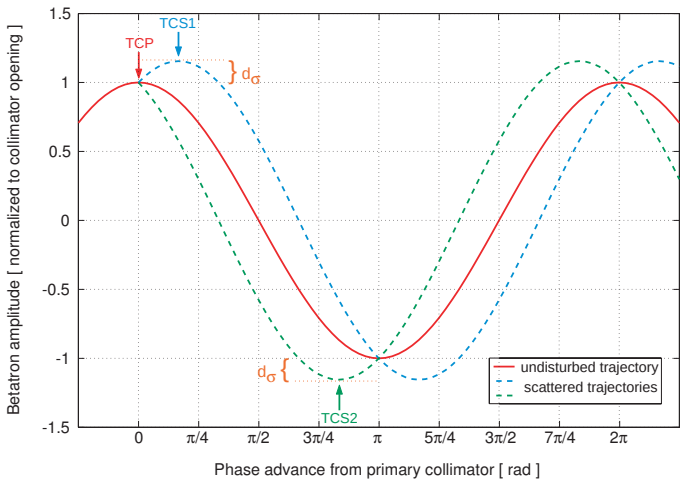

Figure 1.18: Location of two secondary collimators TCS1 and TCS2 designed to clean particles scattered at a given primary collimator TCP as a function of the phase advance from the TCP. The extremum scattered trajectories are represented in dashed lines and reach their peak amplitude at two different location downstream of the TCP, making both TCS1 and TCS2 required for an efficient cleaning. The relative retraction d_σ between primary and secondary jaws is also mentioned; in the LHC case, $d_\sigma = 1\sigma$. From [20].

Not taking coupling between the transverse planes into account, it would therefore be sufficient to install circular collimators separated by $\Delta\mu$ provided that the two transverse planes are characterized with the same local phase advance $\Delta\mu_z(s)$ and same local β_z function. In a real machine, things get more complicated as coupling has to be considered. Collimation creates coupling as a particle impacting in the x plane is scattered in both x

and y direction; this statement alone implies to use more secondary collimators to achieve the best cleaning (i.e. get as low losses in the superconducting parts of the machine as possible). Practically, the cleaning is optimized with a limited number of elements via numerical solutions [7, 8]. As an illustration of the effect of the LHC multi-stage collimation system, Figure 1.19 shows a sample distribution of secondary and tertiary halo particles in normalized radial amplitude at a zero-dispersion location in the machine. The LHC also features 3rd and 4th stage cleaning elements:

- Tertiary collimators (3rd stage) are installed upstream of critical magnets located in the experimental insertions (see Chapter 4 for detailed informations).
- Additional active absorbers (4th stage) are implemented closely to the secondary collimators; these absorbers take care mainly of the *particle showering*, i.e. the low energy particles issued from inelastic interactions which occur in the collimator jaws.

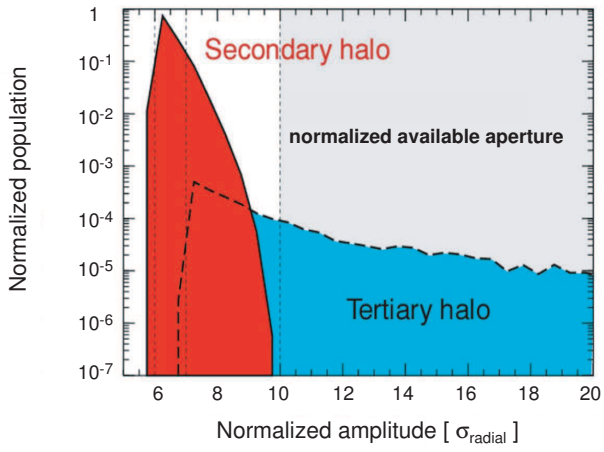

Figure 1.19: Distribution of particles in normalized amplitude depending on their halo type. Courtesy of R. Assmann.

1.7 Efficiency of the collimation system

One needs to define a parameter which qualifies the efficiency of the system. This parameter is called the *cleaning inefficiency* of the collimation system. Its value is given by the ratio of the number of particles escaping the cleaning insertions that reach a normalized amplitude A_{cut} (corresponding to the machine aperture, $A_r \approx 10\sigma$ in the LHC case as mentioned in section 1.3.2) over the total number N of particles impacting on a primary collimator defined by the normalized half-opening n_1:

$$\eta_c(A_{cut}, n_1, n_2) = \frac{1}{N} \cdot \sum_{i=0}^{N} H\left(A_r(i) - A_{cut}\right) \ , \tag{1.37}$$

where $A_r(i) = \sqrt{A_x^2(i) + A_y^2(i)}$ is the radial amplitude of the ith particle and H is the

Heaviside step function returning 1 when $A_r \geq A_{cut}$ and 0 otherwise. η_c is the *leakage rate* at the primary collimators and gives an estimation of the efficiency of the cleaning system. In the LHC case at 7 TeV, the maximum tolerated value for η_c is 10^{-3} [46].

The surviving particles may get lost locally in the machine, these losses being the main source of quenches of the superconducting magnets. It is therefore mandatory to define a limit in the number of losses tolerated per magnet: this limit is known as the *local cleaning inefficiency* $\tilde{\eta}_c$ and corresponds to the total number of particles lost over a given length of the machine normalized to the total number of cleaned protons. It is calculated as:

$$\tilde{\eta}_c = \frac{\eta_c}{L_{dil}} \tag{1.38}$$

with L_{dil} the length over which protons losses are diluted. For the first LHC studies, L_{dil} was taken as 50 metres.

The work presented in this thesis involves numerical simulations of particle performing several hundred turns in the LHC ring. As this multi-turn process may present cases in which a proton hits the same primary collimator more than once, one needs to work with another reference than the number of impacts on a primary jaw. The computing results presented for η_c in the coming chapters are calculated as follows:

$$\eta_c(A_i, n_1, n_2) = \frac{1}{N^{tot}_{absorbed}} \cdot \sum_{j=0}^{N^{tot}} H\left(A_r(j) - A_i\right) \ , \tag{1.39}$$

with H the Heaviside step function already used in equation (1.37) and $N^{tot}_{absorbed}$ the total number of protons that are removed by the simulated collimation system. A proton is considered absorbed by a collimator every time it suffers an inelastic interaction with the jaw material. The local cleaning inefficiency $\tilde{\eta}_c$ is then defined in a similar way:

$$\tilde{\eta}_c(s, n_1, n_2) = \frac{N^{lost}_{protons}(s)}{N^{tot}_{absorbed} \cdot \Delta s_{loss}} \tag{1.40}$$

and gives the number of protons lost in the machine aperture normalized to the total number of absorbed particles over a given length Δs_{loss} which defines the resolution over which losses are measured. In the LHC case, this resolution is taken as 10 cm of the lattice (see also section 3.3.2 for further details). A proton is considered to be lost in the machine the first time its transverse amplitude reaches the limit set by the machine aperture.

The local cleaning efficiency gives an idea on the energy lost in magnets due to direct proton losses within the element and allows looking for possible quench locations on the first order. A large fraction of the beam energy gets lost in the collimator jaws as well though, and the successive inelastic interactions (*showering*) in the collimator jaws material must be simulated to obtain a complete picture of the beam energy lost in the machine. A magnet may present only a low level of proton losses (hence a small value of $\tilde{\eta}_c$) but may still be located close enough to a collimator to absorb an amount of energy coming from particle showers sufficient to make the considered element quench.

Chapter 2

Beam loss in the LHC and required efficiency

As mentioned in the previous chapter, particles moving in a circular machine are distributed around the beam core within a stability limit called the dynamic aperture. Particles that remain inside the dynamic aperture will ideally stay stable for a large number of turns, while particles outside (also called halo particles) get lost in the aperture limitations of the machine. Nevertheless, stable particles can still be kicked out of the dynamic aperture by various processes including the ones induced by machine operation (orbit, tune and chromaticity changes, collisions). These processes create and/or regenerate the beam halo, leading to what is referred to as *regular proton losses*. By studying the different drift processes it is possible to predict the level of these losses.

Particles can also get lost due to *irregular proton losses*, i.e. unexpected (accidental) beam conditions during a relatively short period of time, generally of the order of 1 second. Multiple accident scenarios are considered during every machine design but quantifying the level of losses as they will eventually happen still remains a difficult task.

Taking into account all these processes, one can calculate the corresponding beam lifetimes. One can then give an estimate for the level of local losses that must not be crossed in order to avoid magnet quenches, which translates into cleaning inefficiency values required from the collimation system.

Definition: beam lifetime

First, one needs a parameter to quantify the level of losses: the beam intensity lifetime τ. It describes the evolution of the beam population as a function of time:

$$N_p(t) = N_0 \cdot \exp\left(-\frac{t}{\tau}\right) \ . \tag{2.1}$$

The beam lifetime is defined as the time needed to reduce the number of particles by a fraction $\frac{1}{e}$ of the nominal intensity N_0. In most cases it is possible to determine the contribution to the beam lifetime of a given mechanism.

2.1 Regular proton losses

Regular losses are induced either by beam dynamics or machine operation. These losses are unavoidable and make the case for the need of collimators in a machine to minimize their effect on the elements of the lattice (**cleaning aspect** of the collimation system, see section 1.4). The beam dynamics include scattering of protons with other protons of a same bunch as well as with residual gas atoms. In the LHC case, the maximum achieved beam energy (7 TeV) is large enough to consider the effect of synchrotron radiation. Expected loss mechanisms from LHC operation involve collision between circulating beams and beam-beam effects which may induce resonance crossings; the latter issue is presented with more details in Appendix B.

2.1.1 Single-bunch scattering processes

These processes are treated as *point-like* ones and generally induce changes in the (x', y', p) coordinates only. An offset in the divergences x' and/or y' can clearly lead to a transverse drift of the considered particle outside of the stable area of the beam; a change in the longitudinal divergence p may also lead to the same result, since the motion of any particle is related to both its betatronic part and its momentum offest $\Delta p/p_0$ as stated in equation (1.9) (with p_0 the design momentum of the lattice in the considered optical configuration, see section 1.2).

Intra beam scattering

Intra beam scattering (IBS) refers to Coulomb scattering processes suffered by particles of a same bunch. It involves a continuous exchange of energy between the interacting particles and leads to transverse and longitudinal emittance growth. These effects get nevertheless partially compensated by the quadrupole magnets (for the transverse growth) and the RF voltage (for the longitudinal growth) of the machine.

One property of IBS is that it should leave the total beam energy constant; analytic calculations on the invariant of coupled oscillations in the transverse planes [33] lead to:

$$< H > \cdot \left(\frac{1}{\gamma_{rel}^2} - \frac{1}{\gamma_{trans}^2} \right) + \frac{< \epsilon_x >}{\beta_x} + \frac{< \epsilon_y >}{\beta_y} = const. \tag{2.2}$$

with H the invariant of the momentum spread for a bunched beam as defined in [33] by:

$$H = \frac{\Delta p}{p} + \frac{1}{\Omega_{synch}} \cdot \frac{d}{dt} \left(\frac{\Delta p}{p} \right)$$

with Ω_{synch} the synchrotron frequency of the machine. One can observe that equation (2.2) presents two cases:

- for a beam energy below transition, $\gamma_{rel} < \gamma_{trans}$ and all terms are positive: an increase of the beam size in a given direction is therefore compensated in the other two directions, leading to an equilibrium state of the particle distribution,

- for a beam enery above transition (LHC case), $\gamma > \gamma_{trans}$ and the longitudinal term becomes negative: the equilibrium is broken and any change in the momentum of particles leads to a continuous increase of the beam size and a reduction of the beam lifetime.

The transverse and longitudinal emittance growth times t_ϵ in both the injection and the collision energy case are given in Table 2.1.

Table 2.1: IBS emittance growth time t_ϵ for the transverse and longitudinal planes in the two LHC operation modes. From [1].

	Injection (450 GeV)	**Collision (7 TeV)**
ϵ_{long} growth time [hours]	30	61
ϵ_{trans} growth time [hours]	38	80

Appendix C gives the derivation of the beam lifetime values from the estimated emittance growth rates.

Touschek scattering

This mechanism refers to IBS processes with enough energy change that the particles leave the longitudinal momentum aperture (see section 1.3.3). The loss rate is quadratic with the bunch population N_{bunch} [34]:

$$\frac{dN_{bunch}}{dt} = -\alpha N_{bunch}^2 \ , \tag{2.3}$$

with α a constant slope value; it leads to:

$$\begin{aligned} N_{bunch}(t) &= N_0 \cdot \frac{1}{1+\alpha N_0 t} \\ N_{coast}(t) &= N_0 \cdot \frac{\alpha N_0 t}{1+\alpha N_0 t} \end{aligned} \tag{2.4}$$

with $N_0 = 1.15 \times 10^{11}$ the initial bunch population in the LHC case, and N_{coast} the number of particle outside of the RF bucket circulating in an unbunched way. These particles form what is called the *coasting beam*.

From (2.4) one can define the Touschek lifetime as:

$$\tau_{touschek} = \frac{1}{\alpha \cdot N_0} \ . \tag{2.5}$$

The values for α can be derived from an assumption on the shape of the beam; for round beams [34], one gets:

- at injection energy (450 GeV): $\alpha_{round} \approx 5.0 \times 10^{-19}$ s^{-1} $\Rightarrow \tau_{touschek}^{inj} \sim 4830.9$ hours,
- at collision energy (7 TeV): $\alpha_{round} \approx 2.0 \times 10^{-19}$ s^{-1} $\Rightarrow \tau_{touschek}^{coll} \sim 12077.3$ hours.

2.1.2 Scattering on residual gas

Even in extremely good vacuum conditions, residual gas molecules (generally H, C and O from H_2, CO, CO_2, CH_4, H_2O) may still be present in the beam pipe of an accelerator. Nuclear scattering interactions can then occur between these molecules and circulating protons, which get kicked to large amplitudes out of the stable motion region of the beam and get lost at the next aperture restriction of the machine. The beam emittance can also increase because of residual gas due to *MCS*.

Beam-gas nuclear scattering

There are two possibilities for protons to be scattered by residual gas nucleuses [35]:

- inelastic scattering: the interaction between an incoming proton and a nucleus of a gas molecule produces secondary particles which get lost within 15 metres from the interaction point. These losses are distributed along the machine according to local gas densities,
- elastic scattering: the incoming proton is kicked away transversally by a nucleus of a gas molecule, which leads to emittance growth (small scattering angle) and/or local losses (large scattering angle).

With protons circulating in the beam pipe in the LHC case, [35] refers to proton-proton interactions as "the limiting case". The corresponding cross-sections are reported in Table 2.2, which shows that the inelastic p-p scattering is the most expected mechanism.

Table 2.2: Proton-proton total, elastic and single-diffractive (SD) scattering cross sections. Taken from [35].

Proton energy [GeV]	σ_{pp}^{tot} [mb]	σ_{pp}^{el} [mb]	σ_{pp}^{SD} [mb]
450	~ 40	~ 7	~ 3.3
7000	~ 46.9	~ 8	~ 5.2

In the proton-nucleus case, the cross-sections of nuclei depend on the atomic mass A. According to scaling laws, the total cross-section changes with A as $\sigma(A) \approx \sigma_p \cdot A^{0.77}$ (see section 1.5.3), while the inelastic scattering one reads $\sigma_{inel}(A) \approx \sigma_{inel}(A=1) \cdot A^{0.71}$. As for pp interaction, the inelastic scattering is the dominant mechanism for pN scattering.

To obtain the corresponding cross-sections for molecules, it is sufficient to sum the respective cross-sections of each atom of the molecule. The beam lifetime τ_{gas} is then calculated as follows:

$$\frac{1}{\tau_{gas}} = c \cdot \sigma_{gas}^{tot} \cdot n_{gas} \ ,$$

with c the speed of light and n_{gas} the gas density; if more than one gas are present in the beam pipe, one gets:

$$\frac{1}{\tau_{gas}^{tot}} = c \cdot \sum_{gases} \left(\sigma_i^{tot} \cdot n_i \right) \ , \tag{2.6}$$

where i is the index of each residual gas. In the LHC case, mostly H_2 gas will be present in the vacuum pipe; its cross-sections are about twice the ones listed in Table 2.2. According to [36], the level of losses induced by the nuclear scattering processes will create a "non-negligible heat load". A maximum value of 0.1 W.m^{-1} is set as a design constraint, which translates into a minimum beam-gas scattering beam lifetime of 100 hours in both injection and collision energy cases. From equation (2.6), one can then obtain the maximum allowed residual gas densities; the H_2-equivalent maximum density allowed is therefore 1.4 $\times 10^{15}$ molecules.m^{-3} at 450 GeV and 1.2 $\times 10^{15}$ molecules.m^{-3} at 7 TeV.

Emittance growth

An accumulation of point-like, small angle scattering processes (also known as multiple Coulomb scattering, *MCS*) can lead to large transverse kicks of incoming protons. This will increase the emittance in the corresponding plane with an emittance growth defined by [1]:

$$\frac{d\gamma_{rel}\epsilon_z}{dt} = \bar{\beta_z}\gamma_{rel} \cdot \left(\frac{13.6 \text{ MeV}}{\beta cp}\right)^2 \frac{c \cdot n \cdot m_{gas}}{X_0}, \tag{2.7}$$

where n and m_{gas} are respectively the density and the mass of the gas molecules of the considered species. X_0 is the radiation length of the considered gas in kg.m^{-3} and $\bar{\beta_z}$ the average β-function in the z-plane ($\approx$ 100 m at injection energy and $\approx$ 150 m at collision energy). From (2.7) it appears that the effect of *MCS* is larger at injection than at collision, e.g. for the H_2 gas with a growth time of 17 hours at injection energy and $\approx$ 500 hours at collision energy [16]. Table 2.3 includes the growth times expected at 450 GeV for the gas density derived from a 100 h nuclear scattering lifetime.

Table 2.3: Nuclear scattering cross-section, maximum allowed densities and the accompanying emittance growth time at injection for various gas species. Taken from [1].

molecule	σ_{nucl} **[barn] at 7 TeV**	**n [m^{-3}] at 7 TeV** for τ_{nucl} = 100 h	τ_ϵ **[h] at 450 GeV** for τ_{nucl} = 100 h
H_2	0.078	1.2×10^{15}	17.0
He	0.133	6.9×10^{14}	12.5
CH_4	0.511	1.8×10^{14}	7.6
H_2O	0.510	1.8×10^{14}	9.5
CO	0.751	1.2×10^{14}	7.5
CO_2	1.171	7.9×10^{13}	5.0

2.1.3 Synchrotron radiation

In a circular machine like the LHC, a charged particle following a curved trajectory emits an electromagnetic radiation called *synchrotron radiation* (SR) [37]. Although the beam energy required for this phenomenum to occur is much higher for proton beams than

for electron beams, the LHC will be the first proton storage ring for which SR becomes significant. SR implies some energy loss in the direction where the radiation is emitted, meaning that the momentum of particles in all 3 planes of motion (longitudinal, horizontal and vertical) can be affected. The amount of energy lost per turn U_0 writes:

$$U_0 \text{ [eV]} = 2.65 \times 10^4 \cdot E^3 \text{ [GeV]} \cdot B \text{ [T]} , \tag{2.8}$$

with E the beam energy and B the magnetic field of dipole magnets (see Table 1.1). This energy loss occurs at every location where the trajectory of a circulating proton gets bent. Together with the possible direct loss of transverse momentum due to U_0, it creates deformations of the betatronic oscillations. For machines with significant level of SR, the RF system is set up to compensate the longitudinal momentum loss in addition to its normal usage (accelerating and/or phase stability, see section 1.3.3). It implies that the transverse components of the beam momentum are left unchanged after the energy loss: this is known as *radiation damping*[1].

From [38, 39], the damping time τ_z of the oscillations due to SR in the three degrees of freedom is given for protons in a circular machine by (in practical units):

$$\tau_z \text{ [h]} \cdot J_z = \frac{16644}{E \text{ [TeV]} \cdot B \text{ [T]}^2} \cdot \frac{L}{2\pi\rho} , \tag{2.9}$$

z standing for any of the three coordinates x, y, s. L is the length of the design orbit, ρ is the bending radius of the dipole magnets and J_z is the *Damping Partition Number* as defined by the Robinson theorem [38]:

$$\begin{gathered} J_x + J_y + J_s = 4 \\ J_x \approx 1 \qquad J_y = 1 \qquad J_s \approx 2 \end{gathered} \tag{2.10}$$

The damping times are estimated for the LHC at 7 TeV [1]: $\tau_{x,y} \approx 26.0$ hours in the two transverse planes and $\tau_s \approx 12.9$ hours in the longitudinal plane. The radiation damping may also compensate for emittance dilution due to other processes, such as beam-beam effects.

2.1.4 Beam-beam collisions and related effects

During LHC operation, collisions between the two circulating proton beams take place at top energy (7 TeV) only. The *pp* interaction mechanisms (elastic, inelastic, diffractive) are reviewed in section 1.5. For what concerns emittance growth time, only elastic and diffractive scatterings are to be considered since inelastic interactions are designed to happen within the 4 detectors of the machine. According to [35], "diffractive events, depending on the momentum transfer, will lead to quasi-local losses" in regions close to the interaction points (IPs), or in the momentum cleaning collimation insertion if the momentum transfer δp is small enough for the scattered particle to stay within the longitudinal acceptance.

[1] this expression is a bit misleading, as the damping effect of the betatron motion appears to occur due to the energy gain in the RF cavity, not due to the energy loss U_0 by SR.

Considering *pp* elastic scattering processes, there are basically two expected outcome depending on the amplitude of the scattering angle: if small, protons will start populating the beam halo, inducing emittance growth. If large, most of the time the scattered protons are lost within a few meters. Some halo protons may then get lost at the first aperture restriction if the amplitude of the oscillations is too large. Following equation (1.22), the differential *pp* elastic cross-section reads:

$$\frac{d\sigma}{d(p\theta)^2} = K \cdot \exp\left(-b(s,p,\theta)\cdot(p\theta)^2\right) \ ,$$

with θ the scattering angle, b the slope factor and s the square of the centre of mass energy. This equation allows writing the mean scattering angle as:

$$\sqrt{\langle\theta^2\rangle} = \frac{1}{p\cdot\sqrt{b}} \ . \tag{2.11}$$

At collision energy, the center of mass energy $\sqrt{s}$ is 14 TeV which gives using (1.23): $b = 18.9$ GeV^{-2}. With (2.11), one gets 32.86 μrad as the mean scattering angle for elastic *pp* scattering at 7 TeV. One can compare this value to the estimated rms transverse beam divergence $\sigma' = \sqrt{\epsilon_{rms}/\beta^*}$ at each IP, as reported in Table 2.4.

Table 2.4: Beam divergence σ' at each interaction point of the LHC main ring when running at collision energy (7 TeV). Corresponding values of β^* are taken from Table 1.3. The rms transverse emittance is taken as $\epsilon_{rms} = 0.503 \times 10^{-9}$ m.rad in both x and y planes.

Experiment	β^* [m]	**Beam divergence** σ' [μrad]
ATLAS (IP1)	0.55	30.24
ALICE (IP2)	10.0	7.09
CMS (IP5)	0.55	30.24
$\mathrm{LHC_b}$ (IP8)	1.0	22.43

The main contribution to emittance growth is expected from the high luminosity insertion IP1 and IP5: the σ' there is comparable to the calculated value of mean scattering angle. Only a small fraction of the scattered protons will therefore drift away from the beam core, forming the beam halo. From [35], if one only takes the high luminosity IP's into account, the emittance growth rate writes:

$$\frac{d\epsilon}{dt} \approx \frac{(\beta^*_{IP1}\cdot L_{IP1} + \beta^*_{IP5}\cdot L_{IP5})\cdot\sigma^{el}_{pp}\cdot\langle\theta^2\rangle}{M\cdot N_b} \ , \tag{2.12}$$

where β^*_{IPi} is the value of the betatronic Twiss parameter at the ith interaction point, L_{IPi} is the corresponding beam luminosity value and $\sigma^{el}_{pp} \approx 40$ mbarns is the elastic proton-proton cross-section for 7 TeV head-on collisions. M and N_b correspond respectively to the number of bunches and number of protons per bunch in the LHC during collision energy

runs. Values for all these parameters can be found in Tables 1.2 and 1.3; using the value found for the mean scattering angle at 7 TeV, one gets a transverse emittance growth rate due to beam-beam collisions of about 95 hours. According to [35], this leads to an estimated beam lifetime of more than 300 hours if one considers an aperture limitation at 6 σ_z (set by the opening of betatron cleaning collimators).

Beam-beam effect

In the LHC like in all colliders, each of the circulating beams interacts through its electromagnetic potential with the other one. In the experimental insertions, in spite of the designed beam separation, a given bunch of particles "feels" the effect of the bunches of the other beam, as shown in Figure 2.1. This effect increases with the beam luminosity, since a high luminosity implies high particle density over tight beam dimensions.

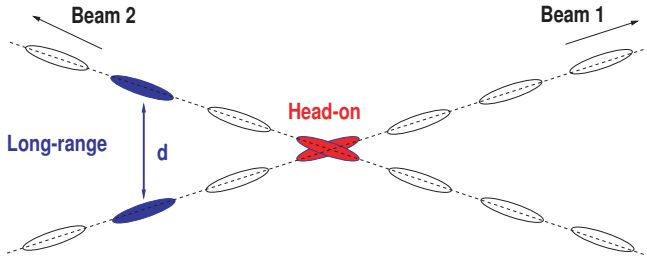

Figure 2.1: Head-on and long-range beam-beam interactions at a LHC interaction point.

Following the derivation presented in [40], one can consider a particle in one of the beams, the *test particle*, and study the effect of the other beam on it. The forces can be either attracting or repelling since this test particle can have the same or opposite charge with respect to the beam creating the forces. To determine the intensity of the effect endured by the test particle, one assumes a Gaussian shape for the density of particles in the incoming beam. In the two-dimensional case, assuming a bi-Gaussian beam density distribution, one has $\rho(x, y) = \rho_x(x) \cdot \rho_y(y)$ with:

$$\rho_z(z) = \frac{1}{\sigma_z\sqrt{2\pi}} \cdot \exp\left(-\frac{z^2}{2\sigma_z^2}\right) \tag{2.13}$$

where z stands for either x or y. From the Poisson equation one can derive the two-dimensional field potential $U(x, y, \sigma_x, \sigma_y)$ as:

$$U(x, y, \sigma_x, \sigma_y) = \frac{ne}{4\pi\varepsilon_0} \cdot \int_0^\infty \frac{\exp\left(-\frac{x^2}{2\sigma_x^2+q} - \frac{y^2}{2\sigma_y^2+q}\right)}{\sqrt{(2\sigma_x^2+q)\cdot(2\sigma_y^2+q)}} dq \tag{2.14}$$

where n is the density of particles in the beam, e the charge of the particle and ε_0 the vacuum permittivity. From this potential, one can get both the transverse electric field $\mathbf{E}$

and the associated magnetic field **B** (generated by charged particles moving at a speed **v**):

$$\begin{aligned} \mathbf{E} &= -\nabla \cdot U(x, y, \sigma_x, \sigma_y) \\ \mathbf{B} &= \mathbf{v} \times \frac{1}{c^2}\mathbf{E} \end{aligned} \tag{2.15}$$

Assuming round beams, $\sigma_x = \sigma_y = \sigma_r$ and the two transverse coordinates x and y combine in a unique radial coordinate r with $r^2 = x^2 + y^2$. Use cylindrical coordinates, one can re-write equation (A.1) for the LHC *pp* case as:

$$\mathbf{F} = e\left(E_r - \beta_{rel} c B_\Phi\right) \cdot \mathbf{r} \tag{2.16}$$

with β_{rel} the relativistic factor. Using (2.14) and (2.15) in (2.16) leads to [40]:

$$F_r(r) = \frac{ne^2 \cdot \left(1 + \beta_{rel}^2\right)}{2\pi\varepsilon_0} \cdot \frac{1}{r} \cdot \left[1 - \exp\left(-\frac{r^2}{2\sigma_r^2}\right)\right] \tag{2.17}$$

Figure 2.2 shows the behaviour of the force versus the distance between the test particle and the opposite beam: it increases when getting closer, has its maximum at the edge of the beam and goes to zero at the beam center. At this location, the effect of every particle in the opposite beam is compensated. For small amplitudes, the force is quasi-linear and so is the electric field. As described in Appendix B, this results in a *quadrupole-like tune change*. For amplitudes larger than 1 σ_r, the force is no longer linear and the tune change is a function of the amplitude.

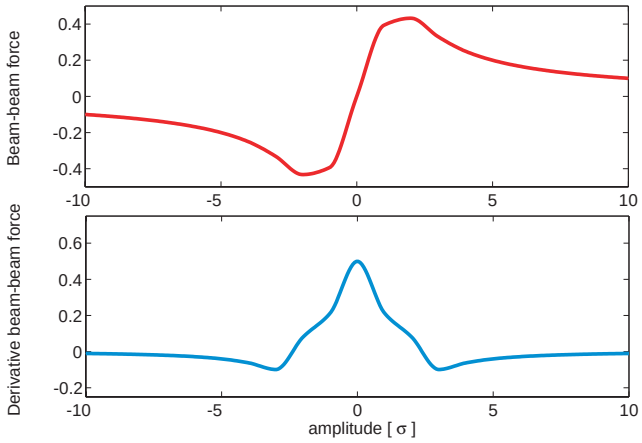

Figure 2.2: Shape of the beam-beam force (top) and its derivative (bottom) for round beams. The amplitude is given in units of rms beam size.

The tune shift of a particle coming close to the opposite beam is related to the derivative of the force versus the amplitude. For a test particle with a small amplitude, ΔQ is given by the slope of F_r at the origin (i.e. the center of the opposite beam), which

is called the *beam-beam parameter* ξ:

$$\xi_{x,y} = \frac{N \cdot r_0 \cdot \beta^*_{x,y}}{2\pi \cdot \gamma_{rel}\sigma_{x,y} \cdot (\sigma_x + \sigma_y)} \ , \qquad r_0 = \text{particle radius} = \frac{e^2}{4\pi\varepsilon_0 mc^2} = 1.54 \times 10^{-18} \text{ m for protons.} \tag{2.18}$$

where N is the beam intensity and β^* is the value of the Twiss parameter β at the interaction point. For particles with large oscillation amplitudes, the tune shift is no longer linear and is therefore calculated doing the average of the derivative of the force over the range of amplitudes. From [40], the tune shift in each transverse plane in the *pp* head-on case:

$$\Delta Q(J)/\xi = -\frac{2}{J} \cdot \left(1 - I_0\left(\frac{J}{2}\right) \cdot \exp\left(-\frac{J}{2}\right)\right) \tag{2.19}$$

with $J = \epsilon\beta/2\sigma^2$ where ϵ, β and σ are respectively the emittance, the Twiss β-function and the real unit beam size (as defined in equation (1.10)). This is valid for any transverse coordinate at a given location along the crossing scheme where the considered test proton performs large oscillations. I_0 is the modified Bessel function of order zero.

In the two-dimensional case, the detuning depends on both horizontal and vertical amplitudes. The detuning ΔQ must therefore be computed in a two-dimensional form, and the corresponding graphical representation is called a *tune footprint*.

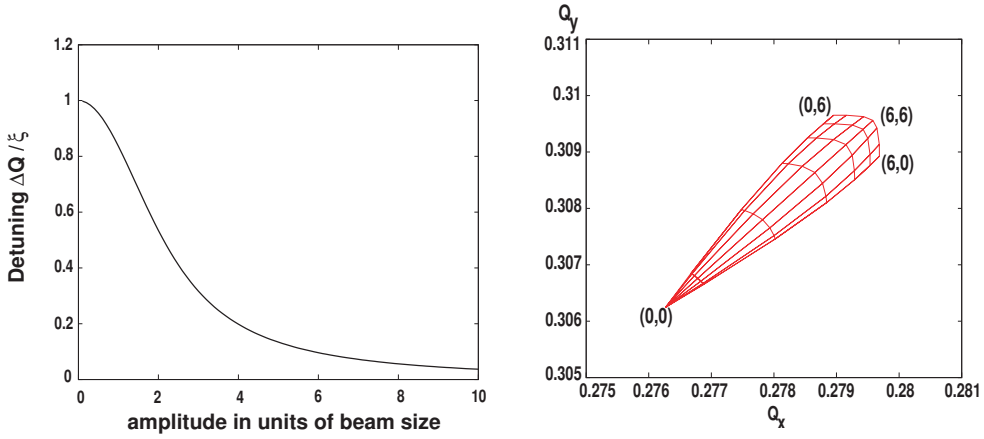

Figure 2.3: Sample plots of detuning in the e^+ - e^- case. Left: Tune shift $\Delta Q(J)/\xi$ as a function of the particle amplitude - Right: two-dimensional tune footprint for the head-on collision case. Courtesy of W. Herr from [40].

Figure 2.3 shows a representation of both ΔQ and the corresponding tune footprint for a head-on collision case. On the plot on the right, each "node" of the 2D map corresponds to a combination of horizontal and vertical amplitudes, from 0 to 6 σ. If the diagram is too large for any of the tunes Q_x or Q_y, there is a possibility of resonance crossing: the tune spread must be small enough so that the footprint fits in a region with a small density of

resonance lines (see Figure B.1). Nevertheless, high order resonances can never be eliminated; the difficulty comes when trying to determine up to which order it can be avoided. In the LHC case, the tolerance for the tune spread is about 0.01-0.015.

In all of the above, only the region close to the interaction point has been considered. One would also have to take into account the crossing schemes that lead to the interaction point though, where *long-range beam-beam interactions* can occur. As seen in Figure 2.1, the passage of one of beam close to the other one also creates a charge effect, hence a Lorentz force. It is obvious that the effect of the long-range interaction must depend on the separation between the two beams. For large distances (usually, larger than 6 σ), the corresponding tune spread ΔQ_{LR} scales as [40]:

$$\Delta Q_{LR} \propto -\frac{N}{d^2} \tag{2.20}$$

where N is the beam intensity and d is the separation between the two beams. The minus sign points out that the tune shift changes its sign once you go to large amplitudes, as it can be seen on Figure 2.2 by the change of the sign of the slope for amplitudes larger than $\pm$ 2 σ. It can be also be noted that even a small change in crossing scheme can turn into a big change in tune shift.

2.2 Irregular proton losses

The regular loss mechanisms described in the previous section are what the LHC collimation system is designed to clean to avoid magnet quenches (quench protection aspect, see section 1.4). Proton losses can also take place due to operational errors and/or equipment failures. The cold aperture of the machine (i.e. the mechanical opening of the superconducting elements) must be protected from such events: LHC collimators therefore need to be designed to bring this passive protection and, at the same time, survive the beam loads from the considered error scenarios without being heavily damaged.

Reviewing the machine protection aspect of the LHC collimation system is not the topic of this thesis. The following therefore briefly presents the various machine scenarios and physics mechanisms involved and the required additional protective elements. It has to be pointed out that these elements were all included in the simulations of the efficiency of the full LHC collimation system (see chapter 4).

2.2.1 Injection errors

Before reaching the LHC main ring, the two beams have to go through transfer lines from the SPS. At each injection point, the corresponding beam could enter the septum magnet and the kicker with incorrect parameters:

- *transverse mismatch*: it can be that the shape of the beam is not the expected one, i.e. that the Twiss parameters at the end of the transfer line and at the injection point are different. This quickly leads to an emittance increase and larger betatron oscillations. Losses will take place if the mechanical aperture downstream of the injection point is not large enough to fit the new maximum amplitude.

- *longitudinal mismatch*: as for the transverse mismatch, the beam can enter the main ring and remain stable even with a momentum offset. Once operators start ramping the machine, particles with a $\Delta p/p_0$ larger than what the separatrix allows will get lost at the location of highest dispersion (see section 1.3.3).

From [41], these errors can create large oscillations in both transverse planes, on the order of 6 to 10 $\sigma_{x,y}$. A set of three dedicated collimators are installed in each of IR2 (Beam 1) and IR8 (Beam 2) injection insertions in order to reduce the amplitude of these oscillations.

2.2.2 Failure of a kicker magnet

Kicker magnets are mainly used in the injection insertions (IR2, IR8) and the beam extraction insertion (IR6). Correction kickers are also installed over the length of the machine; these are divided in two types depending on which transvere plane they act. Basically, two classes of problems exist with kicker magnets:

- kicker misfiring at an injection point or the extraction region [42, 43],
- power failure (e.g. wrong current value) of a given kicker in the ring.

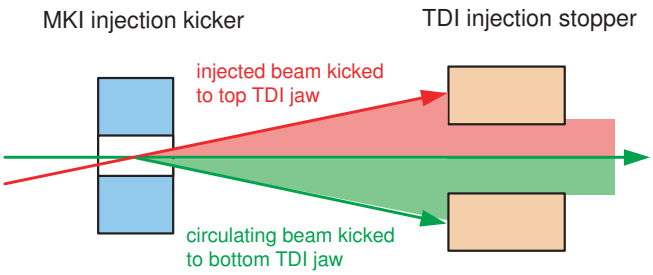

Figure 2.4: Effect of a power failure of an injection kicker magnet on the injected and circulating beams [42]. The colored areas correspond to the regions that can be swept by each beam depending on the effective kicker field. This scheme can be applied in a similar way at the beam dump insertion region for the corresponding kicker magnet.

The difference between a misfiring and a power failure is that one affect the phase of the kick while the other changes the amplitude of the kick. Both have the same overall effect on the beam though, i.e. changing the design orbit not only for the injected/extracted beam but also for the particles already/still circulating in the main ring. The orbit error can reach large figures before being detected and corrected: during the LHC beam injection process, the machine is filled with batches of 72 consecutive proton bunches with 25 ns spacing. Once the last batch is injected, the LHC beams are made of 2808 bunches (see Table 1.2) with the last bunch being 3 μs away from the first bunch, as it can be seen in Figure 2.5. This interval is called the *beam abort gap*; in case that the extraction kickers are not fired within this time interval, the orbit deflection can reach 231 σ_x at top energy [41].

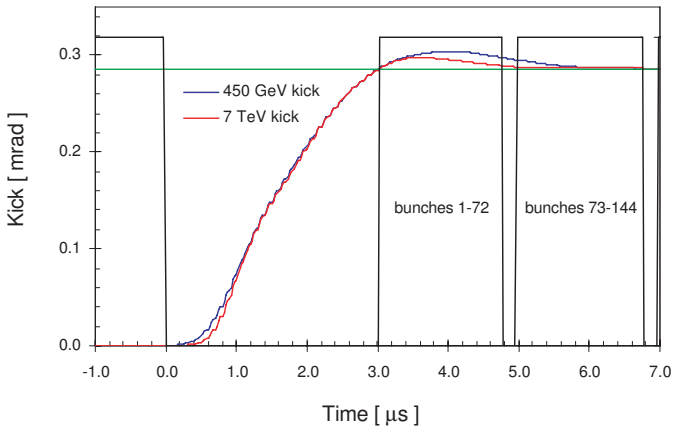

Figure 2.5: Extraction kickers rise time versus beam abort gap. An asynchronous beam dump is due to a desynchronized firing of the kickers with respect to the 3 μs time window. Courtesy of B. Goddard from [44].

Kicker magnets are really sensitive locations of the machine and extra absorbers should be installed close to them. For kicker failures in the injection and extraction regions, additional collimators are installed in order to absorb most of the misdirected beam.

2.2.3 Failures inducing slow (multi-turn) losses

Slow losses are most of the time induced by a failure in one of the magnet powering systems, possibly due to a quench. Other scenarios include the loss of vacuum, a failure of the RF system or an element (e.g. a collimator jaw) moving into the beam pipe creating an aperture limitation. Since the collimators are the closest elements to the beam, particles will end up hitting the collimator jaws after a few turns in case of one of the previous scenarios. A problem though would be the detection of the failure since slow losses also mean low instantaneous loss rates at the Beam Loss Monitors (BLM's, the dedicated detecting devices).

The critical case is a failure of a normal conducting D1 separation magnet located in the insertions IR1 and IR5, generating the kicks required for the crossing schemes; this case has been studied in [45]. The study considers a non-Gaussian beam distribution cut at 3 σ centered between two collimators jaws sitting at 6 σ. In case of a D1 failure, the beam can move as fast as 0.1 σ closer to the collimator per turn, which means that particles in the beam tails will start touching the collimator after 30 turns and the BLM associated to this collimator will start detecting losses. As the beam keeps drifting away, it is more than 10^{12} particles that will impact on the jaws within one turn, which represents about 89 μs. The BLM signal to trigger a beam abort would therefore come too late to avoid any damage on the jaws.

This feature highlights the role of the LHC collimation system for machine protection: with dedicated equipments installed close to the collimator locations, it is possible to set up a high performance beam monitoring system to check for:

- abnormal/fast beam movements, using signal from the Beam Position Monitors (BPM's),
- increasing heat load on the collimator jaws,
- a peak in local loss rates, using signal from the BLM's.

As additional protection against slow losses, it is useful to put collimators/absorbers upstream of the triplet magnets[3] to protect the superconducting quadrupoles. As described above, the beam can be partially deflected by a kicker or some movable element, travel through a complete arc and reach critical magnets. This is particularly true for the triplet magnets:

- in IR5: there is no cleaning between the IR6 beam dump region and the IR5-CMS experimental region in the Beam 2 direction,
- in IR8: the triplet is downstream of the IR7 betatron cleaning region and its movable elements in the Beam 1 direction, so magnet protection relies on the betatron collimation system settings.

2.3 Beam lifetimes and beam loads on collimators

Taking into account all of the mechanisms described in 2.1, the range of acceptable beam lifetimes must be large enough for safe commissioning of the machine and its collimation system in nominal operating conditions [46]. The peak loss rate at injection energy takes place at the start of the ramp, with an expected lifetime of 20 s (up to 5% of the RF-uncaptured beam is estimated to be lost at that moment). For continuous losses a minimum lifetime of 1h is specified for injection and top energy [6]. Table 2.5 lists the estimated minimum lifetimes for each case.

Table 2.5: Specified minimum beam lifetimes τ, their duration T, the proton loss rate R_{loss} and maximum power deposition P_{loss} in the cleaning insertion. From [1].

Mode	T [s]	τ [h]	R_{loss} [p/s]	P_{loss} [kW]
Injection	cont.	1.0	0.8×10^{11}	6
	10	0.1	8.6×10^{11}	63
Ramp	≈ 1	0.006	1.6×10^{13}	1200
Top energy	cont.	1.0	0.8×10^{11}	97
	10	0.2	4.3×10^{11}	487

For fast losses (like injection errors and/or kicker failures), any collimator jaw installed in the machine can be hit. The primary collimators only cover one phase-space location and the failure inducing the losses (e.g. fast orbit bump) can create a transient tune shift: collimators must therefore be designed to withstand the beam impact during these abnormal proton losses without suffering severe damage (on the surface of the jaw or on the metallic

[3] the triplet magnets are four quadrupoles used to reduce the β_z functions at the interaction points in the experimental insertions IR1, IR2, IR5 and IR8.

support, see section 5.3). The specified beam loads over one turn for various error scenarios are reported in Table 2.6. These values refer to nominal LHC beam parameters (reported in Table 1.2); for the asynchronous beam dump scenario, one should consider an average β_x of 410 m at the extraction kicker magnet (labeled MKD in the following) and a beam impact on the collimators between 5 and 10 σ_x.

Table 2.6: Maximum beam load deposited over one turn in the collimator jaws for three scenarios of ultra-fast (one turn) beam losses. From [1].

Scenario	Beam energy [TeV]	Deposited intensity [protons]	Deposited energy [kJ]	Impact duration [ns]
Injection error	0.45	2.9×10^{13}	2073	6250
Asynchronous dump	0.45	6.8×10^{11}	49	150
(all modules)	7.00	4.8×10^{11}	538	100
Asynchronous dump	0.45	10.2×10^{11}	74	225
(single module)	7.00	9.1×10^{11}	1021	200

In addition to these cases, another special failure has to be taken into account for injection errors: a flashover (wrong kick amplitude due to power failure, see Figure 2.4) of one of the injection kicker magnet [47] can lead to up to 80 % of an injected batch (made of 72 bunches) dumped onto a collimator jaw. Considering this scenario along with the other possible injection errors, it is required that the collimator jaws can withstand the impact of a full batch without damage. For beam dump errors, two main scenarios have been taken into account:

- asynchronous firing of the dump kicker magnets with respect to the beam dump gap (see previous section): the beam is swept across the available aperture by the rising kicker voltage,

- single module pre-fire: one of the 15 MKD modules spontaneously triggers, inducing a re-triggering for the other 14 modules that will be out of phase with the beam dump gap.

The frequency of these errors is hard to predict but it has been estimated that they could happen at least once a year. For the LHC case, abnormal beam dump scenarios only affect the horizontal beam distribution, so only horizontal collimators (and a few skew ones to a certain extent) are concerned by the dump errors. It has to be noted however from the values in Table 2.6 that only small fractions of the LHC beam (about a few ‰ of the total beam population of $\approx 3.23 \times 10^{14}$ protons) can be lost on the collimator jaws within one turn.

2.4 Loss rate and local cleaning inefficiency

Studies on quench levels for slow, continuous proton losses [48] give the maximum allowed local proton loss rates for the LHC as:

$$\begin{aligned} R_q^{inj} &= 7 \times 10^8 \text{ protons m}^{-1} \text{ s}^{-1} \text{ (450 GeV)}, \\ R_q^{coll} &= 7.8 \times 10^6 \text{ protons m}^{-1} \text{ s}^{-1} \text{ (7 TeV)}. \end{aligned} \tag{2.21}$$

For the nominal LHC beam intensity of $\sim 3 \times 10^{14}$ protons, losses must be controlled for 10^{-6} to 10^{-8} of the total beam population to avoid limitation in maximum beam intensity and/or beam lifetime. From [6], the required minimum beam lifetimes for each operational mode are:

$$\begin{aligned} \tau_{min}^{inj} &= 0.1 \text{ h at injection energy (450 GeV)}, \\ \tau_{min}^{coll} &= 0.2 \text{ h at collision energy (7 TeV)}, \end{aligned} \tag{2.22}$$

These values are tolerated during operation for a limited time of 10 seconds, as noted in Table 2.5. For longer periods of time, the beam must be dumped; the beam is not removed immediately to allow safe dump action and data recording for "post-mortem" analysis. The lifetime of 0.2 hours for the 7 TeV case corresponds to a loss of 1 % of the beam in 10 s.

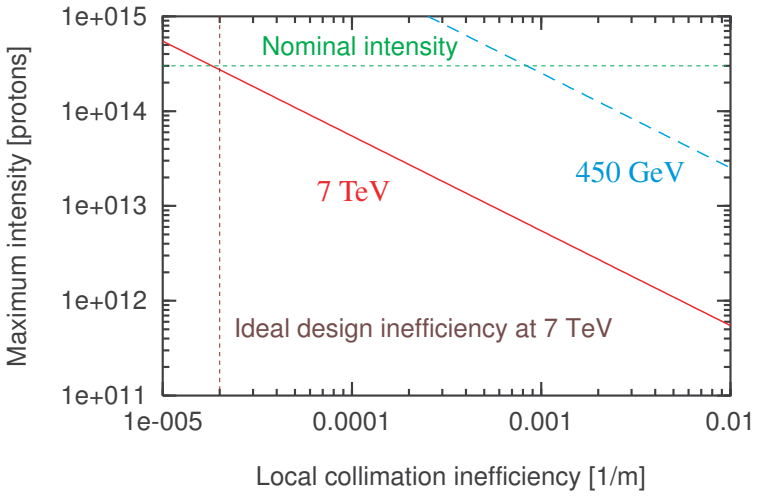

Figure 2.6: Beam intensity versus local cleaning inefficiency for running at the quench limit. Minimum allowed beam lifetimes of 0.2 h (7 TeV) and 0.1 h (450 GeV) are assumed.

For an operationally required minimum beam lifetime τ_{min}, the total intensity limit N_q^{tot} at the quench limit R_q is given by:

$$N_q^{tot} = \frac{\tau_{min} \cdot R_q}{\tilde{\eta}_c} \tag{2.23}$$

where $\tilde{\eta}_c$ is the local cleaning inefficiency as defined in equation (1.40). Figure 2.6 shows the evolution of the intensity limit N_q^{tot} versus local cleaning inefficiency values. To achieve

the design goal in intensity for LHC with the values given in (2.21) and (2.22), $\tilde{\eta}_c$ needs to be less than $10^{-3}\mathrm{m}^{-1}$ at injection energy and $2 \times 10^{-5}\mathrm{m}^{-1}$ at collision energy. These values are taken as the local quench limit values in the following. Results from beam loss simulations will be compared to these references.

It has to be pointed out that what is discussed above only uses a *simplified quench model*, assuming that the proton loss rates R_q calculated for dipole magnets can be applied to all magnet types. Large uncertainties remain for the quench levels of some specific magnets, meaning that even though the quench limit may be represented by a straight line (see chapter 4), local safety margins should be taken into account.

Chapter 3

The LHC Collimation System: design, layout and simulation procedures

This chapter reviews the layout of the LHC collimation system: IR3 is dedicated to *momentum cleaning* and IR7 to *betatron cleaning*. In each one of these regions, a multi-stage cleaning system is designed and installed for both circulating beams of the LHC. The different types of collimators are also introduced in this chapter.

Based on the beam physics mechanisms presented in the previous two chapters, collimators are located and set up using state-of-the-art simulation codes. The following does not include detailed explanations on the encoding part of each program and shall not be taken as a user's manual, as it is more of an introduction to the tracking procedures.

3.1 Collimator requirements and design constraints

As already mentioned in section 1.4.1, the design of the LHC collimation system faces a lot of strong constraints and requirements in order to achieve a very high cleaning efficiency. In addition to the design limitations set by the behaviour in the machine of the circulating beam, the consequences of beam cleaning need to be estimated so as to select the most appropriate mechanical settings for both the collimator jaws but also its support structure and cooling system.

3.1.1 Requirements from beam physics and quench protection

The main goal of collimators is to clean the machine from halo protons that may induce superconducting magnet quenches. This means that the collimators jaws must be the *aperture bottleneck* of the entire ring, i.e. the first element touched by the halo protons. Their gap openings cannot be too large for the system to remain efficient. The collimator jaws should also avoid intercepting any part of the core of the beam (i.e. its most stable part), meaning minimal openings of 4-5 σ_z (unit beam sized as defined in chapter 1). The range of possible operational settings for the collimator jaw openings is also limited by the

impedance shift created by the jaw material getting closer to the circulating beam[1]. Finally, the strongest requirement for the efficiency of a multi-stage system is that the jaws designed to be the primary jaws of the system (i.e. the first one where proton impacts occur) stays so during machine operation. The same argument is true for secondary jaws. The retraction $d_\sigma = 1\sigma_z$ (see section 1.6) between primary and secondary jaws is equivalent to roughly 200 μm at collision energy (7 TeV), which sets tight mechanical tolerances on the material and the movement control.

An appropriate material for the collimator jaws would have to highlight:

- high conductivity to reduce impedance,
- high robustness to resist beam impacts,
- good absorption rate for cleaning efficiency.

Unfortunately, all three conditions cannot be fulfilled by the same material: a robust material (e.g. graphite) is too bad a conductor and would require to run the machine at a lower level of performance, i.e. lower intensity and/or larger beam size. On the other hand, a material fit for the impedance issues (e.g. copper) is not robust enough which means that the collimator jaws can be severely damaged after just a few hours of operation and the cleaning efficieny would drop significantly. This issue is addressed by implementing the LHC collimation system following different installation phases.

3.1.2 Phased approach and choice of material

The *phased approach* relies on the fact that difficulties and performance goals of the LHC are distributed in time. Operating the machine safely requires a collimation system adapted to the beam characteristics.

Phase 1

This phase puts the effort on the robustness and flexibility of the system. The primary and secondary collimators must have a low Z (atomic number) material design for high resistance to beam impacts; the critical case is the one of an irregular beam dump, for which an expected maximum of 8 proton bunches (see Table 1.2 for proton bunch population) can be dumped onto any given primary jaw. To determine the most appropriate material, one has to consider the accident cases described in Table 2.6 and use the estimated deposited beam intensities into finite element models to compute the deposited energy (or temperature increase) and stress values. Results of temperature studies performed with the FLUKA code [50] are shown in Table 3.1 and Figure 3.1.

Temperature studies clearly show that the appropriate material is to be selected between beryllium and graphite. Stress calculations for the irregular beam dump scenario are analyzed for these two materials in [51] and graphite turns out to be about 10 times more robust than beryllium. Impedance remains an issue with graphite though, but solutions can be brought to create a Phase 1 specific design:

[1] A description of the impedance-related instabilities can be found in [49]. One should note that impedance scales with the third power of the inverse of the gap size.

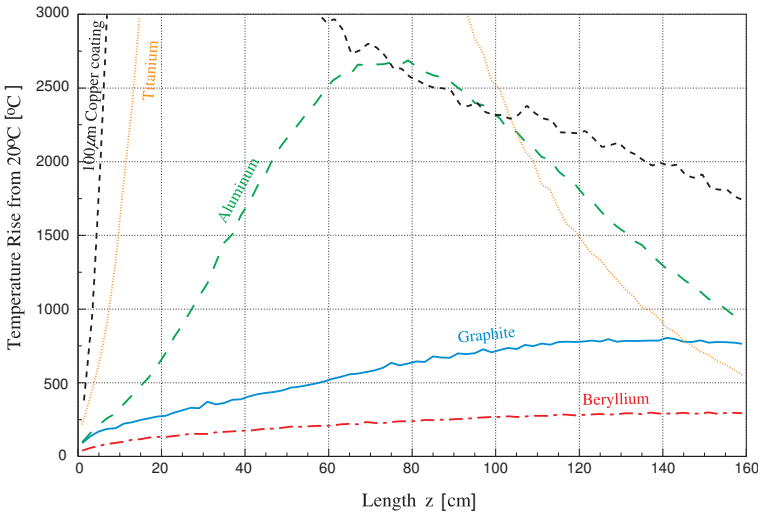

Figure 3.1: Temperature increase of a collimator jaw depending on its length and material type. The considered beam load is the one of an asynchronous beam dump due to the pre-firing of a single module at 7 TeV; the impacting beam spot size is taken as 200 μm. Taken from [1].

Table 3.1: Density, maximum energy deposition, maximum temperature and fraction of energy escaping a 1.4 m long collimator jaw of different materials for a single module dump pre-trigger at 7 TeV. The copper coating is 100 μm thick. Taken from [1].

Material	Density [g.cm^{-3}]	Peak energy load [GeV.cm^{-3}]	T_{max} [$^\circ$K]	Energy escaping [%]
Graphite (C)	1.77	1.3×10^{13}	800	96.4
Beryllium (Be)	1.85	0.9×10^{13}	310	97.0
Aluminium (Al)	2.70	5.3×10^{13}	2700	88.8
Titanium (Ti)	4.54	1.7×10^{14}	> 5000	79.5
Copper coating (Cu)	8.96	7.0×10^{14}	> 5000	34.4

- power deposition:

the impedance induced by graphite has little influence on the beam stability, but because of the image current there is still some heating, which amounts to 240 W/m at injection energy and roughly 4 times larger at collision energy. These values are calculated considering the ultimate LHC beam parameters (intensity, number of bunches, emittances) for primary collimators opened at 6 σ. In the worst case of deposited power distribution along the jaw, severe damage and vacuum problems are expected. A thin layer ($\sim$ 10-20 μm) of copper on the surface of the graphite jaw would reduce the heating to 8 W/m at injection and 32 W/m at collision [52].

- connecting the collimator with the existing vacuum pipes:

with the collimator jaws moving in and out with respect to the beam, one needs to ensure continuous RF contact with the vaccuum chambers on each side of the collimator tank and

avoid impedance issues from large geometric changes. This is achieved by changing the geometry of the jaw to include two tapering angles on each side of the jaw. For the RF issue, copper "fingers" are implemented on each end of the jaw. Each set of RF fingers corresponds to another set installed at the end of the connected vacuum chamber, as seen on Figure 3.3.

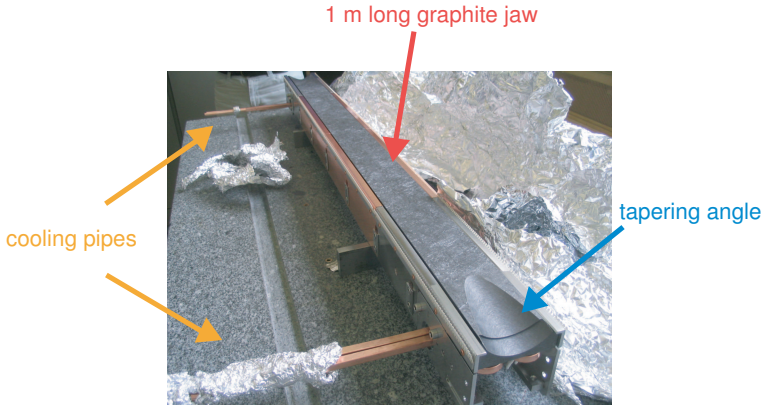

Figure 3.2: Picture of a graphite jaw for a LHC secondary horizontal collimator. The jaw is already clamped on its support which includes the copper cooling pipes. One can notice the tapering angle for geometric continuity with the external vacuum chambers.

In the LHC case, Phase 1 collimators are made of two carbon-based jaws with a 5 μm coating. Primary jaws are 60 cm long while the length of secondary jaws is set to 1 m. Secondary jaws need to be longer because they are the ones which absorb the halo protons. These lengths refer to the effective length of material, i.e. the one "seen" by the beam when passing through the collimator tank. If one includes the tapering angles and the interconnection, the total length of a LHC collimator is 148 cm. A more detailed design description is given in [53, 54].

Phase 2

Phase 2 collimators allow reaching nominal beam intensities and β^* values using low impedance hybrid material for the secondary jaws. These collimators can follow an advanced design and would only be used during stable physics runs, when the probability of a mis-kicked beam impacting on a collimator is small. At the same time, the use of higher Z materials can upgrade the efficiency of the system by a factor 5. The design of the hybrid collimators is not decided yet. The possible options include metallic collimators, beryllium jaws and graphite jaws with a movable metallic foil. For performance estimates, a consumable collimator design with a 1 m long Cu jaw is assumed. The US-LARP collaboration between CERN and laboratories in the USA (SLAC, BNL, Fermilab) is working on the feasability of collimators with rotating jaws [55].

Figure 3.3: RF fingers of a LHC secondary collimator jaw (left and right ones). The set of the external vacuum chamber can also be seen (top and bottom ones). The overall assembly is designed to minimize broad-band impedance and trapped modes due to the movements of the collimator jaw during machine operation [52].

3.2 The LHC cleaning insertions

Two long straight sections, also called *cleaning insertions*, of the LHC main ring are dedicated to collimation. In order to achieve the required low inefficiencies (see section 1.7 and [46]), the layout of the cleaning insertions must comply with several design constraints as well.

3.2.1 Longitudinal layout of the insertions

As stated earlier, the LHC collimation system is designed as a multi-stage system (see section 1.6). Primary collimators intercept the primary beam halo (see Figure 1.3) and generate an on- and off-momentum secondary proton halo. This secondary halo is absorbed by dedicated secondary collimators which leak a tertiary halo. The tertiary halo is then lost in the cold aperture of the machine if not intercepted by absorbers, located close downstream of the secondary jaws. Ideally, the tertiary halo population should be small enough for magnet quenches to be avoided.

At high energies, as in the LHC collision optics case, tertiary collimators may be locally needed for sensitive equipment. In each of the four LHC experimental insertions, two additional tertiary collimators are implemented to protect the triplet magnets (see definition in section 2.2.3). Figure 3.4 gives the schematic of the LHC multi-stage collimation system for both the injection energy case and the top energy case.

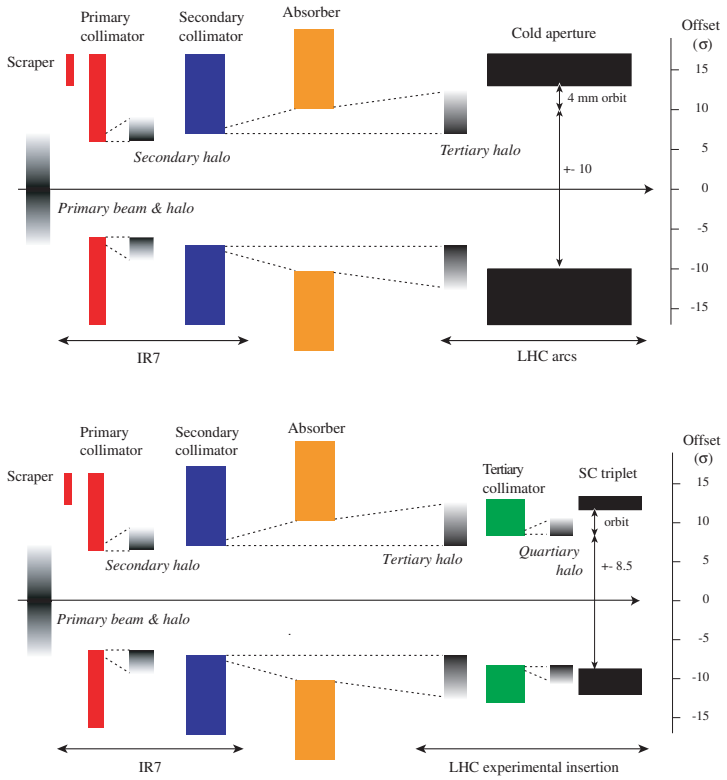

Figure 3.4: Principle of betatron collimation and beam cleaning at injection energies and during the ramp (top) and during 7 TeV collisions (bottom). The primary and secondary collimators in IR7 are set for half intensity and $\beta^* = 1$ m. Courtesy of R. Assmann.

Collimator location

The number of collimators and their relative phase-advance and azimuthal positions were optimized in order to achieve the best coverage in the two transverse phase-spaces $x - x'$ and $y - y'$ [8]. The obtained s location for each collimator is then optimized regarding the β function values, so as to obtain larger gap openings and therefore reduce impedance issues. As much as possible, collimators should be placed in warm regions and closely upstream of warm (i.e. normal conducting) dipole magnets. Warm magnets can tolerate higher local beam losses, like the one induced by particle showers getting out of collimators. In addition, warm dipoles would redirect these showered particles out of the machine aperture close to the collimation region, limiting the propagation of losses into regions further away downstream. Figure 3.5 shows the longitudinal distribution of primary and secondary collimators in the two LHC cleaning insertions. The system also includes two additional phase for efficiency and luminosity upgrades, marked on the two layouts by the placeholders for future collimators.

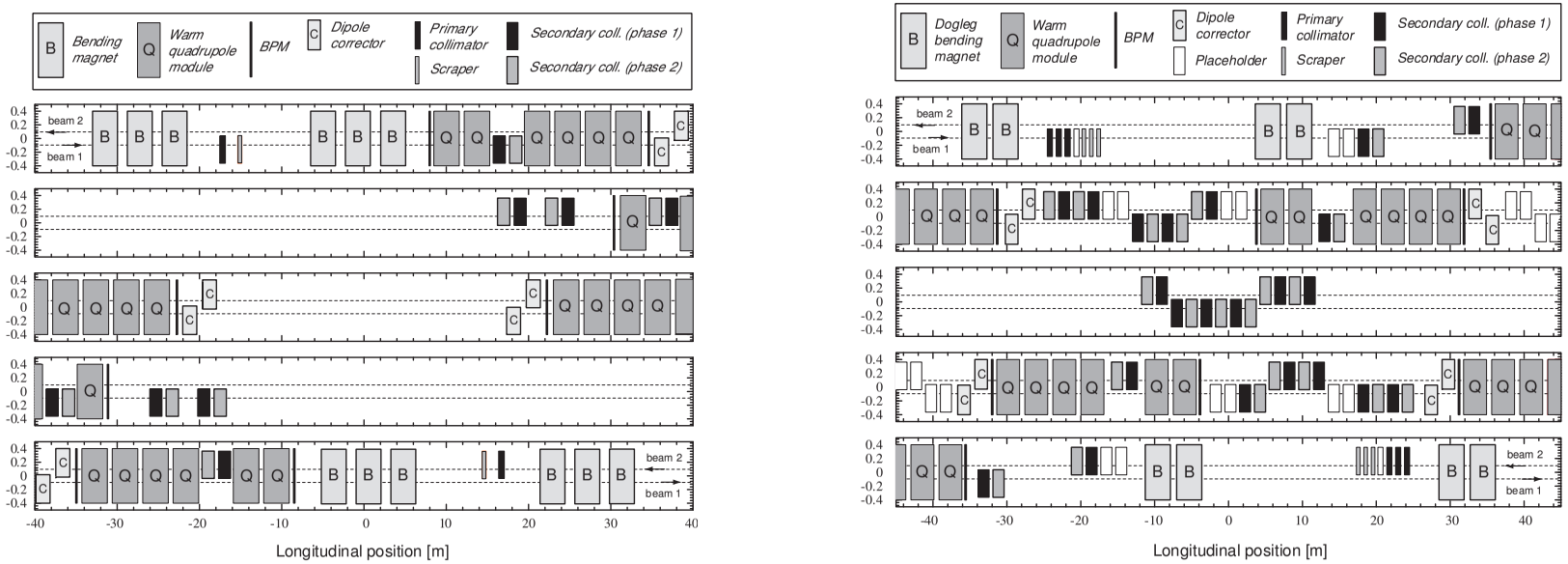

Figure 3.5: Longitudinal layout of the momentum cleaning insertion in IR3 (left) and the betatron cleaning insertion in IR7 (right).

3.2.2 Types of collimators

In addition to the primary and secondary collimators in the two cleaning insertions, additional elements are placed at characteristic locations in the machine. Independently of the collimation phase, the system includes:

- *active and passive absorbers*, placed immediately downstream of the IR3/IR7 cleaning insertions,
- *tertiary collimators* at the experimental insertions to protect the triplet magnets,
- special *injection protection collimators* in IR2/IR8 to protect the main ring from injection kicker magnet faults (see Figure 2.4),
- *beam abort protection collimators* in IR6 to protect the machine from errors of beam dump kicker magnets,
- *collision debris collimators* protecting the machine from particle showerings coming from the IR1/IR5 experimental insertions.

Figure 3.6 gives an overview of the mechanical design of the tank of a secondary collimator. This design is common to primary and secondary collimators and active absorbers.

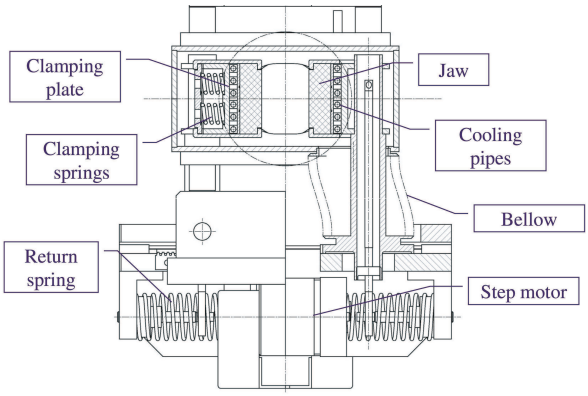

Figure 3.6: Secondary collimator mechanical assembly (cross-section of a horizontal TCSG).

The idea behind this design is the use and optimization of the experience from the LEP collimators (the previous CERN machine stored in the 27 km ring). The tank layout features a quick plug-in system for the cooling system and the vacuum pumps, for the collimator installation and replacement processes to be as fast and simple as possible. The block of material is clamped on each jaw to ensure good thermal conductivity. The main difference between each type of collimator therefore lays in the jaw material and the effective length that the circulating beams will "see". Table 3.2 lists the mechanical configuration of each Phase 1 collimator type, referred to with their respective LHC labels: TCP stands for primary collimator, TCSG for secondary, TCLA for absorbers and TCT for tertiary.

Table 3.2: Functional requirements for the main collimators of the multi-stage cleaning system.

Parameter	**TCP**	**TCSG**	**TCLA/TCT**
Material	C or C-C	C or C-C	W
Effective jaw length [m]	0.6	1.0	1.0
Jaw dimensions [mm^2]	65×25	65×25	65×25
Jaw tapering [cm]	2×10	2×10	2×10
Surface flatness [μm]	25	25	25
Maximum gap [mm]	60	60	60
Minimum gap [mm]	0.5	0.5	0.5
Gap size precision [μm]	50	50	50
Jaw position control [μm]	≤ 10	≤ 10	≤ 10
Jaw-beam angle control [μrad]	≤ 15	≤ 15	≤ 15
Reproducibility [μm]	20	20	20
Position installation precision [μm]	100	100	100
Angular installation precision [μrad]	150	150	150

3.3 Tracking methods and approximations

Simulations of collimation and beam cleaning were previously often performed using simplified models in computing softwares. The increase in available CPU power now allows more realistic simulations. For large machines like LHC it becomes possible to track millions of particles, element by element over hundreds of turns.

The SixTrack code [56] works with the full six-dimensional vector of coordinates and takes into account magnet non-linearities up to very high orders. This code is being used for all LHC tracking simulations and includes well developed linear and non-linear error models. SixTrack was extended for tracking large numbers of halo particles and record their interaction with arbitrarily placed collimators. This extension also features an interface to a program for LHC aperture analysis; the two programs are used to obtain beam loss maps.

3.3.1 Tracking using the thin lens formalism

The softwares mentioned in the following all use the same tracking method relying on a special model of the considered lattice, called the *thin lens formalism*. Extensive tracking for a large number of turns (of the order of 10^5-10^6 for dynamic aperture studies) would require excessive CPU resources with the most detailed accelerator tracking. It is therefore needed to approximate long magnetic elements with drifts and point-like kicks, as it is done for studies of glass lenses in classical optics. The kick of a given element is applied to the initial coordinates (x_0, $p_{x\,0}$, y_0, $p_{y\,0}$) of a particle by using a *transfer matrix* M. One has then to convert the momentum p_z in the corresponding divergence z' for the considered particle. The transfer matrices for the linear accelerator elements are given in [57] as:

- drift space:

$$M^{drift} = \begin{pmatrix} 1 & L_{drift} & 0 & 0 \\ 0 & 1 & 0 & 0 \\ 0 & 0 & 1 & L_{drift} \\ 0 & 0 & 0 & 1 \end{pmatrix} \tag{3.1}$$

- dipole magnet, horizontal bending:

$$M^{dipole} = \begin{pmatrix} 1 & 0 & 0 & 0 \\ \frac{-L_{magnet}}{\rho^2} & 1 & 0 & 0 \\ 0 & 0 & 1 & 0 \\ 0 & 0 & 0 & 1 \end{pmatrix} \tag{3.2}$$

- quadrupole magnet:

$$M^{quadrupole} = \begin{pmatrix} 1 & 0 & 0 & 0 \\ -k \cdot L_{magnet} & 1 & 0 & 0 \\ 0 & 0 & 1 & 0 \\ 0 & 0 & k \cdot L_{magnet} & 1 \end{pmatrix} \tag{3.3}$$

with L being the length of the element, ρ the radius of curvature of the considered dipole magnet, and k the gradient of the considered quadrupole. The most important non-linear elements are sextupoles and octupoles with:

- sextupole magnet:

$$M^{sextupole} = \begin{pmatrix} 1 & 0 & 0 & 0 \\ -\frac{\lambda}{2} \cdot L_{magnet} \cdot x_0 & 1 & \frac{\lambda}{2} \cdot L_{magnet} \cdot y_0 & 0 \\ 0 & 0 & 1 & 0 \\ \frac{\lambda}{2} \cdot L_{magnet} \cdot y_0 & 0 & \frac{\lambda}{2} \cdot L_{magnet} \cdot x_0 & 1 \end{pmatrix} \tag{3.4}$$

- octupole magnet:

$$M^{octupole} = \begin{pmatrix} 1 & 0 & 0 & 0 \\ -\frac{\mu}{6} \cdot L_{magnet} \cdot x_0^2 & 1 & \frac{\mu}{2} \cdot L_{magnet} \cdot y_0^2 & 0 \\ 0 & 0 & 1 & 0 \\ \frac{\mu}{2} \cdot L_{magnet} \cdot x_0^2 & 0 & -\frac{\mu}{6} \cdot L_{magnet} \cdot y_0^2 & 1 \end{pmatrix} \tag{3.5}$$

with λ and μ standing respectively for the gradient of the considered sextupole and octupole magnets; x_0 and y_0 correspond to the initial transverse coordinates of the particle passing through the considered element. In the six-dimensional case, the previous matrices are expanded to a 6x6 size to include energy effects, e.g. synchrotron oscillations.

Figure 3.7: Schematic of the thin-lens formalism: the figure on the left reproduces what an element looks like in the lattice, while on the right is shown its thin lens representation. The considered element is replaced by a drift space of equal length, with a marker at the centre stating the name of the element. In that formalism, distances between two consecutive elements are equivalent to the real inter-distance in the lattice plus the respective half-lengths of the two considered elements.

This formalism allows one to calculate particle coordinates at any location of the machine, provided the transfer matrix M_i of each ith element of the lattice has been properly established. Computing codes like MAD-X [58] deliver all the data needed to calculate these matrices, along with other relevant values like the closed orbit coordinates in each transverse plane and the Twiss parameters for each element. An adequate tracking method using such a software and the data taken from it would for example:

1. define the particle distribution to be tracked,
2. insert in this distribution the offset in each transverse plane due to the closed orbit,
3. calculate the coordinate set (x,x',y,y',Δp,s_{bucket}[2]) after each element using the corresponding transfer matrix.

This method is most commonly known as *element-by-element tracking* and was used for the studies presented in this report. The next section introduces the tools which were used for collimation studies with more details.

[2] The coordinate s_{bucket} refers to the relative position of a given particle within the tracked bucket with respect to the synchronous particle.

3.3.2 Setup of a state-of-the-art tracking tool

The SixTrack program [56] is the standard element-by-element tracking program for the LHC dynamic aperture studies. It takes into account all relevant imperfections, linear and non-linear fields, beam-beam kicks and other errors for the LHC [57]. It performs fully chromatic and coupled tracking, allowing the treatment of time-dependent field errors and the inclusion of the LHC aperture. The very first design studies for the LHC collimation system were done using the K2 scattering procedure [59] and linear transfer matrices (obtained from Twiss functions calculated with MAD). K2 was developed in the 1990s for studies of LHC collimation and was developped into the tracking code COLLTRACK in 2001 [46, 60, 61], providing the following features:

- proton scattering in collimator materials, including single-diffractive scattering,
- various halo and diffusion models,
- tracking of arbitrarily large numbers of particle ($\sim 10^6$) over hundreds of turns,
- use of multiple imperfection models on the beam and collimator properties (e.g. errors in settings, tilts, orbit, beta-beat).

The accuracy of the scattering results was tested by comparison with other commonly used codes [62]. It showed discrepancies in scattering angles of up to a factor three for large angles, which translates into a 30 % uncertainty in cleaning inefficiency predictions. COLLTRACK was also limited in tracking accuracy from chromatic effects. To improve the precision of cleaning studies, it was decided to merge COLLTRACK, SixTrack and a LHC aperture model into a new complete tracking tool.

A problem encountered in the use of SixTrack was its limitation to 64 particles tracked at the same time, while COLLTRACK alone was handling a few millions. At the same time, the tracking method in the COLLTRACK code was not fully covered in energy treatment as e.g. chromatic effects and synchrotron oscillations were missing.

Therefore, implementing the collimation routines of COLLTRACK into the source code of an advanced tracking software like SixTrack allows the user to benefit from the advantages of both tracking models. Reference [13] contains an extensive description of the characteristics of the K2 software. The following will therefore present the reader with the main features of the extended version of SixTrack for collimation studies only.

Collimation database file

Simulations with SixTrack are usually performed using two input files: one which includes the model for the lattice of the machine, and one that contains the tracking parameters (e.g. number of turns, number of particles and their energy). These files can nevertheless be combined into a single file, though one would rather handle them separately for practical reasons. Compared to a normal SixTrack run, collimation studies require the mechanical parameters (angle, length, material) of each collimator and absorber. In order to keep the input files as easy to use as possible, an additional input file was created with

all the specific information needed to simulate the LHC Collimation System. Below is a sample of how this collimator database file looks like:

```
TCP.D6L7.B1              !name in capital letters
tcp.d6l7.b1              !name in minimal letters
6.0                      !nominal opening in number of sigmas
C                        !material type
0.6000000000000000       !length in meters
1.5710000000000000       !angle in radians
0.0000000000000000       !transverse jaws offset in meters
162.1334641330793431     !design horizontal beta-function in metres
76.6595139436011266      !design vertical beta-function in metres
#                        !line jump to the next collimator block
```

The possible types of collimator material include graphite (encoded C), copper (CU), tungsten (W), aluminium (AL), beryllium (BE) and lead (PB). SixTrack will stop if any other material is defined for a collimator in the database file.

Tracking through matter in thin lens

As it was mentioned in the previous section, the LHC lattice used for tracking is modeled using the thin lens approximation. This means that every element is replaced by a transfer matrix located at the center of a drift space of length equal to the element length (see Figure 3.7). The procedure selected to simulate scattering processes along a collimator jaw is illustrated in Figure 3.8. When the code detects an element of the LHC collimation system (collimator or absorber)[3], the distribution of protons has to be tracked back by a half-length of the corresponding element. This is represented by the arrow "1" on Figure 3.8.

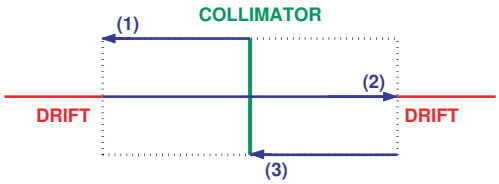

Figure 3.8: Schematic of the method used in SixTrack to simulate the scattering processes taking place in any given collimator. The code needs to track back by a collimator half-length (arrow "1") before eventually applying the interaction processes to the particles distribution (arrow "2"). Finally, one has to track back to the center of the collimator (arrow "3").

After going through the whole length of jaw material (arrow "2"), the code needs to track the protons back to the centre of the collimator (arrow "3") in order for the tracking

[3] The extension of SixTrack for collimation studies can be used to track any collimation system of any lattice. Preliminary studies were performed for the collimation system of the RHIC accelerator at the Brookhaven National Laboratory: results are still being analyzed as the system features L-shaped jaws (i.e. scraping the beam in both transverse planes at once) which required another upgrade of the scattering routines.

to stay consistent along the complete lattice and to prevent errors in the total length of the machine.

Gap opening and change of frame

The main goal when setting up the tracking tool is to track protons within the collimator jaw and to look for impacts on the jaw material in the fastest and most efficient way possible. All collimator jaws are described in a coordinate system in which the collimator extends from $x = 0$ to $x \to +\infty$. For $x < 0$, protons are considered in vacuum.

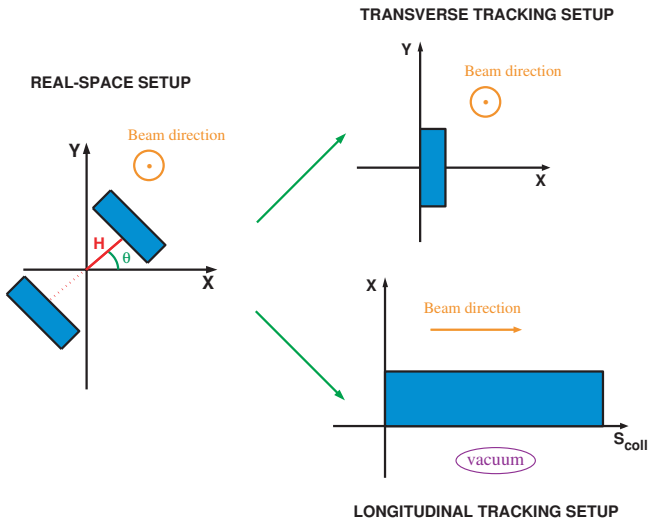

Figure 3.9: Change of frame for tracking along a given collimator jaw. The figure on the left represents the position of the elements taking the closed orbit position as reference. The figure on the right shows the new reference position, the *collimator frame*, as changed within the tracking code.

As seen in Figure 3.9, this change of frame consists in:

- a rotation of an angle θ of the particles distribution around the closed-orbit, so as to align the pair of collimator jaws on the transverse horizontal X-axis,
- an axial symmetry with respect to the newly placed transverse vertical Y-axis,
- a translation on the X-axis of a length H equivalent to the halfgap of the considered collimator taking into account so-called "upper" and "lower" jaw by applying the right sign.

The symmetry is done so that all particles are facing the jaw placed on the positive side of the transverse horizontal X-axis. This process makes it easy to check for impact of particles on the jaw, as in this configuration an impact means a positive value for the transformed x coordinate. Only particles with a positive x coordinate in the collimator frame will be treated via the COLLTRACK scattering routines.

Output files and post-processing

One can find in [63] sample input files to run SixTrack with: the geometry file ″**fort.2**″ containing a model of the LHC lattice, the tracking parameters file ″**fort.3**″ and the collimation database file ″**allelemLTCP**[**type**]**P1.data**″, with [**type**] being either **inj** or **lowb** depending on the type of optics used for the tracking. The output files produced by a SixTrack run include:

- ″**amplitude.dat**″, which gives the average normalized amplitude of particles for all elements of the lattice,
- ″**collgaps.dat**″, which gives the collimator half-gaps as they are calculated by the code,
- ″**efficiency.dat**″, which allows the user to check the cleaning efficiency in each plane of the simulated collimation system,
- ″**coll_summary.dat**″, listing the number of impacting protons, absorbed protons and average impact parameter (see section 1.6) for all collimators listed in the collimation database file,
- ″**tracks2.dat**″, listing trajectories of scattered particles.

Additional files are also created if required. At any location in the machine (magnetic elements as well as drift spaces), one can obtain the corresponding Twiss parameters and particle coordinates. A presentation of these files is done in the following chapter. To obtain the beam loss maps (see also next chapter), the ″**tracks2.dat**″ file is processed by an external program which, together with the new SixTrack version, makes the state-of-the-art LHC tracking program.

A detailed LHC aperture model

The ″**efficiency.dat**″ file mentioned above gives an idea of the global efficiency of the collimation system. To get more accurate information on the level of performance achieved with a given set of collimator settings, one needs to check the *local cleaning inefficiency* values along the LHC ring (see section 1.7). To calculate these values, the trajectories of scattered protons (i.e. of protons which have impacted on one primary collimator at least) are stored in the ″**tracks2.dat**″ file and inserted into a realistic model of the main ring aperture. A dedicated software [18] has been set up together with the extension of SixTrack. This program looks for the elements where particles are lost and then tracks back their positions until it localizes the loss points with a resolution of 10 cm. This is illustrated in Figure 3.10.

With this resolution, one can get a longitudinal distribution of the losses with enough precision to determine whether proton losses in a given element are critical or not regarding magnet quenches. It also allows a detailed analysis with finite element methods for energy deposition studies and the definition of an adequate beam loss monitoring system. Sample pictures and results of such studies are presented in the following chapter.

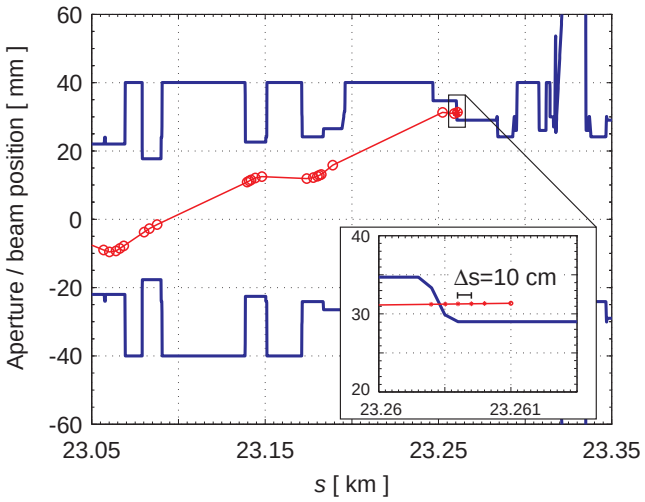

Figure 3.10: Sample trajectory of a halo particle (red line) that hits the LHC aperture (blue line).

3.3.3 Monte Carlo generation of the initial distribution of particles

One matter which has to be addressed during the set-up of the tracking procedures is the type of distribution to be tracked. In particular, two different approaches were considered:

1. a *complete* approach: a full beam distribution is generated (i.e. the phase-space ellipse has to be "filled") and turn-by-turn emittance kicks are applied to this distribution. As diffusion kicks are small in the LHC ($\sim$ 5 nm per turn), computing requirements become excessive and one has to use a typical diffusion speed of 1 μm per turn and large impact parameter,

2. a *simplified* approach: the tracking can be done for a annulus distribution representing the particles which would form the beam halo. Realistic impact parameters can be achieved but no diffusion is applied over the number of turns tracked ($\sim$ 100).

The second approach is conservative as it treats small impact parameters and is efficient regarding computing time.

The size of the annulus distribution is typically given by the half-gaps of the collimators placed in the IR7 betatron cleaning insertion, which will be the closest elements to the beam during operation. The width of the distribution is then addressed by the estimated value of the impact parameter, i.e. the depth of impact of a primary halo proton onto the collimator jaw material (see Figure 3.11). In the LHC case, simulations are typically performed using an offset of 0.003 σ in each transverse plane with respect to the primary aperture. The initial normalized amplitude of the particles are distributed uniformly around 6.003 σ_z (z being either x or y) in the interval [6.0015,6.0045]. This interval converts in term of impact paramater of particles into:

- injection optics (0.45 TeV energy): 1.16 to 5.07 μm,

- collision optics (7 TeV energy): 0.3 to 1.28 μm,

these values being the minimum and maximum ones independently of the transverse plane.

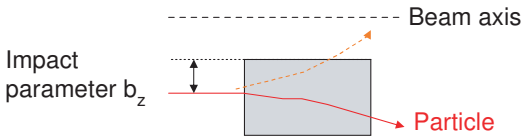

Figure 3.11: Illustration of possible proton trajectories after an impact on a collimator jaw. The transverse offset between the impact location and the edge of the jaw is referred to as the *impact parameter* b_z of the considered particle.

Assuming that N is a possible value for the normalized amplitude of a given particle, the probability $P(N)$ that this particle has an amplitude between N and $N + dN$ writes:

$$P(N) = f(N;\theta) \cdot dN \ . \tag{3.6}$$

The function $f(N;\theta)$ is called the *probability density function* (*pdf*) and may depend on more than one parameter θ. Depending on the case studied, the *pdf* can be complicated and the random variables it describes need to be sampled via dedicated algorithms, called *Monte Carlo Generation techniques* [64].

These techniques rely on a random number generator that can generate uniform and statistically independent values between 0 and 1. The RANLUX program [65] is one of them, and is recognized as one of the best pseudorandom number generators. It even features different performance levels, called *luxury levels*, which consist in a tradeoff between quality of randomness and processing time.

For the LHC collimation studies, as mentioned above, one needs to generate an annulus distribution of particles using the primary collimator opening settings and the estimated impact parameter on the primary jaws. Due to the specific shape of such a distribution, the generation process has to be specific as well. The transverse position z and corresponding divergence z' are related to the transverse emittance and the Twiss parameters at the starting point of the tracking via:

$$\begin{aligned} z &= N_z \cdot \sqrt{\epsilon_z \beta_z} \cdot \sin(\phi) \\ z' &= -\frac{\alpha_z \cdot z}{\beta_z} \pm \sqrt{\frac{\epsilon_z}{\beta_z} - \frac{z^2}{\beta_z^2}} \end{aligned} \tag{3.7}$$

where ϕ is the action angle variable of betatron motion. One can then take:

- u_i as the ith random number between 0 and 1 given by RANLUX,
- N_z as the opening of the primary collimator in the transverse z plane in units of sigma,

- b_z and db_z as the offset and the range of the offset respectively corresponding to the estimated impact parameter of the particles.

Using these variables, the particle distribution is obtained as follows:

1. determine the normalized amplitude A_z of one particle:

$$A_z = (N_z + b_z) + (2 \cdot u_1 - 1) \cdot db_z, \tag{3.8}$$

2. generate the corresponding z coordinate as in equation (3.7):

$$z = A_z \cdot \sqrt{\beta_z \cdot \epsilon_z} \cdot \sin(2\pi \cdot u_2), \tag{3.9}$$

3. calculate the corresponding z' using a third random number u_3:

$$\begin{aligned} z' &= -\frac{\alpha_z \cdot z}{\beta_z} + \sqrt{\frac{\epsilon_z}{\beta_z} - \frac{z^2}{\beta_z^2}} \text{ if } u_3 > 0.5, \\ z' &= -\frac{\alpha_z \cdot z}{\beta_z} - \sqrt{\frac{\epsilon_z}{\beta_z} - \frac{z^2}{\beta_z^2}} \text{ if } u_3 \leq 0.5, \end{aligned} \tag{3.10}$$

4. repeat the same process for the other transverse coordinate using u_4, u_5 and u_6.

On that last point, the routines are flexible: one can decide to generate a different annulus in each transverse plane. Even a distribution with $A_z = 0$ is possible, meaning that the tracking will then focus on the distribution generated in one plane only. A feature was added (as an alternate routine in the main code) to generate a uniform annulus distribution in one plane and a gaussian distribution of 1 σ size in the other plane. Figure 3.12 shows a sample distribution obtained from the routines used in the extended version of SixTrack.

To analyze the efficiency of the simulated collimation system, there are two methods: (1) check the global efficiency of the system, with the file ″**efficiency**.**dat**″ or (2) look for critical level of local losses in superconducting magnets, via postproceesing of ″**tracks2**.**dat**″. Compiling all the loss locations over the machine, one obtains the *beam loss map*. As mentioned in section 1.7, the level of local losses must stay below defined limits called *quench limits*, which are calculated from a simplified definition given in [48].

Statistics and error bars

The main goal of the LHC tracking simulations for collimation studies is to determine how many protons are lost in the cold aperture of the machine out of the total number of protons scattered from the collimator jaws. Since the scattering processes applied to any given proton are totally uncoupled from the motion of the rest of the beam, trajectories of scattered protons are independent one of the others. This is also true for the possible longitudinal s location of the loss. Counting the number of losses in a given element can then be compared to the *measurement of a Poisson noise* and the corresponding error bar

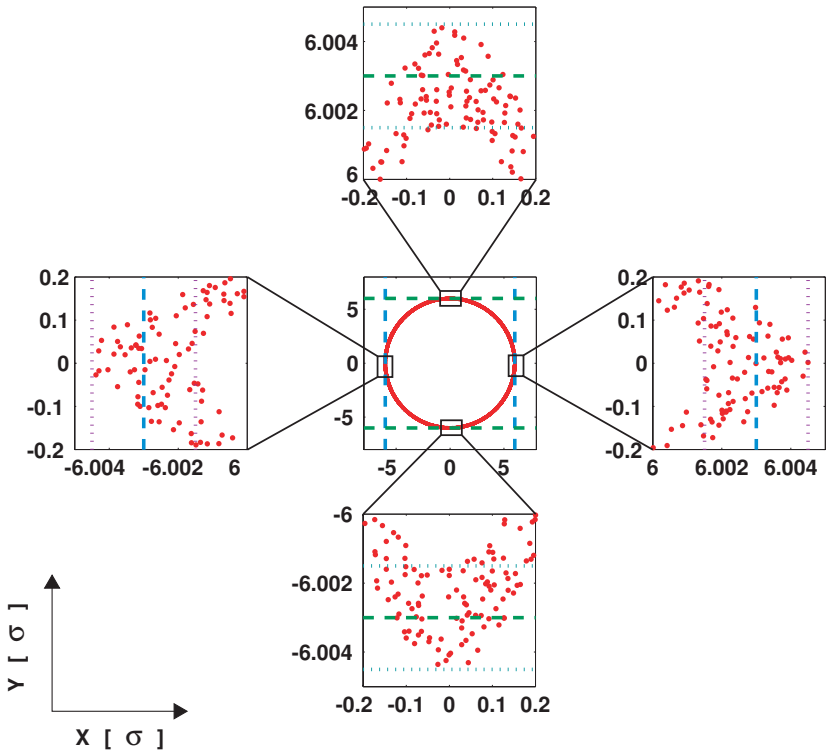

Figure 3.12: Sample particle distribution in normalized real-space $X-Y$ obtained from the extended version of SixTrack for collimation studies. Plots refer to either one of the transverse plane and values are given in units of sigma. The four plots around the central one give a zoomed view of the boxed regions. The dashed line stands for the $N_z + b_z$ term in equation (3.8); the two dotted lines around it represent the offsets $\pm db_z$.

Δ on the level of losses (i.e. number of protons N_p^{lost} lost over the selected 10 cm bin) writes:

$$\Delta = \pm\sqrt{N_p^{lost}} \ . \tag{3.11}$$

In the following chapter, every mention of the error bar Δ on the collimation inefficiency values refers to the quantity described by equation (3.11).

Chapter 4

LHC loss maps for betatron cleaning - optimization of the LHC collimation layout

The simulation tools developped made it possible to have for the first time a prediction of beam losses over the LHC main ring. The following sections present and discuss these results and the ensuing dedicated analysis for imperfections, for energy deposition and background level in experimental regions.

In the Figures below, "cold" ("warm") losses refer to protons lost in the aperture of superconducting (normal conducting) elements of the machine. Most of the results presented in this chapter refer to simulations performed for the beam 1 lattice only, while beam 2 results are only presented in particular cases. Simulations were performed for betatron cleaning in IR7. Momentum collimators in IR3 were included into the simulations.

4.1 Setup of simulations

4.1.1 Tracking parameters

The layout of the two cleaning insertions was introduced in section 3.2. Once the base of the tracking code was set up, the simulation runs were performed with evolving sets of collimators, as collimators were moved and added to improve predicted performance. The corresponding collimator database files (see section 3.3.2) were created, as well as the thin-lens model for the LHC lattice. This model was derived at the time from the version V6.4 of the LHC layout database [66, 67] and later adapted to the latest versions V6.500 and V6.501.

The tracking parameters for the LHC collimation simulations presented here are listed below. Unless stated different, these are the values which were used for the studies:

- number of turns $N_{turns} = 200$,
- number of particles tracked $N_{particles} = 5.12 \cdot 10^6$,

- impact parameter $b_z = 0.003\sigma_z$, impact parameter range $db_z = \pm 0.0015\sigma_z$,
- beam energy at injection $E_{inj} = 450$ GeV, beam energy at collision $E_{lowb} = 7$ TeV.

Table 4.1 lists the nominal half-openings (or *halfgaps*) n_r in units of beam size σ_r for all LHC collimators and collimator-like devices. The corresponding value h in metres is given by:

$$h = n_r \cdot \sqrt{\sigma_x^2 \cdot \cos^2(\theta) + \sigma_y^2 \cdot \sin^2(\theta)} \tag{4.1}$$

where θ is the transverse azimuthal angle of the considered collimator and $\sigma_{x,y}$ is the beam size in each transverse plane. Appendices D and E list the values of θ for each collimator along with the calculated value of h.

Table 4.1: Nominal halfgaps n_r in units of beam size σ_r for the various types of LHC collimators and for both LHC energies. "n/a" means that the concerned type is not used while operating the machine at the corresponding energy. The length and material for each collimator type is also stated; CFC stands for Carbon Fiber Composite. See Appendices D & E for more details.

Type	n_r^{inj} [σ_r]	n_r^{lowb} [σ_r]	**Length** [m]	**Material**
TCP @ IR7	5.7	6.0	0.6	CFC
TCS @ IR7	6.7	7.0	1.0	CFC
TCLA @ IR7	10.0	10.0	1.0	Tungsten
TCP @ IR3	8.0	15.0	0.6	CFC
TCS @ IR3	9.3	18.0	1.0	CFC
TCLA @ IR3	10.0	20.0	1.0	Tungsten
TCT	n/a	8.3	1.0	Tungsten
TCLP	n/a	10.0	1.0	Copper
TCDQ	8.0	8.0	3.0	CFC
TCS @ IR6	7.0	7.5	1.0	CFC
TDI	6.8	n/a	4.0	CFC
TCLI	6.8	n/a	1.0	CFC

Using the flexibility of the tracking code, the horizontal and vertical transverse planes are studied separately. One of the reasons for doing so is that the two planes are mostly decoupled when one does not consider magnet non-linearities: instabilities in one plane then only affect the beam trajectory in that plane. This becomes particularly useful when applying error scenarios, like a horizontal closed-orbit perturbation. In the simulated cases, the beam distribution does not include the bunch length and no energy spread is applied; these features are nevertheless avaiable in the code, and separate studies shown that little influence is expected from tracking with these parameters.

4.1.2 Nominal optics scenarios

The nominal reference cases are defined for specific values of β^*; simulation results are then analyzed with assumed values for the minimum beam lifetimes and the quench levels, listed in Table 4.2. For these parameters, one can generate the design closed-orbit for each case using a dedicated software like MAD-X [58]. Figures 4.1 and 4.2 give the

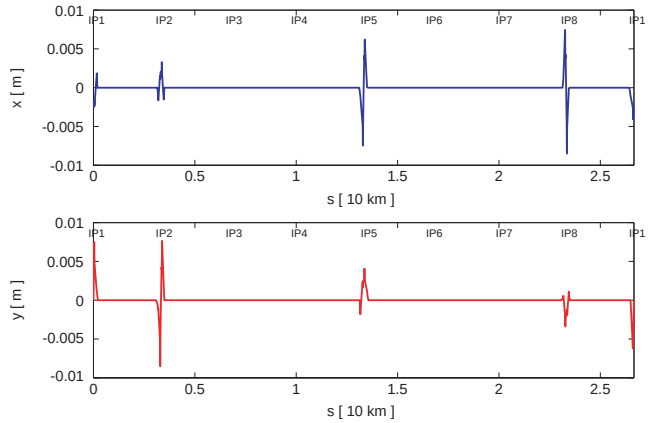

Figure 4.1: Beam 1 transverse design orbit at injection energy (450 GeV): horizontal (top) and vertical (bottom) orbits are shown, along with the locations of the IPs. Bumps show that crossing schemes and separations are switched on in all experimental insertions IR1 (ATLAS), IR2 (ALICE), IR5 (CMS) and IR8 (LHC_b).

transverse closed-orbit in each plane for the two modes of operation (450 GeV and 7 TeV). At 7 TeV, the crossing angles in the high luminosity experiments are in the vertical plane at IP1 (ATLAS) and in the horizontal plane at IP5 (CMS).

At injection energy, the optics is set up so that no beam collisions occur. In the top energy case, the collimation studies focus on the most demanding case in terms of available beam aperture, which corresponds to collisions taking place in the two high luminosity insertions IR1 and IR5 (see section 4.2.3). The crossing schemes in IR2 and IR8 are still applied, but seperator magnets are also switched on so as to avoid collisions at the interaction points. Further studies are planned to investigate scenarios in which collision schemes in IR2 and IR8 are taken into account.

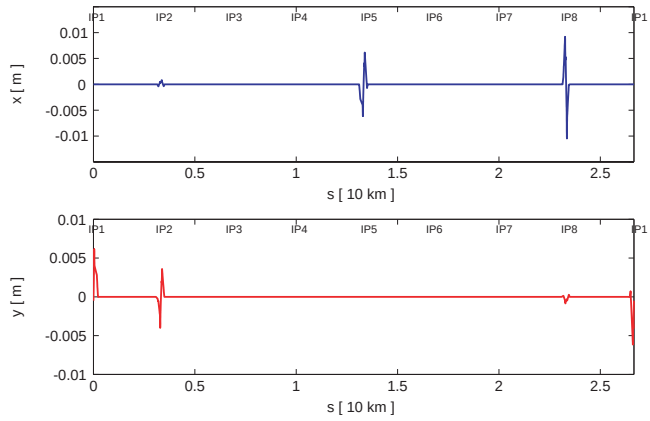

Figure 4.2: Beam 1 transverse design orbit at collision energy (7 TeV): horizontal (top) and vertical (bottom) orbits are shown, along with the locations of the IPs. Bumps show that crossing schemes are on in all IPs but separations are only switched on for IP2 (ALICE) and IP8 (LHC_b).

Table 4.2: Optics parameters of the simulated nominal cases.

Case	**E [TeV]**	**IR 1 & 5**	**IR 2 & 8**	τ **[h]**	$\tilde{\eta}_{quench}$ **[m^{-1}]**
Injection	0.45	$\beta^* = 17$ m	$\beta^* = 10$ m	0.1	10^{-3}
Collision	7	$\beta^* = 0.55$ m	$\beta^* = 10$ m	0.2	2×10^{-5}

4.2 Performance of the IR7 two-stage system

The early LHC collimation layout included only primary and secondary collimators in IR3 and IR7. Simulations started for this inital set of collimators and are presented here as reference. In section 4.3 the beneficial effects of tertiary collimators (labeled TCT) and absorbers (TCLA) are presented.

4.2.1 Injection energy (450 GeV) - Horizontal halo

Figure 4.3 shows the longitudinal loss map for a simulated horizontal halo (generated as described in section 3.3.3) at injection energy. The blue peaks mark the location of proton losses in superconducting elements (*cold losses*), while the red peaks indicate losses in normal conducting magnets (*warm losses*). The green peaks represent the amount of inelastic interactions in each collimator of the cleaning insertion. From this plot it can be seen that the region downstream of IP7 (Beam 1), mainly all of the arc 7-8 plus IR8, shows numerous locations with a high level of losses. The transition region between the IR7 insertion and the arc downstream is called *dispersion suppressor*: it consists in a lattice cell with one dipole magnet missing. Dispersion suppressors are used to reduce the dispersion function inside the insertion regions (IR's).

The most critical peaks (i.e. the ones getting closer to the quench limit) correspond to Q6 (i.e. the quadrupole assembly of cell number 6) in IR7 and IR8. If one sums up all the losses over each element, the five most critical locations are the ones listed in Table 4.3.

Table 4.3: Critical loss locations for a horizontal beam halo at injection energy using only primary and secondary collimators in IR7. The number of lost protons is obtained from the data shown in Figure 4.3 and integrated over the length of each element. Δ refers to the error bar on the inefficiency, as defined in equation (3.11).

Total number of absorbed particles			4820671	
Name	Length [m]	**N**$_{loss}$	η_{total} [1] [**10**$^{-5}$]	**Δ**
MQTLH.A6R7.B1	1.3	433	8.98	0.43
MQ.7R7.B1	3.1	325	6.74	0.37
MB.C15R7.B1	14.3	246	5.10	0.32
MB.B8R7.B1	14.3	189	3.92	0.28
MB.C12R7.B1	14.3	169	3.51	0.27

[1] The inefficiency for each element η_{total} is given by the ratio of the number of particles lost in this element by the number of particles absorbed by the collimation system.

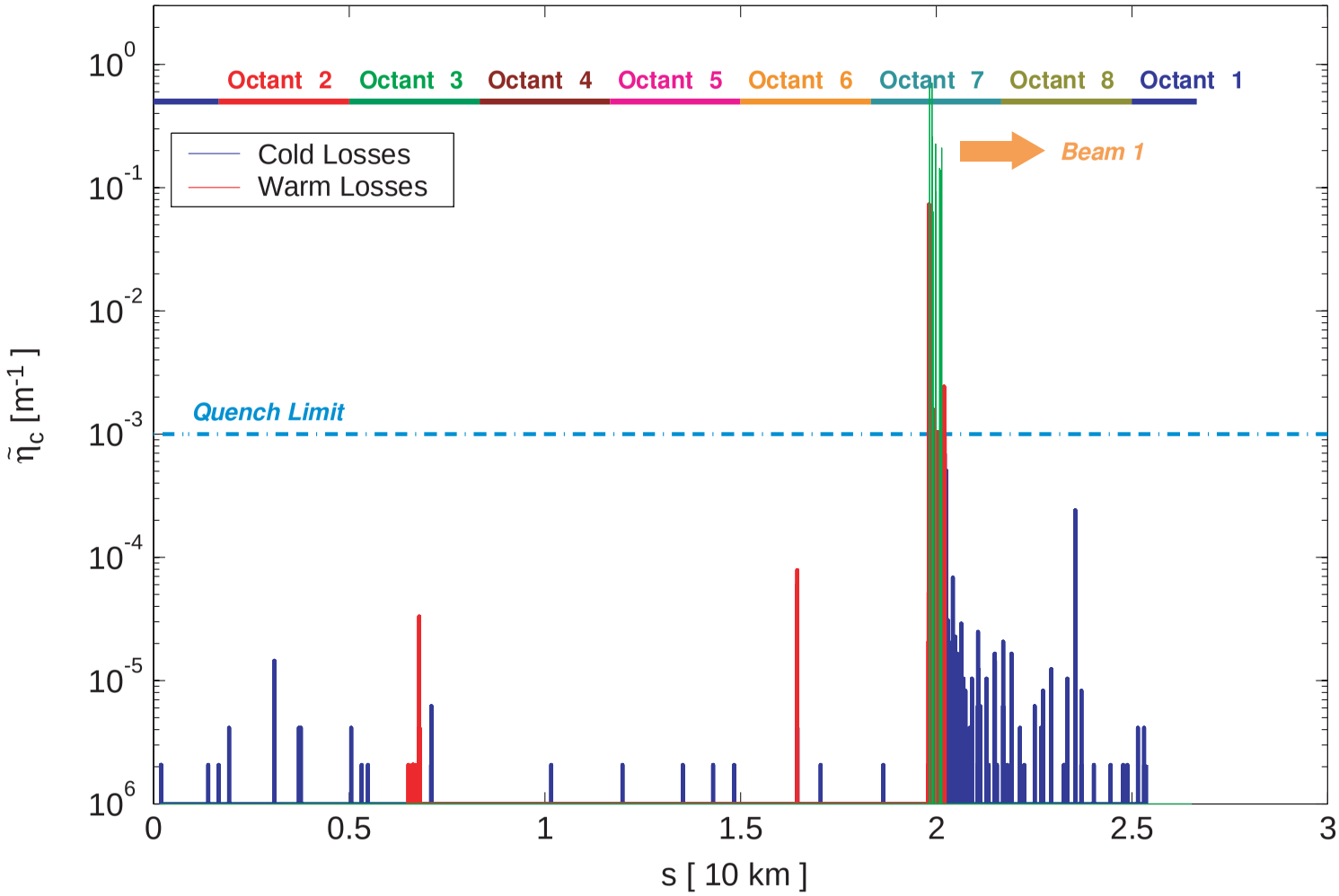

Figure 4.3: Beam loss map at injection energy for the IR7 primary and secondary collimators. The simulated halo is horizontal. Results are shown for Beam 1 only.

The critical elements are all located in the first few cells of the lattice downstream of the cleaning region. In particular, MQTLH.A6R7.B1 [2] is the first aperture restriction after the last secondary collimator, TCSG.6R7.B1. From Figure 4.4, another relevant location can be pointed out: it gets the closest to the quench limit outside of IR7 at injection.

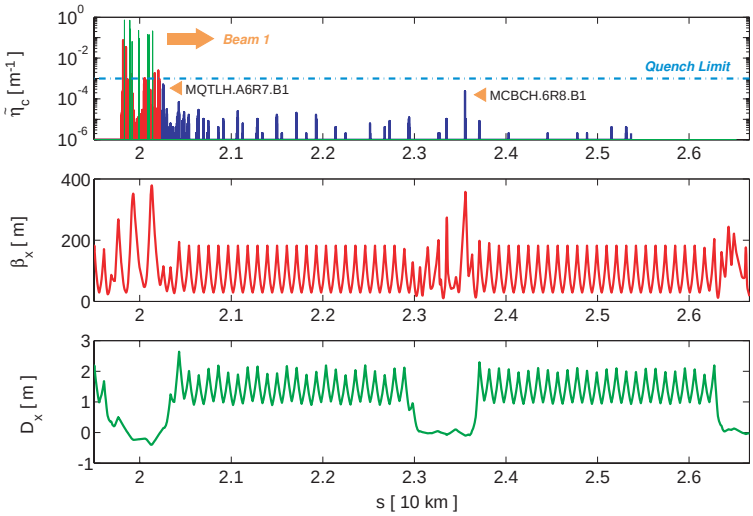

Figure 4.4: Zoom of Figure 4.3 between the IR7 region and IP1 (top). The two most critical peaks of the machine correspond to the location of the Q6 assemblies in IR7 and IR8. Comparison is made with the betatron function β_x (center) and the dispersion function D_x (bottom).

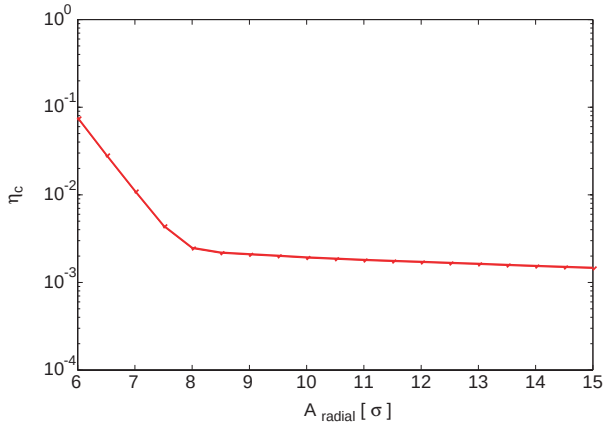

Figure 4.5: Global inefficiency of the two-stage cleaning in IR7 in the injection energy case. The simulated halo is horizontal.

[2] Names of elements are written according to the standard LHC database naming convention [1]: in that case, the considered element is a tuning quadrupole magnet (MQTLH) located in cell number 6 (A6) at the right of IP7 (R7) following the Beam 1 line (B1). This format is applied for all names in the following, unless mentioned otherwise.

The corresponding element, MCBCH.6R8.B1, is particularly important as it indicates the *worst location* in terms of betatronic phase advance and dispersion function. The machine can still be operated safely since no loss spike crosses the assumed quench limit of 10^{-3} m^{-1}. One has to note though that the optics used for this simulation is "perfect", meaning ideal values for all magnetic fields, no perturbation of the design closed-orbit and ideal collimation set-up. The cleaning efficiency will be worse in realistic machine cases with imperfections. Also, the quench level shown on the previous Figures is an estimation and its value will vary locally from one superconducting element to the other. The *global inefficiency* η_c of the collimation system (as introduced in section 1.7) is shown for a horizontal halo in the injection case in Figure 4.5.

4.2.2 Injection energy (450 GeV) - Vertical halo

Figure 4.6 gives the loss map for a simulated vertical halo using the same optics as in the previous case. When comparing these results to the ones in the horizontal halo case, some differences can be spotted in the region downstream of IP7. In the dispersion suppressor region, one can see fewer losses: this is mainly due to the type of halo tracked, since the dispersion function is essentially horizontal and for Figure 4.6 the halo is vertical. For the same reason, the level of losses in the arc downstream is reduced as well. This gets even more pronounced when checking for the height of the peak at the MCBCH.6R8.B1 element: local losses there are about a factor 5 lower than in the horizontal halo case.

Table 4.4: Critical loss locations for a vertical beam halo at injection energy using only primary and secondary collimators in IR7. The number of lost protons is obtained from the data shown in Figure 4.6 and integrated over the length of each element. Δ refers to the error bar on the inefficiency, as defined in equation (3.11).

Total number of absorbed particles			5078474	
Name	Length [m]	$\mathbf{N}_{loss}$	η_{total} [$\mathbf{10^{-5}}$]	$\mathbf{\Delta}$
MB.B8R7.B1	14.3	241	4.75	0.31
MQTLH.A6R7.B1	1.3	213	4.19	0.29
MB.C12R7.B1	14.3	170	3.35	0.26
MB.C15R7.B1	14.3	137	2.70	0.23
MQ.7R7.B1	3.1	124	2.44	0.22

Compared to the values from horizontal halo tracking, the amount of integrated losses in the most critical elements is down by a factor of 2. The level of losses in the dispersion suppressor and the few cells downstream tends to be independent of the type of halo. Figure 4.7 shows that even for a vertical halo tracked (i.e. no initial distribution in the horizontal plane), one finds again the Q6 assembly in IR8 as a critical loss location. This can be explained from the scattering processes suffered by protons impacting on collimator jaws, which include single-diffractive interactions that alter their momentum (inducing losses in regions with high dispersion values) as well as scattering kicks in the horizontal plane. In Figure 4.7, the losses in high β_x-function locations come from these horizontal kicks.

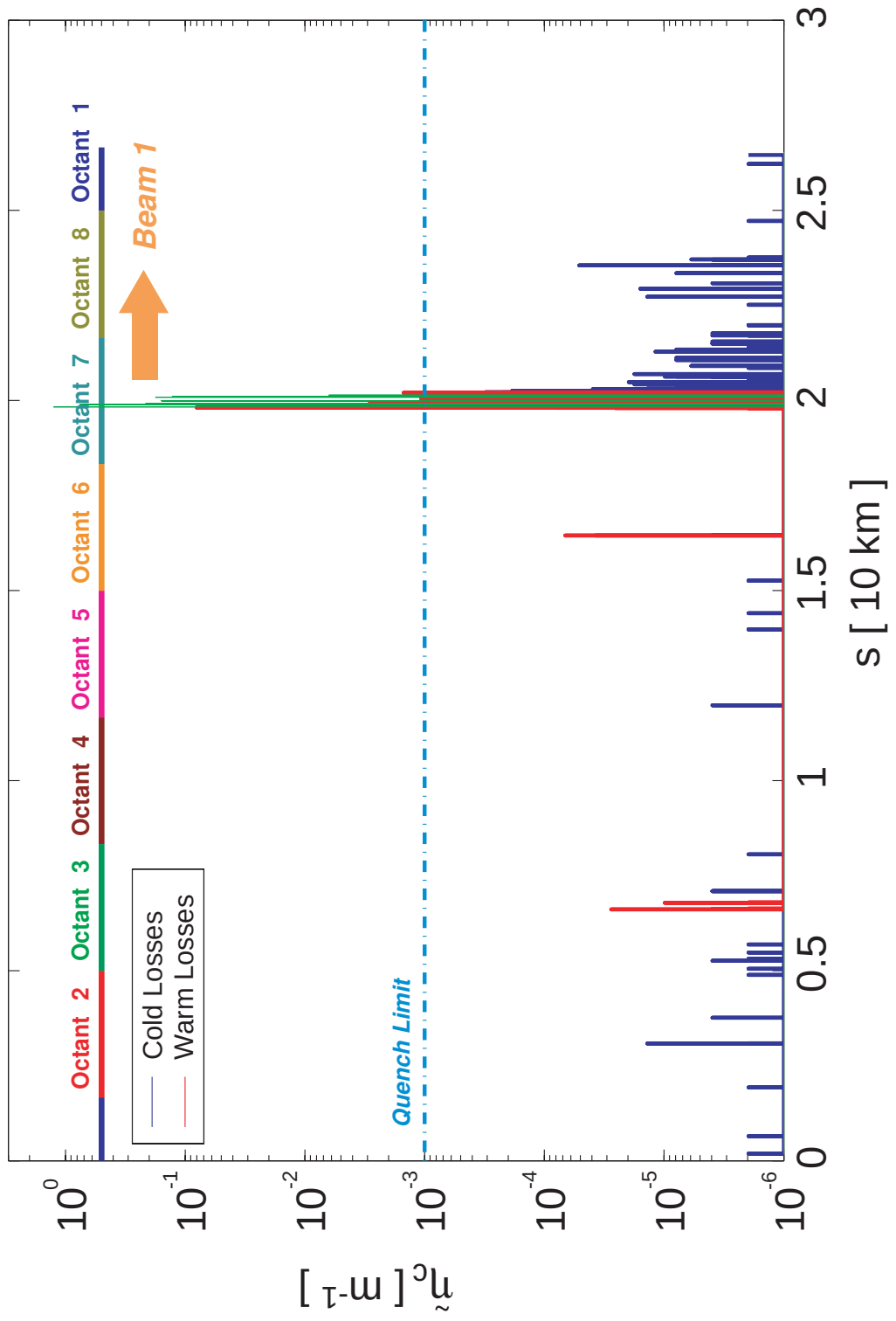

Figure 4.6: Beam loss map at injection energy for the IR7 primary and secondary collimators. The simulated halo is vertical. Results are shown for Beam 1 only.

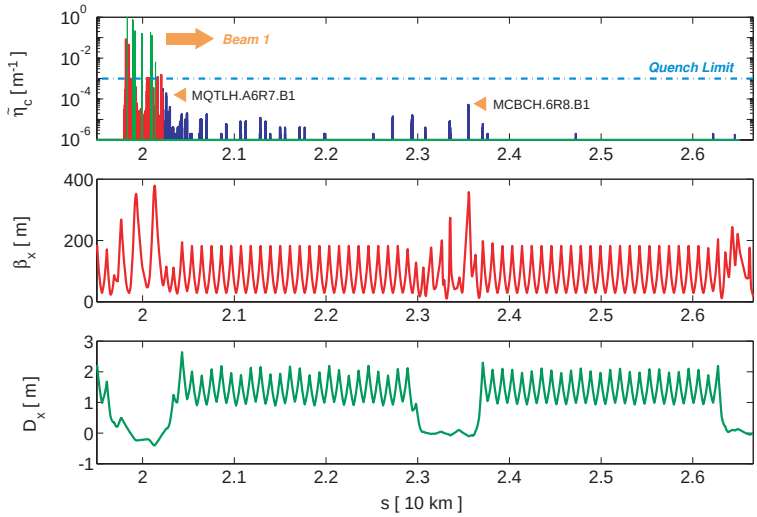

Figure 4.7: Zoom of Figure 4.6 between the IR7 region and IP1 (top). The same two critical peaks for the Q6 assemblies in IR7 and IR8 seen in Figure 4.4 can be spotted. Comparison is made with the betatron function β_x (center) and the dispersion function D_x (bottom).

To understand this reduction of the level of cold losses, one can refer to the shape of the global inefficiency curve shown in Figure 4.8. The cleaning in the vertical plane is more efficient than in the horizontal plane (see Figure 4.5 for comparison).

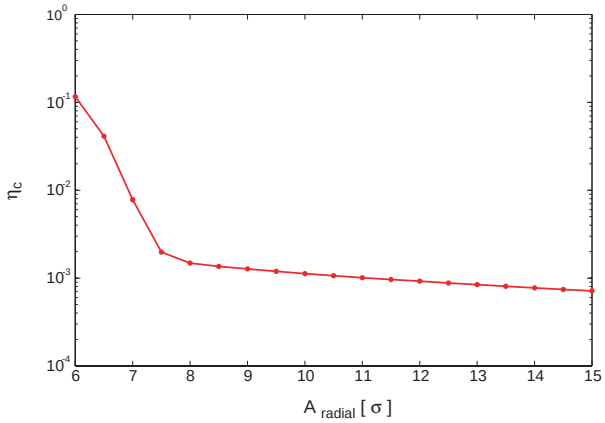

Figure 4.8: Global inefficiency of the two-stage cleaning in IR7 in the injection energy case. The simulated halo is vertical.

4.2.3 Collision energy (7 TeV) - Horizontal halo

Still using primary and secondary collimators in IR7 only, simulations of a horizontal halo for the 7 TeV energy case show that cold loss locations go over the estimated quench limit in three different regions. In Figure 4.9 it can be seen that two of these critical regions

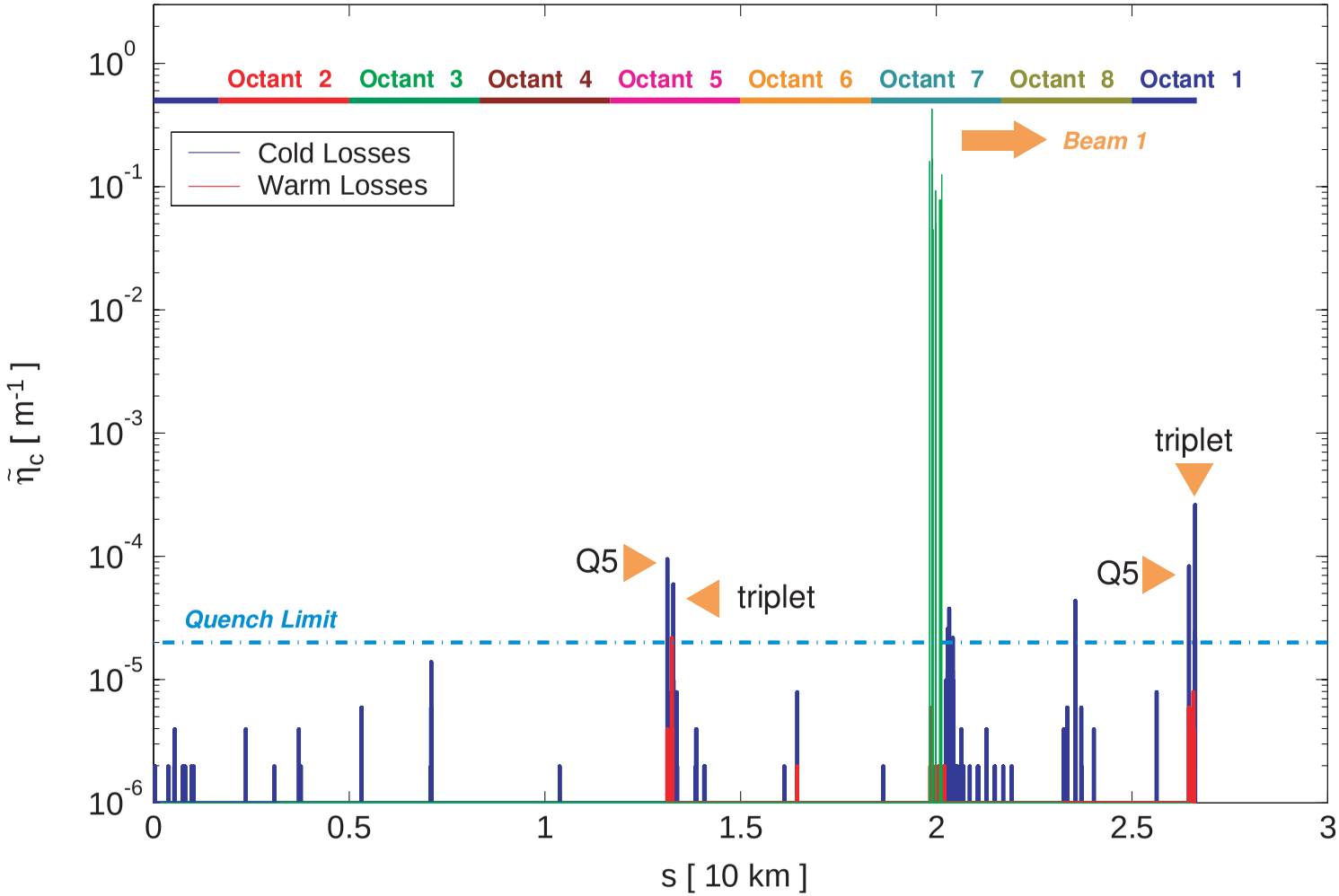

Figure 4.9: Beam loss map at collision energy for the IR7 primary and secondary collimators. The simulated halo is horizontal. Results are shown for Beam 1 only.

correspond to regions already spotted in the injection energy case (the arc 7-8 and the MCBCH.6R8.B1 magnet). Losses in IR1 and IR5 can be explained by the optics configuration used for the collision case (presented in Table 4.2): the value of β^* in each IR is reduced to 0.55 m, a factor ~ 30 lower than in the injection energy case. This is achieved by increasing the β values around the IPs up to about 4500 metres in dedicated magnet assemblies called *triplet magnets* [68], as shown in Figure 4.10. The available aperture gets smaller as the unit beam size gets larger: an aperture bottleneck appears and beam losses are unavoidable.

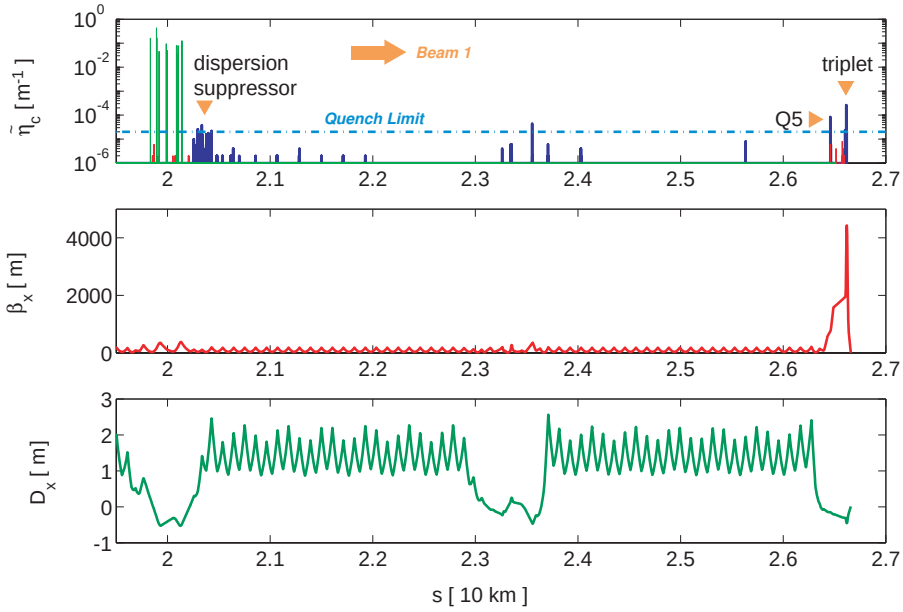

Figure 4.10: Zoom of Figure 4.9 between the IR7 region and IP1 (top). The loss peaks on the far end of the plot correspond to losses in the IR1 triplet magnet assembly. Comparison is made with the horizontal betatron function β_x (center) and the dispersion function D_x (bottom).

Table 4.5: Critical loss locations for a horizontal beam halo at collision energy using only primary and secondary collimators in IR7. The number of lost protons is obtained from the data shown in Figure 4.9 and integrated over the length of each element. Δ refers to the error bar on the inefficiency, as defined in equation (3.11).

Total number of absorbed particles			5052407	
Name	Length [m]	$\mathbf{N}_{loss}$	η_{total} [$\mathbf{10^{-5}}$]	$\boldsymbol{\Delta}$
MB.A9R7.B1	14.3	424	8.39	0.41
MB.B9R7.B1	14.3	334	6.61	0.36
MB.A11R7.B1	14.3	316	6.25	0.35
MQXB.B2L1	5.5	301	5.96	0.34
MB.B11R7.B1	14.3	284	5.62	0.33

The Q5 quadrupole magnet is also a critical element: placed a few metres upstream of the triplet, Q5 is the first high β location and presents the first horizontal aperture restriction as seen in Figure 4.10.

When it comes to the amount of integrated losses, Table 4.5 shows that the most critical elements are the ones located at the end of the IR7 dispersion suppressor. Most of the particles get lost at the first high dispersion point. For the horizontal halo case, the global inefficiency is shown in Figure 4.11.

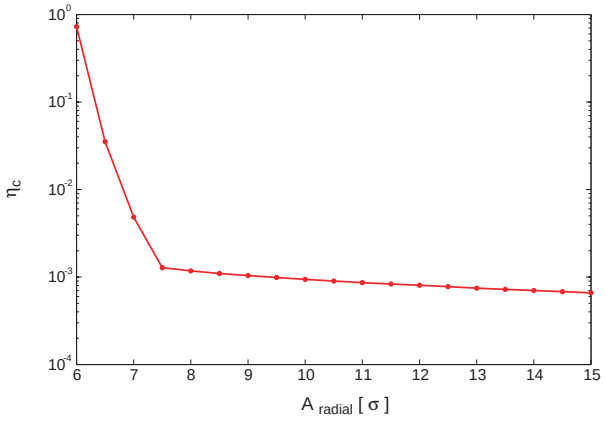

Figure 4.11: Global inefficiency of the two-stage cleaning in IR7 in the collision energy case. The simulated halo is horizontal.

4.2.4 Collision energy (7 TeV) - Vertical halo

As in the previous case, Figure 4.12 shows beam losses for a simulated vertical halo at collision energy that are over the quench limit in various locations. Losses in the dispersion suppressor at the end of IR7 and at the triplet in IR5 occur for the same reasons as in the horizontal halo case: as explained in section 4.2.2, a vertical halo can also create losses at horizontal aperture limitations.

Table 4.6: Critical loss locations for a vertical beam halo at collision energy using only primary and secondary collimators in IR7. The number of lost protons is obtained from the data shown in Figure 4.12 and integrated over the length of each element. Δ refers to the error bar on the inefficiency, as defined in equation (3.11).

Total number of absorbed particles			4998905	
Name	Length [m]	$\mathbf{N}_{loss}$	η_{total} [$\mathbf{10^{-5}}$]	$\boldsymbol{\Delta}$
MB.B9R7.B1	14.3	413	8.26	0.41
MB.A9R7.B1	14.3	410	8.20	0.40
MB.A11R7.B1	14.3	389	7.78	0.39
MB.B11R7.B1	14.3	328	6.56	0.36
MB.C13R1.B1	14.3	130	2.60	0.23

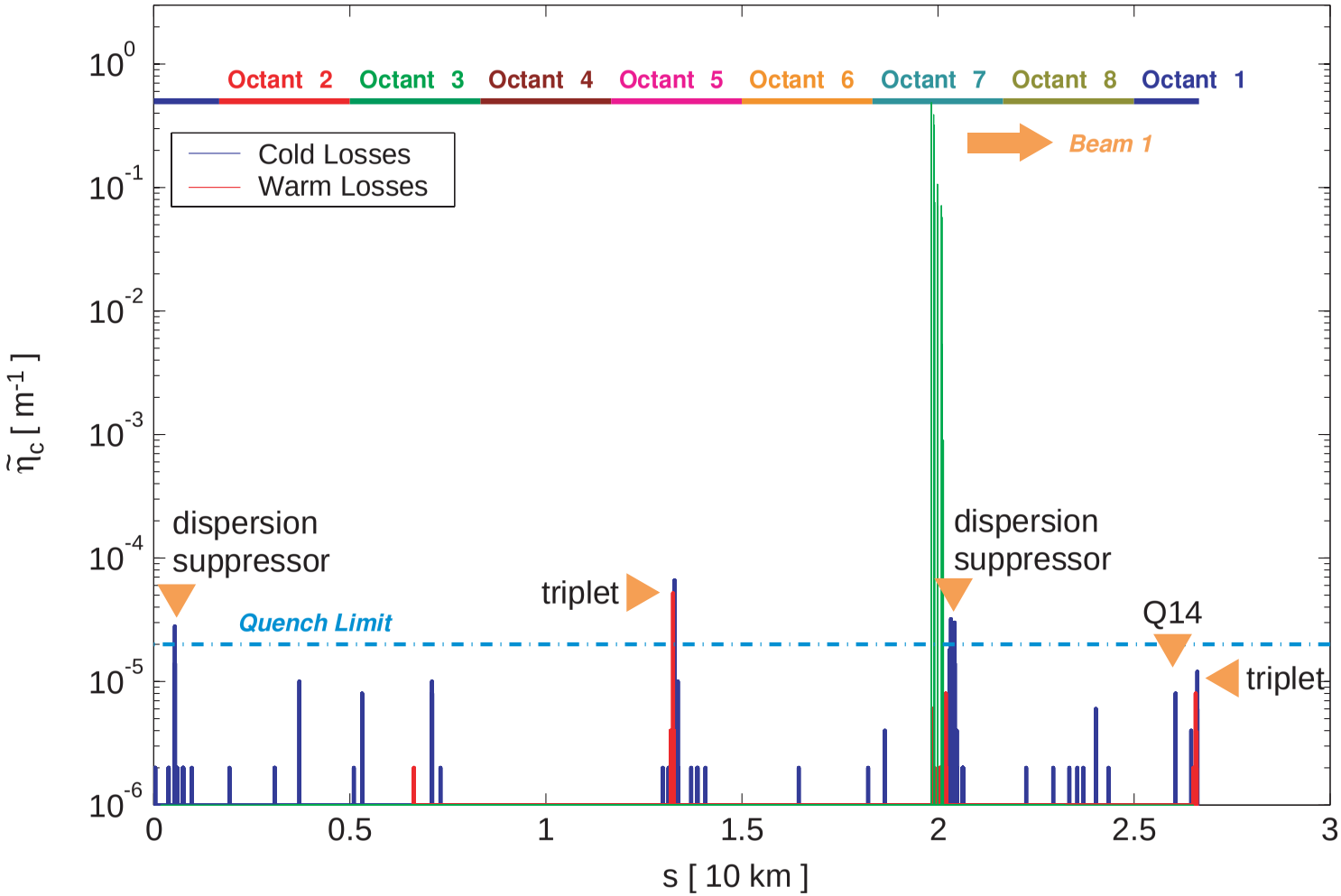

Figure 4.12: Beam loss map at collision energy for the IR7 primary and secondary collimators. The simulated halo is vertical. Results are shown for Beam 1 only.

One can also see that losses occur at the triplet of IR1 but none of them cross the quench limit; this limit is actually crossed at the end of the dispersion suppressor at the right of IP1 (first high peaks around s $\approx$ 540 m on Figure 4.12). Even the beginning of the dispersion suppressor at the left of IP1 presents a relatively high level of losses (Q14 assembley, mentioned on Figure 4.12). A possible reason for such a behavior is that the halo simulated here is vertical, and some off-momentum particles which were not absorbed in the dispersion suppressor of IR7 get lost in the first squeezed insertion the beam goes through. The statistics on the cumulated number of protons lost in any given element, listed in Table 4.6, show that the end of the dispersion suppressor at the right of IP7 appears clearly as the most critical region.

The situation downstream of IP7 in terms of Twiss parameters is identical to what is shown on Figure 4.10. Figure 4.13 presents the situation in the rest of the machine : the highest losses in IR1 are located at the right of IP1, in the corresponding dispersion suppressor. The peaks in the IR5 insertion are essentially due to the high values of the $\beta_{x,y}$ functions as it can be seen in Figure 4.14.

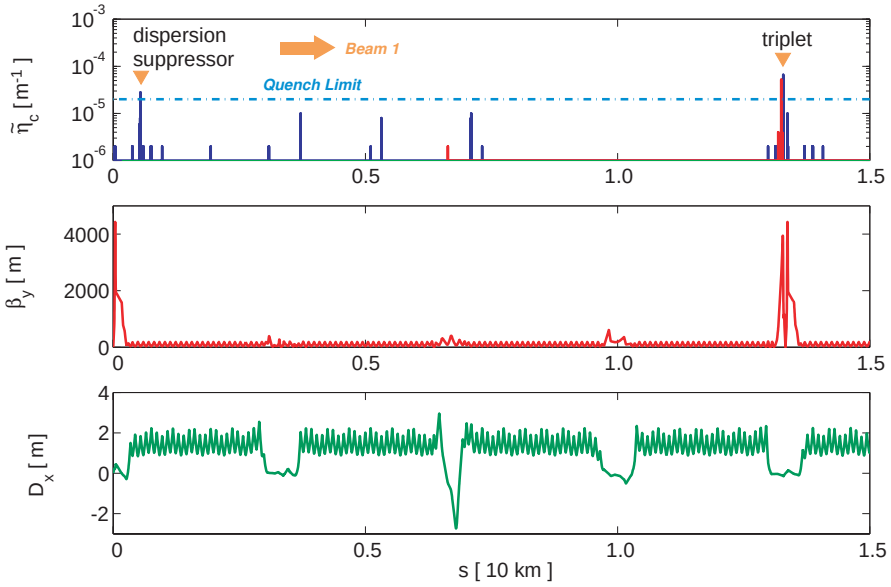

Figure 4.13: Zoom of Figure 4.12 between IP1 and the IR5 region (top). Comparison is made with the vertical betatron function β_y (center) and the dispersion function D_x (bottom). The critical peaks in IR1 are due to the high values of the dispersion function, while it is a large β_y which induces the losses observed in IR5.

As observed in the injection energy case, the global cleaning inefficiency of the reduced system is better for a simulated vertical halo than for a horizontal one, which is illusrated in Figure 4.15. It also has to be noted that the dispersion suppressor downstream of the IR7 cleaning region tends to experience the same amount of losses independently of the type of halo tracked: off-momentum halo is generated at the primary collimators due to single-diffractive scatterings between an incoming proton and the collimator material. The off-momentum protons are then lost at the first high dispersion location.

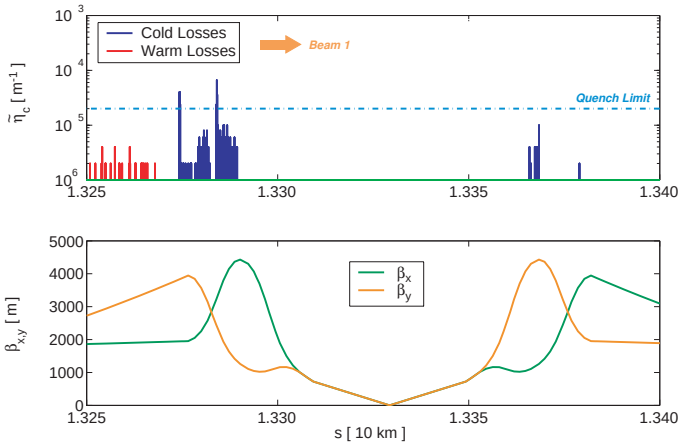

Figure 4.14: Zoom of Figure 4.12 in the IR5 region (top). Comparison is made with the betatron functions β_x and β_y.

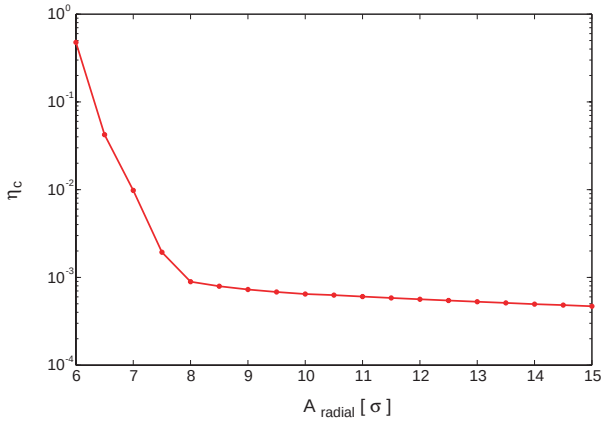

Figure 4.15: Global inefficiency of the two-stage cleaning in IR7 in the collision energy case. The simulated halo is vertical.

4.3 Complete runs: simulations with the improved multi-stage system

The performance of the initial collimation system was illustrated by detailed loss maps and by graphs of the global inefficiency. As limitations appeared, additional collimators of various types were added to the LHC layout. This section reviews the results of simulations performed using the complete list of collimators from Table 4.1. The beam distributions are generated as for the preliminary runs, i.e. decoupling the horizontal plane from the vertical plane. The optics are the ones described in section 4.1.2.

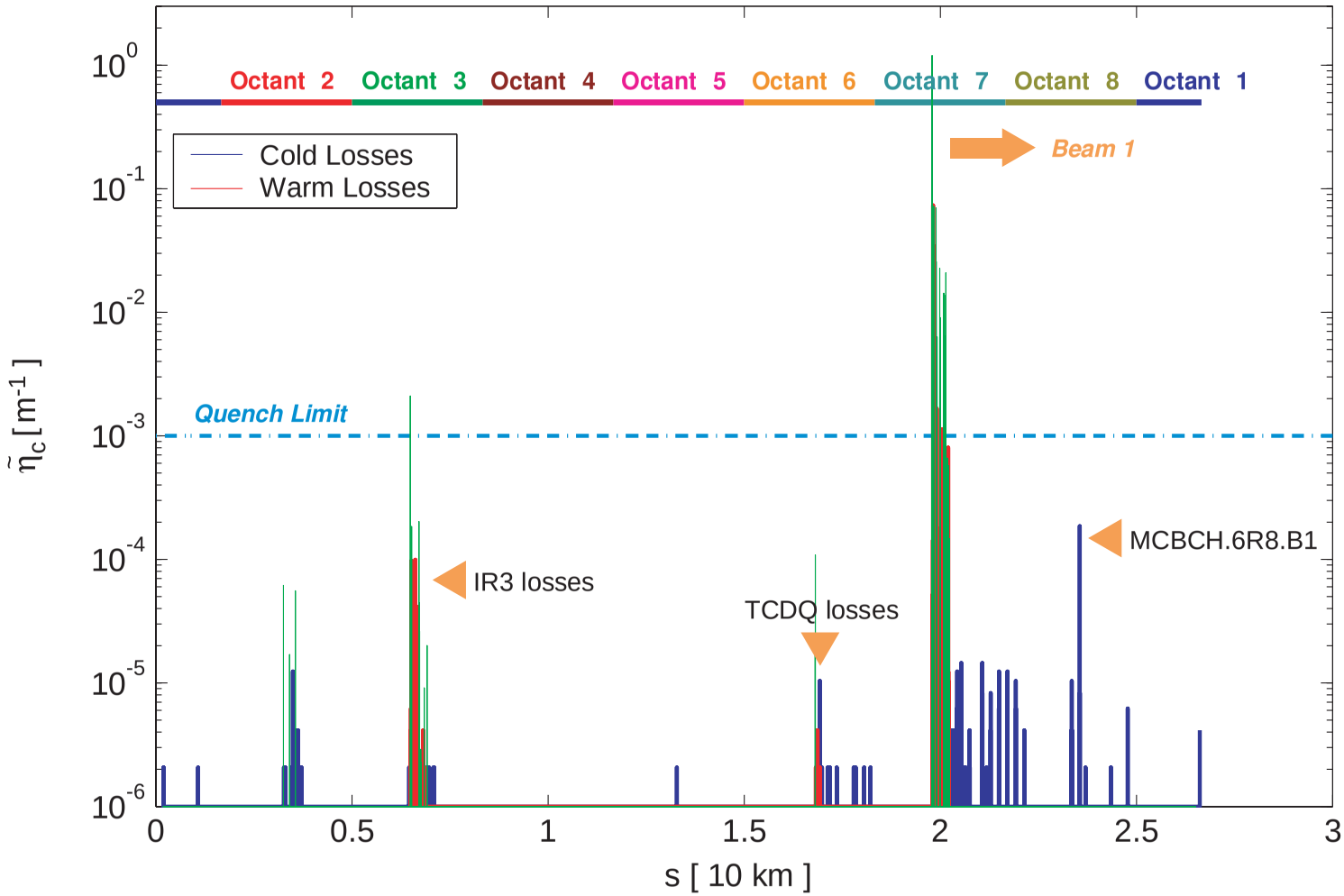

Figure 4.16: Beam loss map at injection energy for the full LHC Phase 1 collimation system. The simulated halo is horizontal. Results are shown for Beam 1 only.

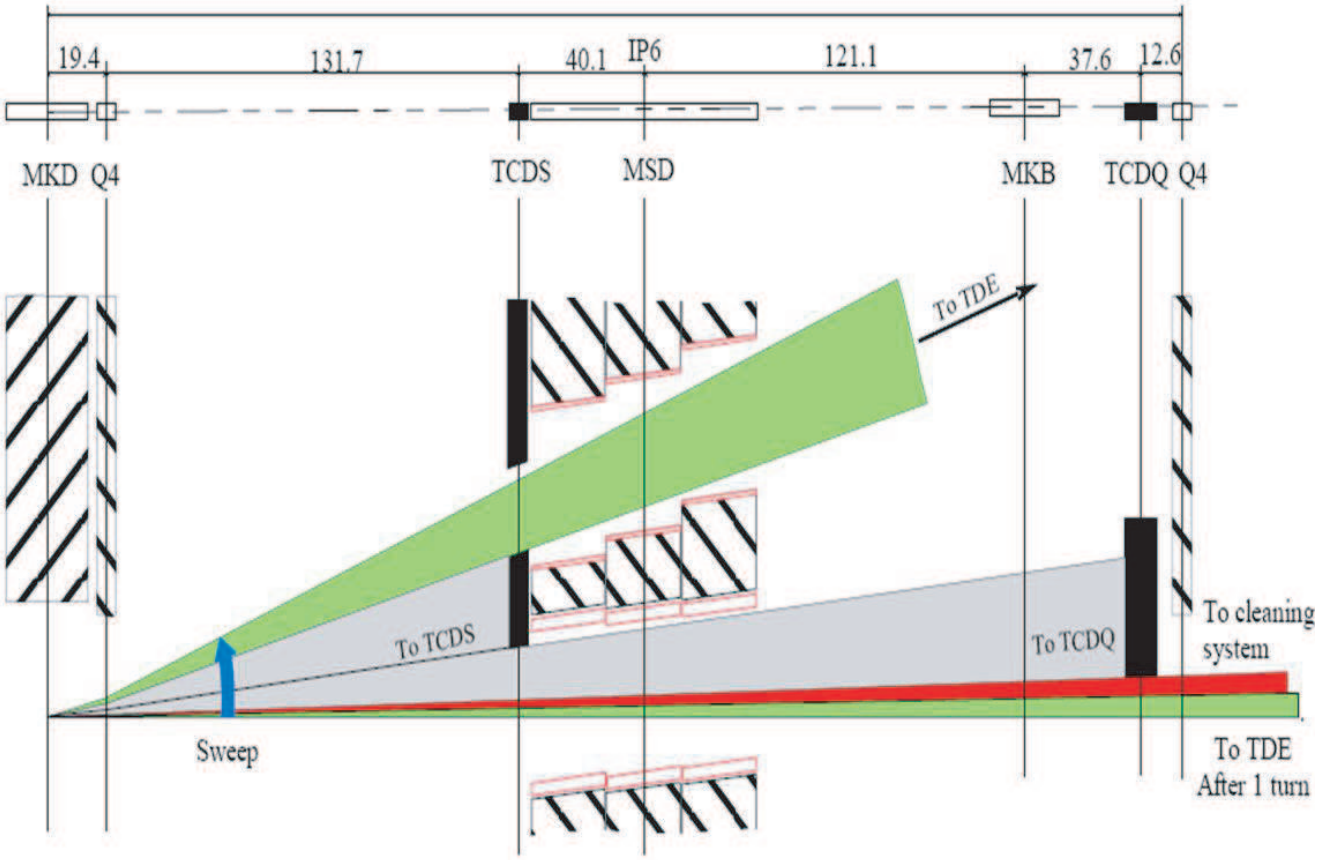

Figure 4.17: Schematic of the beam dump system in IR6. The extraction is done by sweeping the beam towards the dedicated line. Protective equipments are installed locally (TCDS) to prevent damage on the closest elements. The TCDQ collimators (here represented as a single block) are located $\sim$ 350 metres downstream of the extraction kicker and removes the fraction of the swept beam which is heading in the arc downstream. An additional collimator (TCS) is implemented 3 metres downstream of the TCDQ to improve cleaning efficiency.

4.3.1 Injection energy (450 GeV) - Horizontal halo

For the injection energy case, compared to the preliminary runs, the additional collimators are:

- the active absorbers (TCLA) in the IR7 betatron cleaning insertion,
- the IR3 momentum cleaning collimators: primaries, secondaries and active absorbers,
- the injection protection collimators: one TDI and two TCLI at each injection insertion IR2 and IR8,
- the beam dump protection collimators: one TCDQ and its associated secondary collimator TCS, located in IR6; a schematic view is presented in Figure 4.17.

This new set of collimators is referred to as the *LHC Phase 1 collimation system*: as seen in section 3.2.1, further phases of the collimation system include additional secondary collimators in the IR3 momentum cleaning and IR7 betatron cleaning insertions, as well as a change in material for secondary collimator jaws. The optimal location of the TCLA absorbers in the IR7 cleaning insertion was determined by an iterative process using the results of simulations. Studies on particles showering were performed with FLUKA from the location of inelastic scattering in the collimator jaws as given by simulations with SixTrack; the longitudinal positions of the absorbers were then shifted untill the energy deposited in the magnets downstream was lowered to a value below the tolerated radiation dose (see section 4.7.1 for more details).

Inserting all the new elements into the simulations, one gets the new beam loss pattern for a horizontal halo, as shown in Figure 4.16. Losses downstream of IP7 are reduced by a factor 10 compared to the results with the initial collimation system. The Q6 quadrupole assembly does not show any more loss peaks. One can notice from Table 4.7 the significant improvement on integrated losses : the MCBCH.6R8.B1 magnet is now the most critical loss location in the machine (losses in this element reach a level comparable to the one observed with the initial cleaning system). Overall, a factor 3.5 is gained in the highest local loss peak over the machine.

Table 4.7: Critical loss locations for a horizontal beam halo at injection energy using all LHC Phase 1 collimators. The number of lost protons is obtained from the data shown in Figure 4.16 and integrated over the length of each element. Δ refers to the error bar on the inefficiency, as defined in equation (3.11).

Total number of absorbed particles			4826820	
Name	Length [m]	$\mathbf{N}_{loss}$	η_{total} [$\mathbf{10^{-5}}$]	$\mathbf{\Delta}$
MCBCH.6R8.B1	0.9	124	2.57	0.23
MB.C13R7.B1	14.3	121	2.51	0.23
MQXB.A2R8	5.5	67	1.39	0.17
MQML.6R8.B1	4.8	46	0.95	0.14
MB.C31R7.B1	14.3	39	0.81	0.13

One can notice from Figure 4.18 that the arc 7-8 shows fewer peaks of cold losses than in Figure 4.4. This is the effect of the additional active absorbers located just downstream of the last secondary collimator of IR7. Table 4.8 gives a quantitative estimate of the influence of these new elements. The simulations performed are multi-turns, therefore the stated number of impacts correspond to the total number of impacts experienced by each absorber when tracking protons for 200 turns. These absorbers are placed in cells 6 and 7 on the right side of IP7 (for Beam 1) and absorb more than 10^4 particles. This is why no further losses are seen for Q6: every proton gets dumped into the jaws of the absorbers instead. Having the TCLA elements just upstream of the dispersion suppressor also helped in reducing the level of losses in the arc downstream of IP7. The critical location that is the MCBCH.6R8.B1 magnet cannot be avoided since losses there are due to high experimental β-function values, as seen in Figure 4.18.

Table 4.8: Statistics on impacts and absorptions of protons at the IR7 absorbers for a simulated horizontal halo at injection energy.

Name	$\mathbf{N}_{impacts}$	$\mathbf{N}_{absorbed}$
TCLA.A6R7.B1	4099	4072
TCLA.C6R7.B1	3192	3188
TCLA.E6R7.B1	2785	2775
TCLA.F6R7.B1	1718	1711
TCLA.A7R7.B1	725	709

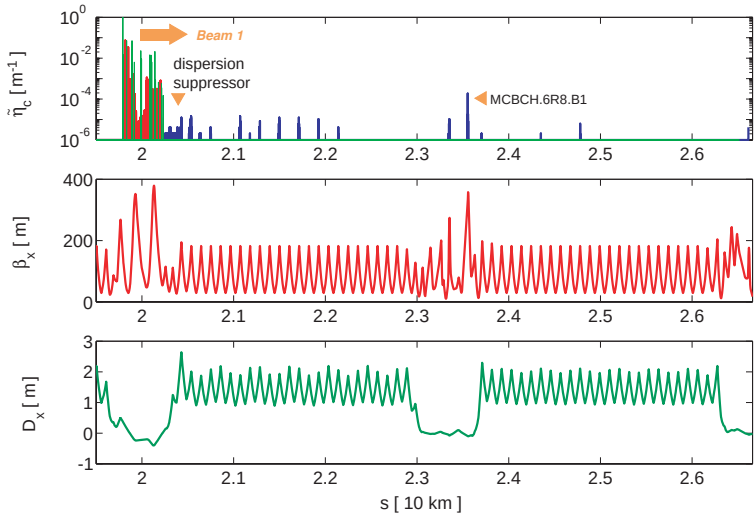

Figure 4.18: Zoom of Figure 4.16 between the IR7 region and IP1 (top). Comparison is made with the β_x function (center) and the dispersion function D_x (bottom).

Considering the rest of the machine, some more cold peaks are showing up in the IR2 insertion compared to the initial system. This is related to the addition of the injection protection collimators and is reviewed in the following section. Warm losses can also be noticed now in the IR3 region: these are due to the inclusion of the IR3 momentum cleaning

collimators; no particular elements close to IR3 get critical in terms of quench protection though. Finally, some more loss peaks show up in the IR6 region: these are due to particles with large amplitudes impacting on the secondary collimator located downstream of the TCDQ collimator (beam dump protection).

Simulations with the full Phase 1 collimation system show an improvement in the global inefficiency of the system as it can be noticed on Figure 4.19. The full system is 1.5 times more efficient when comparing at an amplitude of 7.5 σ. There is at least a factor 4.5 between the initial and the full system when looking at particles over 10 σ.

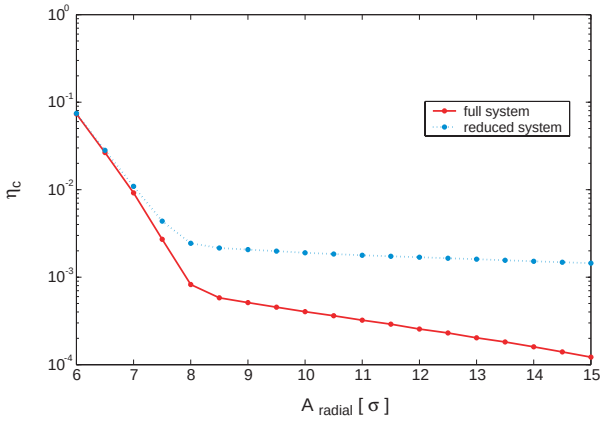

Figure 4.19: Global inefficiency of the full Phase 1 (solid line) and initial (dotted line) LHC collimation system in the injection energy case. The simulated halo is horizontal.

4.3.2 Injection energy (450 GeV) - Vertical halo

The effect of the additional elements is even more noticeable when simulating a vertical halo; the corresponding loss map over the ring is shown in Figure 4.20. Losses downstream of IP7 are nearly avoided: only 1 or 2 particles get lost in the elements of arc 7-8, at the limit of statistical resolution for the simulations performed. The MCBCH.6R8.B1 element still presents a relatively high level of losses.

The most obvious changes are the high peaks in the IR2 region. Particles get lost in this section of the machine because of the injection protection elements. The value listed in Table 4.1 for the half-gap of the TDI collimator is 6.8 σ, and its jaws are placed in the vertical plane to follow the injection scheme established in [1]. Therefore the TDI in IR2 acts as a partial secondary collimator for the vertical halo. Losses can also be noticed in the horizontal halo case, but the peaks are not as high as in Figure 4.20. This explains the results shown in Table 4.9, where out of the 5 most critical elements, 4 are located in the IR2 region. Since the protective elements are concentrated in IR2, there is a higher probability that particles get lost in a region close downstream. This is illustrated in Figure 4.21.

The situation in the regions downstream of IP7 is similar to what was observed in Figure 4.18 for the horizontal halo. Concentrating on IR2, one can spot a group of cold peaks at $s \approx 3.6$ km that can neither be explained by the variations of the β_y function nor

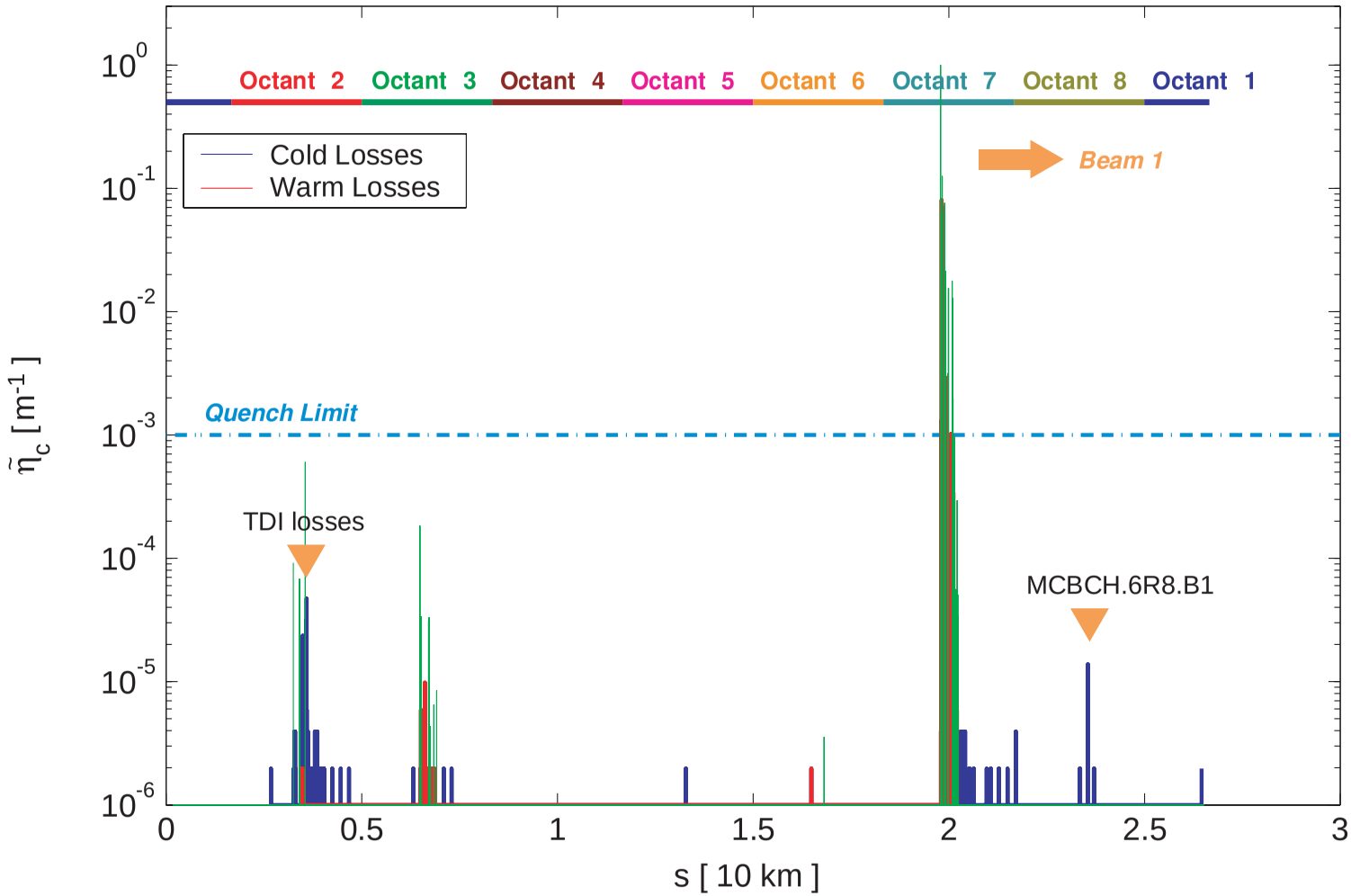

Figure 4.20: Beam loss map at injection energy for the full LHC Phase 1 collimation system. The simulated halo is vertical. Results are shown for Beam 1 only.

Table 4.9: Critical loss locations for a vertical beam halo at injection energy using all LHC Phase 1 collimators. The number of lost protons is obtained from the data shown in Figure 4.20 and integrated over the length of each element. Δ refers to the error bar on the inefficiency, as defined in equation (3.11).

Total number of absorbed particles			5080547	
Name	Length [m]	$\mathbf{N}_{loss}$	η_{total} [$\mathbf{10^{-5}}$]	$\mathbf{\Delta}$
MQM.A7R2.B1	3.4	36	0.71	0.12
MB.B9R7.B1	14.3	24	0.47	0.10
MB.A8R2.B1	14.3	20	0.39	0.09
MB.B8R2.B1	14.3	19	0.37	0.09
MB.B10R2.B1	14.3	16	0.31	0.08

by the values of the dispersion function. Comparing the s location with the LHC layout database, it turns out that the losses take place at the beam screen of an element labeled DFBA, which is the electrical powering source for the superconducting dipoles and quadrupole magnets in the arc downstream of it [69]. Considering the level of losses, this location needs extra attention as a fault in the powering element could provoke a quench of the whole arc 2-3. However, these peaks are due to protons which scatter from the jaws of the injection protection elements and end up being lost a few metres downstream. After the filling phase of the machine, the injection protection elements are retracted and halo protons are then very unlikely to be lost at these locations.

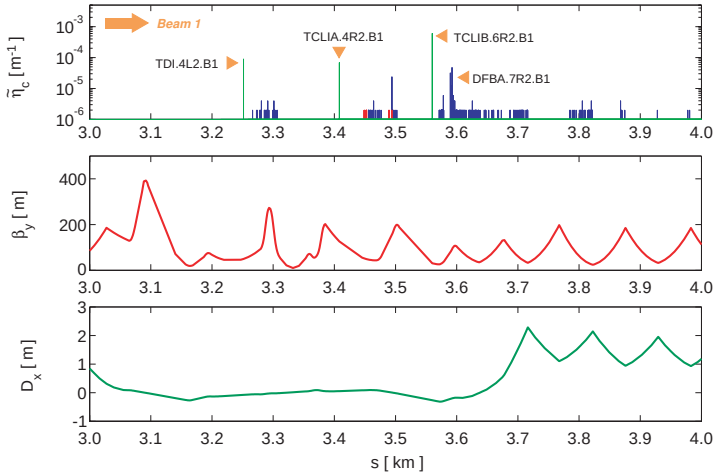

Figure 4.21: Zoom of Figure 4.20 within the IR2 region (top). Comparison is made with the betatron function β_y (center) and the dispersion function D_x (bottom).

Figure 4.22 shows that the result observed in section 4.2 (the global inefficiency of the system is better for vertical than for horizontal halo) is verified when simulating the full LHC Phase 1 collimation system.

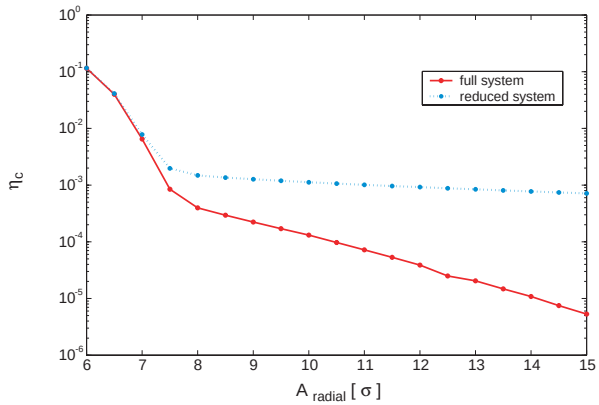

Figure 4.22: Global inefficiency of the full (solid line) and initial (dotted line) LHC collimation system in the injection energy case. The simulated halo is vertical.

4.3.3 Collision energy (7 TeV) - horizontal halo

The loss map for horizontal halo losses at 7 TeV is shown in Figure 4.23. The system is definitely improved compared to the data presented in section 4.2.3. There are no more peaks in the triplet region in the IR1 and IR5 insertions, which were the most critical locations in the preliminary runs. Additional green peaks can now be noticed: these indicate losses in the newly added collimation elements.

Table 4.10: Critical loss locations for a horizontal beam halo at collision energy using all LHC Phase 1 collimators. The number of lost protons is obtained from the data shown in Figure 4.23 and integrated over the length of each element. Δ refers to the error bar on the inefficiency, as defined in equation (3.11).

Total number of absorbed particles			5054636	
Name	Length [m]	$\mathbf{N}_{loss}$	η_{total} [$\mathbf{10^{-5}}$]	$\mathbf{\Delta}$
MB.A9R7.B1	14.3	264	5.22	0.32
MB.B9R7.B1	14.3	254	5.02	0.31
MB.A11R7.B1	14.3	225	4.45	0.30
MB.B11R7.B1	14.3	217	4.29	0.29
MQ.9R7.B1	3.1	54	1.07	0.14

The injection protection collimators are no longer used (their openings are set to 900 σ). The tertiary collimators (TCT) and the collimators for physics debris (TCL) are set to their nominal openings as listed in Table 4.1. The most (and actually only) critical region of the machine is now the dispersion suppressor at the end of the IR7 collimation insertion, as seen in Table 4.10. The magnets with most losses are all located in the final 3 cells (number 9, 10 and 11) of the straight section, which correspond to the first high dispersion locations before the beam reaches the arc 7-8. The worst element is a dipole magnet, MB.A9R7.B1, but losses are 40 % lower as compared to the ones in the initial system case (see Table 4.5).

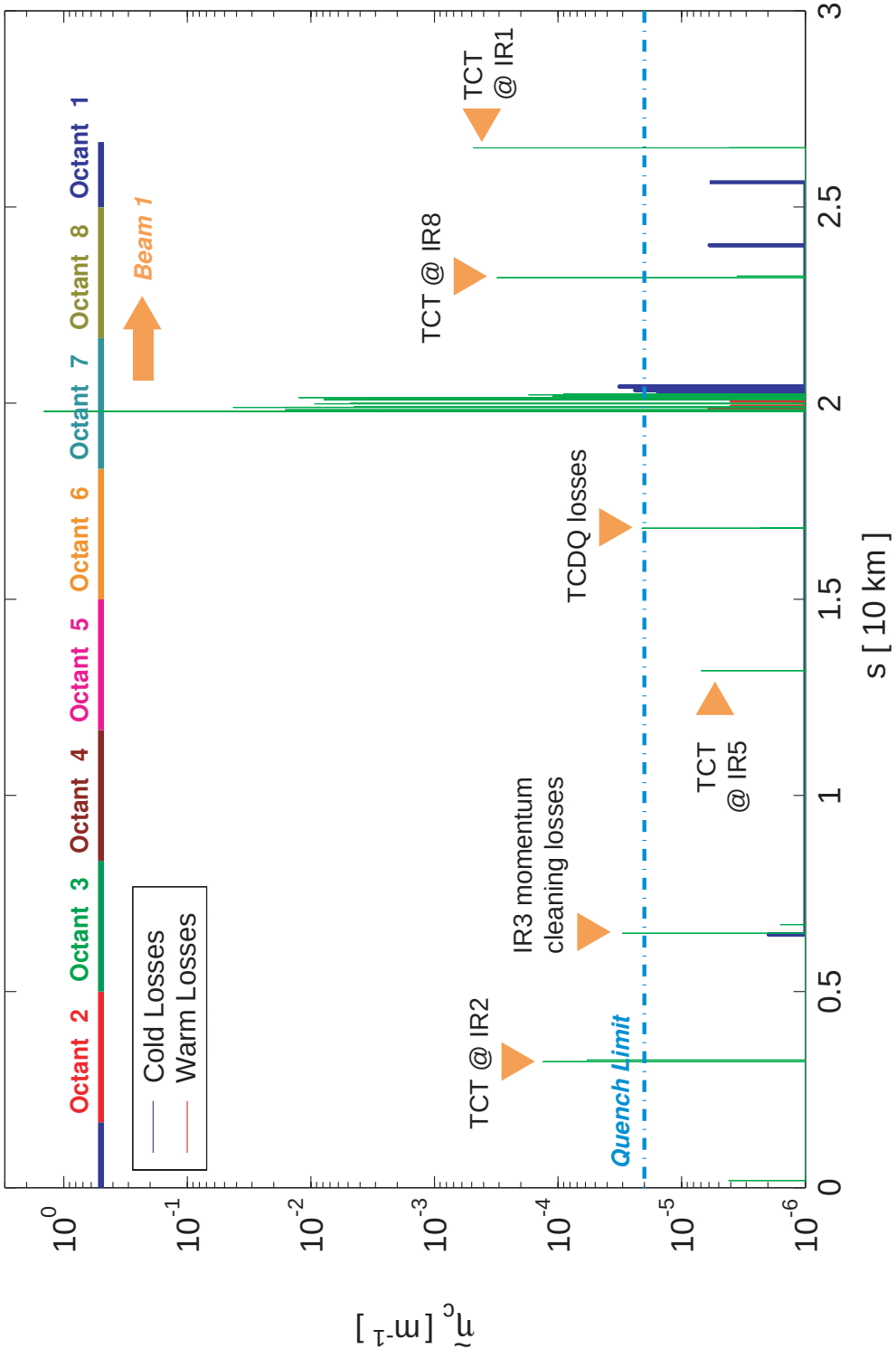

Figure 4.23: Beam loss map at collision energy for the full LHC Phase 1 collimation system. The simulated halo is horizontal. Results are shown for Beam 1 only.

With their openings set to 8.3 σ, the tertiary collimators located in IR8 can capture collimated particles which escape both the absorbers and the dispersion suppressor at the end of IR7. Table 4.11 lists the losses in the LHC tertiary collimators for the considered scenario.

Table 4.11: Statistics on impacts and absorptions of protons at the tertiary collimators for horizontal halo at collision energy.

Name	$\mathbf{N}_{impacts}$	$\mathbf{N}_{absorbed}$
TCTH.4L1.B1	2442	2439
TCTV.4L1.B1	21	21
TCTH.4L2.B1	675	669
TCTV.4L2.B1	295	294
TCTH.4L5.B1	36	35
TCTV.4L5.B1	9	9
TCTH.4L8.B1	1580	1572
TCTV.4L8.B1	18	18

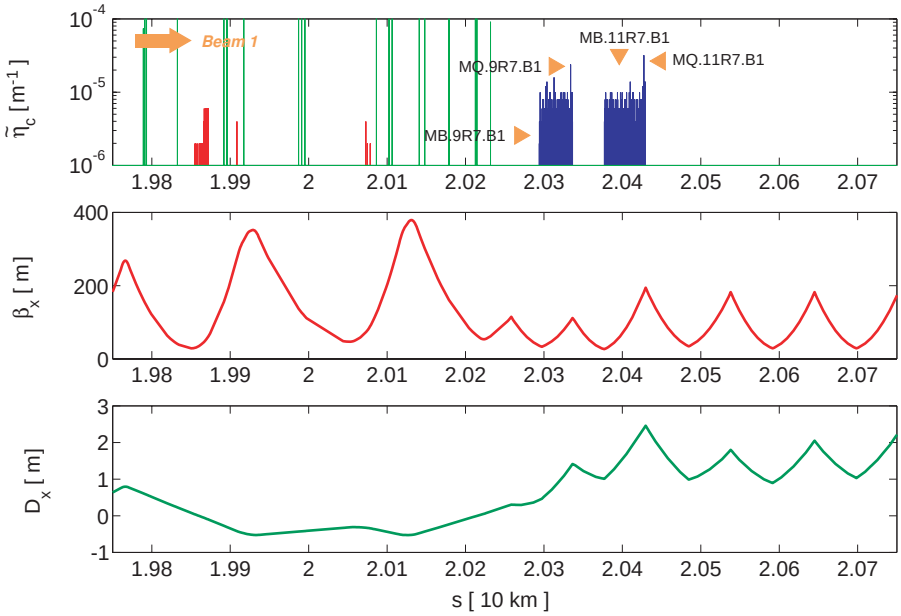

Figure 4.24: Zoom of Figure 4.23 in the dispersion suppressor downstream of IP7 (top). Comparison is made with the betatron function β_x (center) and the dispersion function D_x (bottom).

The global inefficiency of the full system is drastically improved as well, as seen on Figure 4.25. Compared to the case with IR7 primary and secondary collimators only, there is about a factor 10 improvement for particles at 8 σ. For amplitudes larger than 11 σ, the full system performs two orders of magnitude better.

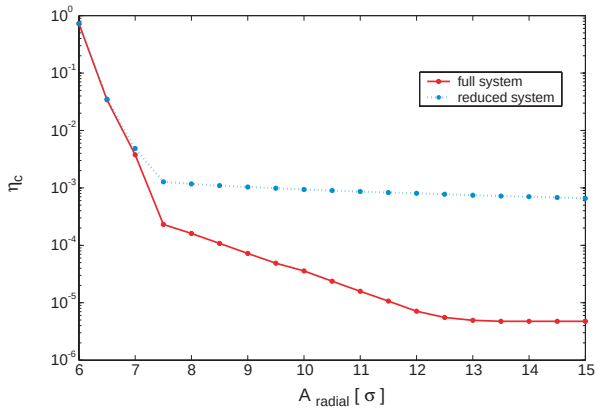

Figure 4.25: Global inefficiency of the full Phase 1 (solid line) and initial (dotted line) LHC collimation system in the collision energy case. The simulated halo is horizontal.

4.3.4 Collision energy (7 TeV) - vertical halo

The beam loss map obtained at collision energy for a vertical halo looks similar to the horizontal halo case, as shown in Figure 4.26. Losses are concentrated at the end of IR7 as the new collimation elements provide additional protection. The best illustration of this is the effect of the tertiary collimators in the experimental insertions (as it was already shown in the previous section). Values in Table 4.12 show lower losses compared to the initial system case, but the improvement is not as significant as observed for the horizontal halo. This can be explained by the fact that the active absorbers are less effective for a vertical halo, meaning that they "see" (and therefore absorb) less particles; the corresponding statistics can be found in Table 4.13. This is mainly due to the effect of the dispersion function on the amplitude of horizontal halo particles that are slightly off-momentum.

Table 4.12: Critical loss locations for a vertical beam halo at collision energy using all LHC Phase 1 collimators. The number of lost protons is obtained from the data shown in Figure 4.26 and integrated over the length of each element. Δ refers to the error bar on the inefficiency, as defined in equation (3.11).

Total number of absorbed particles			5001082	
Name	Length [m]	$\mathbf{N}_{loss}$	η_{total} [$\mathbf{10^{-5}}$]	$\mathbf{\Delta}$
MB.B9R7.B1	14.3	374	7.48	0.39
MB.A11R7.B1	14.3	330	6.60	0.36
MB.A9R7.B1	14.3	323	6.46	0.36
MB.B11R7.B1	14.3	303	6.06	0.35
MQ.9R7.B1	3.1	87	1.74	0.19

The global inefficiency curve shown in Figure 4.27 demonstrates again the improvement achieved with tertiary collimators and absorbers. There is a gain of at least a factor 10 for all particles with normalized amplitude over 8 σ compared to the initial system.

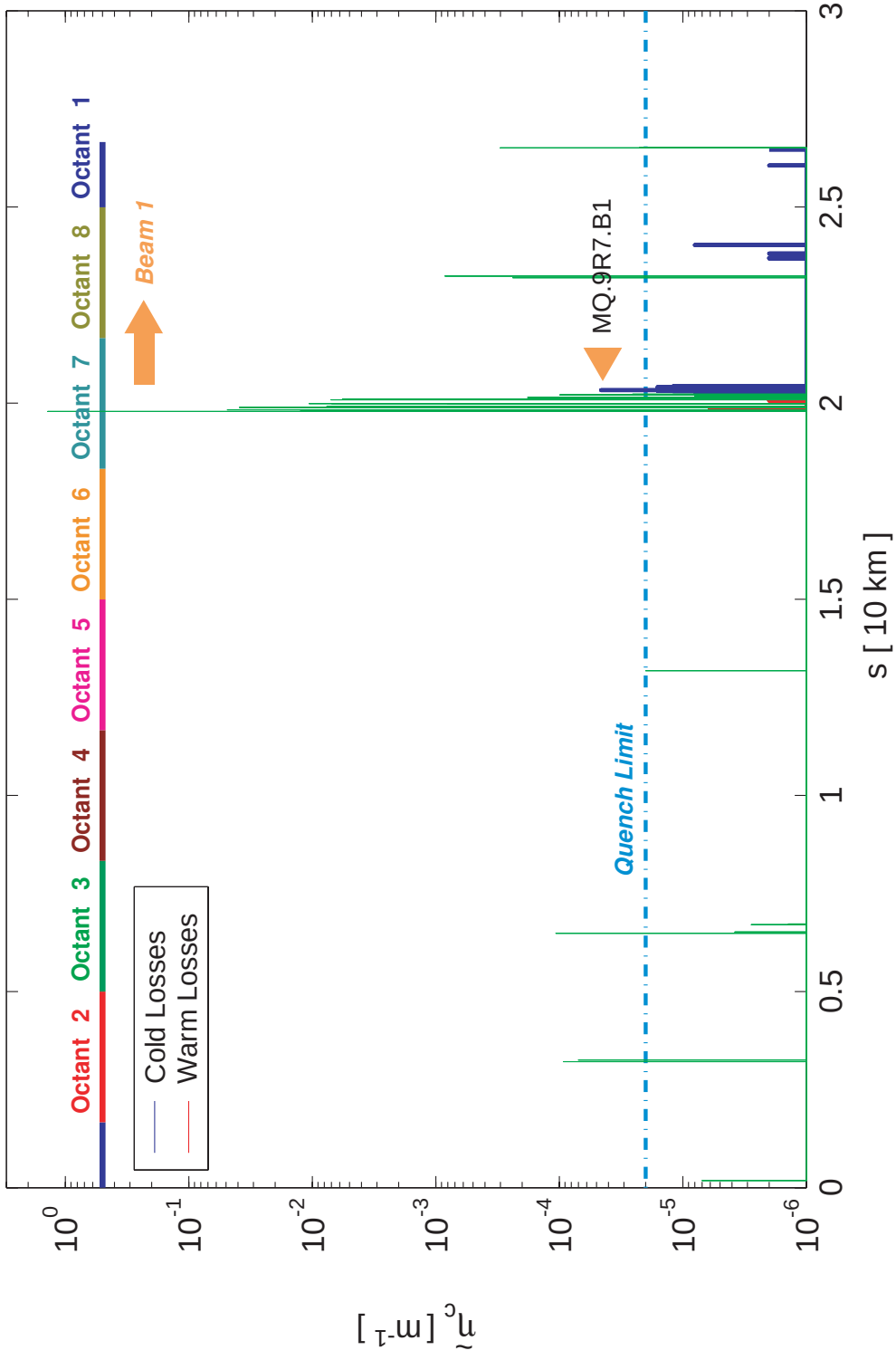

Figure 4.26: Beam loss map at collision energy for the full LHC Phase 1 collimation system. The simulated halo is vertical. Results are shown for Beam 1 only.

Table 4.13: Statistics on impacts and "absorptions" of protons at the IR7 absorbers for horizontal and vertical halo at collision energy.

Name	Horizontal halo		Vertical halo	
	$\mathbf{N}_{impacts}$	$\mathbf{N}_{absorbed}$	$\mathbf{N}_{impacts}$	$\mathbf{N}_{absorbed}$
TCLA.A6R7.B1	682	680	907	903
TCLA.C6R7.B1	558	558	40	40
TCLA.E6R7.B1	875	872	497	496
TCLA.F6R7.B1	820	819	184	184
TCLA.A7R7.B1	464	457	130	128
TOTAL	3399	3386	1758	1751

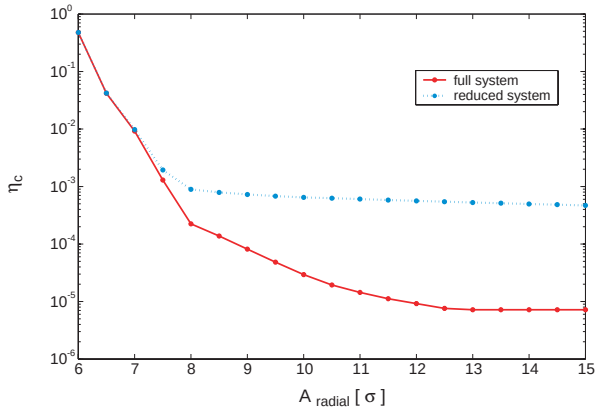

Figure 4.27: Global inefficiency of the full Phase 1 (solid line) and initial (dotted line) LHC collimation system in the collision energy case. The simulated halo is vertical.

4.3.5 Summary: upgrade in performance with the full system

The simulations performed for the two halo types highlighted a good level of performance achieved by the full Phase 1 LHC collimation system, complemented by active absorbers in the betatron and momentum cleaning insertions and tertiary collimators in the four experimental insertions. At injection energy (450 GeV), local losses are globally brought down by a factor at least 10, especially in the dispersion suppressor region immediately downstream of IP7. A few peaks (Q6 in IR8, beam screen of DFBA in IR2) can still be listed as critical, but overall the machine is safe in the ideal case. In the collision case (7 TeV), losses in the squeezed insertions IR1 and IR5 are handled by the addition of tertiary collimators. Most of the cold losses downstream of IR7 are removed with the active absorbers. The few remaining loss locations are the dipole and quadrupole magnets of the dispersion suppressor in cells 9 and 11 at the right of IP7.

Table 4.14 gives the ideal level of performance that can be reached using the full Phase 1 collimation system for Beam 1. The beam intensity is limited in the collision energy case only, as no loss peak go over the quench limit in the injection energy case. The maximum

allowed intensity is then calculated as a fraction of the nominal intensity by taking into account both the peak value of local cleaning inefficiency around the machine and the local cleaning inefficiency at the secondary collimator located in the IR6 beam dump region. A specific quench limit of $\tilde{\eta}_{c,peak}^{TCDQ} = 2.55 \times 10^{-4}$ m^{-1} at 7 TeV is estimated for this region of the machine. This value is derived from the maximum energy deposited in the magnets downstream of the beam dump protection collimators (TCDQ and the associated TCS), as calculated with FLUKA from the output data of Sixtrack.

Table 4.14: Summary on the performance level reached in the ideal machine case for Beam 1 using the initial and the full Phase 1 LHC collimation system. The performance of each system is given by the maximum allowed intensity, derived from the simulated local cleaning inefficiencies in the machine. The limiting factor is stated in bold values.

Case	$\tilde{\eta}_{\mathbf{c,peak}}^{\mathbf{cold}}$ [m^{-1}]	$\tilde{\eta}_{\mathbf{c,peak}}^{\mathbf{TCDQ}}$ [m^{-1}]	I_{max}/I_{nom} [%]
Initial collimation system			
450 GeV, horizontal halo	$\mathbf{6.91 \times 10^{-4}}$	n/a	144.72 ± 7.93
450 GeV, vertical halo	$\mathbf{3.11 \times 10^{-4}}$	n/a	321.54 ± 25.59
7 TeV, horizontal halo	$\mathbf{2.61 \times 10^{-4}}$	n/a	7.66 ± 0.67
7 TeV, vertical halo	$\mathbf{6.60 \times 10^{-5}}$	n/a	30.30 ± 5.28
Full Phase 1 collimation system			
450 GeV, horizontal halo	$\mathbf{1.86 \times 10^{-4}}$	1.09×10^{-4}	537.63 ± 56.74
450 GeV, vertical halo	$\mathbf{4.72 \times 10^{-5}}$	3.54×10^{-6}	2118.64 ± 432.65
7 TeV, horizontal halo	$\mathbf{3.17 \times 10^{-5}}$	2.10×10^{-5}	63.09 ± 15.76
7 TeV, vertical halo	$\mathbf{4.60 \times 10^{-5}}$	2.00×10^{-7}	43.48 ± 9.06

In the collision energy case, the improvement for the horizontal halo is significant (nearly one order of magnitude). The limitation clearly comes from the vertical halo, setting the maximum allowed intensity in the ideal machine case at $\sim$ 44 % of the nominal LHC beam intensity (as given in Table 1.2).

4.4 Systematic differences between Beam 1 and Beam 2

4.4.1 Predicted differences at injection energy (450 GeV)

The Beam 1 and Beam 2 optics are mostly symmetrical. However, detailed analysis of the beam loss patterns show that there are different behaviors for halo particles depending on which beam is considered. As seen in Figure 4.28, the IR6 beam dump insertion where the TCDQ and TCS collimators are located clearly shows differences. Figure 4.29 presents the detail of the loss distribution in this region.

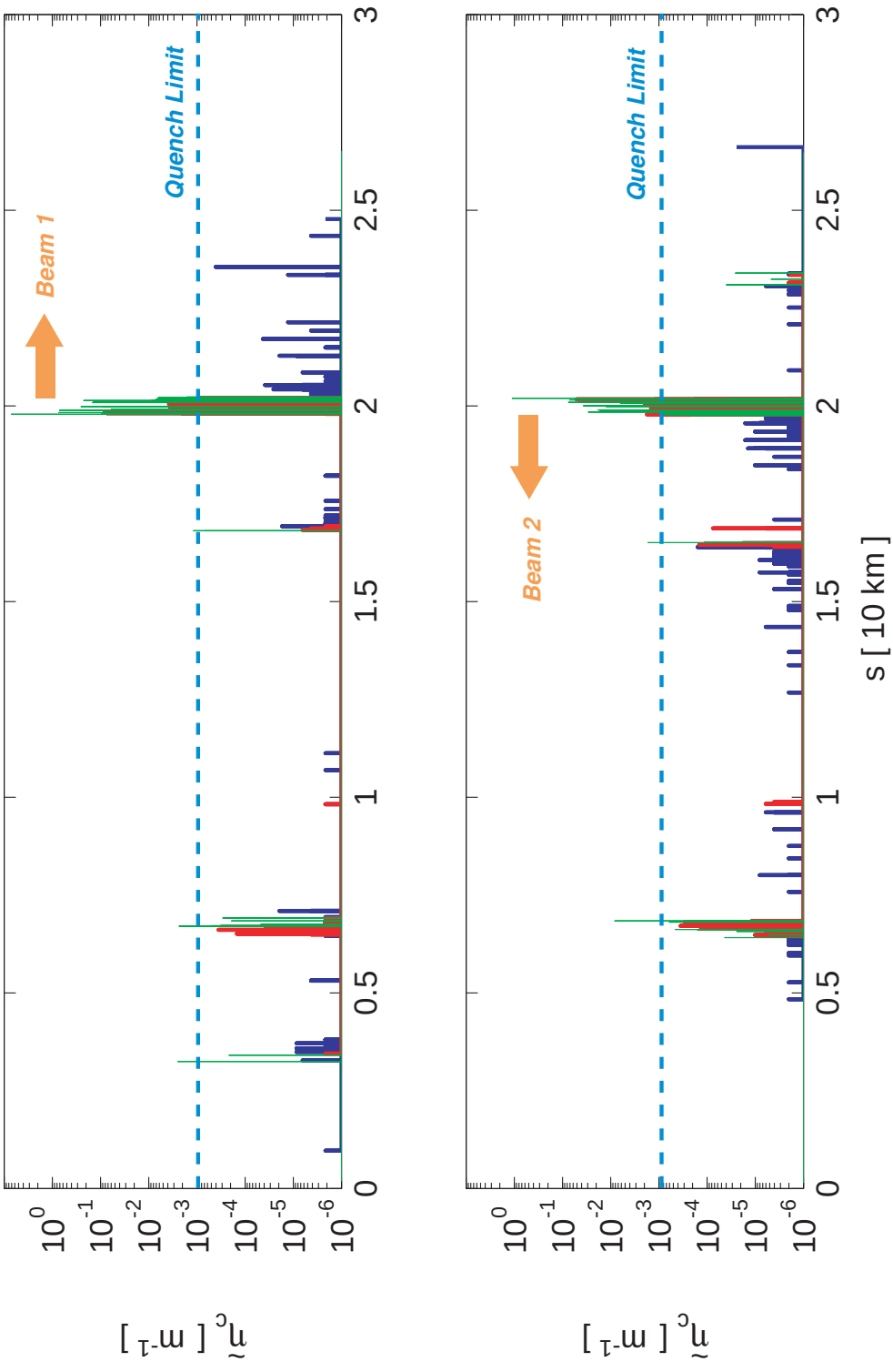

Figure 4.28: Beam 1 (top) and Beam 2 (bottom) loss map at injection energy for the full Phase 1 collimation system. The simulated halo is horizontal.

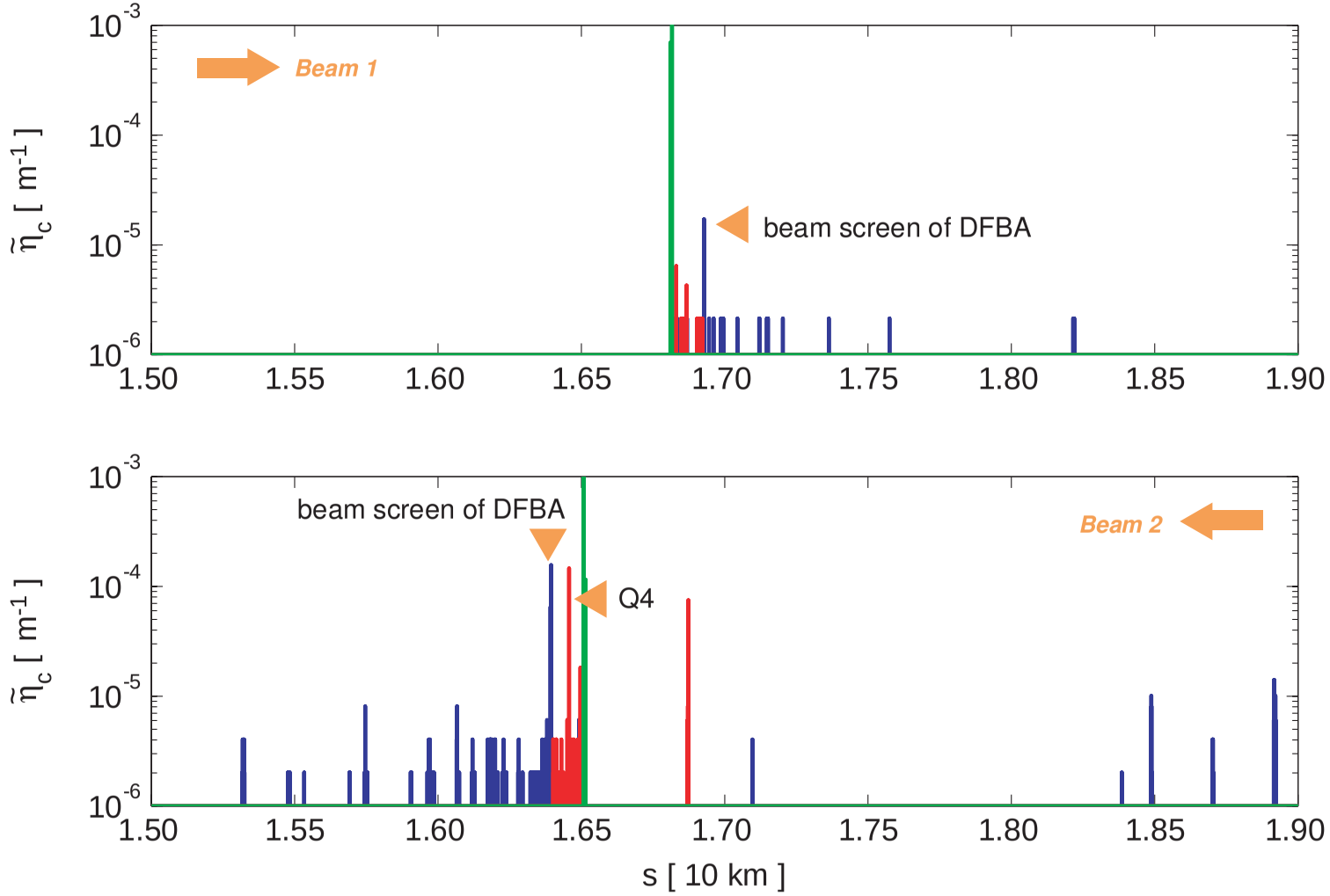

Figure 4.29: Zoom of Figure 4.28 around IP6. The green lines correspond to the location of the beam dump protection elements. The simulated halo is horizontal.

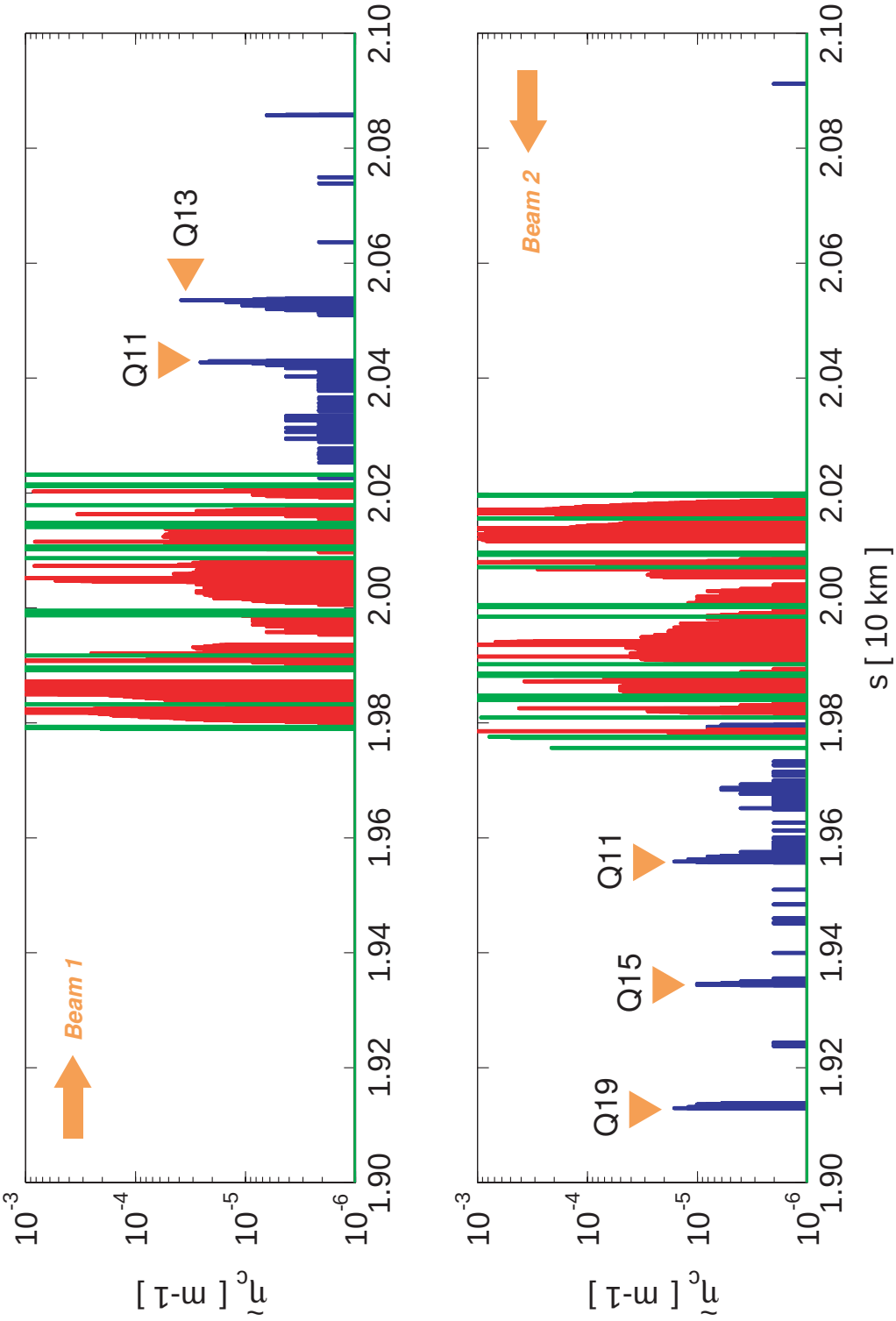

Figure 4.30: Zoom of Figure 4.28 around IP7. The simulated halo is horizontal.

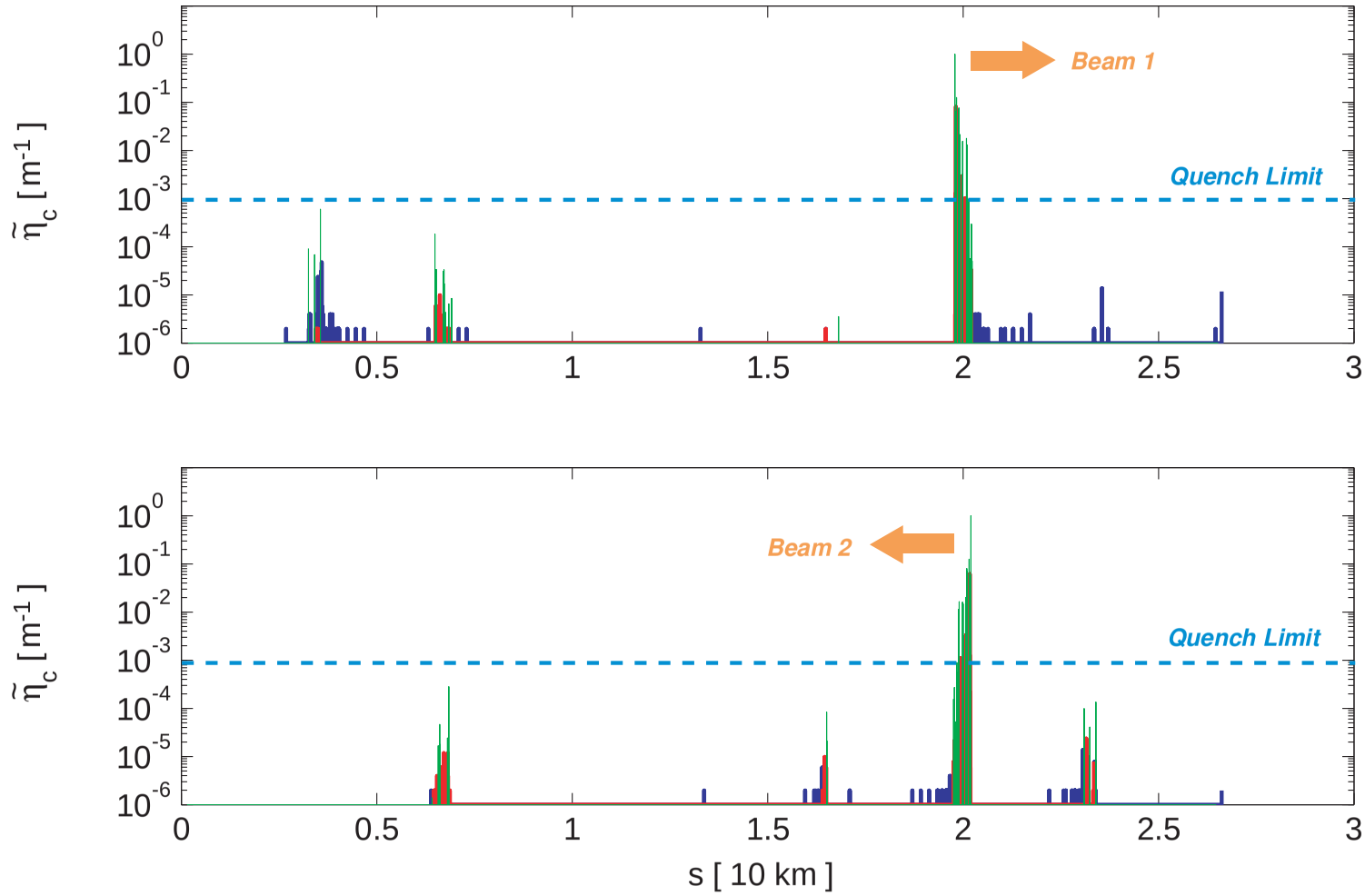

Figure 4.31: Beam 1 (top) and Beam 2 (bottom) loss map at injection energy for the full Phase 1 collimation system. The simulated halo is vertical.

Protons scattered by the primary collimators of IR7 form the *secondary halo* and are handled by the rest of the system made of secondary collimators and absorbers. A small fraction of the secondary halo still escapes and ends up circulating in the machine as tertiary halo; these are the particles that might then get lost in cold elements. For Beam 2, IR6 is the closest insertion downstream of the IR7 betatron cleaning insertion. The nominal half-opening of the secondary collimator installed in IR6 is set to 7 σ in the injection energy case, which has to be compared with the nominal opening of 6.7 σ for the IR7 secondary collimators. The difference is small enough for the TCS in IR6 to be "seen" by the surviving beam halo. Protons are then scattered and get lost at the first high dispersion location, i.e. at the beam screen of the DFBA cryogenic element, located just before the start of the IR6 dispersion suppressor on each side of IP6, as seen in Figure 4.29. Table 4.15 gives the main statistics on the amount of protons lost per element over the machine.

Table 4.15: Critical loss locations for a horizontal Beam 2 halo at injection energy using all LHC Phase 1 collimators. The number of lost protons is obtained from the data shown in Figure 4.28 and integrated over the length of each element. Δ refers to the error bar on the inefficiency, as defined in equation (3.11).

Total number of absorbed particles			4848906	
Name	Length [m]	$\mathbf{N}_{loss}$	η_{total} [$\mathbf{10}^{-5}$]	$\mathbf{\Delta}$
MB.C15L7.B2	14.3	111	2.29	0.22
MB.C19L7.B2	14.3	43	0.89	0.13
MQ.19L7.B2	3.1	40	0.82	0.13
MQ.15L7.B2	3.1	38	0.78	0.13
MB.A9L7.B2	14.3	32	0.66	0.12

The other main difference between Beam 1 and Beam 2 losses is observed in the two regions downstream of IR7, as shown in Figure 4.30. Up to the Q11 quadrupole, the distribution of cold losses looks symmetrical around IP7. Once outside of the dispersion suppressor though, the situation changes as there are no loss peak at Q13, while losses occur in Q15 and Q19. The explanation of this phenomenon is illustrated in Figure 4.32: the dispersion functions around IP7 are not symmetric in amplitude. A higher dispersion is observed for Beam 1 than for Beam 2, inducing more proton losses in cells 11 and 13 for comparable levels of statistics at the collimators and absorbers. The Beam 2 protons after Q13 are lost at the next high dispersion locations, which are Q15 and Q19 (see dashed line in Figure 4.32)[3].

An equivalent study has been performed for a vertical halo as illustrated in Figure 4.31: the same asymmetry in loss locations is found downstream of IR7. No critical loss locations appear in IR6, as the TCDQ and TCS collimators in this insertion both work in the horizontal plane (plane of the extracted beam). Also, Beam 2 particles are injected through the IR8 insertion: a pattern similar to the one in IR2 for Beam 1 is found in the regions close to the Beam 2 injection protection equipments.

[3] Following Beam 2 direction (from right to left on Figure 4.32), one can see that the values of D_x for Beam 2 from Q15 onwards are higher than the values in Q11 and Q13.

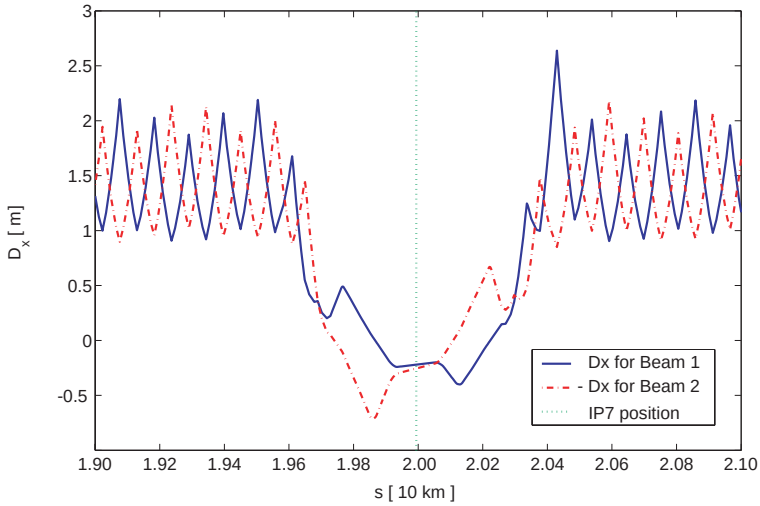

Figure 4.32: Comparison of the Beam 1 (solid) and Beam 2 (dashed) dispersion functions around IP7 at injection energy. The green line corresponds to the location of IP7.

4.4.2 Predicted differences at collision energy (7 TeV)

The loss maps for Beam 1 and Beam 2 are shown in Figure 4.33: they look similar except for some loss locations in the IR6 region. These losses are due to the beam dump protection elements (TCDQ and TCS) located there. Table 4.16 shows that, compared to the values in the Beam 1 case, there are twice as many protons getting lost in the MB9 dipole magnet on the left side (made of the MB.A9L7.B2 and MB.B9L7.B2 modules) than in the MB9 on the right side (made of the MB.A9R7.B1 and MB.B9R7.B1 modules).

Table 4.16: Critical loss locations for a horizontal Beam 2 halo at collision energy using all LHC Phase 1 collimators. The number of lost protons is obtained from the data shown in Figure 4.33 and integrated over the length of each element. Δ refers to the error bar on the inefficiency, as defined in equation (3.11).

Total number of absorbed particles			5113611	
Name	Length [m]	$\mathbf{N}_{loss}$	η_{total} [$\mathbf{10^{-5}}$]	$\boldsymbol{\Delta}$
MB.A9L7.B2	14.3	566	11.07	0.46
MB.B9L7.B2	14.3	479	9.37	0.43
MB.B11L7.B2	14.3	268	5.24	0.32
MB.A11L7.B2	14.3	119	2.33	0.21
MQ.8L7.B2	3.1	48	0.94	0.13

Additional losses appear in the Q13 quadrupole magnet for Beam 2. Comparing the variation of the Twiss parameters in this area of the machine (as shown in Figure 4.34), it can be seen that β_x(s) has higher values in cells 9 and 10 for Beam 2 than for Beam 1: peak values are $\hat{\beta}_x^{B1} \approx 111.558$ m and $\hat{\beta}_x^{B2} \approx 137.010$ m. With a larger unit beam size, more halo

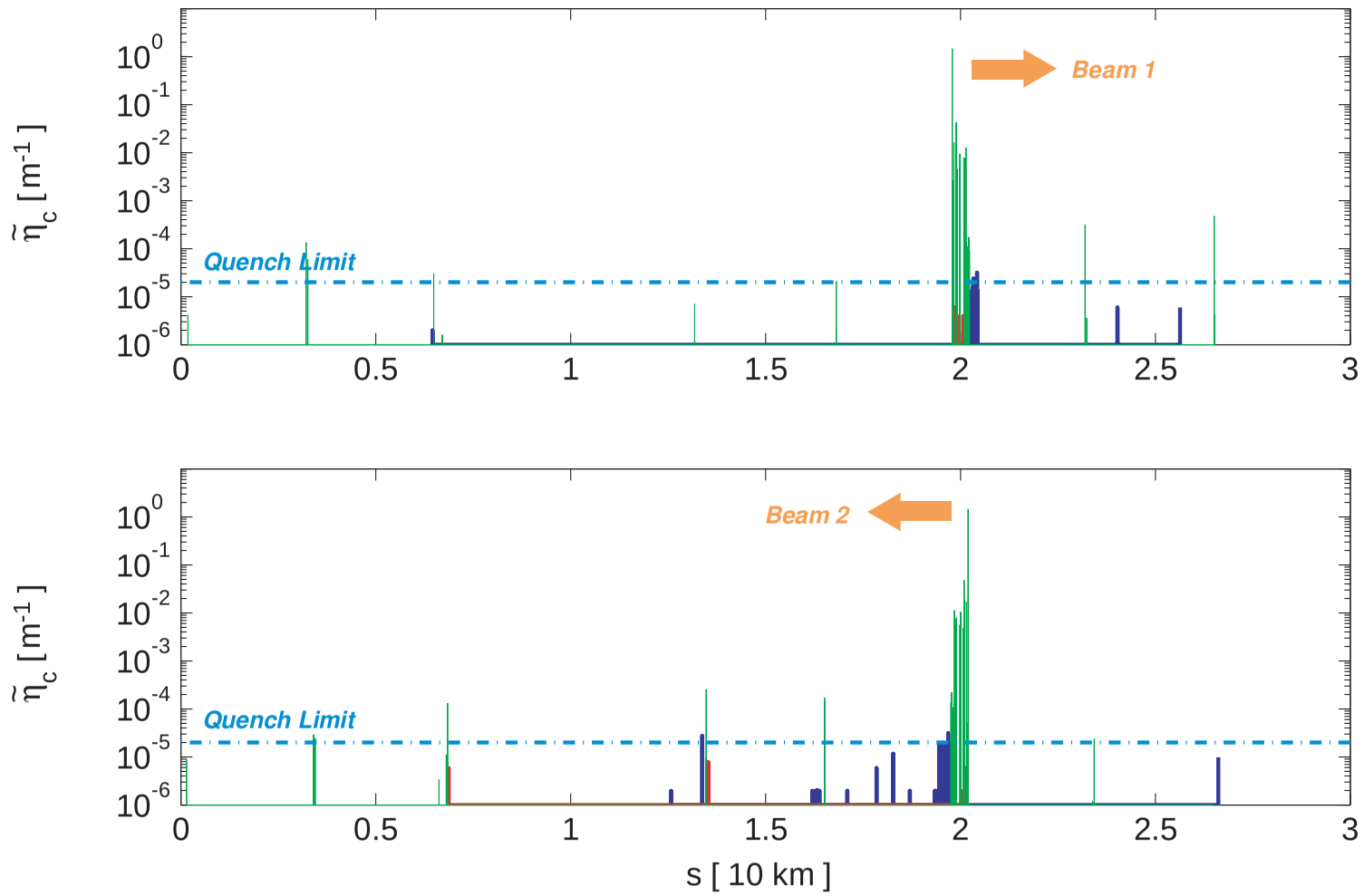

Figure 4.33: Beam 1 (top) and Beam 2 (bottom) loss maps at collision energy for the full Phase 1 collimation system. The simulated halo is horizontal.

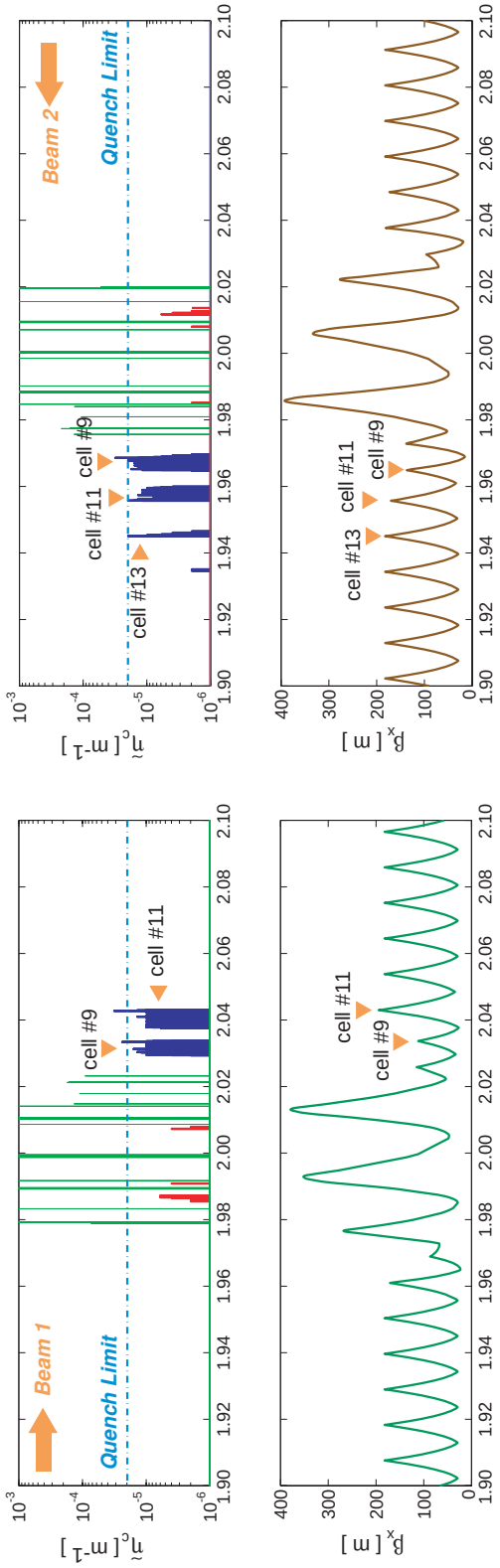

Figure 4.34: Comparison of Beam 1 (left) and Beam 2 (right) loss maps (top two figures) with the β_x functions (bottom two figures) around IP7 at collision energy.

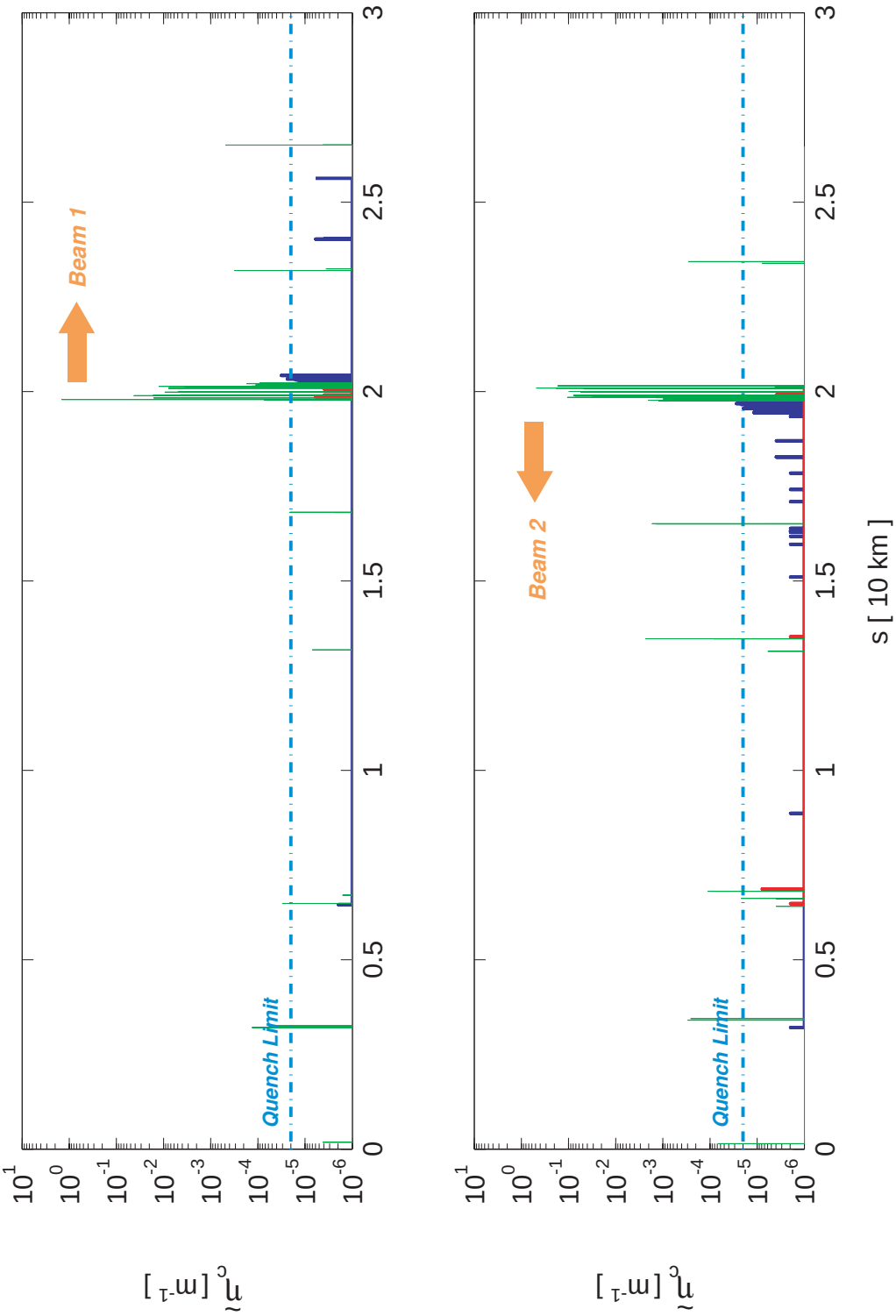

Figure 4.35: Beam 1 (top) and Beam 2 (bottom) loss maps at collision energy for the full Phase 1 collimation system. The simulated halo is vertical.

protons are lost in these elements. Also, for Beam 2, $\beta_x^{B2}(Q13) > \beta_x^{B2}(Q11)$: together with the asymmetry of the dispersion function (shown in the previous section), the protons that still escape the end of the IR7 dispersion suppressor (cells 9 to 11) are lost at the next high β_x(s) and high D_x(s) location. This happens in the Q13 magnet in the collision energy case for Beam 2.

Beam loss maps at collision energy have also been studied for the vertical halo case. This is presented in Figure 4.35: features similar to the ones described above for the horizontal halo were found. Table 4.17 gives the performance level achieved on the Beam 2 line.

Table 4.17: Summary on the performance level reached in the ideal machine case for Beam 2 using the full Phase 1 LHC collimation system. The performance is given by the maximum allowed intensity, derived from the simulated local cleaning inefficiencies in the machine. The limiting factor is stated in bold values.

Case	$\tilde{\eta}^{\mathbf{cold}}_{\mathbf{c,peak}}$ [m^{-1}]	$\tilde{\eta}^{\mathbf{TCDQ}}_{\mathbf{c,peak}}$ [m^{-1}]	I_{max}/I_{nom} [%]
Full Phase 1 collimation system			
450 GeV, horizontal halo	$\mathbf{1.09 \times 10^{-4}}$	1.38×10^{-3}	917.43 ± 126.19
450 GeV, vertical halo	$\mathbf{1.38 \times 10^{-5}}$	8.36×10^{-5}	7246.38 ± 2736.55
7 TeV, horizontal halo	$\mathbf{2.74 \times 10^{-5}}$	1.50×10^{-4}	72.99 ± 19.50
7 TeV, vertical halo	$\mathbf{2.56 \times 10^{-5}}$	5.00×10^{-5}	78.13 ± 21.66

The limitation on beam intensity for Beam 2 is set by horizontal halo losses at collision energy: the ideal machine case tolerates around ~ 73 % of the nominal LHC beam intensity (as given in Table 1.2).

4.5 Study of an imperfection: closed-orbit perturbation

Studies presented in the previous sections of this chapter were performed for an ideal machine, i.e. no gradient field errors, no misalignment of elements and therefore no need to switch on orbit corrector magnets. This section describes the study of cleaning performance with a perturbed orbit. Results for Beam 1 and Beam 2 simulations are discussed, comparing the ideal loss patterns and the maps obtained with a perturbed orbit. The beam halo is generated as for the ideal machine studies: protons are distributed in one plane only (zero distribution in the non-collimated plane) with no energy errors; the bunch length is also set to zero. As mentioned previously, only small differences are expected if one was to perform the same simulations taking bunch length and energy error into account.

4.5.1 Generating the orbit distortion

Perturbations of the closed orbit in a machine can be generated by many causes, like for example misaligned quadrupole magnets. Considering the results presented in sections

4.2 and 4.3, the horizontal plane is the most critical for beam losses. The following study therefore focuses on a *horizontal closed orbit pertubation* at injection and collision energy.

A misaligned quadrupole generates a dipole kick on the beam, hence creating a distortion of the ideal trajectory in the machine. This can be simulated by powering a dipole corrector magnet (steerer). When studying orbit error scenarios, one would like to scan all possible phases for any given amplitude of the perturbation. In order to perform this scan, *two* steerers are used. In first order approximation, the angular kick $\delta x_i'$ given by one of the selected correctors (indexed with i) produces an orbit distortion $x_i(s)$ that writes [70, 71]:

$$x_i(s) = \frac{1}{2\sin(\pi Q_x)} \cdot \sqrt{\beta_x(s) \cdot \beta_x^{K_i}} \cdot \delta x_i' \cdot \cos\left(\pi Q_x - |\mu_x(s) - \mu_x^{K_i}|\right), \tag{4.2}$$

where $\beta_x^{K_i}$ and $\mu_x^{K_i}$ stands respectively for the betatron amplitude and phase advance at the location of the ith steerer. Looking at Figure 4.36, one can see why two steerers allow scanning all phases Φ of orbit error. By selecting two steerers separated by $\pi/2$ phase advance and alternating the sign of each $\delta x_i'$, it becomes possible to achieve all required values for Φ within the interval $[-\pi; \pi]$.

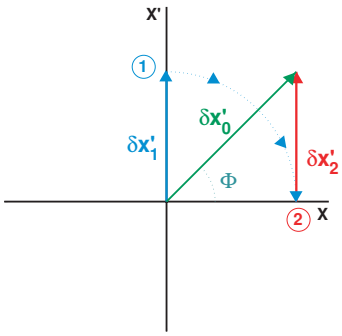

Figure 4.36: Scheme in phase space $x - x'$ of the two-steerer method to generate orbit perturbation in the LHC lattice. The two selected steerers are separated by $\pi/2$ phase advance. The cumulated effect of the two angular kicks $\delta x_1'$ and $\delta x_2'$ is equivalent to having a virtual steerer magnet located at a phase advance Φ from steerer 1 and producing an angular kick $\delta x_0'$.

From equation (4.2), the individual effects of the two corrector magnets are added when calculating the total perturbation Δx:

$$\begin{aligned}\Delta x(s) = &\frac{1}{2\sin(\pi Q_x)} \cdot \sqrt{\beta_x(s) \cdot \beta_x^{K_1}} \cdot \delta x_1' \cdot \cos\left(\pi Q_x - \left|\mu_x(s) - \mu_x^{K_1}\right|\right) + \\ &\frac{1}{2\sin(\pi Q_x)} \cdot \sqrt{\beta_x(s) \cdot \beta_x^{K_2}} \cdot \delta x_2' \cdot \cos\left(\pi Q_x - \left|\mu_x(s) - \mu_x^{K_2}\right|\right).\end{aligned} \tag{4.3}$$

In the LHC, two elements separated by $\sim\pi/2$ phase advance have roughly the same $\beta_{x,y}$

value, so equation (4.3) can be simplified with a unique $\sqrt{\beta_x^K}$. Also, using the example given in Figure 4.36, one can parametrize the two angular kick of the correctors as follows:

$$\begin{aligned} \delta x_1' &= \delta x_0' \cdot \cos(\theta), \\ \delta x_2' &= \delta x_0' \cdot \sin(\theta). \end{aligned} \tag{4.4}$$

Inserting (4.4) in (4.3) yields:

$$\begin{aligned} \Delta x(s) = \frac{1}{2\sin(\pi Q_x)} \cdot \sqrt{\beta_x(s) \cdot \beta_x^K} \cdot \delta x_0' \cdot [\cos\left(\pi Q_x - \left|\mu_x(s) - \mu_x^{K_1}\right|\right) \cdot \cos(\theta) + \\ \cos\left(\pi Q_x - \left|\mu_x(s) - \mu_x^{K_2}\right|\right) \cdot \sin(\theta)]. \end{aligned} \tag{4.5}$$

Since K_1 and K_2 are separated by $\pi/2$, one has $\mu_x^{K_2} \approx \mu_x^{K_1} + \pi/2$. Using this and basic trigonometric formulas, the final expression of the orbit perturbation at any given location s of the machine writes:

$$\boxed{\Delta x(s) = \frac{1}{2\sin(\pi Q_x)} \cdot \sqrt{\beta_x(s) \cdot \beta_x^K} \cdot \delta x_0' \cdot \cos\left(\pi Q_x - |\mu_x(s) - \mu_x^{K_1}| - \theta\right).} \tag{4.6}$$

Ideally, the selected K_1 and K_2 magnets should be located in a region with very small values of the dispersion function to avoid parasitic effects. The magnets finally selected for this study were MCBH.15L4.B1 and MCBH.13L4.B1, two horizontal kickers dedicated to orbit correction in the arc between IR3 and IR4.

To run simulations efficiently, i.e. looking at the largest range of phases and amplitudes for the available amount of CPU time, one had to decide how to scan the $[-\pi;\pi]$ interval. Different LHC lattices and orbits were created using phase steps of $\theta = 30$ degrees, which means running 7 different orbit phases (-180, -120, -60, 0, 60, 120 and 180) to scan a given orbit amplitude. A complete scan with 1 mm amplitude steps was performed for injection, while only the closest case to tolerance requirements was studied at collision energy. Figure 4.37 shows a sample closed orbit perturbation at 7 TeV for Beam 2.

This whole process (phase + amplitude scan) was done following a *static situation*: all collimators are recentered around the perturbed closed orbit. For the nominal optics described in Table 4.2, the closed orbit tolerances correspond to a ± 4 mm perturbation anywhere in the machine except at collision for which the tolerances are reduced to ± 3 mm in the insertion regions[4][72].

4.5.2 Orbit simulation results and implications

The following section will highlight a list of critical loss locations that can be used as a baseline for a minimum workable BLM system for commissionning and early operations of the LHC collimation system. To monitor LHC losses, about 3700 Beam Loss Monitors

[4] For LHC aperture calculations, tolerances are reduced to ± 3 mm everywhere in the machine in the collision energy case.

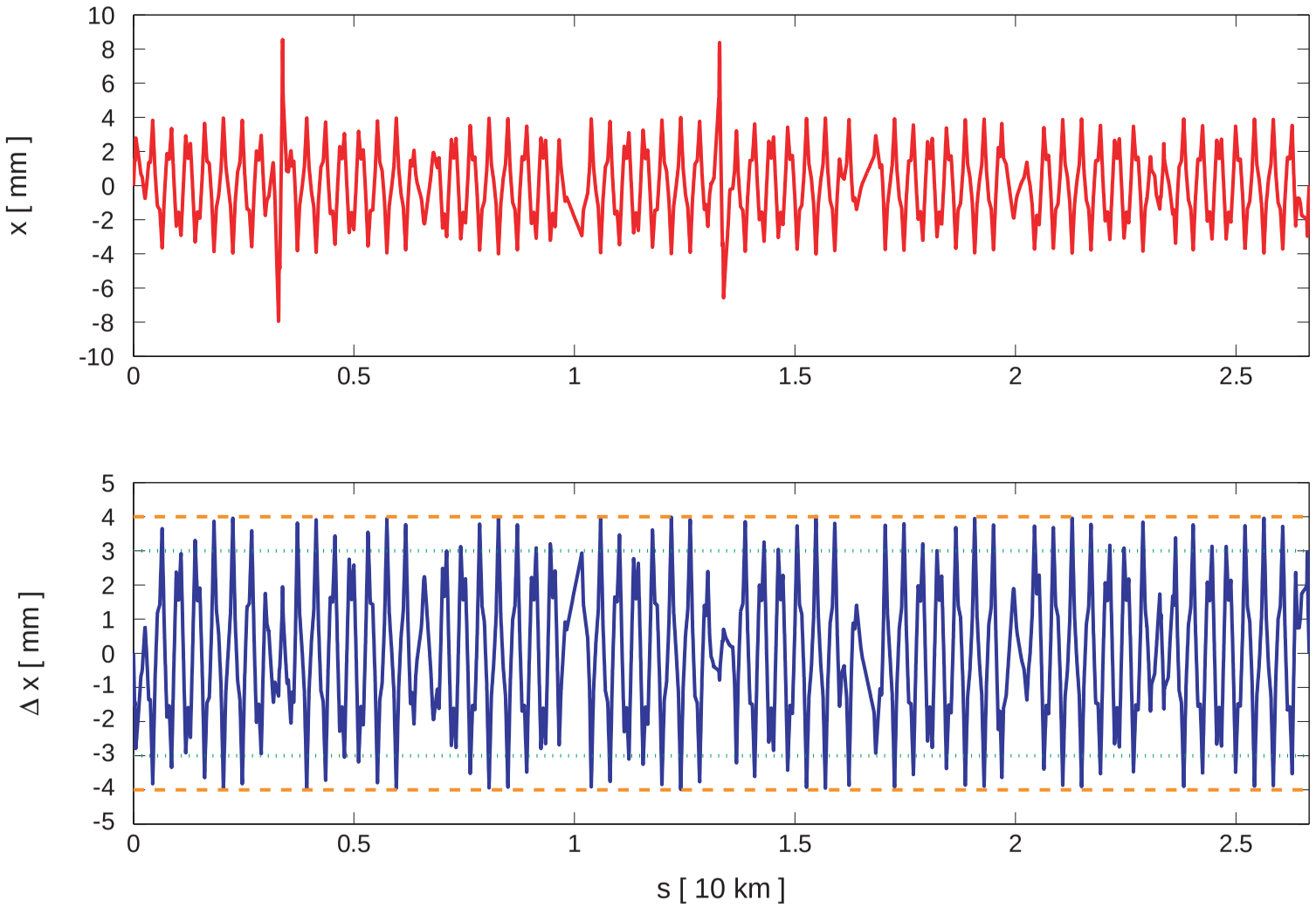

Figure 4.37: Horizontal closed orbit at collision for Beam 2 (top); the orbit perturbation (bottom) was corrected to ± 3 mm (dotted line) in all insertion regions and to ± 4 mm (dashed line) in the arcs.

Table 4.18: Closed orbit tolerances for the nominal optics.

Case	Arc tolerances	IR tolerances
Injection energy	± 4 mm	± 4 mm
Collision energy	± 4 mm	± 3 mm

(BLM's) are being installed in the LHC for the two beams. In the early stages of machine commissioning, the full set of BLM information may not be required. By comparing the ideal machine patterns with the perturbed cases, one can spot the critical loss locations in the superconducting regions of the machine.

Beam 1, injection energy

When scanning over the phases of orbit error, the worst case was selected and then a scan in amplitude was performed. For runs at injection energy, one loss location was already pointed out in section 4.2 as critical: the MCBCH.6R8.B1 magnet, part of the Q6 quadrupole in the IR8 insertion region. The worst phase scenario would therefore be the one for which the level of losses at this particular element gets to its maximum value. Figure 4.38 shows that for Beam 1, the most critical perturbation of the horizontal closed orbit is achieved for a phase Φ of 60 degrees.

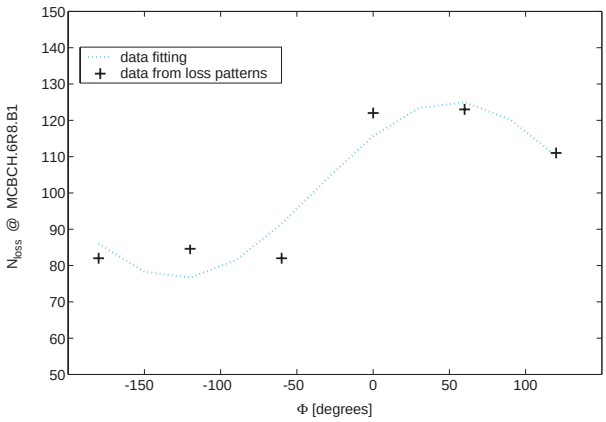

Figure 4.38: Scan in phase of a horizontal closed orbit perturbation at injection energy. The vertical axis gives the number of protons lost at the MCBCH.6R8.B1 magnet, the most critical loss location of the machine. Results are shown for Beam 1. The data taken from simulations was fitted with a regular sin(Φ) function.

Loss maps for the maximum orbit distortion set by the tolerances (± 4 mm) combined with the selected worst phase are shown in Figure 4.39 and do not show major differences with the ideal orbit. The effect of a horizontal closed orbit perturbation is seen better on the level of local losses. Figure 4.40 compares the loss patterns of the ideal and perturbed orbit cases from the IR7 straight section to the position of IP1. At the dispersion suppressor of IR7 and the Q6 magnet in IR8, there is a *loss of a factor 2 in local cleaning inefficiency.* Loss levels at these elements come closer to the quench threshold but still do not cross the

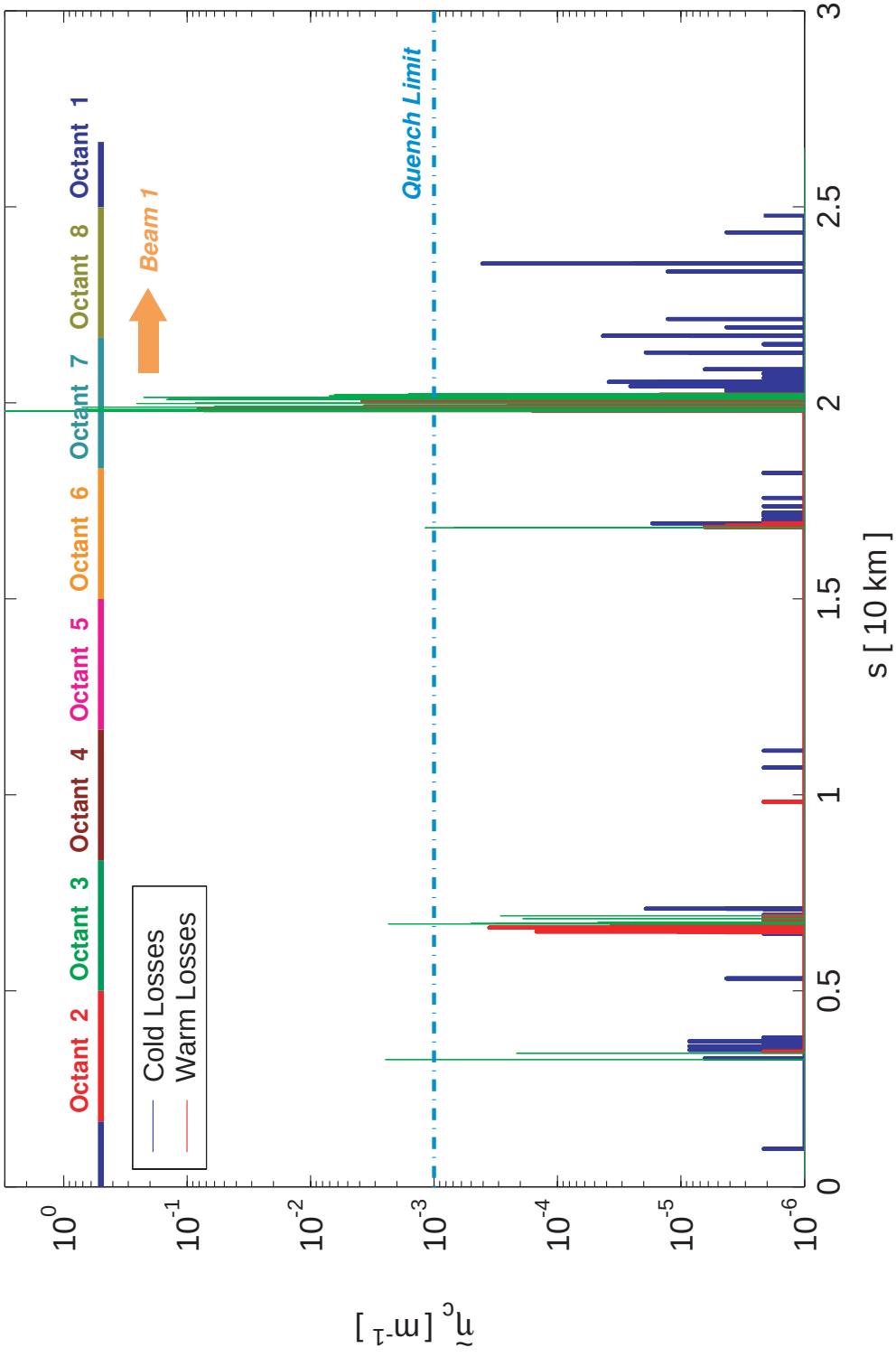

Figure 4.39: Beam 1 loss map at injection energy with the full Phase 1 collimation system for the worst phase of a horizontal closed orbit pertubation of $\pm$ 4 mm amplitude. The simulated halo is horizontal.

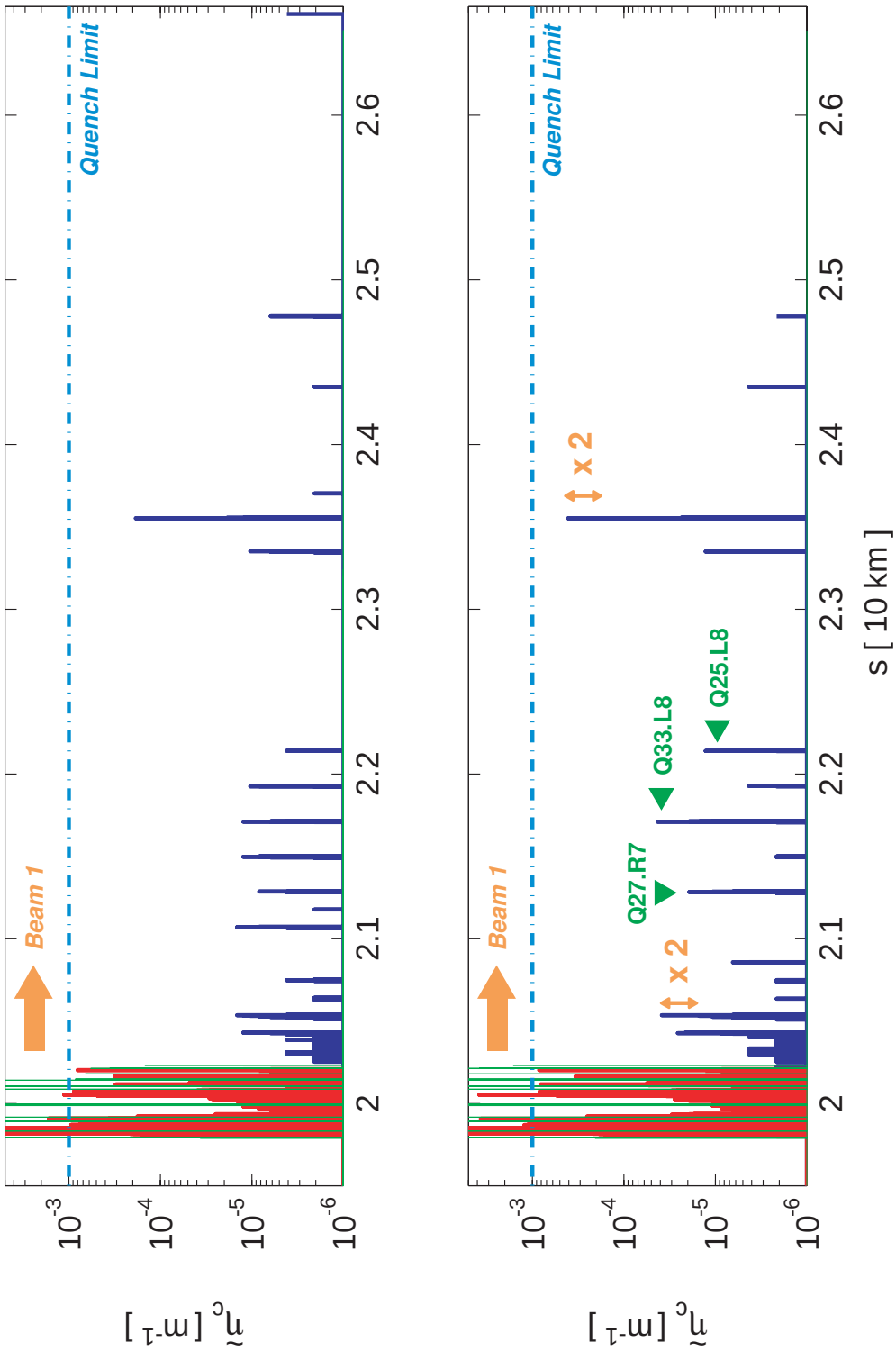

Figure 4.40: Comparison of beam losses for a horizontal halo at injection energy downstream of IR7 between the ideal closed orbit (top) and a ± 4 mm horizontal orbit perturbation (bottom). Results are shown for Beam 1 only.

limit. One can notice that loss locations are identical between the ideal and the perturbed case in this region. Compared to the ideal case summarized in Table 4.7, Table 4.19 shows a factor 2 increase in the number of protons lost per element in the region close to the IR7 cleaning insertion.

Table 4.19: Critical loss locations for a horizontal Beam 1 halo at injection energy using the worst phase of a perturbation in the horizontal closed orbit. The number of lost protons is obtained from the data shown in Figure 4.39 and integrated over the length of each element. Δ refers to the error bar on the inefficiency, as defined in equation (3.11).

Total number of absorbed particles			4674682	
Name	Length [m]	$\mathbf{N}_{loss}$	η_{total} [$\mathbf{10^{-5}}$]	$\mathbf{\Delta}$
MCBCH.6R8.B1	0.9	239	5.11	0.33
MB.C13R7.B1	14.3	213	4.56	0.31
MQML.6R8.B1	4.8	97	2.075	0.21
MQ.11R7.B1	3.1	73	1.56	0.18
MQ.33L8.B1	3.1	50	1.07	0.15

As already mentioned in section 4.2.4, losses in the dispersion suppressor and the first few meters of the arc downstream cannot be avoided, as it corresponds to the first region of high dispersion, catching off-momentum protons generated by the collimator interaction. Orbit errors in the simulations do not remove nor add any other critical loss locations in this area of the machine: *unique characteristic locations* are found for proton losses, as illustrated in Figure 4.40.

Beam 2, injection energy

For Beam 2, the worst phase Φ for the orbit perturbation at injection energy was found to be -60 degrees. Figure 4.41 shows the loss patterns at this phase for the maximum tolerated deviation of $\pm$ 4 mm. Similar features as for Beam 1 are observed: with the perturbed orbit the local cleaning inefficiency is higher by a factor 1.5 (IR7) to 2 (beam screen at the DFBA in the dispersion suppressor of the left side of IP6, see Figure 4.30).

Looking at the summary of integrated losses shown in Table 4.20, one can notice that the highest Beam 2 losses occur in arc elements. This is another consequence of the asymmetry of the dispersion function between the two beams (see section 4.4.1). This feature creates more losses in the region downstream of the IR7 dispersion suppressor, which in Beam 2 direction corresponds to the first cells of arc 7-6. Additional characteristic beam loss locations can be identified from Figure 4.42. This list includes elements of the IR6 beam dump insertion, once again caused by the effect of the extra collimator installed as a complement to the TCDQ dump protection collimator.

For the injection optics, taking into account all critical beam loss locations (including the ones induced by phase values different than the worst overall phase), it was possible to identify 43 elements and magnets (counting both Beam 1 and Beam 2) over the full length

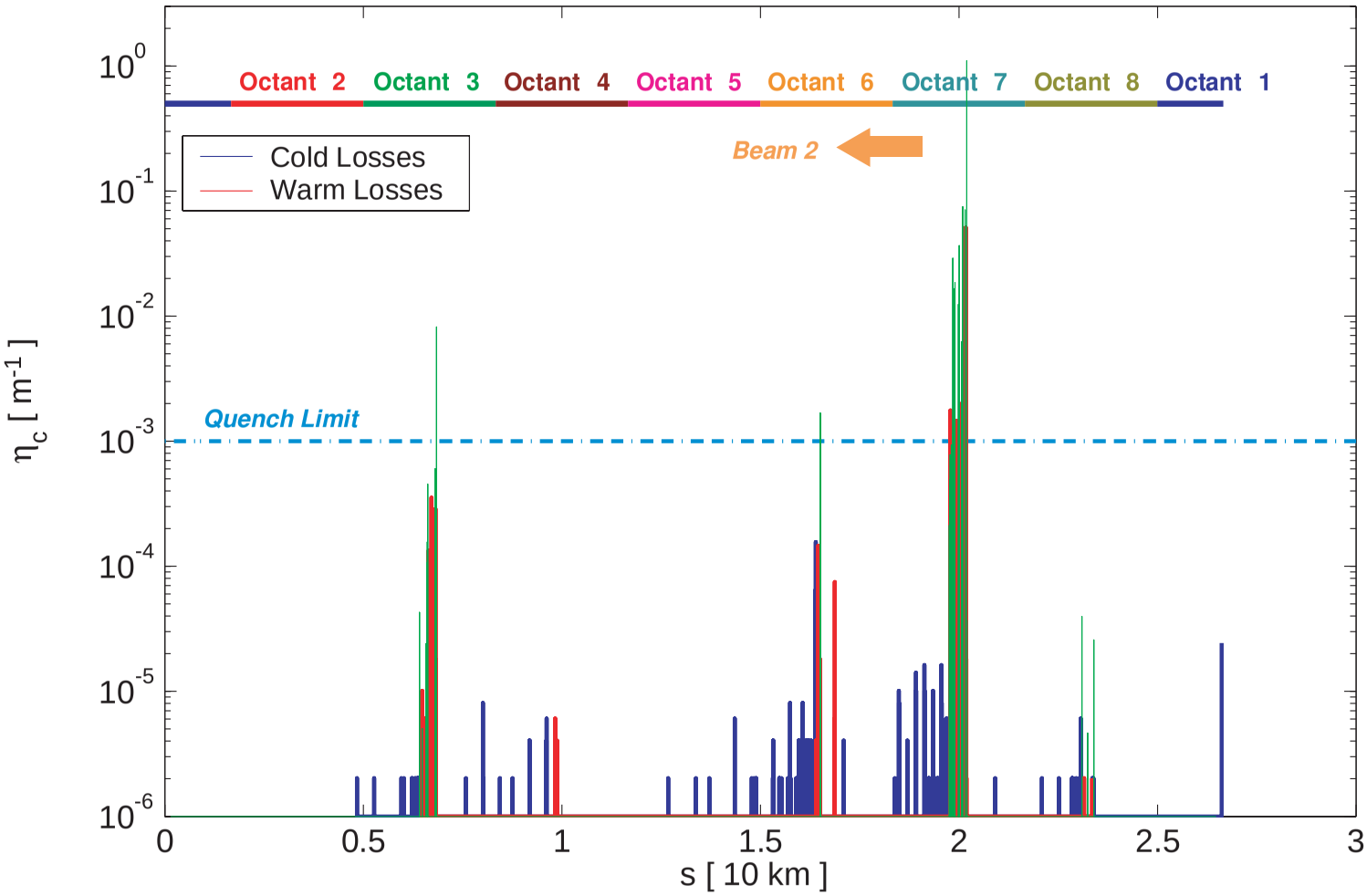

Figure 4.41: Beam 2 loss map at injection energy with the full Phase 1 collimation system for the worst phase of a horizontal closed orbit pertubation of ± 4 mm amplitude. The simulated halo is horizontal.

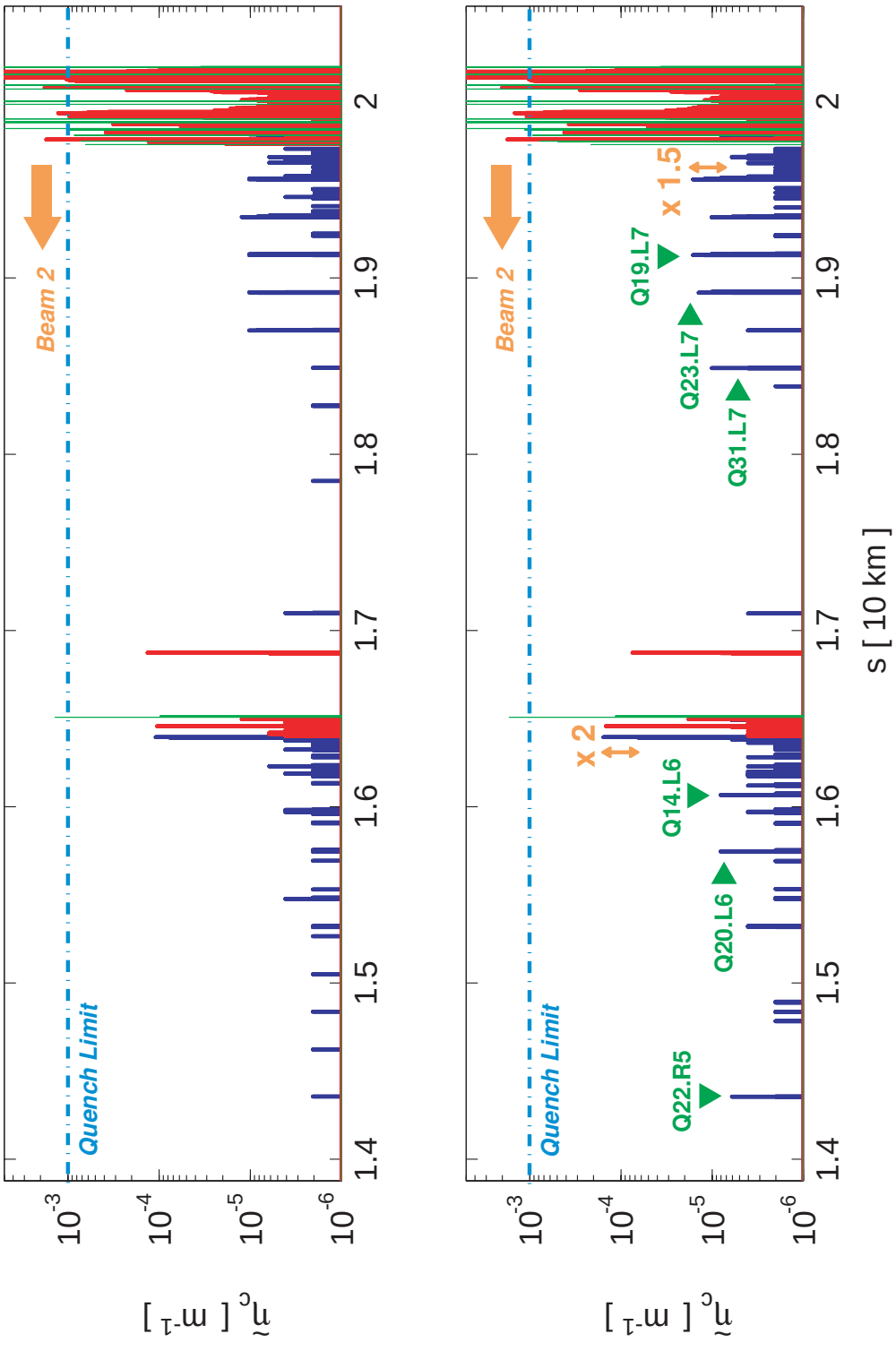

Figure 4.42: Comparison of beam losses for a horizontal halo at injection energy downstream of IR7 between the ideal closed orbit (top) and a ± 4 mm horizontal orbit perturbation (bottom). Results are shown for Beam 2 only.

of the machine. It is suggested that initial operation of the LHC BLM system should cover these locations. The list of critical loss locations can be found in Appendix F.

Table 4.20: Critical loss locations for a horizontal Beam 2 halo at injection energy using the worst phase of a perturbation in the horizontal closed orbit. The number of lost protons is obtained from the data shown in Figure 4.39 and integrated over the length of each element. Δ refers to the error bar on the inefficiency, as defined in equation (3.11).

Total number of absorbed particles			4945798	
Name	Length [m]	$\mathbf{N}_{loss}$	η_{total} [$\mathbf{10^{-5}}$]	$\mathbf{\Delta}$
MB.C19L7.B2	14.3	107	2.16	0.21
MQ.19L7.B2	3.1	52	1.05	0.15
MB.C23L7.B2	14.3	52	1.05	0.15
MQ.11L7.B2	3.1	40	0.81	0.13
MQ.23L7.B2	3.1	38	0.77	0.12

Beam 1, collision energy

At collision energy, it is more demanding to generate a perturbed orbit, as tolerances are different in the arcs and in the insertion regions (see Table 4.18). For every phase studied, a perturbed orbit is created for each case (arc or insertion) and the two files are then merged into a target orbit. Simulations were performed for the maximum deviation amplitudes only, which can be refered to as the *nominal orbit case* as it corresponds to realistic operation conditions.

For Beam 1, the worst phase was found as $\Phi = 60$ degrees. Figure 4.43 shows the distribution of beam losses as obtained with this orbit perturbation. As in the ideal orbit scenario, less loss locations occur along the machine compared to the injection optics case. However at the same time losses reach and extend beyond the estimated quench limit.

Table 4.21: Critical loss locations for a horizontal Beam 1 halo at collision energy using the worst phase of a perturbation in the horizontal closed orbit. The number of lost protons is obtained from the data shown in Figure 4.43 and integrated over the length of each element. Δ refers to the error bar on the inefficiency, as defined in equation (3.11).

Total number of absorbed particles			4745207	
Name	Length [m]	$\mathbf{N}_{loss}$	η_{total} [$\mathbf{10^{-5}}$]	$\mathbf{\Delta}$
MB.A9R7.B1	14.3	305	6.43	0.37
MB.A11R7.B1	14.3	281	5.92	0.35
MB.B9R7.B1	14.3	279	5.88	0.35
MB.B11R7.B1	14.3	246	5.18	0.33
MQ.9R7.B1	3.1	46	0.97	0.14

Comparing the ideal orbit with the nominal closed orbit ($\pm$ 3/4 mm), it can be seen in Figure 4.44 that the most critical loss locations are once again the dipole and quadrupole magnets located in cells 9 and 11 of the IR7 dispersion suppressor.

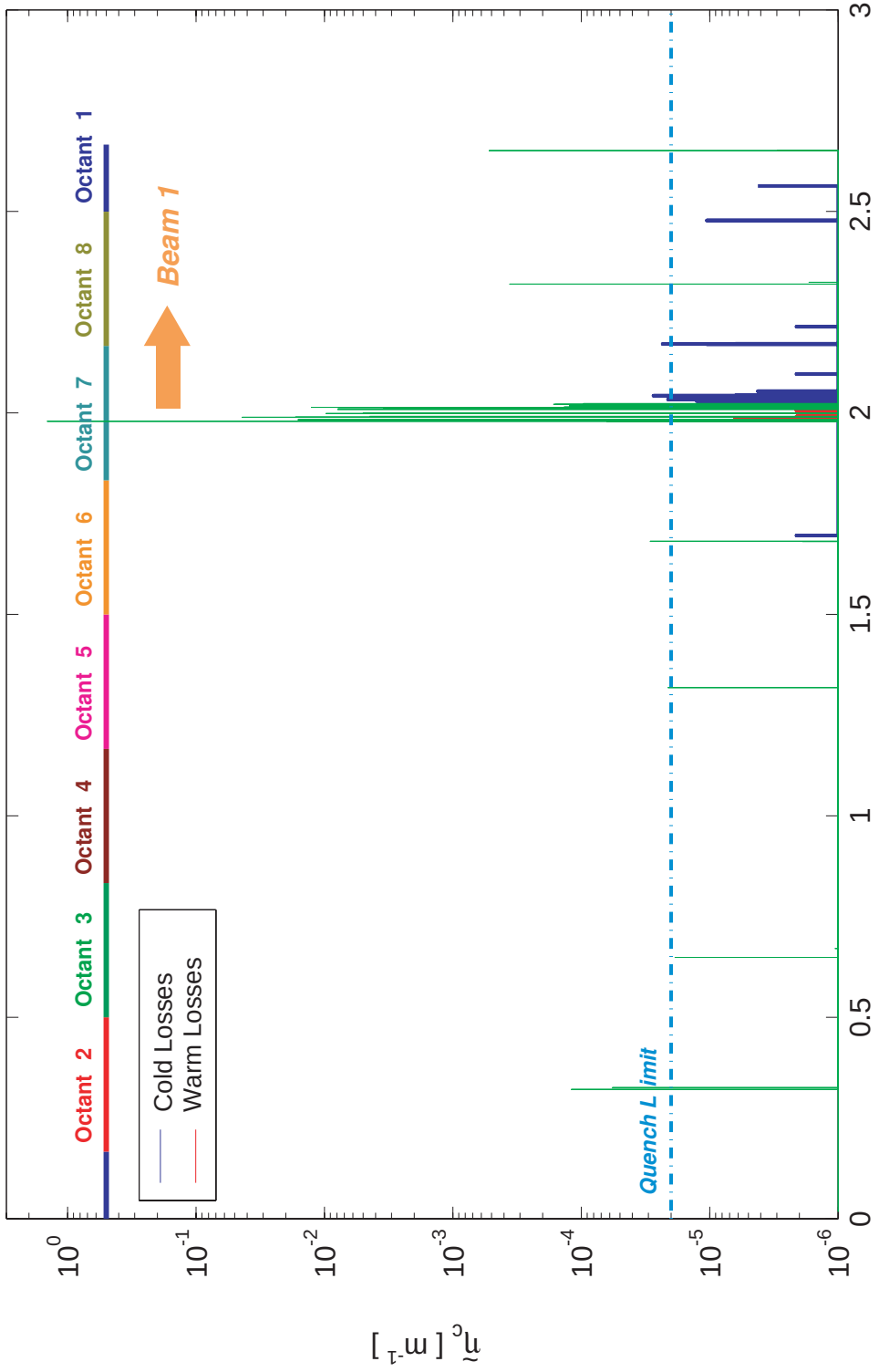

Figure 4.43: Beam 1 loss map at collision energy with the full Phase 1 collimation system for the worst phase of a horizontal closed orbit pertubation of $\pm$ 4 mm amplitude in the arcs and $\pm$ 3 mm amplitude in the IR's . The simulated halo is horizontal.

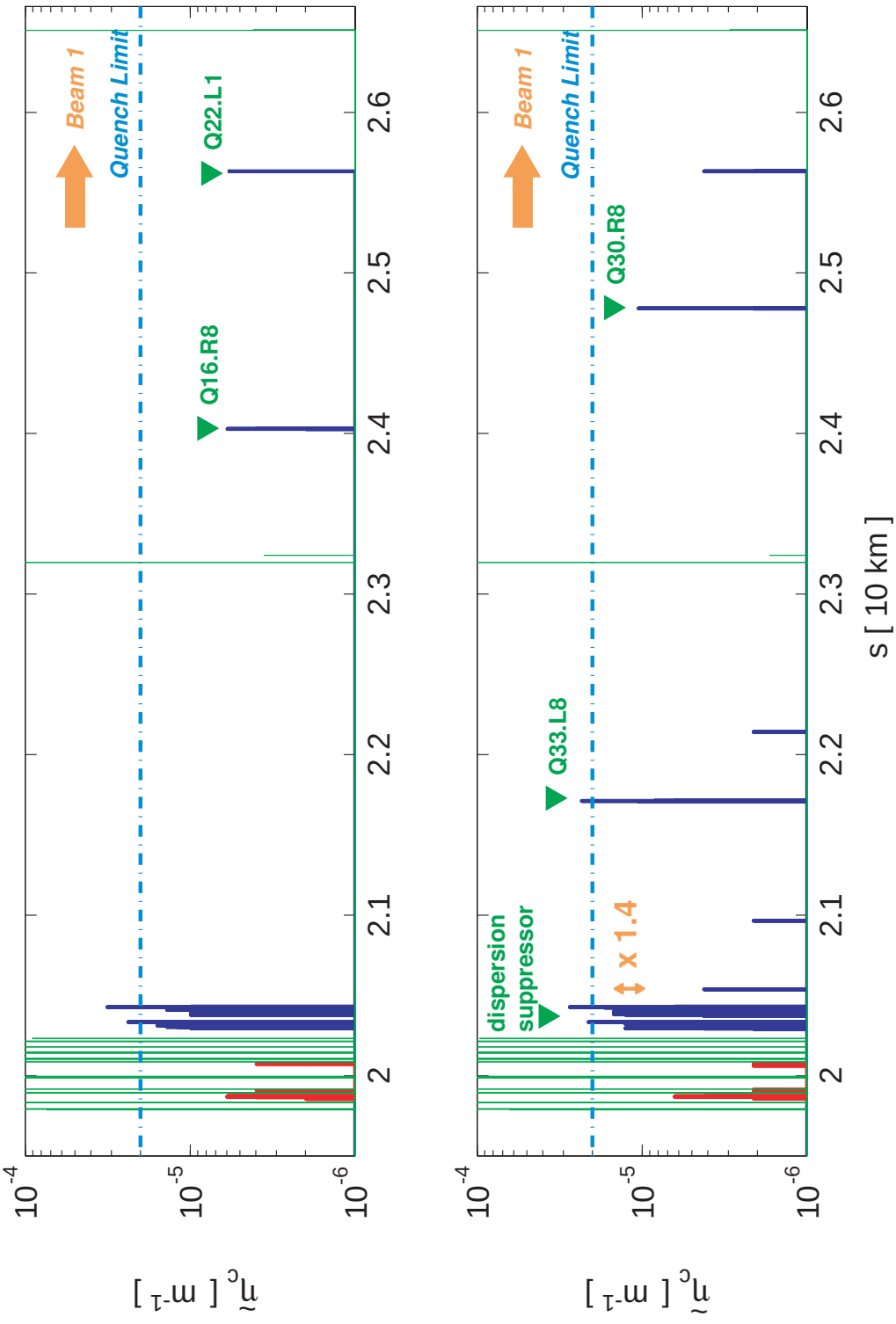

Figure 4.44: Comparison of beam losses for a horizontal halo at collision energy downstream of IR7 between the ideal closed orbit (top) and a horizontal orbit error (bottom). Results are shown for Beam 1 only.

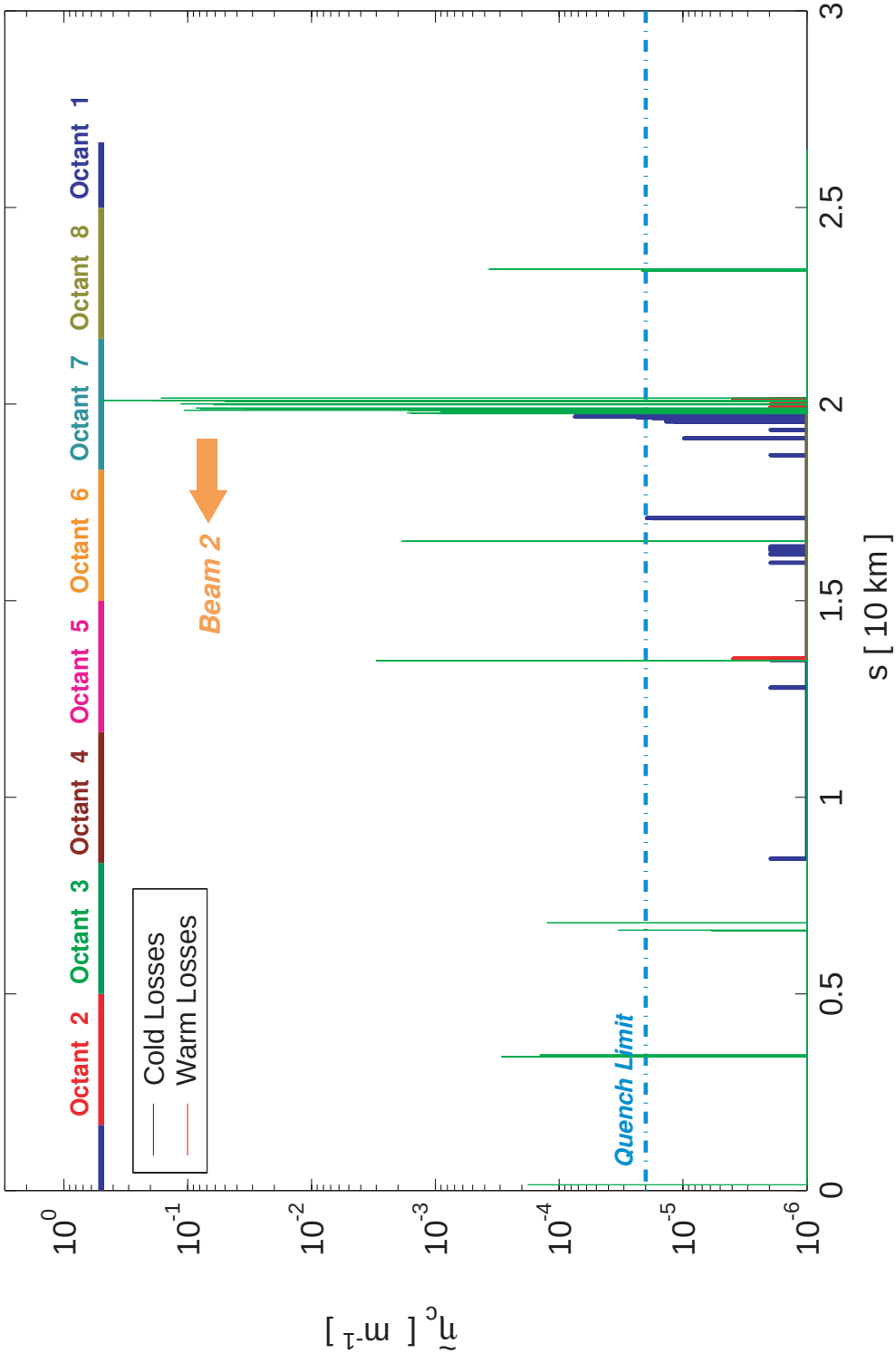

Figure 4.45: Beam 2 loss map at collision energy with the full Phase 1 collimation system for the worst phase of a horizontal closed orbit pertubation of $\pm$ 4 mm amplitude in the arcs and $\pm$ 3 mm amplitude in the IR's . The simulated halo is horizontal.

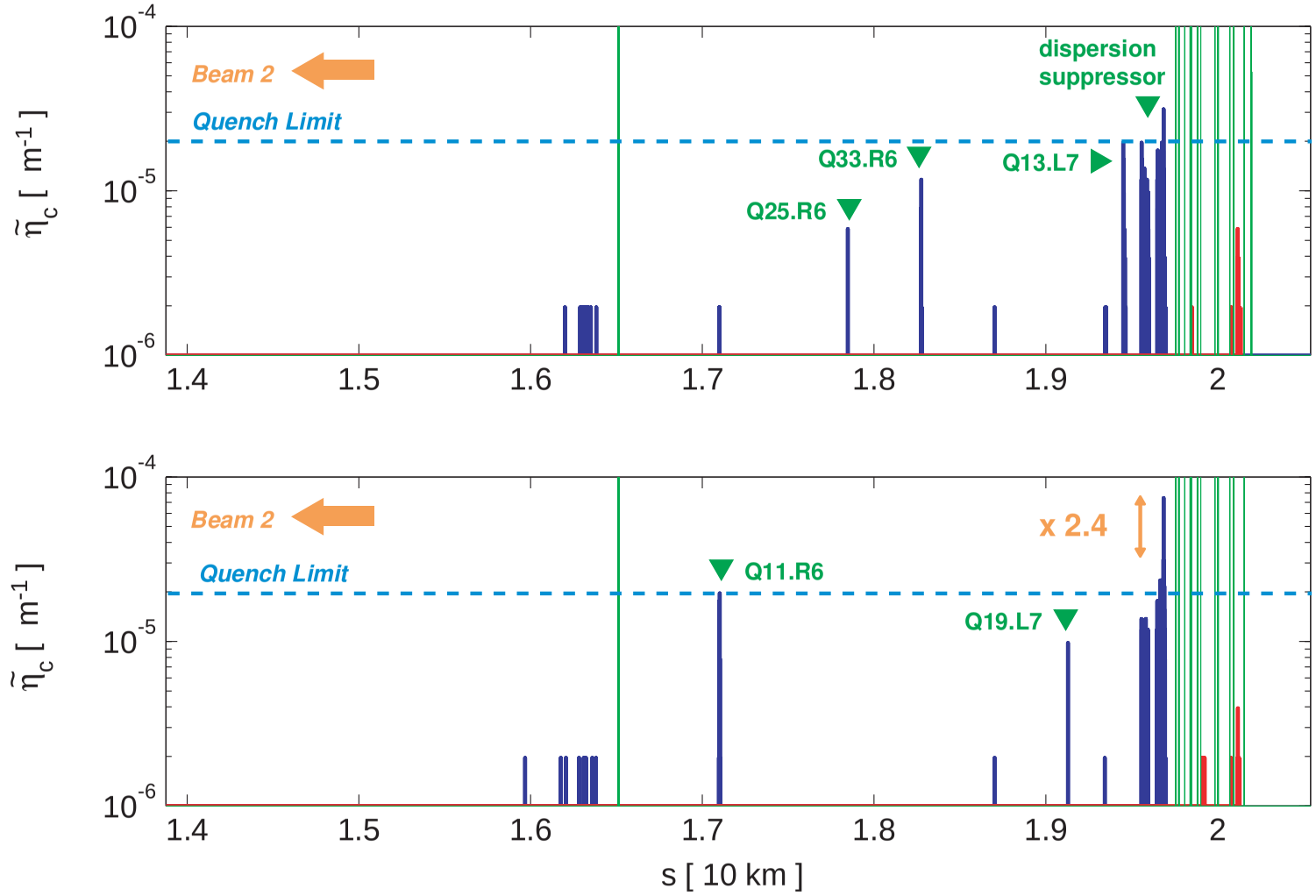

Figure 4.46: Comparison of beam losses for a horizontal halo at collision energy downstream of IR7 between the ideal closed orbit (top) and a horizontal orbit perturbation (bottom). Results are shown for Beam 2 only.

Local cleaning inefficiencies increase by about 40 %. This translates to 10 to 15 % more protons getting lost inside the corresponding overall elements, as listed in Table 4.21 for the perturbed case. New loss locations do appear even reaching the quench threshold, e.g. the beam screen of a Beam Position Monitor (BPM) placed upstream of the Q33.L8 quadrupole assembly. It is noted that the Q33.L8 region was identified in the study of the injection energy scenarios (ideal and perturbed orbit) as a region to be monitored by the LHC BLM system. This remark can be applied to most of the loss locations listed as critical at collision energy; one of the new elements showing a high level of cold losses is the Q30.R8 quadrupole magnet assembly, identified with a green arrow on Figure 4.44 above.

Beam 2, collision energy

The worst phase of orbit error for Beam 2 is Φ = -60 degrees. The loss pattern in Figure 4.46 looks similar to the ideal orbit scenario. No region other than the IR6 and IR7 insertions show beam losses. Therefore a zoom between these two regions is discussed in this section. The cleaning system performances loose up to a factor 2.4 at the dipole magnets of cell 9 at the left side of IP7, resulting in losses up to 3 times over the quench limit. Looking at the cumulated proton losses in Table 4.22, the worst locations are still the MB.A9L7.B2 and MB.B9L7.B2 dipole magnets (30 % more losses than in the ideal orbit case). The Q11.R6 quadrupole magnet in the IR6 insertion is reaching the quench limit, as it is seen in Figure 4.46.

As for Beam 1, most of the critical loss locations found for Beam 2 are identical to the ones identified for injection energy and the ideal orbit (e.g. the Q13.L7 and Q19.L7 quadrupoles). Considering the betatron cleaning collimation system only, 29 elements in total (both beams) must be added to the list of locations that the initial operation of the LHC BLM system must cover to ensure safe machine operation. The list of critical locations for collision energy is reported in Appendix F. It is noted that BLM's at similar locations around IR3 and at the triplet magnets must be added, though not simulated here.

Table 4.22: Critical loss locations for a horizontal Beam 2 halo at collision energy using the worst phase of a perturbation in the horizontal closed orbit. The number of lost protons is obtained from the data shown in Figure 4.46 and integrated over the length of each elements. Δ refers to the error bar on the inefficiency, as defined in equation (3.11).

Total number of absorbed particles			5102476	
Name	Length [m]	$\mathbf{N}_{loss}$	η_{total} [$\mathbf{10^{-5}}$]	$\boldsymbol{\Delta}$
MB.A9L7.B2	14.3	766	15.01	0.54
MB.B9L7.B2	14.3	569	11.15	0.47
MB.B11L7.B2	14.3	324	6.35	0.35
MQ.8L7.B2	3.1	165	3.23	0.25
MB.A11L7.B2	14.3	78	1.53	0.17

4.5.3 Summary on static orbit studies

With the specified LHC orbit errors, critical loss locations were identified and can now be used to define a minimum workable BLM system for the commissioning and set-up

of the collimators during the early stages of LHC operation. The dispersion suppressor immediately downstream of IP7 is the most critical region of the machine, with many losses concentrated over a few elements. Table 4.23 gives the update on performance reach for a machine with nominal orbit (± 3/4 mm orbit error). As in the non-perturbed case, limitations on maximum beam intensity are addressed by collision energy runs.

Table 4.23: Summary on the performance level reached at collision energy for the worst phase of horizontal closed orbit perturbation using the full Phase 1 LHC collimation system. The performance is estimated from the maximum allowed intensity derived from the simulated local cleaning inefficiencies in the machine. The limiting factor is stated in bold values.

Case	$\tilde{\eta}^{\mathbf{cold}}_{\mathbf{c,peak}}$ [m^{-1}]	$\tilde{\eta}^{\mathbf{TCDQ}}_{\mathbf{c,peak}}$ [m^{-1}]	$\mathrm{I}_{max}/\mathrm{I}_{nom}$ [%]
Injection energy			
Beam 1	$\mathbf{4.06 \times 10^{-4}}$	1.18×10^{-4}	246.31 ± 17.88
Beam 2	$\mathbf{1.56 \times 10^{-4}}$	1.68×10^{-3}	641.03 ± 72.97
Collision energy			
Beam 1	$\mathbf{4.12 \times 10^{-5}}$	4.94×10^{-5}	48.54 ± 10.59
Beam 2	$\mathbf{7.45 \times 10^{-5}}$	1.75×10^{-4}	26.85 ± 4.35

4.6 Predicted cleaning performance

Simulations were performed for the first time with state-of-the-art tracking tools for the two LHC beams. The full Phase 1 collimation system was used for both the ideal machine and the machine with nominal orbit scenario (i.e. orbit error at the maximum of tolerances, ± 3/4 mm over the machine). Table 4.24 gives an overview of the beam intensity limitations in all cases studies (for both Beam 1 and Beam 2); the minimum beam lifetimes τ are stated for each scenario considered. The proton loss rates are derived from the quench levels for each beam energy as stated in [48]: $R_q^{inj} = 7 \times 10^8$ protons/m/s and $R_q^{coll} = 7.6 \times 10^6$ protons/m/s.

At injection, no limitations are seen; one can nevertheless notice a reduction of more than a factor 2 when taking the nominal orbit into account. For collision energy, the maximum allowed intensity is ~ 37 % lower in realistic orbit conditions compared to predictions in the ideal orbit case, and $I_{max} = 0.27 \cdot I_{nom}$. This is calculated with simplified quench limits, therefore I_{max} could get even more reduced with detailed quench models.

In addition, only error models for closed orbit perturbations were applied so far. Future studies will include nominal β-functions error, coupling between the two transverse planes, non-linearities of the superconducting magnets and collimator offsets (off-center gap and/or longitudinal tilt) with respect to the closed orbit. Preliminary estimates have been already made for some of these scenarios [46]. To go beyond the limitations on the maximum beam intensity, the use of the LHC Phase 2 Collimation System seems to be required, especially when considering the plans for running the machine with ultimate intensity parameters (2808 bunches of 1.6×10^{11} protons, 40 % more than I_{nom}).

Table 4.24: Summary on the performance level for different machine scenarios using the full Phase 1 LHC collimation system. The performance is estimated in both maximum allowed intensity and maximum allowed loss rate R_{loss}^{max}. The limiting factor is stated in bold values.

Scenario	**Energy** [TeV]	$\tilde{\eta}_{\mathbf{c,peak}}^{\mathbf{cold}}$ [10^{-5} m^{-1}]	τ [h]	I_{max}/I_{nom}	$\mathbf{R_{loss}^{max}}$ [10^{10} protons/s]
Ideal machine	0.45	18.65 ± 1.96	0.1	5.38 ± 0.57	376.34 ± 39.72
	7.00	4.60 ± 0.96	0.2	0.43 ± 0.09	16.52 ± 3.44
Ideal machine	0.45	40.60 ± 2.95	0.1	2.46 ± 0.18	172.41 ± 12.51
with nominal orbit	7.00	7.45 ± 1.21	0.2	0.27 ± 0.04	10.20 ± 1.66

4.7 Complementary studies

The extended version of SixTrack makes it possible to produce estimates of the operational conditions in the LHC machine. Some of the data obtained can be used in other analysis and in programs like FLUKA for calculations of deposited energy. This section reviews the studies done in parallel with the tracking effort previously presented.

4.7.1 Energy deposition studies: FLUKA simulations

The FLUKA software [50] is a fully integrated particle physics MonteCarlo simulation package. FLUKA has many applications in e.g. high energy experimental physics, engineering and shielding (among others). For studies in the LHC Collimation Project, FLUKA is being used to analyze data from the collimation scattering routines and to determine which elements receive most energy and dosse. This is done by simulating particle showering induced by the inelastic interaction of beam halo protons in the collimator jaws. These studies are critical in the cleaning insertions but also for regions dowsntream of the tertiary collimators (triplet magnet assemblies) and the beam dump protection equipment. For this latter case, most of the simulations are performed using dedicated error scenarios instead of data coming from "regular" simulation runs.

Cleaning-induced showers propagating in IR7

Design beam losses of up to 0.5 MW can occur in the betatron cleaning insertion IR7. It is essential to understand where this power goes. In the tracking code, a particle is considered as "lost" if the interaction between this particle and the collimator jaw material is determined as *inelastic* by the Monte Carlo routines. The program then stops tracking that particle and dumps its coordinate inside the jaw material into a dedicated file: this is the file that gets passed to the FLUKA simulation team. A 3D model of the IR7 cleaning region was set up so that FLUKA can calculate and track the showers induced by all the inelastic interactions recorded during the SixTrack runs. During this thesis, many input

datasets for FLUKA studies were provided. A few highlight results are reviewed.

The results obtained were particularly useful when trying to determine the most adequate position for the additional absorbers, to be installed immediately downstream of the secondary collimators. By checking the radiation levels in some critical elements, one could do iterations on the locations of the absorbers and set the optimal number of required elements and their longitudinal distribution in the straight section.

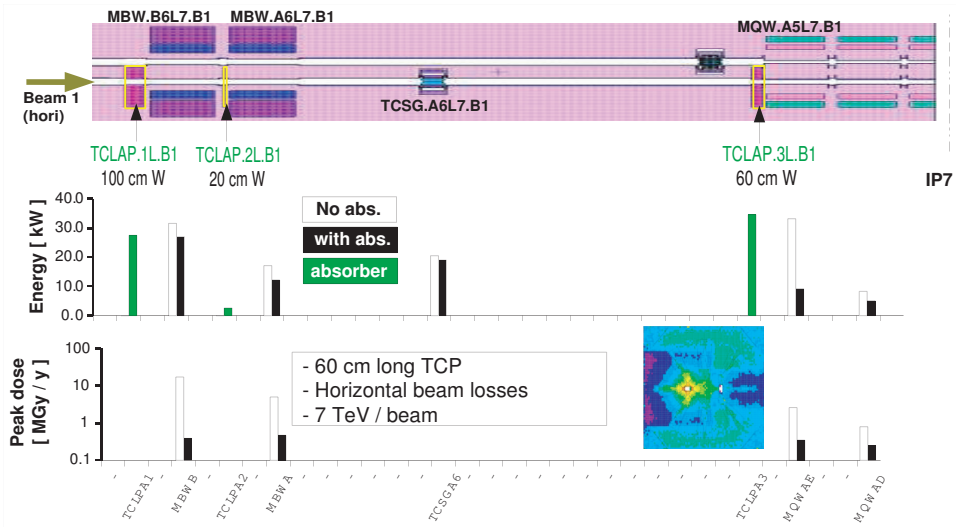

Figure 4.47: Longitudinal distribution of energy deposited by particle showers from collimators and absorbers of IR7 for Beam 1. The results shown with the white histogram bars highlight the need of additional passive protection (labeled as "absorbers" in the legend of histograms) and their effect on dose levels can be seen with the black bars. Courtesy of M. Magistris.

Figure 4.47 shows the longitudinal distribution of the deposited energy (in kW) along with peak dose rates (in MGy per year) for a series of magnets downstream of the IR7 primary collimators. Values are given for the collision energy case (7 TeV). The radiation limit for the warm IR7 magnets is set to a maximum dose of 50 MGy. The replacement of magnets is foreseen after 10 years of nominal operation and the maximum tolerated dose per year is 5 MGy. The histogram with white bars shows that even with the addition of active absorbers (and their multi-turn absorption power) the peak dose rates for some elements is still very high and reaches 20 MGy/y in one warm dipole magnet on the left of IP7 (MBWB.B6L7.B1).

This feature highlights the need of additional *passive absorbers*, which consist of blocks of material (copper or tungsten, to be still determined) with fixed apertures (hence the "passive" qualification). These elements act as shielding and are implemented a few meters upstream of the magnets with the highest dose rates. The black histograms in Figure 4.47 show that at the worst element the peak dose rate is reduced by about a factor 40, down to 0.5 MGy/y. All other critical magnets downstream present dose rates lower than 1 MGy/y, and the deposited energy is significantly lowered after the third passive absorber.

Showers propagating in the IR6 beam dump region

As seen in section 4.4, the IR6 straight section shows high level of local losses on Beam 2, due to the collimators (two TCDQ and one TCS) for protection against malfunctions of the beam dump system. Figure 4.48 is a 2D representation of the model used in FLUKA for IR6 energy deposition studies.

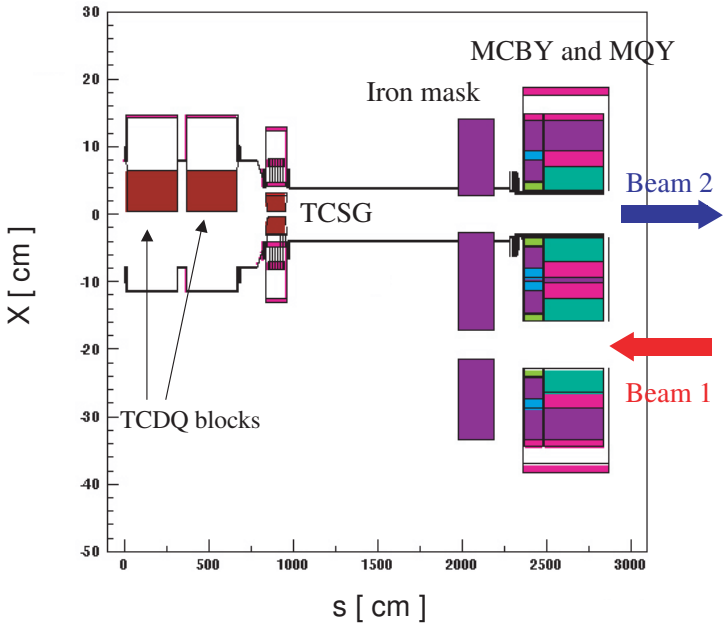

Figure 4.48: 2D FLUKA model of the region in the IR6 straight section where the collimators for beam dump protection are implemented. Studies are done for Beam 2. Critical magnets are indicated. Courtesy of L. Sarchiapone.

Studies of deposited energy in critical elements allow checking the margins with respect to the quench limits for nominal operation scenarios. In Figure 4.49 the case of the first two magnets after the IR6 collimators is presented. Two parameters have to be checked: the local peak energy density and the total power deposition. In both cases, analysis of data files produced from SixTrack lead to heat loads below the estimated quench limits (5 $\mathrm{mW.cm^{-3}}$ for local peaks, 20 W for total energy deposition). Tests for magnet quench in real operation conditions are still underway at CERN. The estimated quench values may be revised from one magnet type to the other. Depending on these results, the nominal jaw openings of the secondary collimator close to the TCDQ might need to be modified accordingly.

4.7.2 Background in experimental insertions

The main goal of the LHC is to find proofs of the existence of the Higgs boson. It is planned to be done thanks to two of the biggest detectors built so far for particle physics, the ATLAS and CMS detectors [2, 4]. With a design luminosity of 10^{34} $\mathrm{cm^{-2}s^{-1}}$, operating

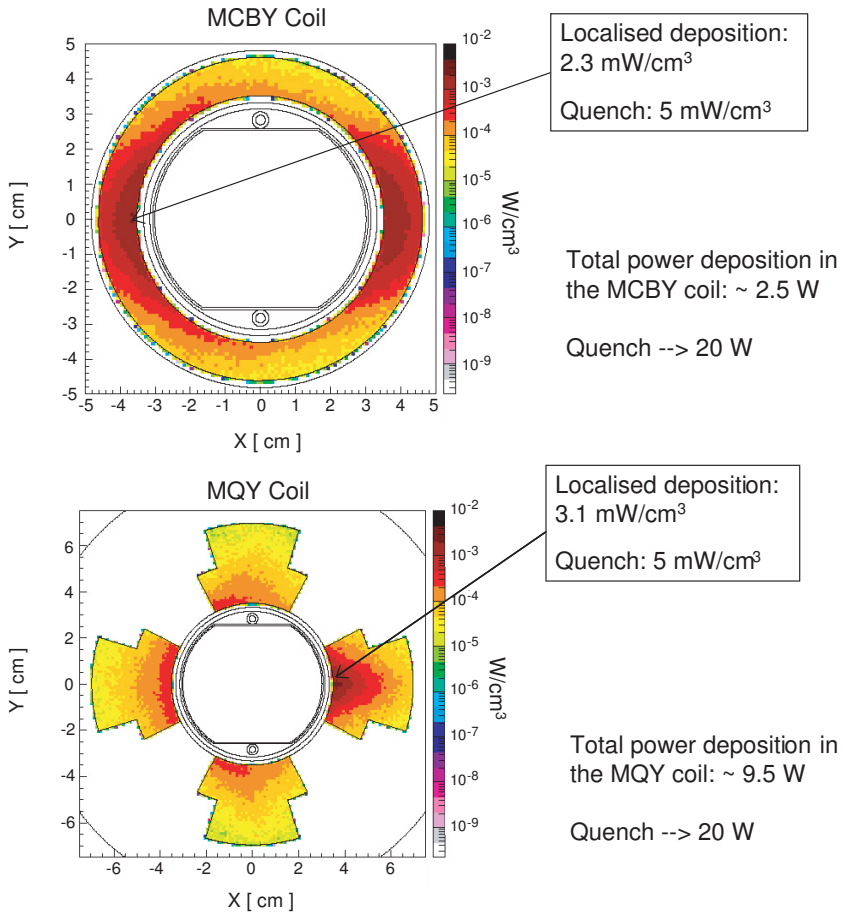

Figure 4.49: Transverse map of energy deposition in the MCBY (top) and MQY (bottom) magnets donwstream of the beam dump collimators. These two magnets are part of the Q4 quadrupole magnet assembly downstream of IP6. Each plot gives the peak deposited energy and compares it with the estimated quench threshold for the considered element. Courtesy of L. Sarchiapone.

the machine for one year (roughly 10^7 seconds of running time) will produce about 10^{16} events, out of which about 1000 are expected to correspond to a "Higgs" event. According to what can be read in [73], a Higgs discovery can only be claimed if at least 25 of the corresponding events are detected. During the counting process, many parasitic effects get in the way, and on top of them are *background events* i.e. events which produce a signal very similar to the expected one. In the LHC case, the *machine induced background* [74] is coming from particles showering due to proton losses in the tunnel that reach the detector region. To get rid of this "experimental noise", the data collected from ATLAS and CMS is cross-checked with some characteristic requirements e.g. the energy of the decay particles and/or their spacial distribution [75]. Real "Higgs" event might be eliminated from the datasets due to these requirements, which means more data is required from the detectors.

One can list three main sources of machine induced background in the LHC case [74]:

- interaction of circulating particles with residual gas in the vacuum chamber,

- particle showers induced by inelastic interactions of secondary/tertiary halo protons (leaking from the cleaning insertions) either within the jaw material of a given collimator or when lost in one of the aperture limitations of the lattice,
- debris from collisions in neighboring interaction points, especially true when considering the consecutive IP8, IP1 and IP2 points.

Compared to preliminary estimates of collimation induced background, the design of the cleaning system changed by including tertiary collimators (TCT) in front of the triplet magnet assemblies at each experimental insertion. Since the experimental insertion of IP8 is for Beam 1 the closest IR downstream of the IR7 celaning region, it might experience the highest level of tertiary background. To determine how critical this level can be, tracking data from the extended SixTrack version was used, containing the 3D coordinates of all proton-matter inelastic interactions within the TCT jaws (the same way as it is already done for FLUKA studies). Cascade simulations in the Beam 1 direction were performed and results can be compared to previous estimates for the beamgas background [74]. Table 4.25 lists the various fluxes of considered showering particles.

Table 4.25: Tertiary background flux in particles per second for charged hadrons and muons from the tertiary collimators of the IR8 insertion. Considered is a "realistic" worst case scenario for beam halo. Values are given with and without the full shielding configuration planned around the detection region. Courtesy of V. Talanov.

Case	**Collimator type**	**Charged hadrons [particle.s^{-1}]**	**Muons [particle.s^{-1}]**
Without shielding	TCTV	5.9×10^6	1.8×10^6
	TCTH	9.0×10^4	4.8×10^4
With shielding	TCTV	6.2×10^4	5.1×10^5
	TCTH	3.5×10^2	2.4×10^4

The shielding mentioned in the caption of Figure 4.50 is a 80 cm concrete wall, followed by a 80 cm iron plus 120 cm concrete wall, located upstream of IP8 in Beam 1 direction. As seen in Figure 4.50, the inclusion of shielding between collimators and the detector region allows reducing most of the background induced by charged hadrons by two orders of magnitude, while a factor 2 to 3 reduction can be noticed for muons. When comparing the new results obtained from collimation tracking with previous estimates on other machine induced sources, one can note that beam-gas background is dominant for small distances away from the center of the beam line when shielding is used. Muons take over as the main background source for radii larger than 120 meters.

It is noted that the rates of showers issued from tertiary collimators (listed in Table 4.25) were calculated with a beam lifetime of $\tau = 30$ hours. For the minimum beam lifetimes tolerated for LHC collimation related issues (see Table 2.5), one should expect a significant increase since the tertiary background level is directly related to the loss rate at the IR7 primary collimator jaws and since smaller lifetimes mean higher loss rates. Even though these minimum beam lifetimes should only occur occasionally during a physics fill of the

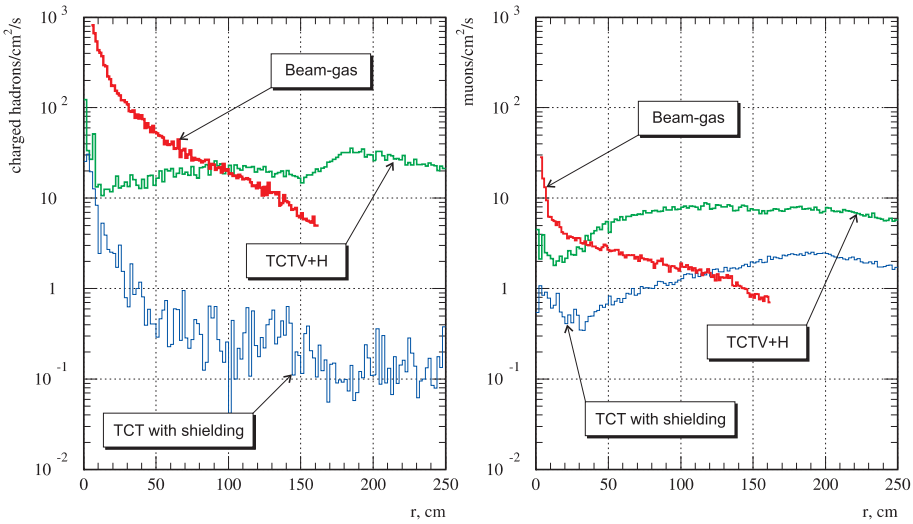

Figure 4.50: Radial distribution of the flux density of charged hadrons (left) and muons (right) responsible of the machine induced background issued from the tertiary collimators in the IR8 region. The data is taken from simulations at the entrance of the LHC$_b$ cavern. The effect of adequate shielding on showers from the TCTs is shown. Beam-gas data is given as comparison. Courtesy of G. Corti and V. Talanov.

LHC and last for not more than 10 seconds, the tertiary background might become the main source of machine induced background over that period of time.

Chapter 5

Collimator prototype test in the SPS with LHC beam conditions

A prototype of a LHC secondary collimator was installed in the SPS (Super Proton Synchrotron), CERN's second biggest accelerator, and tested with realistic LHC beam conditions. It allowed testing most of the design features that are required for LHC operations, including possible commissioning procedures like beam-based alignement. The external components could also be tested, like the beam monitoring system and the temperature sensors.

This chapter reviews the main result of these beam tests, from the signal acquisition of the beam loss monitors (BLM's) and how they have been used with the jaw alignment procedure to the analysis of the data from temperature sensors and their comparison to simulations.

5.1 Setup of the prototype test

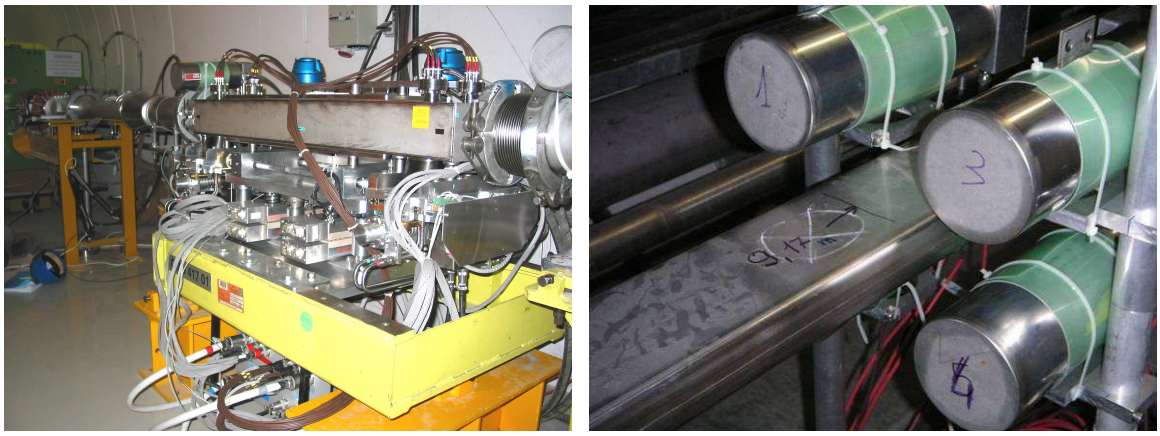

Figure 5.1: Collimator prototype (left) and dedicated BLMs (right) installed in the SPS ring.

Tables 5.1 gives the reference parameters for the two types of runs performed during the tests. Once the collimator prototype was positioned in the Point 5 region of the SPS main ring, the setup of the control system could start along with the calibration of all sensors (temperature, motor movement). This stage is particularly critical since the collimator operator needs to have a good reading of the jaw positions during the alignment procedure (described in a section below). An adequate BLM system was also implemented in order to measure and record the effect of the movement of the jaws on the losses of the circulating beam. Figure 5.1 shows the collimator and its associated BLMs once installed in the machine.

Table 5.1: Beam conditions during the SPS tests of a collimator prototype.

Beam parameter	**Low intensity**	**High intensity**
Bunch population	1.1×10^{11}	
Number of bunches	1-16	288
Energy	270 GeV	
Emittance	~ 1 μm	~ 3.75 μm
Horizontal beam size at collimator	~ 0.4 mm	~ 0.7 mm

5.1.1 The collimator control software

The mechanical design of the LHC collimators, shown in Figure 3.6, includes four motors at each corner of the tank (2 per jaw), all controlled individually. This allows for longitudinal alignment of the jaw with respect to the shape of the circulating beam and independent movement of each jaw. The remote control of the opening of LHC collimators is done using a dedicated software. It relies on the readings of the various sensors and monitors located on the moving table indicated on Figure 5.2. The setup allows getting a fixed reference for the collimator gap opening by making one of the sensors measure the interval between the two jaw supports.

The control software allows moving the jaws in a variety of ways:

- amplitude of movement: by motor steps ($\sim$ 10 μm), direct position value or half-opening value to reach,
- single motor movement (for longitudinal tilt adjustment),
- single jaw movement,
- symmetric two jaws movement (gap closing),
- asymmetric two jaws movement (gap recentering).

In order to avoid a wrong manipulation of the jaws, mechanical switches are installed to stop the movement in extreme cases. The two extremes considered are the "fully opened" and the "minimum gap" positions, which were determined by defining a maximum outside position and limiting the displacement amplitude of each jaw to 35 mm. If the command

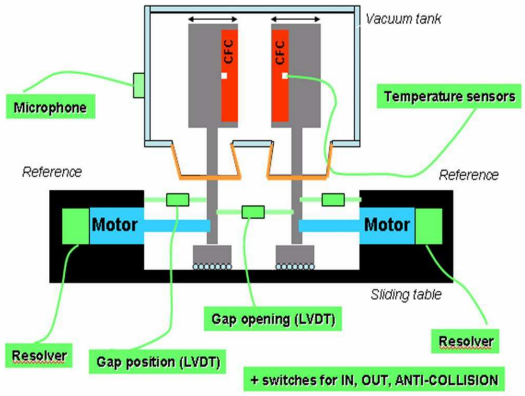

Figure 5.2: Schematic of the sensors and controllers installed around a collimator tank. The gap position and gap opening magnetic sensors (LVDT) are installed on the moving table that supports the jaws. Courtesy of R. Assmann.

entered would make any jaw go over one of the switches, the software lets the jaw reach the switch and then triggers a motor stop. This feature will be complemented by another triggering coming from the BLM system that will automatically react if the level of losses gets too high and would mean risks of damages on the jaw material.

5.1.2 The BLM data acquisition system

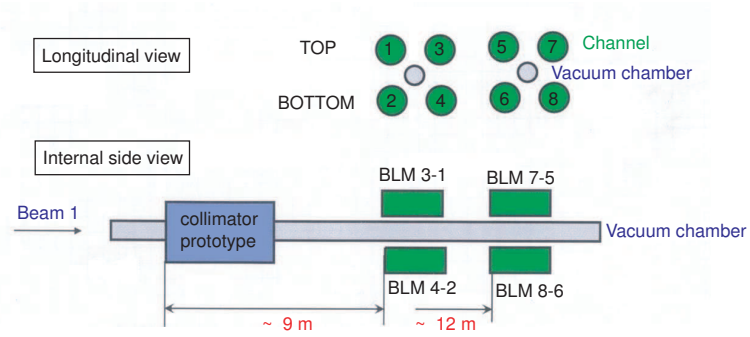

Figure 5.3: Schematic of the transverse and longitudinal locations of the BLM's dedicated to the SPS tests of a prototype LHC secondary collimator. Courtesy of B. Holzer and L. Ponce.

Two sets of 4 beam loss monitors (BLMs) were installed around the vacuum chamber according to what is shown in Figure 5.3. Two different resolutions were available for the electronic chambers of each BLM, so as to adapt to the two beam intensities planned for the tests (see table 5.1). From the transverse distribution of BLM's around the vacuum pipe, one can see that the four channels can be combined to give information on the level of losses for each jaw individually. Since the tested prototype was installed as a horizontal collimator, it is useful to look at the cumulated losses on the left and right sides separately. The 8 BLMs are splitted into two groups, with one group being assigned the lower value of

resolution while the other working with the higher value; most of the time the lower value is assigned to the BLMs closest to the prototype.

The data from the BLMs' electronics is received on one of the control room computers and treated by a real-time plotting software [76]. It allowed performing the alignment and centering of the jaws with respect to the beam: moving one of the jaws, the moment it touches the edge of the beam corresponds to a steep increase in the BLM's signal. Due to betatron motion, both sides of the beam get cut into sharp edges. To get a centered gap, one would therefore have to start moving the other jaw until losses can be observed on the real time curves. The precision of this process, illustrated in Figure 5.4, is then equivalent to the step size of the motor. As previously mentioned, one of the modes of jaw movement includes moving only one corner at a time: doing so would allow adjusting the jaw angle with respect to the beam envelope.

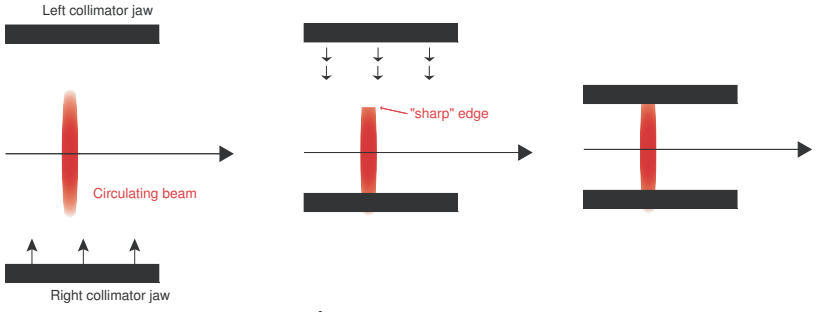

Figure 5.4: Centering procedure for the collimator jaws as applied during the SPS beam tests. A jaw is moved towards the beam until it scrapes it, generating a "sharp-edged" beam. The other jaw is then sent in direction of the beam and is stopped when the signal from BLM's increases again, proof that the second jaw touched the beam. Courtesy of S. Redaelli [18].

5.2 Highlight results

During two shifts of 24 hours, the collimator prototype was tested for the first time in realistic machine conditions and with beam. The following sections review some of the main results, i.e. the ones with major outcome for future LHC operation.

5.2.1 Jaw positioning

Data shown in Figure 5.5 is taken from the first attempt of jaw centering with the highest intensity beam (about 3×10^{13} protons from 4 batches of 72 bunches). The first high BLM peak corresponds to the right jaw moving down to a distance of 6 σ from the beam center, taking into account a horizontal beam size of 0.7 mm as measured in the machine. The beam center is determined after about 0.3 hours of operations when, after scraping the beam with the right jaw at a 5.2 σ half-opening, the left jaw is moved in steps of 100 μm until another high peak is observed on the BLM signal.

Smaller movements were then performed to ensure that the two jaws were really placed symmetrically around the beam: with a series of motor steps of 50 μm for each

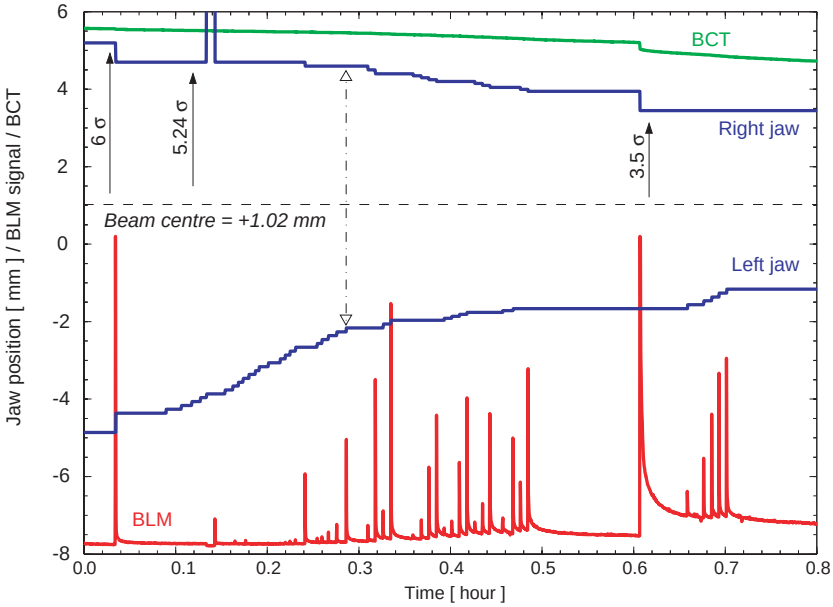

Figure 5.5: Example of a jaw centring performed during the SPS prototype beam tests as shown in Figure 5.4. Jaw positions (blue lines) are given in millimetres with respect to the collimator centre, the BLM signal (red line) and the beam intensity as measured with a Beam Current Transformer (green line) are given in arbitrary units. The top time scale gives the time of the day in absolute value while the bottom scale gives the amount of time spent since the start of the shift. The beam size for these tests was measured as $\sigma = 0.7$ mm. See also [18].

jaw alternatively (between 0.3 and 0.5 hours), the signal returned by the BLM presented sequences of loss peaks of comparable heights. The centering of the collimator gap around the beam with 50 μm accuracy was achieved. The following remarks should be noted:

- a displacement deeper into the beam of one of the two jaws provoked a significant drop in beam intensity, as it can be seen in Figure 5.5 when the right jaw moved from 4 to 3.5 σ (around 0.6 hours),

- informations like beam size and half-openings of jaws in units of sigma come from emittance measurements with wire scans and MAD calculations of Twiss parameters at the collimator location,

- as mentioned above, the alignment and centering procedure described in this section refers to the very first attempts at high intensities, which required extra attention and a longer time (0.5 hour) than the other cases at lower intensities (usually 10 to 20 minutes),

- centering the prototype jaws around the beam implies for the beam orbit to be accurately controled: a stability of $\pm$ 10 μm for up to 16 circulating bunches was established most of the time during the test.

5.2.2 Beam tail population

One feature of the beam losses that was observed early during the tests was the influence of beam tail repopulation on the shape of the BLM signal. Figure 5.6 presents a zoom on one of the signal peaks measured when moving one of the jaw closer to the beam.

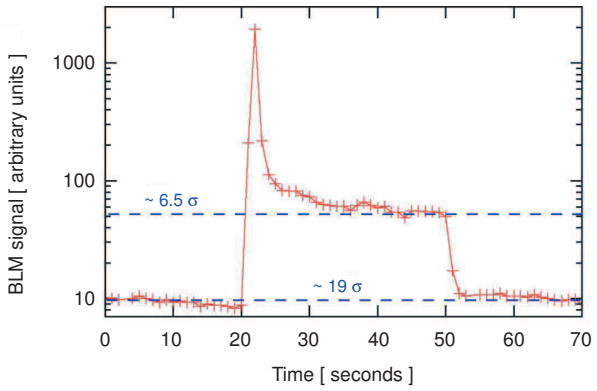

Figure 5.6: Shape of the BLM signal while moving a prototype jaw. One of the jaws is moved from $\sim 19\ \sigma$ (maximum retraction) down to $6.5\ \sigma$ around $t = 20$ s, and the ensuing peak follows an exponential decrease over 30 seconds, when it was expected to drop back to its original level shortly after.

The BLM signal jumps when the jaw touches the beam (after 20 seconds), but does not drop back fast to its original value, as one would naively expect since the jaw only cuts part of the beam (see Figure 5.5). Instead the signal decreases following an exponential-like law and reaches a plateau up until 50 seconds. After that time, the jaw is moved out back to $19\ \sigma$ (fully retracted position) and simultaneously the BLM signal drops down to its original level meaning that no more losses are detected. After the first SPS session, the team in charge of the electronics did several tests along with the analysis of the many measurements performed with the prototype: the conclusion was that this feature is a true beam related signal coming from a physics process that is not well understood. During the second session, experiments were performed to analyze this beam tail phenomenon. Basically, a jaw movement is done with two degrees of freedom: (1) the time interval between consecutive displacements and (2) the amplitude of the jaw movement.

Repopulation rate

The speed at which the depleted section of the beam distribution gets repopulated was studied using the prototype collimator. This is done by moving one of the jaws from "out" to a constant half-opening setting ($6.5\ \sigma$ in the studied example) with different time intervals between the IN and OUT positions. In the following, the basic time interval is taken as $\tau = 30$ seconds. Experiments were performed with increasing and decreasing waiting times: Figure 5.7 gives the relation between BLM signal and repopulation time, which allows concluding that the amount of beam repopulated at the sharp edge created by a collimator jaw is *proportional with time*.

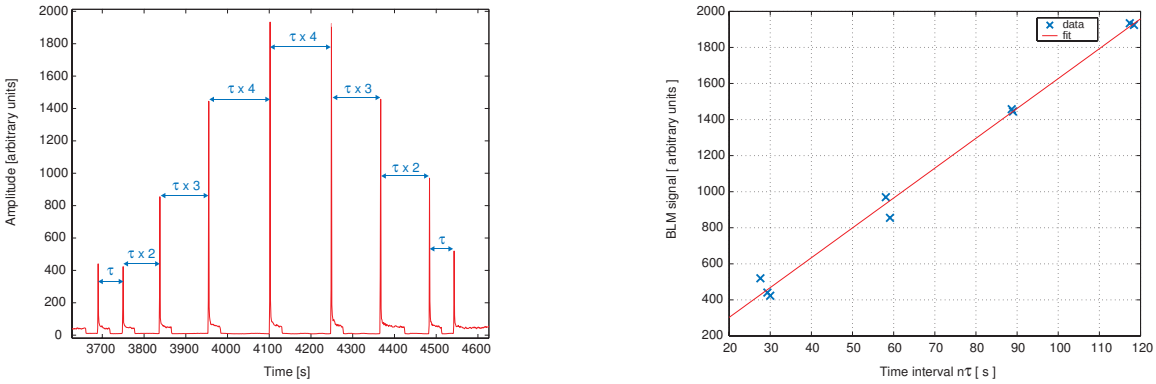

Figure 5.7: Left: Scan of the beam tail population performed during the SPS beam tests at low beam intensities using one prototype jaw. Jaw displacements are done with increasing time intervals (in units of τ, with $\tau = 30$ s) to check for the time dependance of the beam tail repopulation. A test with decreasing time intervals was also performed immediately afterwards. - Right: Fit of data from the scan of beam tail repopulation rate. Time intervals are taken from the end of each plateau to the next high signal event.

Shape of the beam edge

One can get an idea of the shape of the beam edge by scraping it with one of the collimator jaws at variable depth, with regular time intervals to get the same tail population for each displacement (as the reshaping rate is directly proportional with time, see previous section). Results of prototype tests at high intensities are shown in Figure 5.8. Similar profiles were measured with beams of different intensities and with different collimator depths. The data shows that *the beam distribution at the beam edges presents an exponential shape*.

The SPS results show that it is rather difficult to have a precision beyond 50 μm on the knowledge of the collimation center after calibration in the SPS: after setting the first jaw to its nominal position, the repopulation of the tail of the beam distribution creates a disturbing effect on the alignment of the second jaw. Future beam tests could allow having a better understanding of the dynamics involved and the shape of the reconstructed tails. This is important for the design of the automatic alignment procedure for LHC operation.

5.3 Collimator jaw robustness to direct beam impact

Another prototype of LHC horizontal secondary collimator was installed in the SPS TT40 beam extraction line to perform robustness tests of the whole collimator structure (jaw, tank, supports, cooling and electronics). The test facility allows extracting $3{\times}10^{13}$ protons at 450 GeV onto a collimator. The pulse length is 7 μs and the transverse size of the extracted beam is $0.7{\times}1.2$ mm^2. These parameters lead to a total amount of 2 MJ of extracted energy dumped which gets dumped onto a prototype jaw. For comparison, this corresponds to the full Tevatron beam or 0.5 kg of TNT. The LHC collimators are designed to survive *twice* that number according to accident scenarios. To measure the

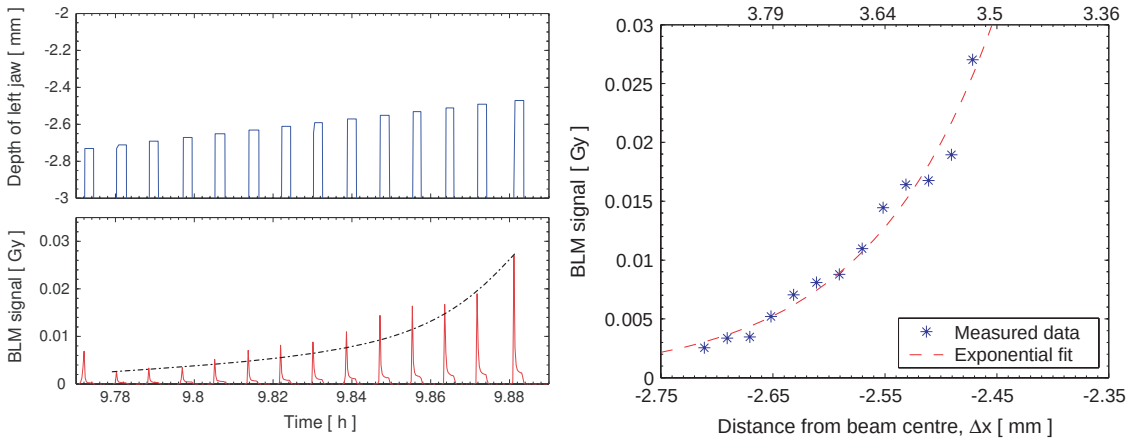

Figure 5.8: Scan of the beam tail population performed during the SPS beam tests with high beam intensities. Jaw displacements are done with increasing depth values (left). Before each step, the jaw is retracted and kept at a distance of $\sim 25\ \sigma$ from the beam centre for a fixed time to reproduce the same tail population. The shape of the repopulated tail is seen to follow an exponential law (right). Courtesy of S. Redaelli [18].

evolution of temperature in the jaw material after each impact, 4 temperature sensors (one at each corner, see Figure 5.9 below) are installed about 1 mm deep inside the CFC and graphite blocks. Each jaw was repeatedly hit by five full intensity shots with different impact parameters, from 1 to 5 mm. Several shots were then performed at a constant offset of 5 mm but with lower beam intensity.

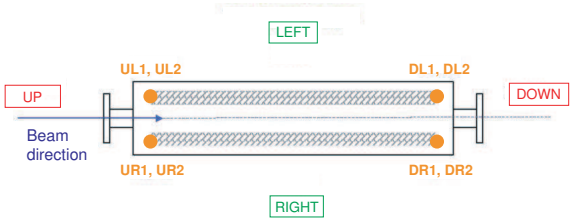

Figure 5.9: Locations of the temperature sensors in the collimator jaws for the TT40 prototype experiments. Sensors are named after their position in the collimator: UL stands for Up-Left corner, DR for Down-Right, and so on.

After a period of time needed to lower the radiation level induced by this test, the prototype was disassembled and checked. No sign of damage was observed, except the progressing loss of temperature sensors in the jaws after each high intensity impact, as seen on Figure 5.10. This plot also shows that the maximum temperature increase observed for impacts at full intensity is of the order of 20 $^{\circ}$C, which agrees with estimation done with ANSYS [77]. This feature would have to be further studied, as radiation may have altered the data taken by the sensors (some of them even stopped working). The temperature acquisition rate was too low (30 sec) for the peaks to be considered as the real temperature extrema.

Besides the jaws, the robustness of the support structure was also tested during the

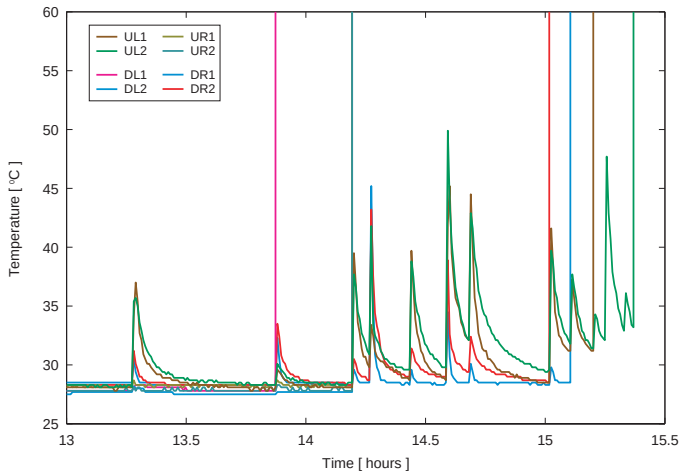

Figure 5.10: Variation along time of the temperature measured by the different sensors located within the collimator jaws for the TT40 prototype experiments. Each temperature peak is created by the impact of a LHC-like beam of increasing intensity onto the two prototype jaws. The peaks that reach a temperature larger than 55 °C could not be used for the rest of the measurements. This problem is still under investigations.

TT40 experiments. Checking the prototype after the tests showed that the support eventually suffered some deformation, on the order of 300-350 μm. This can be explained from calculations performed with ANSYS, which indicate that the expected deformation of the support, taking into account all thermodynamic effects and elasto-plastic behaviour of components, reaches a peak value of 357 μm, as seen in Figure 5.11. The deformation is avoided by the use of different materials in the jaw support. This will be demonstrated in future studies.

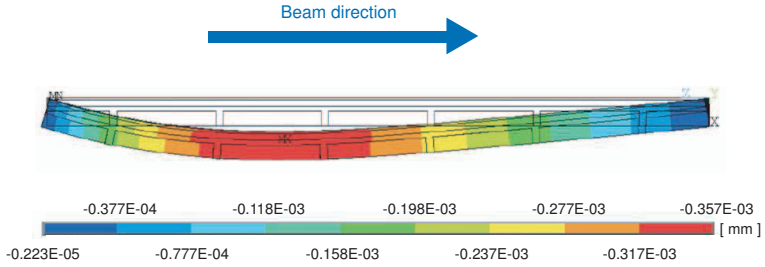

Figure 5.11: Results of ANSYS simulations on permanent deformation of the copper support of the collimator prototype jaws. The peak deviation is estimated at 357 μm. Courtesy of A. Bertarelli and A. Dallocchio [78].

Conclusion (french)

Le Large Hadron Collider (LHC) du Conseil Européen pour la Recherche Nucléaire (CERN) fait circuler et se collisionner des faisceaux de protons à 7 TeV, une énergie entre 100 et 1000 fois supérieure à celle des expériences les plus abouties à ce jour. Ce rapport de thèse présente le design et le niveau de performance du système de collimation de faisceau permettant d'atteindre une telle énergie sans risquer d'endommager l'un des aimants supraconducteurs de la machine.

La partie théorique des travaux de thèse consistait en l'élaboration d'un programme informatique afin de simuler (1) les faisceaux de protons du LHC, (2) leurs interactions avec le système de collimation et les 144 blocs de matériaux dont celui-ci est constitue (72 collimateurs comprenant 2 blocs chacun) et (3) la statistique des pertes éventuelles de protons à l'intérieur des divers éléments de la machine. Les outils numériques développes permettent de localiser les protons perdus avec une résolution de 10 cm, à comparer avec les 27 km de circonférence pour l'anneau du LHC. Le niveau de performance des divers stages de développement du système de collimation est évalué à partir de campagnes de simulations portant sur plusieurs millions de particules dont les trajectoires sont suivis et enregistrées sur quelques centaines de tours. Les études des cartes de pertes protoniques présentées dans ce rapport constituent une première en terme de détails pour une machine de cette envergure. L'inefficacité locale du système est appréciée avec une résolution de 0.000002 % (soit 2×10^{-6}/m) quand le niveau de quench (simplifié) pour des pertes lentes de faisceau à 7 TeV est estime à 0.00002 % (soit 2×10^{-5}/m). Une telle précision a permis d'optimiser le système de collimation dans toutes ses phases. Une liste des éléments et régions de la machine présentant des niveaux de pertes locales jugés trop élevés a pu être établie. Les prédictions les plus récentes indiquent que le système de collimation complet peut supporter un taux de perte d'environ 1.6×10^{11} protons/s pour l'énergie de faisceau maximale (7 TeV). A partir de cette valeur, si on considère un temps de vie de faisceau égal au minimum toléré lors des opérations (soit 0.2 h), l'intensité maximale de chaque faisceau est limité à 40 % de la valeur nominale initialement prévue (3×10^{14} protons). Si on tient compte des différents modèles d'erreurs pouvant s'appliquer au LHC, l'intensité est alors encore plus réduite. Le cas traité pour cette thèse est celui d'une erreur sur l'orbite idéale du faisceau, et les études donnent une limitation à 27 % de l'intensité nominale seulement. Par contre, si la machine est utilisée avec des faisceaux maintenus à leur énergie d'injection (450 GeV), le taux de perte toléré est alors de 3.8×10^{12} protons/s pour un temps de vie minimum de 0.1 h (environ 540 % de l'intensité nominale). Dans ces conditions, une erreur

d'orbite peut réduire la performance du système de collimation par un facteur 2.

Les tests expérimentaux menés au SPS (Super Proton Synchrotron, au CERN) pendant la thèse ont permis d'obtenir les premières données sur l'interaction d'un prototype de collimateur avec un faisceau de protons à 270 GeV. Le signal indiquant les pertes présentent une forme inattendue et suit une décroissance exponentielle ; cette allure est liée aux phénomènes physiques de repopulation de faisceau dans les régions "nettoyées" par le collimateur. Le temps de décroissance du signal induit alors une limitation dans la précision de l'alignement des mâchoires du prototype autour du faisceau. Un deuxième prototype a par ailleurs été utilisé pour vérifier la solidité du matériau choisi pour les mâchoires des collimateurs.

Les travaux présentés dans cette thèse de doctorat donnent une référence sur la performance attendue du système de collimation betatronique complet (avant toute amélioration) du LHC au cours des premières années de fonctionnement. En l'état, l'efficacité de la collimation pour le LHC est déjà supérieure à celle de tout autre système similaire implanté dans d'autres machines. D'autres études sont en cours au CERN afin d'estimer avec la même précision l'efficacité des collimateurs chargés de nettoyer la distribution en énergie de chaque faisceau (c.a.d. d'éliminer les protons dont l'énergie est trop différente de l'énergie nominale). Avec les résultats obtenus au cours de cette thèse, ceci devrait permettre de mettre en place une procédure générale de mise en service pour l'ensemble du système de collimation du LHC (tous les 72 collimateurs). La prochaine étape consiste à trouver des solutions mécaniques (nouveaux matériaux et/ou nouveau design) afin d'optimiser la collimation de faisceau de sorte à atteindre les valeurs d'intensité nominale et "ultime".

Conclusion

The Large Hadron Collider (LHC) at the European Organization for Nuclear Research (CERN) requires beams with unprecedented stored energy. The present state-of-the-art is extended by 2-3 orders of magnitude. This doctoral thesis describes the final design of a sophisticated collimation system that will allow handling these high intensity 7 TeV proton beams, while avoiding heat deposition into the super-conducting accelerator magnets.

In the theoretical part of the work powerful computer models were set up for simulating (1) proton beam halo in the LHC, (2) its interaction with the 144 blocks of collimator materials (72 two-sided collimators) and (3) residual proton losses in the machine elements. Losses were analyzed with a spatial resolution of 0.1 m over the 27 km of the LHC lattice. Massive tracking campaigns were performed for millions of particles over hundreds of turns in order to estimate the performance of the LHC collimation system during its various stages of development. It is the first time that beam losses in an accelerator are analyzed with this detail over this length.

The loss studies achieved a resolution in cleaning efficiency of 0.000002 % (2×10^{-6}/m) over the quoted 0.1 m of accelerator length. This is lower than the predicted (simplified) quench limit for slow losses at 7 TeV of 0.00002 % (2×10^{-5}/m). Extensive simulation studies guided the optimization of the overall collimation system. The performance of the final system (which is presently under construction) was analyzed in detail. Critical loss locations for betatron losses were identified and the overall performance limits established. It is predicted that the LHC collimation system (before its possible upgrade) can handle loss rates of up to 1.6×10^{11} p/s at 7 TeV beam energy. For the specified minimum beam lifetime of 0.2 h this would correspond to about 40 % of the foreseen nominal LHC beam intensity (3×10^{14} p). The performance reach is lower with imperfections (for example it reduces to 27 % with the nominal LHC orbit allowance). At injection energy of 450 GeV, loss rates of up to 3.8×10^{12} p/s can be handled (corresponding to $\sim$ 540 % of nominal intensity) with a minimum beam lifetime of 0.1 h. The specified orbit reduces performance reach at injection by about a factor 2.

In the experimental part of the thesis the first beam loss measurements with an LHC prototype collimator are presented from experiments in the SPS accelerator at 270 GeV. Unexpected but physical tails in beam losses are shown. The observed slow decay of beam losses due to collimator movements did limit the accuracy in the collimator setup and will induce limitations in the accuracy and speed of beam-based collimator optimization for the LHC. Other experiments verified the required robustness of LHC collimators.

The work presented here establishes the expected ideal performance of the LHC betatron collimation system during the first years of operation (before any upgrade). The system will be much more efficient than any comparable system before. Presently further studies are ongoing at CERN to analyze the momentum cleaning system in similar detail, to develop detailed plans for commissioning of the overall system with its 144 blocks of material and to include further imperfections into the simulation of cleaning efficiency. Studies will also start in the near future on solutions for a system upgrade that would then allow achieving the foreseen nominal and ultimate intensities for the LHC.

Bibliography

[1] *LHC Design Report - Volume I: The LHC Main Ring*, CERN Editorial Board, CERN-2004-003, 2004.

[2] http://atlas.web.cern.ch/Atlas/index.html, ATLAS collaboration.

[3] http://aliceinfo.cern.ch/, ALICE collaboration.

[4] http://cmsinfo.cern.ch/Welcome.html, CMS collaboration.

[5] http://lhcb.web.cern.ch/lhcb/, LHC$_b$ collaboration.

[6] *Requirements for the LHC collimation system*, R. Assmann et al., proceedings of the European Particle Accelerator Conference EPAC02, Paris, France, 2002.

[7] *Optics of a two stage collimation system*, J.B. Jeanneret, Physical Review Special Topics: Accelerators and Beams, 1998.

[8] *Numerical optimization of collimator jaw orientations and locations in the LHC*, D. Kaltchev, M.K. Craddock, R.V. Servranckx and J.B. Jeanneret, proceedings of the Particle Accelerator Conference PAC97, Vancouver, Canada, 1997.

[9] *CAS - CERN Accelerator School: 5th General accelerator physics course*, CERN 94-01 vol. 1, 1994.

[10] *Transverse beam dynamics*, M. Martini, lecture from the JUAS course, 2003.

[11] *Longitudinal beam dynamics*, L. Rinolfi, lecture from the JUAS course, 2003.

[12] *Total cross section, elastic scattering and diffraction dissociation at the LHC*, TOTEM collaboration, CERN/LHCC 97-49, pp. 10-21, 1997.

[13] *Transverse and Longitudinal Beam Collimation in a High-Energy Proton Collider (LHC)*, N. Catalan-Lasheras, CERN-THESIS-2000-019.

[14] *Overview of the LHC dynamic aperture studies*, M. Böge et al., proceedings of the Particle Accelerator Conference PAC97, Vancouver, Canada, 1997.

[15] *The LHC dynamic aperture*, J.-P. Koutchouk for the LHC Team, proceedings of the Particle Accelerator Conference PAC99, Portland, USA, 1999.

[16] *Equilibrium beam distribution and halo in the LHC*, R. Assmann, F. Schmidt, F. Zimmermann, proceedings of the European Particle Accelerator Conference EPAC02, Paris, France, pp. 1326-1328, 2002.

[17] *USPAS Jan 2002 Accelerator School - Introduction to accelerator physics*, G. Dugan from Cornell University, Lecture 10 - Single particle acceleration, http://www.lns.cornell.edu/dugan/USPAS/, 2002.

[18] *LHC aperture and commissioning of the collimation system*, S. Redaelli, R. Assmann, G. Robert-Demolaize, proceedings of the Chamonix XIV Workshop, 2005.

[19] *The Construction of the Low-β triplets for the LHC*, R. Ostojic et al., LHC Project Report 836, 2005.

[20] *The proton collimation system of HERA*, M. Seidel, PhD report, DESY-94-103, 1994.

[21] *Moliere's theory of multiple scattering*, H.A. Bethe, Physical Review 89, pp. 1256-1266, 1953.

[22] *Passage of particles through matter*, Particle Data Group web page, the Review of Particle Physics: 2005 Reviews Tables and Plots (http://durpdg.dur.ac.uk/lbl/index.html), 2005.

[23] *Cosmic-ray theory*, B. Rossi and K. Greisen, Review of Modern Physics vol. 13, pp. 262-268, 1941.

[24] *Cross-section formulae for specific processes*, R.M. Barnett et al., Physical Review D, vol. 54 Issue 1, pp. 179-198, 1996.

[25] *Correlations between total cross sections and slopes*, A.F. Martini, M.J. Menon and J. Montanha, Brazilian Journal of Physics vol. 34, pp. 263-267, 2004.

[26] *Diffractive interactions of hadrons at high energies*, K. Goulianos, Physics Reports vol. 101, pp. 171-219, 1983.

[27] *Atomic and nuclear properties of materials*, R.M. Barnett et al., Physical Review D, vol. 54 Issue 1, pp. 72-73, 1996.

[28] *Proton-nuclei cross-section at 20 GeV*, G. Bellettini et al., Nuclear Physics vol. 79, pp. 609-624, 1966.

[29] *Neutron-nucleus inelastic cross-sections from 160 to 375 GeV/c*, T.J. Roberts et al., Nuclear Physics vol. 159, p. 56, 1979.

[30] *Hadron-nucleus elastic scattering at 70, 125 and 175 GeV/c*, A. Schiz et al., Physical Review D, vol. 21 Issue 11, pp. 3010-3022, 1980.

[31] *The Scattering of alpha and beta particles by matter and the structure of the atom*, E. Rutherford, Philosophical Magazine Series 6 vol. 21,pp. 669-688, 1911.

[32] *HyperPhysics* website, http://hyperphysics.phy-astr.gsu.edu/hbase/hframe.html, 2005.

[33] *Single-beam lifetime*, A. Wrulich in CERN Accelerator School "5th General accelerator physics course", CERN 94-01 v1, 1994.

[34] *Touschek scattering in HERA and LHC*, F. Zimmermann, M.P. Zorzano, LHC Project Note 244, 2000.

[35] *Estimates of annual proton doses in the LHC*, M. Lamont, LHC Project Note 375, 2005

[36] *The LHC vacuum system*, O. Gröbner in CERN Accelerator School on "Vacuum Technology for Particle Accelerators", Snekersten, Denmark, CERN Yellow Report CERN-99-05, 1999, pp. 291-306.

[37] *Synchrotron radiation*, R.P. Walker in CERN Accelerator School "5th General accelerator physics course", CERN 94-01 v1, 1994.

[38] *Radiation damping*, R.P. Walker in CERN Accelerator School "5th General accelerator physics course", CERN 94-01 v1, 1994.

[39] *Synchrotron radiation dominated hadron colliders*, E. Keil, CERN SL/97-13 (AP), April 1997.

[40] *Beam-beam interactions*, W. Herr in CERN Accelerator School "5th Intermediate accelerator physics course", CERN 2006-002, 2006, pp. 379-410.

[41] *Preliminary beam-based specifications for the LHC collimators*, R. Assmann et al., LHC Project Note 277, 2002.

[42] *Safe injection into LHC*, E. Carlier, proceedings of the Chamonix XII Workshop, 2003.

[43] *Reliability analysis of the LHC beam dumping system*, R. Filippini, E. Carlier, L. Ducimetiere, B. Goddard, J. Uythoven, LHC Project Report 811, proceedings of the Particle Accelerator Conference PAC05, Knoxville, USA, 2005.

[44] *Protection of the LHC against unsynchronised beam aborts*, B.Goddard, R.Assmann, E.Carlier, J.Uythoven, J.Wenninger, W.Weterings, proceedings of the European Particle Accelerator Conference EPAC06, Edinburgh, Scotland, 2006.

[45] *How can we loose the beam ? Beam loss scenarios and strategies for the design of the protection systems*, R. Schmidt, proceedings of the Chamonix XII Workshop, 2003.

[46] *Collimators and cleaning: could that limit the LHC performance ?*, R. Assmann, proceedings of the Chamonix XII Workshop, 2003.

[47] *Impact of injection kicker failures*, B. Goddard, presentation at the LHC Collimation Working Group, March 2003.

[48] *Quench levels and transient beam losses in the LHC magnets*, J.B. Jeanneret, D. Leroy, L. Oberli and T. Trenckler, LHC Project Report 44, 1996.

[49] *Instabilities*, K. Schindl in CERN Accelerator School "5th Intermediate accelerator physics course", CERN 2006-002, 2006, pp 321-342.

[50] Official FLUKA website, http://www.fluka.org/

[51] Collimator design proposal to the AB LHC Technical Committee (LTC) on June 25th, 2003.

[52] *Requirements for the LHC collimators associated to impedance/heating aspects*, F. Ruggiero and L. Vos, presentation at the LHC Collimation Working Group, January 31st, 2003.

[53] *An improved collimation system for the LHC*, R. Assmann et al., proceedings of the European Particle Accelerator Conference EPAC04, Lucerne, Switzerland, 2004.

[54] *The mechanical design for the LHC collimators*, A. Bertarelli et al., proceedings of the European Particle Accelerator Conference EPAC04, Lucerne, Switzerland, 2004.

[55] *LARP meetings: the Secondary Collimator project*, CERN-LARP collaboration webpage, www-project.slac.stanford.edu/ilc/ilcdocs_interface/meetings2/editor/larp_meeting_list.asp

[56] *SixTrack, Users Reference Manual*, F. Schmidt, CERN SL/94-56 (AP), 1994.

[57] *A symplectic sixdimensional thin-lens formalism for tracking*, G. Ripken and F. Schmidt, CERN-SL-95-12, 1995.

[58] *The MAD program, user's reference manual*, H. Grote and F.C. Iselin, CERN-SL/90-13, revised 1995.

[59] *K2, A software package evaluating collimation systems in circular colliders (manual)*, T. Trenkler and J.B. Jeanneret, CERN SL/94105 (AP), 1994.

[60] *Status of Robustness Studies for the LHC Collimation*, R. Assmann, J.B. Jeanneret and D. Kaltchev, proceedings of the Asian Particle Accelerator Conference APAC01, Beijing, China, 2001.

[61] *Efficiency for the Imperfect LHC Collimation System*, R. Assmann, J.B. Jeanneret and D. Kaltchev, proceedings of the European Particle Accelerator Conference EPAC02, Paris, France, 2002.

[62] *Tools for Predicting Cleaning Efficiency in the LHC*, R. Assmann et al., LHC Project Report 639, 2003.

[63] Collimation Project webpage for the extended version of the SixTrack tracking code for collimation studies: http://lhc-collimation-project.web.cern.ch/lhc-collimation-project/code-tracking.htm .

[64] *Monte Carlo techniques*, Particle Data Group web page, the Review of Particle Physics: 2005 Reviews Tables and Plots (http://durpdg.dur.ac.uk/lbl/index.html), 2005.

[65] *RANLUX: a FORTRAN implementation of the high-quality pseudorandom number generator of Lüscher*, F. James, Computer Physics Communications 79, pp. 111-114, 1994.

[66] LHC optics web home: http://proj-lhc-optics-web.web.cern.ch/proj-lhc-optics-web/

[67] LHC functional layout database webpage: http://layout.web.cern.ch/layout/

[68] *The Construction of the Low-β triplets for the LHC*, R. Ostojic et al., LHC Project Report 836, 2005.

[69] *Boites de distribution pour l'alimentation electrique du LHC*, P. Trilhe, TS-Note-2004-017, 2004.

[70] *Transverse beam dynamics*, E. Wilson in CERN Accelerator School "5th General accelerator physics course", CERN 94-01 v1, 1994.

[71] S. Fartoukh and J.B. Jeanneret (CERN), private conversation.

[72] *Quadrupole alignment and closed orbits at LEP: a test ground for LHC*, J. Wenninger, LHC Project Note 104, 1998.

[73] *Racing to the 'God Particle'*, discussion forum, http://www.freerepublic.com/focus/news/734739/posts

[74] *Aspects of machine induced background in the LHC experiments*, G. Corti, V. Talanov, proceedings of the Chamonix XV Workshop, 2006.

[75] *Standard Model Higgs Discovery Potential of CMS in the $H \rightarrow WW \rightarrow l\nu l\nu$ channel*, A.-S. Giolo-Nicollerat, CMS Conference Report, presented at Physics at LHC, Cracow, Poland, July 2006.

[76] *RtPlot - Real Time Plotting Uitility*, http://members.surfbest.net/dbai@surfbest.net/RtPlot/

[77] *Mechanical design for robustness of the LHC collimators*, A. Bertarelli et al., proceedings of the Particle Accelerator Conference PAC05, Knoxville, USA, 2005.

[78] *Effects of the 450GeV accident case (TT40 experiment) on the jaw metal support (intermediate report)*, A. Bertarelli and A. Dallocchio, presentation at the LHC Collimation Working Group, September 2005.

[79] *Non-linearities and resonances*, E. Wilson in CERN Accelerator School "5th General accelerator physics course", CERN 94-01 v1, 1994.

[80] S. Fartoukh (CERN), private conversation.

[81] *Space charge*, K. Schindl in CERN Accelerator School "5th Intermediate accelerator physics course", CERN 2006-002, 2006, pp. 305-320.

[82] *Single-beam collective effects in the LHC*, E. Keil and F. Ruggiero, CERN SL/95-09, LHC Note 313, 1995 (see also http://rgo2.home.cern.ch/rgo2/lhc95/lhc95.html).

Appendix A

Derivation of the equations of motion in a circular accelerator

For all accelerators, particles should ideally travel on one particular trajectory known as the *design orbit*. In the particular case of circular machines (as shown in Figure *A*.1) like the LHC, the design orbit is curved and requires **bending forces**.

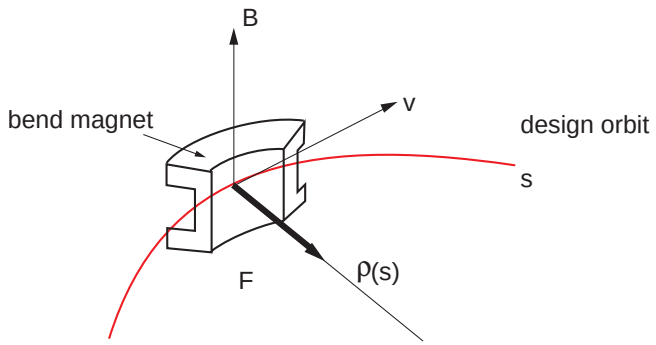

Figure A.1: Example of a reference trajectory (in red), i.e. design orbit, along a given lattice; ρ stands for the bending radius of the dipole magnets of the lattice. Taken from [10].

In a realistic beam of finite size, particles are distributed in the transverse planes around the design orbit. Considering any given longitudinal s location in the machine, the transverse position of the design orbit corresponds to the *beam centre*. The deviations of ther particles away from the beam centre must remain small all along the path of the design orbit, therefore **focusing forces** are needed. Both bending and focusing forces can be achieved with electromagnetic fields; such forces can be expressed by the Lorentz force:

$$\mathbf{F} = q \cdot (\mathbf{E} + \mathbf{v} \times \mathbf{B}) \ , \tag{A.1}$$

with q the electric charge of the considered particles, $\mathbf{v}$ the velocity of these particles and $\mathbf{E}$, $\mathbf{B}$ respectively the electric and magnetic fields used in the considered accelerator. These two fields are handled separately, with the magnetic component being used to bend and

focus the beam while the electric component accelerates the beam and works to keep its structure constant versus time.

Let's consider the case of a circular machine and neglect the drift spaces in between the magnets: the design orbit is then a circle, also assumed to be in the horizontal plane, and one can then consider a *moving* coordinate system $(\mathbf{u}_x, \mathbf{u}_y, \mathbf{u}_s)$ travelling along the design orbit, as pictured in Figure A.2. With this Figure, if one considers a magnetic field pointing in the positive z direction, then a positively (negatively) charged particle will circulate in a clockwise (counterclockwise) direction. In this moving coordinate system, one can define the curvatures ρ_x and ρ_y of trajectories in both planes; the arc length s is used as independent coordinate (instead of time t) to define the particle trajectory. Therefore, with $\mathbf{r}$ being the radius vector describing the particle position, one gets:

$$\mathbf{v} = \frac{d\mathbf{r}}{dt} = \frac{dl}{dt} \cdot \frac{d\mathbf{r}}{dl} = \frac{dl}{dt} \cdot \frac{ds}{dl} \cdot \frac{d\mathbf{r}}{ds} = v \cdot \frac{ds}{dl} \cdot \frac{d\mathbf{r}}{ds} = v \cdot \frac{1}{l'} \cdot \mathbf{r}'$$

and

$$\frac{d^2\mathbf{r}}{dt^2} = \frac{d}{dt}(\frac{v}{l'} \cdot \mathbf{r}') = \frac{v}{l'} \cdot \frac{d}{ds}(\frac{v}{l'} \cdot \mathbf{r}') = \frac{v^2}{l'^2} \cdot (\mathbf{r}'' - \frac{l''}{l'}\mathbf{r}')$$

with the prime $'$ standing for $\frac{d}{ds}$. Hence:

$$\mathbf{p} = m\gamma \cdot \frac{d\mathbf{r}}{dt} = \frac{m\gamma \cdot v}{l'} \cdot \mathbf{r}' = \frac{p}{l'} \cdot \mathbf{r}'$$

and

$$\frac{d\mathbf{p}}{dt} = m\gamma \cdot \frac{d^2\mathbf{r}}{dt^2} = \frac{p \cdot v}{l'^2} \cdot (\mathbf{r}'' - \frac{l''}{l'} \cdot \mathbf{r}')$$

assuming no acceleration, i.e. $\mathbf{E} = 0$, $\gamma = cstt$.

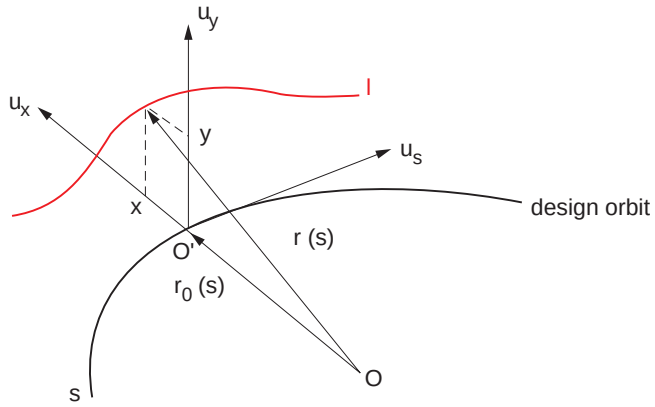

Figure A.2: Representation of the moving coordinate system $(\mathbf{u}_x, \mathbf{u}_y, \mathbf{u}_s)$ used in the following, with a particle trajectory (*black*, l coordinate) and the design orbit (*red*, s coordinate). Taken from [10].

The general equation of motion for a proton derived from (A.1) is then:

$$\mathbf{r}'' - \frac{l''}{l'} \cdot \mathbf{r}' = \frac{e}{p} \cdot l' \cdot (\mathbf{r}' \times \mathbf{B}) \tag{A.2}$$

Assuming that the design orbit bends in the horizontal plane only (no horizontal nor longitudinal components for the magnetic field), one gets the derivative of the three base vectors $(\mathbf{u}_x, \mathbf{u}_y, \mathbf{u}_s)$ as for a cylindrical coordinate system:

$$d\mathbf{u_s} = -d\theta \cdot \mathbf{u_x}, \quad d\mathbf{u_x} = d\theta \cdot \mathbf{u_s}, \quad d\mathbf{r_0} = ds \cdot \mathbf{u_s}$$

$$ds = \rho_x \cdot d\theta$$

Then by defining the *horizontal curvature* $K_x(s)$ as the inverse of the *bending radius* $\rho_x(s)$:

$$\begin{gathered} \mathbf{u_s}' = -K_x \cdot \mathbf{u_x}, \quad \mathbf{u_x}' = K_x \cdot \mathbf{u_s}, \quad \mathbf{u_y}' = 0 \\ \mathbf{r_0}' = \mathbf{u_s} \end{gathered} \tag{A.3}$$

Now from Figure A.2, one can express $\mathbf{r}$ and $\mathbf{B}$ as functions of the three coordinates x, y, s:

$$\mathbf{r}(x, y, s) = \mathbf{r_0}(s) + x \cdot \mathbf{u_x}(s) + y \cdot \mathbf{u_y}(s)$$

$$\mathbf{B}(x, y, s) = B_s(x, y, s) \cdot \mathbf{u_s}) + B_x(x, y, s) \cdot \mathbf{u_x}(s) + B_y(x, y, s) \cdot \mathbf{u_y}(s)$$

Therefore:

$$\mathbf{r}' = (1 + K_x \cdot x) \cdot \mathbf{u_s} + x' \cdot \mathbf{e_x} + y' \cdot \mathbf{e_y}$$

$$\mathbf{r}'' = (K_x' \cdot x + 2K_x \cdot x') \cdot \mathbf{u_s} + (x'' - K_x - K_x^2 \cdot x) \cdot \mathbf{e_x} + y'' \cdot \mathbf{e_y}$$

Assuming that there is no solenoid field, i.e. $B_s = 0$, one gets:

$$\mathbf{r}' \times \mathbf{B} = (x' \cdot B_y - y' \cdot B_x) \cdot \mathbf{u_s} - (1 + K_x \cdot x) \cdot B_y \cdot \mathbf{e_x} + (1 + K_x \cdot x) \cdot B_x \cdot \mathbf{e_y}$$

Inserting these expressions into the equation of motion (A.2) and identifying the coefficients of $\mathbf{u_x}$ and $\mathbf{u_y}$ yields:

$$\begin{gathered} x'' - \frac{l''}{l'} \cdot x' = (1 + K_x \cdot x) \cdot (K_x - \frac{e}{p} \cdot l' \cdot B_y) \\ y'' - \frac{l''}{l'} \cdot y' = (1 + K_x \cdot x) \cdot \frac{e}{p} \cdot l' \cdot B_x \end{gathered} \tag{A.4}$$

On the design orbit:

$$x = x' = y = y' = 0 \ \text{(equilibrium)}$$

$$p = p_0 \ \text{(design momentum)}$$

$$l' = \frac{dl}{ds} = 1$$

$$B_y(0,0,s) = B_{y_0}, \quad B_x(0,0,s) = 0$$

Then from (A.4): $\frac{1}{\rho_x} = \frac{e}{p_0} \cdot B_{y_0}$; in practical units, this expression can be rewritten:

$$B_{y_0} \cdot \rho_x \, [Tesla \cdot m] = 3.3356 \cdot p_0 \, [GeV/c] \tag{A.5}$$

Remark: (A.4) can be generalized to design orbits in 3-dimensional space (with *radial* ρ_x and *vertical* ρ_y bendings) as follows:

$$\begin{aligned} x'' - \frac{l''}{l'} \cdot x' &= (1 + K_x \cdot x + K_y \cdot y) \cdot (K_x - \frac{e}{p} \cdot l' \cdot B_y) \\ y'' - \frac{l''}{l'} \cdot y' &= (1 + K_x \cdot x + K_y \cdot y) \cdot (K_y - \frac{e}{p} \cdot l' \cdot B_x) \end{aligned} \tag{A.6}$$

The system (A.4) can also be linearized using:

- a $1^s t$ order approximation of the path length element dl:

$$d\sigma \simeq (\rho_x + x) \cdot d\theta = (\rho_x + x) \cdot K_x \cdot ds = (1 + K_x \, x) \cdot ds$$

$$\Leftrightarrow \sigma' = 1 + K_x$$

- a $1^s t$ order expansion of particle momentum p in terms of *momentum deviation* δ:

$$p = p_0 \cdot (1 + \delta) \Leftrightarrow \delta = \frac{p - p_0}{p_0} \equiv \frac{\Delta p}{p_0},$$

  with p_0 the design momentum,

- a $1^s t$ order series expansion of fields B_x and B_y: one has

$$B_x(x,y,s) = B_{x_0} + (\frac{\partial B_x}{\partial x})_0 \cdot x + (\frac{\partial B_x}{\partial y})_0 \cdot y \ ,$$

$$B_y(x,y,s) = B_{y_0} + (\frac{\partial B_y}{\partial x})_0 \cdot x + (\frac{\partial B_y}{\partial y})_0 \cdot y \ .$$

With B_{x_0} neglected (curvature in the horizontal plane only) and

$$\begin{aligned} K_0 &= \frac{e}{p_0} \cdot (\frac{\partial B_y}{\partial x})_0, \\ \underline{K_0} &= \frac{e}{p_0} \cdot (\frac{\partial B_x}{\partial x})_0, \end{aligned} \tag{A.7}$$

respectively the regular and skew normalized quadrupole gradients, one can use Maxwell equations for the magnetic field

$$\nabla \cdot \mathbf{B} = 0, \quad \nabla \times \mathbf{B} = \mathbf{0}$$

to get

$$\frac{\partial B_x}{\partial x} = -\frac{\partial B_y}{\partial y}, \quad \frac{\partial B_y}{\partial x} = \frac{\partial B_x}{\partial y},$$

then using (A.7) with the previous result in the series expansion of the fields gives:

$$\begin{aligned} \frac{e}{p_0} \cdot B_x(x,y,s) &\simeq \underline{K_0} \cdot x + K_0 \cdot y \\ \frac{e}{p_0} \cdot B_y(x,y,s) &= \frac{1}{\rho_x} + K_0 \cdot x - \underline{K_0} \cdot y \end{aligned} \tag{A.8}$$

Inserting these three approximations into (A.4) gives, to the 1^{st} order in x, x', y ,y' and δ:

$$\boxed{\begin{aligned} x'' + (K_0 + \frac{1}{\rho_x^2}) \cdot x &= \frac{1}{\rho_x} \cdot \frac{\Delta p}{p_0} + \underline{K_0} \cdot y \\ y'' - K_0 \cdot y &= \underline{K_0} \cdot x \end{aligned}} \tag{A.9}$$

The term $\underline{K_0}$ introduces *linear coupling*; the term in δ is the *chromatic* term which causes an equilibrium orbit shift due to momentum deviation. The terms K_0 and ρ_x^{-2} are the *gradient focusing* and *weak sector magnet focusing*.

<u>*Remark*</u>: equation (A.9) can be generalized to design orbits in 3-dimensional space (with *radial* ρ_x and *vertical* ρ_y bendings) to get the equations of motion in the approximation of linear beam optics:

$$\begin{aligned} x'' + (K_0 + \frac{1}{\rho_x^2}) \cdot x &= \frac{1}{\rho_x} \cdot \frac{\Delta p}{p_0} + (\underline{K_0} - \frac{1}{\rho_x \cdot \rho_y}) \cdot y \\ y'' - (K_0 - \frac{1}{\rho_y^2}) \cdot y &= \frac{1}{\rho_y} \cdot \frac{\Delta p}{p_0} + (\underline{K_0} - \frac{1}{\rho_x \cdot \rho_y}) \cdot x \end{aligned} \tag{A.10}$$

Most design orbits are made of *piecewise flat curves* either in the horizontal or vertical plane, hence one can consider $\rho_x^{-1}(s) \cdot \rho_y^{-1}(s) = 0$. The transverse linear equations of

motion (A.10) describe the individual particle trajectory measured from the desing orbit (which is the trivial solution $x = y = 0$ for $\delta = 0$).

Using z for either transverse coordinate x or y and $K_z(s)$ the corresponding focusing function, and assuming that all particles have no energy spread (ie. $\frac{\Delta p}{p_0} = 0$), equation (A.9) can be generalized to:

$$z''(s) + K_z(s) \cdot z(s) = 0 \tag{A.11}$$

Equation (A.11) is also called the Hill's equation. It is useful to think of this equation as the harmonic oscillator one with a time dependent spring constant. In the case of a circular machine like the LHC, the focusing function $K_z(s)$ has the peridocity of the lattice

$$K_z(s + L) = K_z(s), \tag{A.12}$$

where L is the length of a machine's cell (the machine being composed of N identical cells, the circumference $\mathcal{C}$ of the machine comes as $\mathcal{C} = N \cdot L$). A solution to Hill's equation can be written as:

$$z(s) = z_{betatron}(s) = \sqrt{A_z \beta_z(s)} \sin(\mu_z(s) + \mu_{z_0}), \tag{A.13}$$

$\beta_z(s)$ is the amplitude modulation of the oscillation in the according plane and is referred to as the *betatron function*, and $\mu_z(s)$ is the *phase advance* of this oscillation, defined as:

$$\mu_z(s) = \int_0^s \frac{ds}{\beta_z(s)}$$

From equation (A.13), the invariants of motion are the amplitude A_z and the initial phase μ_{z_0}. By taking the derivative of the Hill's solution, one has:

$$z'(s) = \sqrt{A_z \beta_z(s)} \sin(\mu_z(s) + \mu_{z_0}) \cdot \frac{1}{2} \beta_z' \frac{1}{\beta_z} \; + \; \sqrt{A_z \beta_z(s)} \cos(\mu_z(s) + \mu_{z_0}) \cdot \frac{d\mu_z'(s)}{ds}$$

which leads to:

$$\beta_z(s)(z'(s))^2 - \beta_z'(s)\, z(s)\, z'(s) + \frac{1}{\beta_z(s)} z^2(s) = -A_z \sin^2(\mu_z(s) + \mu_{z_0}) \cdot \frac{1}{4}(\beta_z'(s))^2 \; + \; A_z$$

hence

$$\boxed{\beta_z(s) \cdot (z'(s))^2 + 2\alpha_z(s) \cdot z(s) \cdot z'(s) + \gamma_z(s) \cdot z^2(s) = A_z} \tag{A.14}$$

with $\alpha_z(s) = -\frac{1}{2}\beta_z'(s)$ and $\gamma_z(s) = \frac{1+\alpha_z^2(s)}{\beta_z(s)}$. The parameters α_z, β_z and γ_z are called the *Twiss parameters*; from equation (A.14), it appears that, for a given position s in the machine, the projection of the particle trajectory in a one-dimensional phase space $z - z'$ has an elliptic shape of area πA_z (e.g. Figure A.3).

This area remains constant for any s along the machine, even though the shape of the ellipse is s-dependent: all trajectories will remain inside or on this phase-space ellipse when the particles move around the accelerator. Since the area is invariant, the Louisville's theorem implies that the phase-space density is invariant close to any phase-space trajectory in each plane (assuming the particle energy constant and neglecting any coupling effects).

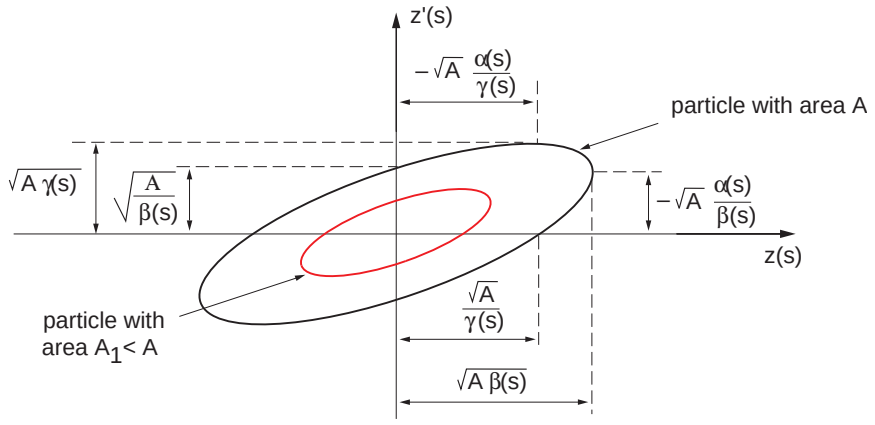

Figure A.3: Dimensions of the phase-space ellipse at a given location in the machine in function of the corresponding Twiss parameters. Taken from [10].

It is convenient here to define the notion of *beam emittance* related to the area of the ellipse as follows:

$$\text{area of the ellipse} = \pi \cdot \epsilon$$

One can define a statistical quantity, the root mean square emittance

$$\epsilon_{rms,z} = \sqrt{\overline{z^2 z'^2} - \overline{z z'}^2}.$$

From there, one can define the *betatronic beam size* $\sigma_z^\beta(s)$ and the *beam divergence* $\omega_z(s)$ (see Figure A.4):

$$\begin{aligned} \sigma_z^\beta(s) &= z_{max}(s) = \sqrt{\epsilon_{rms,z}\beta_z(s)} \\ \omega_z(s) &= z'_{max}(s) = \sqrt{\epsilon_{rms,z}\gamma_z(s)} \end{aligned} \tag{A.15}$$

To simplify the equation of motion (A.10) in the uncoupled case, the transverse coordinates z, z' can be normalized locally; starting from equation (A.14), one gets:

$$\beta_z(s) \cdot (z'(s))^2 + 2\alpha_z(s) \cdot z(s) \cdot z'(s) + \gamma_z(s) \cdot z^2(s)$$

$$= \beta_z(s) \cdot [\frac{\gamma_z(s)}{\beta_z(s)} \cdot z^2(s) + (z'(s))^2 + 2\frac{\alpha_z(s)}{\beta_z(s)} \cdot z(s) \cdot z'(s)]$$

$$= \beta_z(s) \cdot [\frac{\gamma_z(s)}{\beta_z(s)} \cdot z^2(s) + (z'(s) + \frac{\alpha_z(s)}{\beta_z(s)} \cdot z(s))^2 - \frac{\alpha_z^2(s)}{\beta_z^2(s)} \cdot z^2(s)]$$

$$= \beta_z(s) \cdot [(\frac{\gamma_z(s)}{\beta_z(s)} - \frac{\alpha_z^2(s)}{\beta_z^2(s)}) \cdot z^2(s) + (z'(s) + \frac{\alpha_z(s)}{\beta_z(s)} \cdot z(s))^2]$$

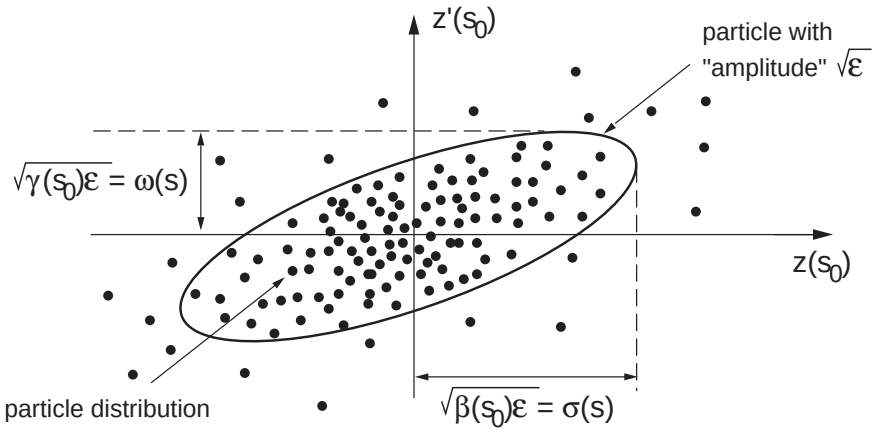

Figure A.4: Sample particle distribution in phase space z-z' for an emittance ϵ_z. Taken from [10].

$$= \frac{1}{\beta_z(s)}(\beta_z(s)\gamma_z(s) - \alpha_z^2(s)) \cdot z^2(s) + \frac{1}{\beta_z(s)}(\beta_z(s) \cdot z'(s) + \alpha_z(s) \cdot z(s))^2$$

$$= \frac{1}{\beta_z(s)} \cdot z^2(s) + \frac{1}{\beta_z(s)}(\beta_z(s) \cdot z'(s) + \alpha_z(s) \cdot z(s))^2$$

$$= \epsilon_z \quad \text{by definition of the invariant of motion.}$$

From there one can use (Z, Z') as the normalized coordinates for (z, z'), defined by:

$$Z^2 + Z'^2 = N_z^2$$

with:

$$\begin{aligned} Z(s) &= \frac{1}{\sigma_z(s)} \cdot z(s) \\ Z'(s) &= \frac{1}{\sigma_z(s)}(\alpha_z(s) \cdot z(s) + \beta_z(s) \cdot z'(s)) \end{aligned} \tag{A.16}$$

and N_z an integer number referred to as the *normalized amplitude* of the considered particle; the system above writes with matrices:

$$\begin{pmatrix} Z(s) \\ \\ Z'(s) \end{pmatrix} = \frac{1}{\sigma_z(s)} \begin{pmatrix} 1 & 0 \\ \\ \alpha_z(s) & \beta_z(s) \end{pmatrix} \begin{pmatrix} z(s) \\ \\ z'(s) \end{pmatrix} \tag{A.17}$$

Using these normalized coordinates, one can treat the motion of particles in a circular accelerator as a rotation, and calculate the coordinates at any point of the machine using an according transformation matrix. From equations (A.13) and (A.16):

$$Z(s) = \frac{1}{\sigma_z(s)} \cdot z(s) = \sin(\mu_z(s) + \mu_{z_0}) \tag{A.18}$$

and

$$Z'(s) = \frac{1}{\sigma_z(s)}(\alpha_z(s) \cdot z(s) + \beta_z(s) \cdot z'(s))$$

$$\Leftrightarrow Z'(s) = \alpha_z(s) \cdot \sin(\mu_z(s) + \mu_{z_0}) + \frac{1}{2}\beta'_z(s) \cdot \sin(\mu_z(s) + \mu_{z_0}) + \cos(\mu_z(s) + \mu_{z_0})$$

$$\Leftrightarrow Z'(s) = \cos(\mu_z(s) + \mu_{z_0}) \tag{A.19}$$

using the definition given for the Twiss parameters. Therefore, for a particle travelling from point 1 to point 2 in the machine, one gets:

$$\begin{pmatrix} Z_2(s) \\ \\ Z'_2(s) \end{pmatrix} = \begin{pmatrix} \cos(\Delta\mu_{1-2}) & \sin(\Delta\mu_{1-2}) \\ \\ -\sin(\Delta\mu_{1-2}) & \cos(\Delta\mu_{1-2}) \end{pmatrix} \begin{pmatrix} Z_1(s) \\ \\ Z'_1(s) \end{pmatrix} \tag{A.20}$$

with $\Delta\mu_{1-2}$ the difference in phase advance between the two locations. An important quantity is the *tune* $Q_z = \frac{\Delta\mu_{turn}}{2\pi}$ of the machine, i.e. the phase advance over one turn. In circular accelerators, the tune is always chosen to be an irrational number to avoid resonances.

The solution to the equation of motion for any on-momentum particle is now well established; considering now the real case of a distribution of particles with some energy spread, one has to add a term to the betatronic solution to Hill's equation:

$$z(s) = z_{betatron}(s) + D_z(s) \cdot \frac{\Delta p}{p_0}, \tag{A.21}$$

with $\frac{\Delta p}{p_0}$ the relative momentum deviation from p_0 and $D_z(s)$ the dispersion function in the corresponding transverse plane that fulfills the particular inhomogeneous Hill's equation:

$$D''_z(s) + K_x(s) \cdot D_z(s) = \frac{1}{\rho(s)}.$$

As for the $\beta_z(s)$ function, $D_z(s)$ depends only on the lattice and not on the beam parameters. In the following, the dispersion function $D_x(s)$ in the horizontal plane will be considered larger than the vertical one $D_y(s)$.

Appendix B

Resonances in a circular accelerator

In section 1.1.2 it was mentioned that the tune Q_z in a given plane must always be chosen to be an irrational number to avoid resonances. The reason stands in the form of the solutions of Hill's equation (A.11) to get the equation of the closed orbit for off-momentum particles. Considering that a spread Δp in momentum can form an additional component $F(s)$ to the Lorentz force, equation (A.11) now writes:

$$z''(s) + K_z(s) \cdot z(s) = F(s) \tag{B.1}$$

In [9] is given the general periodic solution $Z(s)$ to (B.1):

$$Z(s) = \frac{\sqrt{\beta(s)}}{2\sin(\pi Q)} \cdot \oint \sqrt{\beta(t)} F(t) \cos(|\Phi(t) - \Phi(s)| - \pi Q) dt \tag{B.2}$$

From (B.2) it appears that integer values for the tune must be avoided in order to get a functional closed orbit. Some other order of resonances can be found studying the effect of magnetic field errors. If the main dipole field gets a spread ΔB, as for the momentum spread this will create an additional s-dependent component to the Lorentz force. The periodic solution $Z(s)$ is then of the same form as in equation (B.2), only $F(t)$ is different. In case of a quadrupole gradient error, a term $\Delta K(s)$ is to be added in equation (A.11):

$$z''(s) + (K_z(s) + \Delta K(s)) \cdot z(s) = 0. \tag{B.3}$$

Using transformation matrices as in [9], it can be demonstrated that the considered gradient error induces a tune shift of:

$$\Delta Q = \frac{1}{4\pi} \cdot \oint \beta(s) \Delta K(s) ds. \tag{B.4}$$

The tune shift is therefore proportional to both the gradient error and the beta function value at the location of the error. This gradient error also changes the value of $\beta(s)$ [9]:

$$\Delta\beta(s) = \frac{\beta(s)}{2\sin(2\pi Q)} \cdot \oint \beta(t) \Delta K(t) \cos(2|\Phi(t) - \Phi(s)| - 2\pi Q) dt. \tag{B.5}$$

From equation (B.5) it can be seen that half-integer values must be avoided for Q_z. Furthermore, quadrupole gradient error should be avoided in the interaction region quadrupole as the amplitude of the error is directly proportional to the amplitude of the beta function itself.

The fact that dipole field errors give integer tune resonances, and quadrupole field errors give half-integer tune resonances would tend to show that sextupole errors would lead to third-integer tune resonances. This is confirmed and reviewed in [79]. One also has to take into account occasional coupling between the two transverse planes, as seen in equation (A.9). All of the above leads to a more generic formulation of the resonance condition:

$$m \cdot Q_x + n \cdot Q_y + l = 0. \tag{B.6}$$

If equation (B.6) is fulfilled at some location of the machine, the amplitude of particles there can grow indefinitely, and a fraction of the beam can get lost. One can obtain the working diagram of the machine by drawing a straight line for each m, n, l values derived from equation (B.6) in a (Q_x, Q_y) plot, as in Figure B.1.

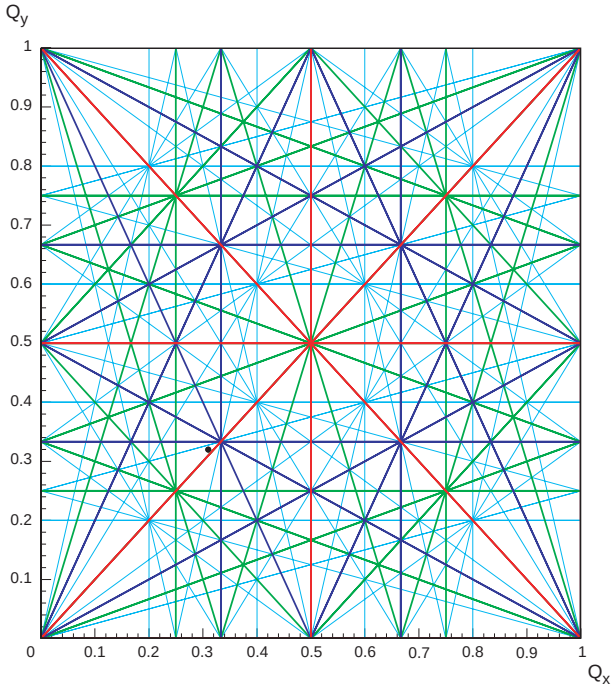

Figure B.1: LHC working diagram for the transverse tunes. The first 5 orders of resonances only are shown. The black spot represents the LHC working at 7 TeV. Courtesy of S. Fartoukh.

When trying to find the optimal combination of parameters $<m, n, l>$, one has to find a location in the working diagram far away from the first 10 to 15 orders in order to avoid strong effects [80]. From Figure B.1, it can be seen that it is convenient to look for such a position close to the diagonals of the second order of resonances (red lines, representing the cases $Q_x = Q_y$ and $Q_x = -Q_y$), where the density of resonance lines gets smaller.

Example of beam-induced tune shift: space charge effect

Within a LHC beam, the Coulomb forces between protons are such that the generated field is equivalent to a defocusing force. At the same time, while travelling at a speed $v = \beta_{rel}c$ close to the speed of light (β_{rel} being the relativistic factor), these protons also generate current lines that are attracted to eahc other due to the induced magnetic fields. The overall effect of these two forces is still defocusing but decreases with speed and even cancels at the speed of light.

Using circular coordinates and Maxwell's equations [81] and considering an unbunched beam with a circular cross-section a, one gets the expressions for the radial electric field E_r and the corresponding magnetic field B_Φ:

$$\begin{aligned} E_r &= \frac{I}{2\pi\varepsilon_0\beta_{rel}c} \cdot \frac{r}{a^2}, \\ B_\Phi &= \frac{I}{2\pi\varepsilon_0 c^2} \cdot \frac{r}{a^2}, \end{aligned} \tag{B.7}$$

where I stands for the beam current and ε_0 for the vacuum permittivity. Both fields are null at the center of the beam and increase linearly with r up to the edge of the beam. These two fields combine into a Lorentz force that, applied on a test proton at a radius r within the beam, writes:

$$F_r = e\left(E_r - \beta_{rel}cB_\Phi\right) \tag{B.8}$$

Using (B.7) in (B.8) yields:

$$F_r = \frac{eI}{2\pi\varepsilon_0 \cdot \beta_{rel}c} \cdot \left(1 - \beta_{rel}^2\right) \cdot \frac{r}{a^2} = \frac{eI}{2\pi\epsilon_0 \cdot \beta_{rel}c} \cdot \frac{1}{\gamma_{rel}^2} \cdot \frac{r}{a^2} \tag{B.9}$$

In the $\left(1 - \beta_{rel}^2\right)$ term of equation (B.9) the 1 stands for the electric force and the β_{rel}^2 represents the magnetic force. As described earlier, the two forces annihilate for $\beta_{rel} = 1$. By analogy, direct space-charge acts the same way as a quadrupole magnet, only that the induced force is defocusing in both planes.

Still using the same reasoning as for equation (B.3), one gets:

$$z''(s) + \left(K_z(s) + K_{SC}(s)\right) \cdot z(s) = 0 \tag{B.10}$$

with $K_{SC}(s)$ the perturbation term from the defocusing action from direct space-charge. One can expand this term using equation (B.9) (converted to transverse cartesian coordinates) and the round beams assumption in the expression of z":

$$z" = \frac{d^2z}{ds^2} = \frac{1}{\beta_{rel}^2c^2} \cdot \frac{d^2z}{dt^2} = \frac{\ddot{z}}{\beta_{rel}^2c^2} = \frac{1}{\beta_{rel}^2c^2} \cdot \frac{F_z}{m_0\gamma_{rel}} = \frac{2r_0I}{e\beta_{rel}^3c \cdot \gamma_{rel}^3 \cdot a^2} \cdot z \tag{B.11}$$

with r_0 the classical particle radius as defined for equation (2.18). This leads to:

$$z''(s) + \left(K_z(s) - \frac{2r_0I}{e\beta_{rel}^3c \cdot \gamma_{rel}^3 \cdot a^2}\right) \cdot z(s) = 0 \tag{B.12}$$

In equation (B.12), the negative sign of the direct space-charge term represents its overall defocusing effect. By integrating $K_{SC}(s)$ over the circumference of the machine, one gets the direct space-charge tune shift for round, bunched beams and small amplitude particles [82]:

$$\Delta Q_{SC} = -\frac{r_0 N \sqrt{2\pi}}{\sigma_s \cdot R \cdot \epsilon_N \cdot \beta_{rel} \gamma_{rel}^2} \quad , \tag{B.13}$$

with N is the beam density, σ_s the rms bunch length, $R = 4242.89$ m the average machine radius and ϵ_N the normalized beam emittance. In the LHC case, one has

$$\Delta Q_{SC}^{inj} = -1.34 \times 10^{-3} \text{ at 450 GeV}$$

$$\Delta Q_{SC}^{coll} = -9.57 \times 10^{-6} \text{ at 7 TeV},$$

values small enough not to cause significant reduction of beam lifetime.

Appendix C

Beam lifetime from emittance growth

The effect on the beam shape from mechanisms like intra-beam scattering and Touschek scattering is characterized by the corresponding *emittance growth time* t_ϵ, which is defined by:

$$\epsilon(t) = \epsilon_0 \cdot \exp\left(\frac{t}{t_\epsilon}\right) \tag{C.1}$$

where ϵ_0 is the initial value of the beam emittance. As defined in equation (2.1), the beam lifetime τ corresponds to the amount of time required to reduce the initial beam population by a factor e:

$$N_p(t) = N_0 \cdot \exp\left(-\frac{t}{\tau}\right) \ . \tag{C.2}$$

One can then correlate the emittance growth time to the beam lifetime stating $\tau = k \cdot t_\epsilon$. An analytic expression for k can be derived from calculations on the beam population. Figure C.1 illustrates the principles of such calculations.

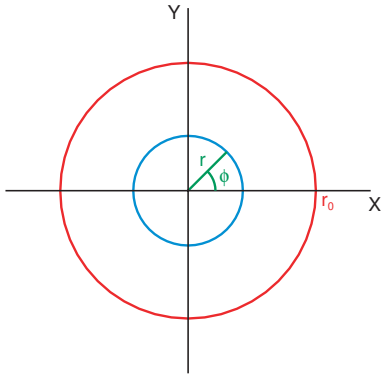

Figure C.1: Definition of parameters for calculations on beam population. Cylindrical coordinates are used to define the particles distribution in normalized real-space $X - Y$. r_0 is taken as the maximum allowed radius of the beam distribution.

In normalized space, the beam population can be represented by a Gaussian distribution function, using cylindrical coordinates r, ϕ. After a time $t = \tau$, from equation (C.2) one gets:

$$\frac{N_p(\tau)}{N_0} = \frac{1}{2\pi \cdot \sigma^2} \cdot \int_0^{r_0} \exp\left(-\frac{r^2}{2 \cdot \sigma^2}\right) r dr \cdot \int_0^{2\pi} \phi \cdot d\phi = \frac{1}{e} \ , \tag{C.3}$$

where $\sigma = \sqrt{\beta \cdot \epsilon(\tau)}$ is the betatron unit beam size in the transverse motion case (see Appendix A). With the change of variable $u = \frac{r^2}{2\sigma^2}$, the first integral in equation (C.3) writes:

$$\int_0^{r_0} \exp\left(-\frac{r^2}{2 \cdot \sigma^2}\right) r dr = \int_0^{\frac{r_0^2}{2\sigma^2}} \sigma^2 \cdot \exp(-u) du = \sigma^2 \cdot \left[1 - \exp\left(\frac{r_0^2}{2\sigma^2}\right)\right] \ . \tag{C.4}$$

With $\int_0^{2\pi} \phi \cdot d\phi = 2\pi$, inserting equation (C.4) into equation (C.3) leads to:

$$1 - \exp\left(\frac{r_0^2}{2\sigma^2}\right) = \frac{1}{e} \ . \tag{C.5}$$

In Figure C.1, r_0 is set either by the geometric aperture (e.g. aperture restriction from collimators) of by the dynamic aperture if it is smaller than the geometric one (see section 1.3.2). This limitation is given as $r_0 = n \cdot \sqrt{\beta \cdot \epsilon_0}$ with n an integer number. Together with equation C.5, this gives:

$$1 - \exp\left(\frac{n^2}{2} \cdot \frac{\epsilon_0}{\epsilon(\tau)}\right) = \frac{1}{e} \ . \tag{C.6}$$

Using equation (C.1), one gets:

$$\begin{aligned} &\frac{n^2}{2} \cdot \frac{1}{\exp\left(\frac{\tau}{t_\epsilon}\right)} = ln\left(1 - \frac{1}{e}\right) \\ \\ &\Leftrightarrow \frac{n^2}{2} \cdot \frac{1}{ln\left(1 - \frac{1}{e}\right)} = \exp(k) \\ \\ &\Leftrightarrow k = ln\left[\frac{n^2}{2} \cdot \frac{1}{ln\left(1 - \frac{1}{e}\right)}\right] \end{aligned} \tag{C.7}$$

The obtained expression for k is valid for both transverse and longitudinal motion and for all machines; the only difference comes from the value chosen for n:

- $n = n_1$ in transverse motion, with n_1 the normalized half-opening of the aperture limitation of the machine (half-gap of collimators in the LHC case).
- $n = \frac{\Delta E_b/E}{\delta E/E_0}$ in longitudinal motion, where $\Delta E_b/E$ is the RF bucket half height (see section 1.3.3) and $\delta E/E_0$ is the beam rms-energy spread.

Appendix D

Collimation database - 450 GeV

Table D.1: Tracking parameters for collimators installed on the Beam 1 line for injection energy

Name	**Length [m]**	**Angle [rad]**	**Material**	**Halfgap [m]**	**N$_z$ [σ]**
TCL.5R1.B1	1.00	0.000	CU	1.116	900.0
TCTH.4L2.B1	1.00	0.000	W	0.548	900.0
TDI.4L2	4.00	1.571	C	4.100×10^{-3}	6.8
TCTV.4L2.B1	1.00	1.571	W	0.584	900.0
TCLIA.4R2	1.00	1.571	C	6.531×10^{-3}	6.8
TCLIB.6R2	1.00	1.571	C	3.232×10^{-3}	6.8
TCP.6L3.B1	0.60	0.000	C	7.848×10^{-3}	8.0
TCSG.5L3.B1	1.00	0.000	C	5.878×10^{-3}	9.3
TCSG.4R3.B1	1.00	0.000	C	4.066×10^{-3}	9.3
TCSG.A5R3.B1	1.00	2.980	C	5.261×10^{-3}	9.3
TCSG.B5R3.B1	1.00	0.189	C	5.896×10^{-3}	9.3
TCLA.A5R3.B1	1.00	1.571	W	1.135×10^{-2}	10.0
TCLA.B5R3.B1	1.00	0.000	W	1.053×10^{-2}	10.0
TCLA.6R3.B1	1.00	0.000	W	9.726×10^{-3}	10.0
TCLA.7R3.B1	1.00	0.000	W	6.952×10^{-3}	10.0
TCTH.4L5.B1	1.00	0.000	W	1.001	900.0
TCTV.4L5.B1	1.00	1.571	W	0.744	900.0
TCL.5R5.B1	1.00	0.000	CU	1.114	900.0
TCDQA.4R6.B1	3.00	0.000	C	1.495×10^{-2}	8.0
TCDQB.4R6.B1	3.00	0.000	C	1.512×10^{-2}	8.0
TCSG.4R6.B1	1.00	0.000	C	1.339×10^{-2}	7.0

continued on next page

Name	Length [m]	Angle [rad]	Material	Halfgap [m]	N_z [σ]
continued from previous page					
TCP.D6L7.B1	0.60	1.571	C	4.263×10^{-3}	5.7
TCP.C6L7.B1	0.60	0.000	C	6.037×10^{-3}	5.7
TCP.B6L7.B1	0.60	2.225	C	5.044×10^{-3}	5.7
TCSG.A6L7.B1	1.00	2.463	C	6.087×10^{-3}	6.7
TCSG.B5L7.B1	1.00	2.504	C	7.226×10^{-3}	6.7
TCSG.A5L7.B1	1.00	0.710	C	7.374×10^{-3}	6.7
TCSG.D4L7.B1	1.00	1.571	C	4.767×10^{-3}	6.7
TCSG.B4L7.B1	1.00	0.000	C	6.699×10^{-3}	6.7
TCSG.A4L7.B1	1.00	2.349	C	6.650×10^{-3}	6.7
TCSG.A4R7.B1	1.00	0.808	C	6.680×10^{-3}	6.7
TCSG.B5R7.B1	1.00	2.470	C	7.683×10^{-3}	6.7
TCSG.D5R7.B1	1.00	0.897	C	7.713×10^{-3}	6.7
TCSG.E5R7.B1	1.00	2.277	C	7.726×10^{-3}	6.7
TCSG.6R7.B1	1.00	0.009	C	1.057×10^{-2}	6.7
TCLA.A6R7.B1	1.00	1.571	W	5.865×10^{-3}	10.0
TCLA.C6R7.B1	1.00	0.000	W	1.083×10^{-2}	10.0
TCLA.E6R7.B1	1.00	1.571	W	1.056×10^{-2}	10.0
TCLA.F6R7.B1	1.00	0.000	W	6.823×10^{-3}	10.0
TCLA.A7R7.B1	1.00	0.000	W	6.718×10^{-3}	10.0
TCTH.4L8.B1	1.00	0.000	W	0.528	900.0
TCTV.4L8.B1	1.00	1.571	W	0.558	900.0
TCTH.4L1.B1	1.00	0.000	W	1.001	900.0
TCTV.4L1.B1	1.00	1.571	W	0.744	900.0

Table D.2: Tracking parameters for collimators installed on the Beam 2 line for injection energy

Name	Length [m]	Angle [rad]	Material	Halfgap [m]	N_z [σ]
TCL.5L1.B2	1.00	0.000	CU	1.120	900.0
TCTH.4R8.B2	1.00	0.000	W	5.282×10^{-1}	900.0
TDI.4R8.B2	4.00	1.571	C	3.879×10^{-3}	6.8
TCTV.4R8.B2	1.00	1.571	W	5.584×10^{-1}	900.0
TCLIA.4L8	1.00	1.571	C	6.434×10^{-3}	6.8
TCLIB.6L8.B2	1.00	1.571	C	2.529×10^{-3}	6.8
continued on next page					

Name	Length [m]	Angle [rad]	Material	Halfgap [m]	N_z [σ]
continued from previous page					
TCP.D6R7.B2	0.60	1.571	C	4.168×10^{-3}	5.7
TCP.C6R7.B2	0.60	0.000	C	6.167×10^{-3}	5.7
TCP.B6R7.B2	0.60	2.225	C	5.059×10^{-3}	5.7
TCSG.A6R7.B2	1.00	2.466	C	6.029×10^{-3}	6.7
TCSG.B5R7.B2	1.00	2.506	C	7.080×10^{-3}	6.7
TCSG.A5R7.B2	1.00	0.709	C	7.230×10^{-3}	6.7
TCSG.D4R7.B2	1.00	1.571	C	4.781×10^{-3}	6.7
TCSG.B4R7.B2	1.00	0.000	C	6.824×10^{-3}	6.7
TCSG.A4R7.B2	1.00	2.306	C	6.662×10^{-3}	6.7
TCSG.A4L7.B2	1.00	0.735	C	6.664×10^{-3}	6.7
TCSG.B5L7.B2	1.00	2.470	C	7.800×10^{-3}	6.7
TCSG.D5L7.B2	1.00	0.897	C	7.810×10^{-3}	6.7
TCSG.E5L7.B2	1.00	2.278	C	7.831×10^{-3}	6.7
TCSG.6L7.B2	1.00	0.009	C	1.074×10^{-2}	6.7
TCLA.A6L7.B2	1.00	1.571	W	5.742×10^{-3}	10.0
TCLA.C6L7.B2	1.00	0.000	W	1.092×10^{-2}	10.0
TCLA.E6L7.B2	1.00	1.571	W	1.052×10^{-2}	10.0
TCLA.F6L7.B2	1.00	0.000	W	6.751×10^{-3}	10.0
TCLA.A7L7.B2	1.00	0.000	W	6.865×10^{-3}	10.0
TCDQA.4L6.B2	3.00	0.000	C	1.601×10^{-2}	8.0
TCDQB.4L6.B2	3.00	0.000	C	1.620×10^{-2}	8.0
TCSG.4L6.B2	1.00	0.000	C	1.437×10^{-2}	7.0
TCTH.4R5.B2	1.00	0.000	W	1.001	900.0
TCTV.4R5.B2	1.00	1.571	W	7.441×10^{-1}	900.0
TCL.5L5.B2	1.00	0.000	CU	1.119	900.0
TCP.6R3.B2	0.60	0.000	C	7.889×10^{-3}	8.0
TCSG.5R3.B2	1.00	0.000	C	5.912×10^{-3}	9.3
TCSG.4L3.B2	1.00	0.000	C	4.067×10^{-3}	9.3
TCSG.A5L3.B2	1.00	2.981	C	5.287×10^{-3}	9.3
TCSG.B5L3.B2	1.00	0.189	C	5.929×10^{-3}	9.3
TCLA.A5L3.B2	1.00	1.571	W	1.143×10^{-2}	10.0
TCLA.B5L3.B2	1.00	0.000	W	1.060×10^{-2}	10.0
TCLA.6L3.B2	1.00	0.000	W	9.759×10^{-3}	10.0
TCLA.7L3.B2	1.00	0.000	W	6.896×10^{-3}	10.0
TCTH.4R2.B2	1.00	0.000	W	5.477×10^{-1}	900.0
TCTV.4R2.B2	1.00	1.571	W	5.838×10^{-1}	900.0
TCTH.4R1.B2	1.00	0.000	W	1.001	900.0
TCTV.4R1.B2	1.00	1.571	W	7.441×10^{-1}	900.0

Appendix E

Collimation database - 7 TeV

Table E.1: Tracking parameters for collimators installed on the Beam 1 line for collision energy

Name	**Length [m]**	**Angle [rad]**	**Material**	**Halfgap [m]**	**N$_z$ [σ]**
TCL.5R1.B1	1.00	0.000	CU	2.894×10^{-3}	10.0
TCTH.4L2.B1	1.00	0.000	W	1.326×10^{-3}	8.3
TDI.4L2	4.00	1.571	C	0.142	900.0
TCTV.4L2.B1	1.00	1.571	W	1.413×10^{-3}	8.3
TCLIA.4R2	1.00	1.571	C	0.227	900.0
TCLIB.6R2	1.00	1.571	C	0.112	900.0
TCP.6L3.B1	0.60	0.000	C	3.862×10^{-3}	15.0
TCSG.5L3.B1	1.00	0.000	C	2.986×10^{-3}	18.0
TCSG.4R3.B1	1.00	0.000	C	2.066×10^{-3}	18.0
TCSG.A5R3.B1	1.00	2.980	C	2.672×10^{-3}	18.0
TCSG.B5R3.B1	1.00	0.189	C	2.995×10^{-3}	18.0
TCLA.A5R3.B1	1.00	1.571	W	5.959×10^{-3}	20.0
TCLA.B5R3.B1	1.00	0.000	W	5.529×10^{-3}	20.0
TCLA.6R3.B1	1.00	0.000	W	5.105×10^{-3}	20.0
TCLA.7R3.B1	1.00	0.000	W	3.649×10^{-3}	20.0
TCTH.4L5.B1	1.00	0.000	W	7.551×10^{-3}	8.3
TCTV.4L5.B1	1.00	1.571	W	4.774×10^{-3}	8.3
TCL.5R5.B1	1.00	0.000	CU	2.898×10^{-3}	10.0
TCDQA.4R6.B1	3.00	0.000	C	3.924×10^{-3}	8.0
TCDQB.4R6.B1	3.00	0.000	C	3.968×10^{-3}	8.0
TCSG.4R6.B1	1.00	0.000	C	3.766×10^{-3}	7.5

continued on next page

Name	Length [m]	Angle [rad]	Material	Halfgap [m]	N_z [σ]
continued from previous page					
TCP.D6L7.B1	0.60	1.571	C	1.178×10^{-3}	6.0
TCP.C6L7.B1	0.60	0.000	C	1.668×10^{-3}	6.0
TCP.B6L7.B1	0.60	2.225	C	1.394×10^{-3}	6.0
TCSG.A6L7.B1	1.00	2.463	C	1.669×10^{-3}	7.0
TCSG.B5L7.B1	1.00	2.504	C	1.981×10^{-3}	7.0
TCSG.A5L7.B1	1.00	0.710	C	2.022×10^{-3}	7.0
TCSG.D4L7.B1	1.00	1.571	C	1.307×10^{-3}	7.0
TCSG.B4L7.B1	1.00	0.000	C	1.837×10^{-3}	7.0
TCSG.A4L7.B1	1.00	2.349	C	1.824×10^{-3}	7.0
TCSG.A4R7.B1	1.00	0.808	C	1.832×10^{-3}	7.0
TCSG.B5R7.B1	1.00	2.470	C	2.107×10^{-3}	7.0
TCSG.D5R7.B1	1.00	0.897	C	2.115×10^{-3}	7.0
TCSG.E5R7.B1	1.00	2.277	C	2.118×10^{-3}	7.0
TCSG.6R7.B1	1.00	0.009	C	2.897×10^{-3}	7.0
TCLA.A6R7.B1	1.00	1.571	W	1.539×10^{-3}	10.0
TCLA.C6R7.B1	1.00	0.000	W	2.841×10^{-2}	10.0
TCLA.E6R7.B1	1.00	1.571	W	2.772×10^{-2}	10.0
TCLA.F6R7.B1	1.00	0.000	W	1.791×10^{-3}	10.0
TCLA.A7R7.B1	1.00	0.000	W	1.763×10^{-3}	10.0
TCTH.4L8.B1	1.00	0.000	W	1.279×10^{-3}	8.3
TCTV.4L8.B1	1.00	1.571	W	1.352×10^{-3}	8.3
TCTH.4L1.B1	1.00	0.000	W	7.551×10^{-3}	8.3
TCTV.4L1.B1	1.00	1.571	W	4.775×10^{-3}	8.3

Table E.2: Tracking parameters for collimators installed on the Beam 2 line for collision energy

Name	Length [m]	Angle [rad]	Material	Halfgap [m]	N_z [σ]
TCL.5L1.B2	1.00	0.000	CU	3.103×10^{-3}	10.0
TCTH.4R8.B2	1.00	0.000	W	1.279×10^{-3}	8.3
TDI.4R8.B2	4.00	1.571	C	1.347×10^{-1}	900.0
TCTV.4R8.B2	1.00	1.571	W	1.352×10^{-3}	8.3
TCLIA.4L8	1.00	1.571	C	2.235×10^{-1}	900.0
TCLIB.6L8.B2	1.00	1.571	C	8.785×10^{-2}	900.0
continued on next page					

Name	Length [m]	Angle [rad]	Material	Halfgap [m]	N_z [σ]
continued from previous page					
TCP.D6R7.B2	0.60	1.571	C	1.152×10^{-3}	6.0
TCP.C6R7.B2	0.60	0.000	C	1.704×10^{-3}	6.0
TCP.B6R7.B2	0.60	2.225	C	1.398×10^{-3}	6.0
TCSG.A6R7.B2	1.00	2.466	C	1.653×10^{-3}	7.0
TCSG.B5R7.B2	1.00	2.506	C	1.941×10^{-3}	7.0
TCSG.A5R7.B2	1.00	0.709	C	1.982×10^{-3}	7.0
TCSG.D4R7.B2	1.00	1.571	C	1.311×10^{-3}	7.0
TCSG.B4R7.B2	1.00	0.000	C	1.871×10^{-3}	7.0
TCSG.A4R7.B2	1.00	2.306	C	1.827×10^{-3}	7.0
TCSG.A4L7.B2	1.00	0.735	C	1.827×10^{-3}	7.0
TCSG.B5L7.B2	1.00	2.470	C	2.139×10^{-3}	7.0
TCSG.D5L7.B2	1.00	0.897	C	2.141×10^{-3}	7.0
TCSG.E5L7.B2	1.00	2.278	C	2.147×10^{-3}	7.0
TCSG.6L7.B2	1.00	0.009	C	2.946×10^{-3}	7.0
TCLA.A6L7.B2	1.00	1.571	W	1.507×10^{-3}	10.0
TCLA.C6L7.B2	1.00	0.000	W	2.866×10^{-3}	10.0
TCLA.E6L7.B2	1.00	1.571	W	2.761×10^{-3}	10.0
TCLA.F6L7.B2	1.00	0.000	W	1.772×10^{-3}	10.0
TCLA.A7L7.B2	1.00	0.000	W	1.802×10^{-3}	10.0
TCDQA.4L6.B2	3.00	0.000	C	4.201×10^{-3}	8.0
TCDQB.4L6.B2	3.00	0.000	C	4.252×10^{-3}	8.0
TCSG.4L6.B2	1.00	0.000	C	4.040×10^{-3}	7.5
TCTH.4R5.B2	1.00	0.000	W	7.551×10^{-3}	8.3
TCTV.4R5.B2	1.00	1.571	W	4.774×10^{-3}	8.3
TCL.5L5.B2	1.00	0.000	CU	3.100×10^{-3}	10.0
TCP.6R3.B2	0.60	0.000	C	3.882×10^{-3}	15.0
TCSG.5R3.B2	1.00	0.000	C	3.003×10^{-3}	18.0
TCSG.4L3.B2	1.00	0.000	C	2.066×10^{-3}	18.0
TCSG.A5L3.B2	1.00	2.981	C	2.685×10^{-3}	18.0
TCSG.B5L3.B2	1.00	0.189	C	3.012×10^{-3}	18.0
TCLA.A5L3.B2	1.00	1.571	W	6.000×10^{-3}	20.0
TCLA.B5L3.B2	1.00	0.000	W	5.561×10^{-3}	20.0
TCLA.6L3.B2	1.00	0.000	W	5.122×10^{-3}	20.0
TCLA.7L3.B2	1.00	0.000	W	3.620×10^{-3}	20.0
TCTH.4R2.B2	1.00	0.000	W	1.369×10^{-3}	8.3
TCTV.4R2.B2	1.00	1.571	W	1.419×10^{-3}	8.3
TCTH.4R1.B2	1.00	0.000	W	7.551×10^{-3}	8.3
TCTV.4R1.B2	1.00	1.571	W	4.774×10^{-3}	8.3

Appendix F

Critical beam loss locations

Table F.1: Critical loss locations for both Beam 1 and Beam 2 at injection energy (450 GeV). This list does not include locations from the IR3 momentum cleaning insertion.

Beam 1		**Beam 2**			
Q11.R3	Q27.R7	Q28.R3	MB20.L6	Q31.L7	MB11.L7
DFBA.R6	Q31.R7	Q18.L4	MB16.L6	Q27.L7	MB9.L7
MB9.R7	Q33.L8	Q10.L4	MB14.L6	Q23.L7	Q8.L7
MB11.R7	Q29.L8	Q22.R5	MB12.L6	Q19.L7	MB8.L7
Q11.R7	Q25.L8	Q28.L6	MB9.L6	MB19.L7	
MB13.R7	Q2.R8	MB28.L6	MB8.L6	Q15.L7	
Q13.R7	Q6.R8	Q25.L6	Q4.L6	MB15.L7	
Q23.R7		Q20.L6	Q11.R6	Q11.L7	

Table F.2: Critical loss locations for both Beam 1 and Beam 2 at collision energy (7 TeV). This list does not include locations from the IR3 momentum cleaning insertion.

Beam 1		**Beam 2**	
Q6.L3	Q21.R7	Q11.R6	Q9.L7
Q8.R7	MB34.L8	MB12.R6	MB9.L7
MB9.R7	Q33.L8	Q25.R6	Q8.L7
Q9.R7	Q25.L8	Q33.R6	MB8.L7
Q10.R7	Q17.L8	Q19.L7	
MB11.R7	Q16.R8	Q13.L7	
Q11.R7	Q30.R8	MB13.L7	
Q13.R7	Q22.L1	Q11.L7	
MB21.R7		MB11.L7	